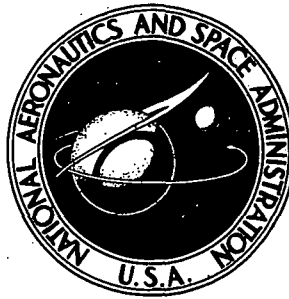


**NASA CONTRACTOR
REPORT**



N73-16778
NASA CR-2171

NASA CR-2171

**CASE FILE
COPY**

**HIGHLY LOADED MULTI-STAGE
FAN DRIVE TURBINE -
CASCADE TEST PROGRAM**

by D. G. Cherry, T. K. Staley, and M. W. Thomas

Prepared by

GENERAL ELECTRIC COMPANY

Cincinnati, Ohio 45215

for Lewis Research Center

NATIONAL AERONAUTICS AND SPACE ADMINISTRATION • WASHINGTON, D. C. • JANUARY 1973

1. Report No. NASA CR-2171	2. Government Accession No.	3. Recipient's Catalog No.	
4. Title and Subtitle HIGHLY LOADED MULTI-STAGE FAN DRIVE TURBINE - CASCADE TEST PROGRAM		5. Report Date January 1973	
		6. Performing Organization Code	
7. Author(s) D. G. Cherry, T. K. Staley, and M. W. Thomas		8. Performing Organization Report No. 72AEG268	
9. Performing Organization Name and Address General Electric Company Cincinnati, Ohio 45215		10. Work Unit No.	
		11. Contract or Grant No. NAS 3-14304	
12. Sponsoring Agency Name and Address National Aeronautics and Space Administration Washington, D. C. 20546		13. Type of Report and Period Covered Contractor Report	
		14. Sponsoring Agency Code	
15. Supplementary Notes Project Manager, Thomas P. Moffitt, Fluid System Components Division, NASA Lewis Research Center, Cleveland, Ohio			
16. Abstract Test results are presented for 19 cascades involving five plain and two tandem blade sections. High camber and/or negative reaction is associated with six of the sections. Exit Mach numbers range up to slightly above sonic. Cascade efficiency, exit flow angle and static pressure, and blade surface pressure data are reported with incidence angle, Mach number, solidity, and relative position of the tandem blades as independent variables.			
17. Key Words (Suggested by Author(s)) Cascade test High camber Low reaction Tandem blade		18. Distribution Statement Unclassified - unlimited	
19. Security Classif. (of this report) Unclassified	20. Security Classif. (of this page) Unclassified	21. No. of Pages 153	22. Price* \$3.00

TABLE OF CONTENTS

<u>Section</u>	<u>Page</u>
SUMMARY	1
INTRODUCTION	2
CASCADE SELECTION AND DESIGN	4
TEST APPARATUS AND INSTRUMENTATION	6
TEST PROCEDURE	7
DATA REDUCTION PROCEDURE	8
RESULTS AND DISCUSSION	10
APPENDICES	
A. Probe Design and Calibration Data	14
B. Definition of Symbols	16
REFERENCES	18
TABLES	19
ILLUSTRATIONS	23

LIST OF TABLES

<u>Table</u>		<u>Page</u>
I.	Comparative Vector Diagram Requirements - Stage One Rotor Hub Sections.	19
II.	Cascade Geometric Data.	20
III.	Relative Uncertainty in Calculated Efficiency.	21
IV.	Probe Calibration, Polynomial Coefficients for Static Pressure Correction Factor.	22

LIST OF ILLUSTRATIONS

<u>Figure</u>	<u>Page</u>
1. Flowpath, N1R in Turbine Design Configuration.	23
2. Flowpath, B1R in Turbine Design Configuration.	24
3. Flowpath, N2R in Turbine Design Configuration.	25
4. Flowpath, TN2R in Turbine Design Configuration.	26
5. Flowpath, B3R in Turbine Design Configuration.	27
6. Flowpath, TB3R in Turbine Design Configuration.	28
7. Flowpath, AB1R in Turbine Design Configuration.	29
8. Cascade Nomenclature.	30
9. Cascade Photograph, N1R Turbine Design Configuration.	31
10. Cascade Photograph, B1R Turbine Design Configuration.	32
11. Cascade Photograph, N2R Turbine Design Configuration.	33
12. Cascade Photograph, TN2R Turbine Design Configuration.	34
13. Cascade Photograph, B3R Turbine Design Configuration.	35
14. Cascade Photograph, TB3R Turbine Design Configuration.	36
15. Cascade Photograph, AB1R Turbine Design Configuration.	37
16. Cascade Tunnel Schematic.	38
17. Typical Traverse Chart.	39
18. Cascade Efficiency Vs. Mach Number, N1R, $i = 0^\circ$.	40
19. Exit Flow Angle Vs. Normalized Tangential Location, N1R, $i = 0^\circ$.	41
20. Exit Static Pressure Coefficient Vs. Normalized Tangential Location, N1R, $i = 0^\circ$.	42
21. Blade Surface Static Pressure Coefficient Vs. Normalized Axial Location, N1R, $\sigma/\sigma_d = 1.0$, $i = 0^\circ$.	43
22. Blade Surface Static Pressure Coefficient Vs. Normalized Axial Location, N1R, $\sigma/\sigma_d = 0.9$, $i = 0^\circ$.	44
23. Blade Surface Static Pressure Coefficient Vs. Normalized Axial Location, N1R, $\sigma/\sigma_d = 0.8$, $i = 0^\circ$.	45
24. Cascade Efficiency Vs. Mach Number, B1R.	46
25. Exit Flow Angle Vs. Normalized Tangential Location, B1R, $\sigma/\sigma_d = 1.0$.	47

LIST OF ILLUSTRATIONS (continued)

<u>Figure</u>	<u>Page</u>
26. Exit Flow Angle Vs. Normalized Tangential Location, BlR, $\sigma/\sigma_d = 0.92$.	48
27. Exit Flow Angle Vs. Normalized Tangential Location, BlR, $\sigma/\sigma_d = 0.85$.	49
28. Exit Static Pressure Coefficient Vs. Normalized Tangential Location, BlR, $\sigma/\sigma_d = 1.0$.	50
29. Exit Static Pressure Coefficient Vs. Normalized Tangential Location, BlR, $\sigma/\sigma_d = 0.92$.	51
30. Exit Static Pressure Coefficient Vs. Normalized Tangential Location, BlR, $\sigma/\sigma_d = 0.85$.	52
31. Blade Surface Static Pressure Coefficient Vs. Normalized Axial Location, BlR, $\sigma/\sigma_d = 1.0$, $i = -5.3^\circ$.	53
32. Blade Surface Static Pressure Coefficient Vs. Normalized Axial Location, BlR, $\sigma/\sigma_d = 1.0$, $i = -0.3^\circ$.	54
33. Blade Surface Static Pressure Coefficient Vs. Normalized Axial Location, BlR, $\sigma/\sigma_d = 1.0$, $i = 3.5^\circ$.	55
34. Blade Surface Static Pressure Coefficient Vs. Normalized Axial Location, BlR, $\sigma/\sigma_d = 0.92$, $i = -5.2^\circ$.	56
35. Blade Surface Static Pressure Coefficient Vs. Normalized Axial Location, BlR, $\sigma/\sigma_d = 0.92$, $i = -0.3^\circ$.	57
36. Blade Surface Static Pressure Coefficient Vs. Normalized Axial Location, BlR, $\sigma/\sigma_d = 0.92$, $i = 3.7^\circ$.	58
37. Blade Surface Static Pressure Coefficient Vs. Normalized Axial Location, BlR, $\sigma/\sigma_d = 0.85$, $i = -3.3^\circ$.	59
38. Blade Surface Static Pressure Coefficient Vs. Normalized Axial Location, BlR, $\sigma/\sigma_d = 0.85$, $i = 0.5^\circ$.	60
39. Cascade Efficiency Vs. Mach Number, N2R	61
40. Exit Flow Angle Vs. Normalized Tangential Location, N2R, $\sigma/\sigma_d = 1.0$.	62
41. Exit Flow Angle Vs. Normalized Tangential Location, N2R, $\sigma/\sigma_d = 0.9$.	63

LIST OF ILLUSTRATIONS (continued)

<u>Figure</u>	<u>Page</u>
42. Exit Flow Angle Vs. Normalized Tangential Location, N2R, $\sigma/\sigma_d = 0.8$.	64
43. Exit Static Pressure Coefficient Vs. Normalized Tangential Location, N2R, $\sigma/\sigma_d = 1.0$.	65
44. Exit Static Pressure Coefficient Vs. Normalized Tangential Location, N2R, $\sigma/\sigma_d = 0.9$.	66
45. Exit Static Pressure Coefficient Vs. Normalized Tangential Location, N2R, $\sigma/\sigma_d = 0.8$.	67
46. Blade Surface Static Pressure Coefficient Vs. Normalized Axial Location, N2R, $\sigma/\sigma_d = 1.0$, $i = -5.5^\circ$.	68
47. Blade Surface Static Pressure Coefficient Vs. Normalized Axial Location, N2R, $\sigma/\sigma_d = 1.0$, $i = -0.5^\circ$.	69
48. Blade Surface Static Pressure Coefficient Vs. Normalized Axial Location, N2R, $\sigma/\sigma_d = 1.0$, $i = 4.3^\circ$.	70
49. Blade Surface Static Pressure Coefficient Vs. Normalized Axial Location, N2R, $\sigma/\sigma_d = 0.9$, $i = -5.1^\circ$.	71
50. Blade Surface Static Pressure Coefficient Vs. Normalized Axial Location, N2R, $\sigma/\sigma_d = 0.9$, $i = -0.3^\circ$.	72
51. Blade Surface Static Pressure Coefficient Vs. Normalized Axial Location, N2R, $\sigma/\sigma_d = 0.9$, $i = 2.7^\circ$.	73
52. Blade Surface Static Pressure Coefficient Vs. Normalized Axial Location, N2R, $\sigma/\sigma_d = 0.9$, $i = 5.0^\circ$.	74
53. Blade Surface Static Pressure Coefficient Vs. Normalized Axial Location, N2R, $\sigma/\sigma_d = 0.8$, $i = -5.5^\circ$.	75
54. Blade Surface Static Pressure Coefficient Vs. Normalized Axial Location, N2R, $\sigma/\sigma_d = 0.8$, $i = -0.2^\circ$.	76
55. Blade Surface Static Pressure Coefficient Vs. Normalized Axial Location, N2R, $\sigma/\sigma_d = 0.8$, $i = 2.4^\circ$.	77
56. Cascade Efficiency Vs. Mach Number, TN2R with N2R at $\sigma/\sigma_d = 1.0$.	78
57. Exit Flow Angle Vs. Normalized Tangential Location, TN2R Turbine Design Configuration.	79

LIST OF ILLUSTRATIONS (continued)

<u>Figure</u>	<u>Page</u>
58. Exit Static Pressure Coefficient Vs. Normalized Tangential Location, TN2R Turbine Design Configuration.	80
59. Blade Surface Static Pressure Coefficient Vs. Normalized Axial Location, TN2R Turbine Design Configuration, $i = -5.1^\circ$.	81
60. Blade Surface Static Pressure Coefficient Vs. Normalized Axial Location, TN2R Turbine Design Configuration, $i = 0^\circ$.	82
61. Blade Surface Static Pressure Coefficient Vs. Normalized Axial Location, TN2R Turbine Design Configuration, $i = 4.6^\circ$.	83
62. Cascade Efficiency Vs. Mach Number, B3R.	84
63. Exit Flow Angle Vs. Normalized Tangential Location, B3R, $\sigma/\sigma_d = 1.0$.	85
64. Exit Flow Angle Vs. Normalized Tangential Location, B3R, $\sigma/\sigma_d = 0.92$.	86
65. Exit Flow Angle Vs. Normalized Tangential Location, B3R, $\sigma/\sigma_d = 0.85$.	87
66. Exit Static Pressure Coefficient Vs. Normalized Tangential Location, B3R, $\sigma/\sigma_d = 1.0$.	88
67. Exit Static Pressure Coefficient Vs. Normalized Tangential Location, B3R, $\sigma/\sigma_d = 0.92$.	89
68. Exit Static Pressure Coefficient Vs. Normalized Tangential Location, B3R, $\sigma/\sigma_d = 0.85$.	90
69. Blade Surface Static Pressure Coefficient Vs. Normalized Axial Location, B3R, $\sigma/\sigma_d = 1.0$, $i = -5.1^\circ$.	91
70. Blade Surface Static Pressure Coefficient Vs. Normalized Axial Location, B3R, $\sigma/\sigma_d = 1.0$, $i = -0.3^\circ$.	92
71. Blade Surface Static Pressure Coefficient Vs. Normalized Axial Location, B3R, $\sigma/\sigma_d = 1.0$, $i = 4.6^\circ$.	93
72. Blade Surface Static Pressure Coefficient Vs. Normalized Axial Location, B3R, $\sigma/\sigma_d = 0.92$, $i = -5.3^\circ$.	94
73. Blade Surface Static Pressure Coefficient Vs. Normalized Axial Location, B3R, $\sigma/\sigma_d = 0.92$, $i = -0.3^\circ$.	95

LIST OF ILLUSTRATIONS (continued)

<u>Figure</u>	<u>Page</u>
74. Blade Surface Static Pressure Coefficient Vs. Normalized Axial Location, B3R, $\sigma/\sigma_d = 0.92$, $i = 4.2^\circ$.	96
75. Blade Surface Static Pressure Coefficient Vs. Normalized Axial Location, B3R, $\sigma/\sigma_d = 0.92$, $i = 10.2^\circ$.	97
76. Blade Surface Static Pressure Coefficient Vs. Normalized Axial Location, B3R, $\sigma/\sigma_d = 0.85$, $i = -5.2^\circ$.	98
77. Blade Surface Static Pressure Coefficient Vs. Normalized Axial Location, B3R, $\sigma/\sigma_d = 0.85$, $i = 0^\circ$.	99
78. Blade Surface Static Pressure Coefficient Vs. Normalized Axial Location, B3R, $\sigma/\sigma_d = 0.85$, $i = 5.0^\circ$.	100
79. Blade Surface Static Pressure Coefficient Vs. Normalized Axial Location, B3R, $\sigma/\sigma_d = 0.85$, $i = 9.5^\circ$.	101
80. Cascade Efficiency Vs. Mach Number, TB3R at Turbine Design e_t .	102
81. Cascade Efficiency Vs. Mach Number, TB3R at Turbine Design e_{ax} .	103
82. Exit Flow Angle Vs. Normalized Tangential Location, TB3R Turbine Design Configuration.	104
83. Exit Flow Angle Vs. Normalized Tangential Location, TB3R, e_{ax} Reduced.	105
84. Exit Flow Angle Vs. Normalized Tangential Location, TB3R, e_{ax} Increased.	106
85. Exit Flow Angle Vs. Normalized Tangential Location, TB3R, e_t Reduced.	107
86. Exit Flow Angle Vs. Normalized Tangential Location, TB3R, e_t Increased.	108
87. Exit Static Pressure Coefficient Vs. Normalized Tangential Location, TB3R Turbine Design Configuration.	109
88. Exit Static Pressure Coefficient Vs. Normalized Tangential Location, TB3R, e_{ax} Reduced.	110
89. Exit Static Pressure Coefficient Vs. Normalized Tangential Location, TB3R, e_{ax} Increased.	111

LIST OF ILLUSTRATIONS (continued)

<u>Figure</u>	<u>Page</u>
90. Exit Static Pressure Coefficient Vs. Normalized Tangential Location, TB3R, e_t Reduced.	112
91. Exit Static Pressure Coefficient Vs. Normalized Tangential Location, TB3R, e_t Increased.	113
92. Blade Surface Static Pressure Coefficient Vs. Normalized Axial Location, TB3R Turbine Design Configuration, $i = -4.1^\circ$.	114
93. Blade Surface Static Pressure Coefficient Vs. Normalized Axial Location, TB3R Turbine Design Configuration, $i = -0.1^\circ$.	115
94. Blade Surface Static Pressure Coefficient Vs. Normalized Axial Location, TB3R Turbine Design Configuration, $i = 4.5^\circ$.	116
95. Blade Surface Static Pressure Coefficient Vs. Normalized Axial Location, TB3R Turbine Design Configuration, $i = 11.4^\circ$.	117
96. Blade Surface Static Pressure Coefficient Vs. Normalized Axial Location, TB3R, e_{ax} Reduced, $i = -4.2^\circ$.	118
97. Blade Surface Static Pressure Coefficient Vs. Normalized Axial Location, TB3R, e_{ax} Reduced, $i = -0.7^\circ$.	119
98. Blade Surface Static Pressure Coefficient Vs. Normalized Axial Location, TB3R, e_{ax} Reduced, $i = 4.7^\circ$.	120
99. Blade Surface Static Pressure Coefficient Vs. Normalized Axial Location, TB3R, e_{ax} Reduced, $i = 9.9^\circ$.	121
100. Blade Surface Static Pressure Coefficient Vs. Normalized Axial Location, TB3R, e_{ax} Increased, $i = -4.2^\circ$.	122
101. Blade Surface Static Pressure Coefficient Vs. Normalized Axial Location, TB3R, e_{ax} Increased, $i = -0.4^\circ$.	123
102. Blade Surface Static Pressure Coefficient Vs. Normalized Axial Location, TB3R, e_{ax} Increased, $i = 4.6^\circ$.	124
103. Blade Surface Static Pressure Coefficient Vs. Normalized Axial Location, TB3R, e_{ax} Increased, $i = 9.6^\circ$.	125
104. Blade Surface Static Pressure Coefficient Vs. Normalized Axial Location, TB3R, e_t Reduced, $i = -4.3^\circ$.	126
105. Blade Surface Static Pressure Coefficient Vs. Normalized Axial Location, TB3R, e_t Reduced, $i = -0.1^\circ$.	127

LIST OF ILLUSTRATIONS (concluded)

<u>Figure</u>	<u>Page</u>
106. Blade Surface Static Pressure Coefficient Vs. Normalized Axial Location, TB3R, e_t Reduced, $i = 4.5^\circ$.	128
107. Blade Surface Static Pressure Coefficient Vs. Normalized Axial Location, TB3R, e_t Reduced, $i = 9.7^\circ$.	129
108. Blade Surface Static Pressure Coefficient Vs. Normalized Axial Location, TB3R, e_t Increased, $i = -4.3^\circ$.	130
109. Blade Surface Static Pressure Coefficient Vs. Normalized Axial Location, TB3R, e_t Increased, $i = -0.3^\circ$.	131
110. Blade Surface Static Pressure Coefficient Vs. Normalized Axial Location, TB3R, e_t Increased, $i = 4.3^\circ$.	132
111. Blade Surface Static Pressure Coefficient Vs. Normalized Axial Location, TB3R, e_t Increased, $i = 10.7^\circ$.	133
112. Cascade Efficiency Vs. Mach Number, AB1R.	134
113. Exit Flow Angle Vs. Normalized Tangential Location, AB1R.	135
114. Exit Static Pressure Coefficient Vs. Normalized Tangential Location, AB1R.	136
115. Blade Surface Static Pressure Coefficient Vs. Normalized Axial Location, AB1R, $\sigma/\sigma_d = 1.0$, $i = -5.3^\circ$.	137
116. Blade Surface Static Pressure Coefficient Vs. Normalized Axial Location, AB1R, $\sigma/\sigma_d = 1.0$, $i = -0.6^\circ$.	138
117. Probe Nomenclature and Dimensional Data.	139
118. Probe Calibration, Flow Angle Correction Factor.	140
119. Probe Calibration, Static Pressure Correction Factor, P_{co}/P_I Parametric.	141
120. Probe Calibration, Static Pressure Correction Factor, θ Parametric, Negative Incidence.	142
121. Probe Calibration, Static Pressure Correction Factor, θ Parametric, Positive Incidence.	143

SUMMARY

The results of the cascade test program conducted under Task II of Contract NAS3-14304 are presented. A total of seven blade sections was selected from the plain and tandem blade turbine designs of Task III. Scale factors were determined with consideration for throat aspect ratio, number of passages, surface instrumentation, and Reynolds number. A cascade of each blade section was tested over a range of Mach numbers and incidence angles surrounding its turbine design point. Plain blade sections were tested at two successively smaller solidities in addition to their respective turbine design value. Five variations of the relative position of the forward and aft blades of one of the tandem sections were tested. Total pressure loss, exit flow angle, and exit static pressure in each case were obtained along a midspan traverse line using a calibrated, conically tipped pressure probe. Blade surface pressure data also were obtained.

Sensitivity to positive incidence, amplified by reductions in solidity, is noted for two highly cambered plain blade sections, both of which operate in the high subsonic Mach no. range. At design incidence and Mach number, there was a modest penalty in efficiency for both tandem blade sections tested compared to their corresponding plain blade sections. However, both of the tandem blade sections showed improved performance compared to the plain blade sections at high positive incidence angles. The performance of a given tandem blade pair also is seen to be markedly diminished when the passage between forward and aft blades diverges.

INTRODUCTION

The development of high-bypass-ratio turbofan engines for future aircraft propulsion schemes required the development of fan drive turbines with increasingly lower blade speeds. The requirements of minimized weight and size of such turbofan engines produce a need for turbines with increasingly high stage loading. In order to maintain high turbine efficiencies at high stage loading, advances are required in the technology of producing increased aerodynamic load capability in turbine blading by means of improved design techniques and high-lift devices.

The specific objectives of this program are to:

- Investigate analytically and experimentally aerodynamic means for increasing the turbine stage loading and turbine blade loading consistent with high efficiency for multistage highly loaded fan drive turbine configurations.
- Develop sufficient design information to determine the relative importance of changes in engine size, weight, and performance and give primary consideration to use of tandem rotors and stators, where applicable, to reduce weight or extend or improve the blading performance.
- Modify an existing three-stage highly loaded turbine rig, and adapt the rig to an overall performance test program of sufficient extent so as to obtain blade element performance.

This is a 24-month analytical and experimental investigation program to provide a turbine high-stage-loading and high-blade-loading aerodynamic technology that will be specifically applicable to multistage fan drive turbine configurations for advanced high-bypass-ratio turbofan propulsion system application. The program will be divided into two phases encompassing nine task items of activity.

The first phase will cover Task Items I, II, and III of the program which are to investigate requirements of selected advanced high-bypass-ratio turbofan systems, to carry out parametric turbine vector diagram studies, to conduct a cascade test and evaluation program, to select one design for future study, to complete a detailed aerodynamic turbine design for an existing rig, to complete the detailed blading aerodynamic design for the rig, to perform detailed blading mechanical design for the rig, to perform the turbine rig mechanical design, and to prepare the turbine rig modification drawings required to utilize the existing three-stage highly-loaded-fan turbine rig. The second phase will cover Task Items IV through IX of this proposed program to fabricate, procure, vibration bench test, fatigue endurance test, and inspect the turbine rig modifications; to instrument and calibrate the rig vehicle; to conduct a test program and to report progress, analysis, and design, as well as test and performance results.

The Task I vector diagram study results have been reported (Reference 1). Based on the results of this study, a velocity diagram was chosen for three highly loaded turbine configurations: (1) a turbine using plain blades, (2) a turbine using tandem blades and (3) another turbine using high-lift devices. Blade sections were selected from both the plain and tandem blade turbine designs (References 2 and 3, respectively) for evaluation in cascade tests. The purpose of this report is to present the results of the cascade test program (Task II).

CASCADE SELECTION AND DESIGN

Seven blade section profiles, as shown in Figures 1 through 7, were selected for evaluation in the cascade test program; four were from the plain blade turbine design (see Reference 2), two from the tandem blade turbine design (see Reference 3), and one plain section (Figure 7) corresponding to an alternate vector diagram. With the exception of the stage one stator hub section, chosen as a bench mark, blade sections were selected based on their high potential for aerodynamic problems. Relative aerodynamic challenge was judged from vector diagram requirements and predicted surface velocity distributions, taking into consideration Mach number, reaction, and gas turning angle. An identification code for the selected sections and their correspondence with the appropriate turbine design are indicated in the following list:

- N1R plain, stage 1, stator hub
- B1R plain, stage 1, rotor hub
- N2R plain, stage 2, stator hub
- TN2R tandem, stage 2, stator hub
- B3R plain, stage 3, rotor hub
- TB3R tandem, stage 3, rotor hub
- AB1R plain, stage 1, rotor hub (alternate)

The alternate plain blade section (AB1R) for the rotor hub of stage one arose from using a reduction in rotor reaction as a means of reducing the gas turning angle in the following stator. The challenging aspects of B1R (high turning angle and Mach number) and B3R (negative reaction) are combined in this blade section. Pertinent vector diagram requirements for both B1R and AB1R are given for comparison in Table I. Loading and blockage criteria and the procedure employed in designing AB1R were the same as for the plain blade turbine (see Reference 2).

Each of the five plain sections was tested at three solidities including the turbine design value. The two tandem sections were tested at turbine design solidity only. Five variations of the relative position of the forward and aft blades of the tandem rotor section were tested, including the turbine design relative position.

The principal concern in the design of the cascades was scale factor determination. The following criteria were used to select the scale factors:

- The throat aspect ratio (RH/d_o) should be greater than four in the interest of obtaining a central region of two-dimensional flow.
- The minimum number of passages should be greater than seven to allow for dissipation of end effects.
- Sections should be large enough to accommodate precision in the placement of surface instrumentation sized for adequate response time.

- Reynold's no. should be kept at a level comparable to the intended application.

Geometric data on the passages of each cascade are given in Table II; nomenclature is graphically defined in Figure 8. Photographs of each blade section assembled in its respective turbine design configuration are presented in Figures 9 through 15.

TEST APPARATUS AND INSTRUMENTATION

Testing was carried out in the General Electric Transonic Cascade Tunnel at Evendale, Ohio. The tunnel is schematically represented in Figure 16. This facility consists of a horizontal tunnel of 4 × 12 inch cross section, a 10-foot-diameter tank which houses the tunnel and serves as its exhaust plenum, connecting piping to a central air supply system, and an adjacent control room.

Dried air enters the tunnel from a four-foot screened plenum through a flexible nozzle. Semicircular drums, rotatable about a horizontal axis perpendicular to the tunnel, form the tunnel side walls. A cascade is mounted to the diametral edge of the drums at the tunnel discharge so as to direct the horizontal inlet flow downward into the tank, which exhausts to vacuum headers.

The tunnel is instrumented for measurement of both inlet and exhaust plenum conditions. Static pressure taps are located within the tunnel along the centerline of both top and bottom walls and along each drum in a plane just upstream of the cascade mounting surface. A probe mount, for traversing downstream of a cascade, and its remotely controlled drive mechanism are fixed to one of the drums.

A five-hole conically tipped probe was used to survey total and static pressure and flow angle downstream of the cascades. The probe was calibrated over a Mach number range up to 1.05 for pitch angles up to eight degrees on each side of zero. Probe design and calibration data are presented in Appendix A.

Static pressure taps, generally five on a pressure surface and five on a suction surface, were located on adjacent blade sections so as to obtain surface pressures within a given passage (see Figures 1 through 7). Tap locations were selected for definition of pressure gradients as indicated by predicted pressure distributions.

With the exception of downstream total pressure, all pressures were sensed by absolute pressure transducers having a 0 to 25 psia range and a manufacturer quoted repeatability of 0.006 psi. Downstream total pressure was sensed relative to upstream total pressure by a 0 to 5 psi range differential pressure transducer with a manufacturer quoted repeatability of 0.005 psi. All of these transducers are of the bonded strain gage type and are periodically calibrated. Each set of calibration data is compared to a polynomial curve fitted to previous data. The standard deviation from the fitted curve is typically 0.1 percent of reading.

A two-pen X-Y recorder, with inputs from pressure transducers and a linear motion potentiometer,^a was used to record total pressure loss versus probe position and inlet total pressure during each traverse. The potentiometer has a 0.002 inch resolution and a 0.5 percent linearity. The pressure scale of the recorder was calibrated using a dead weight gage. All other data were automatically read from a digital voltmeter and recorded on punched paper tape.

TEST PROCEDURE

With the blade spacing fixed, a cascade was assembled by setting all blades at the same stagger angle (γ°) and then uniformly adjusting the angle until all throat openings (d_o) fell within a ± 1 percent band about the intended value. Blade sequence was maintained for cascades of a given set of blades but varying in either solidity or relative blade position.

Each cascade was mounted to the drums and initially set for maximum positive incidence. In cases where the tunnel was not filled, the cascade position was adjusted such that the end openings were equal. The probe pitch was set at the nominal discharge angle with its roll and yaw angles at zero. Axial clearance between the blade trailing edges and the line of transverse was set, according to the cascade scale factor, to be equivalent to 150 mils at turbine design size. Cascade angle (β_1) and probe pitch angle were determined by triangulation using a combination square and a plumb line off the blade trailing edges. The uncertainty in these measurements is estimated to be ± 0.1 degree. All traversing was done at midspan.

Inlet flow uniformity was checked by monitoring the static pressures at the cascade inlet. The ratio of upstream total pressure to downstream static pressure (measured in the tank) was controlled during test as the independent flow parameter. The central passages were surveyed at the first pressure ratio to check for the presence of end effects or a separation so severe that the entire passage was filled by wake flow. In cases where the latter occurred, the incidence angle was reduced until the wake occupied approximately half or less of each passage.

Generally three or four central passages were selected for data traversing. Within one of these passages, the probe was stopped at a number of points (from 15 to 20 at zero degrees incidence and design Mach no. and 5 for all other conditions) for acquisition of digital data. The relative location of these points was marked on the traverse chart by nulling the pressure input.

DATA REDUCTION PROCEDURE

The following items were evaluated for each cascade, at each incidence angle and pressure ratio:

- cascade efficiency
- flow angle versus relative distance along the traverse line
- static pressure versus relative distance along the traverse line
- blade surface static pressure at each instrumented location

Cascade efficiency, as reported herein, is defined by the following relation:

$$\eta \equiv \left[\frac{V_{2\infty}}{V_o} \right]^2 = \frac{1 - (P_{2\infty}/P_{T2\infty})^{\frac{\gamma-1}{\gamma}}}{1 - (P_{2\infty}/P_{T1})^{\frac{\gamma-1}{\gamma}}}$$

where

$$V_{2\infty} \equiv \frac{\int (\rho_2 V_2^2) dy}{\int (\rho_2 V_2) dy}$$

Since $V_{2\infty}$ represents the velocity in the fully mixed state, implicit to the above definitions is the assumption that losses occurring between the traverse station and the fully mixed state are the result of a constant static pressure ($P_{2\infty}$) mixing process. The integrals are evaluated, assuming adiabatic two-dimensional flow, over an integral number of passages from discrete point input using the trapezoidal rule and the following streamtube equation:

$$\frac{\rho_2 V_2}{\rho_o V_o} = \left[1 - \left(\frac{P_{2\infty}}{P_{T1}} \right)^{\frac{\gamma-1}{\gamma}} \right]^{-\frac{1}{2}} \left\{ \left(\frac{P_{T2}}{P_{T1}} \right)^{\frac{\gamma-1}{\gamma}} \left[1 - \left(\frac{P_{2\infty}}{P_{T2}} \right)^{\frac{\gamma-1}{\gamma}} \right]^{\frac{1}{2}} \right\}$$

An existing General Electric computer program was used for the actual calculation of efficiencies. This program examines the input data for each streamtube and applies the Rayleigh correction when required. Values for P_{T1} and $P_{2\infty}$ were input directly from digitally acquired data. Input values for ΔP_T and y/t were read in discrete pairs from the X-Y chart. Ten to 30 pairs of data were input for each passage, depending on the complexity of the ΔP_T versus y trace. A minimum of two passages was evaluated for each X-Y chart. Cascade efficiency was determined by numerically averaging the passage efficiencies. For consistency, the same passages were evaluated for all conditions involving cascades of the same blades.

A typical traverse is shown on Figure 17. The uncertainty in reading points from the trace is ± 0.1 chart unit. Relative uncertainty depends on the proportion of the pressure scale utilized by the trace and, hence, on both efficiency level and pressure ratio. Estimated values of relative uncertainty in calculated efficiency contributed by instrumentation and reading the X-Y chart are itemized in Table III for a 0.96 efficiency level with the base of the wake assumed to occupy 25 percent of the blade spacing.

Flow angle and static pressure along the traverse line were determined using a separate computer program. Probe calibration curves (see Appendix A) and a routine for interpolating among them are built into this program. The program also checks for, and flags, indicated flow conditions beyond the calibrated range of the probe. The four static pressures from the probe and P_{T1} were input directly from digital data. The total pressure at the probe (P_{T2}) was determined from P_{T1} and the ΔP_T value read, together with relative distance along the traverse line, from the X-Y chart.

RESULTS AND DISCUSSION

Beginning with Figure 18, reduced data are presented according to the following sequence:

- each incidence angle (negative to positive)
- at each solidity (highest to lowest) or relative blade position
- for each evaluated quantity (η , β_2 , C_{p2} , C_{ps})
- for each blade section (N1R, B1R, N2R, TN2R, B3R, TB3R, AB1R)

For example, the N2R efficiency data follow the B1R surface static pressure coefficient (C_{ps}) plot for the lowest solidity and most positive incidence angle.

The coefficient form in which the blade surface and exit static pressure data are presented is defined below:

$$C_{p2} \equiv \frac{P_2 - P_{2\infty}}{P_{T1} - P_{2\infty}} \qquad C_{ps} \equiv \frac{P_{T1} - P}{P_{T1} - P_{2\infty}}$$

Exit flow angle and static pressure are plotted versus y/t , where y is tangential distance referenced to a wake center (see Figures 8 and 17). Surface pressures are plotted versus x/AW , where x is axial distance referenced to the leading edge.

The exit flow angle and static pressure data are presented as dashed lines in regions of wake flow because of small but unknown uncertainties as reported in Reference 4. The uncertainty is due to flow distortion induced by the probe in a transverse total pressure gradient. Dashed lines also are used where data are considered insufficient. The curves shown on each surface pressure figure represent the pressure distribution calculated for an incompressible potential flow. In the case of the plain blade sections, these were generated using a computer program based on the method of Bueckner and Schnackel (Reference 5). A similar program, with input specification of the trailing edge stagnation point for the forward blade, was used for the tandem blade pressure distributions.

The commentary which follows is intended, in the absence of extensive crossplotting, to bring attention to some of the significant comparisons and trends which are not directly evident in the presentation of the data.

N1R (Figures 18 through 23)

Note that these three cascades were tested at the design inlet flow angle ($i = 0^\circ$) only. Figure 18 shows a cascade efficiency of 0.98 at turbine design conditions, highest of the sections tested in this program and comparable with past General Electric experience for similar sections. Inspection of the β_2 and C_{p2} data (Figures 19 and 20) indicates a β_2 minimum (C_{p2} maximum) which shifts toward the suction side of the passage as solidity is reduced. The result is more nearly symmetric β_2 and C_{p2} profiles at $\sigma/\sigma_d = 0.8$. Except for this shift, β_2 and C_{p2} values are significantly altered by solidity

changes only in their magnitude in wake flow regions. Of interest among the surface pressure data (Figures 21 through 23) is the correlation between increasing suction surface velocity and decreasing efficiency as solidity is reduced.

B1R (Figures 24 through 38)

The performance of this high-camber section may be characterized by its sensitivity to positive incidence. Even a 15 percent reduction in solidity from the turbine design value has little effect on cascade efficiency at -5° incidence (Figure 24). At the design inlet flow angle, the two higher solidities also give about the same efficiency (0.97), while the lowest solidity results in an efficiency loss of about one percent. In this case, a thickened suction side boundary layer was revealed by the corresponding traverse charts. The marked drop in efficiency as incidence is increased to $+3.5^\circ$ is the result of a suction-side separation, and a substantial additional loss in efficiency is clearly associated with reduced solidity at this angle.

In comparison with N1R, the β_2 and C_{p2} relations with both incidence and solidity are stronger, even considering only unseparated cases. The exit flow angle at $i = 0^\circ$ is about 1° lower than at $i = 5^\circ$ for $\sigma/\sigma_d = 1.0$ (Figure 25). This difference increases as solidity is reduced and apparently surpasses 4° at the lowest solidity (Figure 27). Similar to N1R, the β_2 and C_{p2} profiles become more nearly symmetric at the lowest solidity.

A flattening of the pressure side C_{ps} distribution near midchord is indicated for the design solidity at -5° incidence (Figure 31). Such behavior is often associated with a pressure side separation. The acceleration on approaching the trailing edge confirms reattachment. Corresponding traverse charts displayed a steep linear total pressure gradient through the pressure side boundary layer, but rounded at the outer edge. The phenomenon is more prominent for $\sigma/\sigma_d = 0.92$ as may be seen on Figure 34. Figures 33 and 36 show, for $\sigma/\sigma_d = 1.0$ and 0.92 respectively, the erratic behavior of suction-side pressures under the separation at positive incidence.

N2R (Figures 39 through 55)

Similar to B1R, a lack of tolerance for even modest positive incidence angles is observed for this section, which is also highly cambered. A notable difference (Figure 39) is the upward trend in cascade efficiency with increasing Mach number for cases involving a suction-side separation. Sensitivity to positive incidence is again amplified by a reduction in solidity. In this regard, recall that maintaining the ratio d_o/t as solidity is reduced results in an increase in stagger angle (see Table II) and, hence, in the effective angle of attack for a given inlet flow angle.

As with efficiency, β_2 and C_{p2} are not significantly affected by incidence angle in the absence of a flow separation. Comparing Figures 40 through 42 for β_2 and Figures 43 through 45 for C_{p2} again reveals a trend toward more symmetric profiles as solidity is reduced from the turbine design value. Blade surface static pressure data for positive incidence (Figures 48, 51, and 55) indicate a substantial amount of diffusion on the suction surface near the leading edge and

separation in the vicinity of $x/AW = 0.8$. There was a response problem with the pressure side tap near $x/AW = 0.9$, and these data therefore have been omitted from Figures 46 through 55.

TN2R (Figures 56 through 61)

Note that this blade section was designed to the same vector diagram requirements as N2R and was tested in its turbine design configuration only. Figure 56 presents the efficiency data together with those for N2R in its design configuration. At design Mach number, these data show an efficiency penalty of about 0.75 percent for the tandem blade at all incidence angles tested. The tandem blade, however, does show less sensitivity to positive incidence, having substantially higher efficiencies at subsonic Mach numbers. In addition, comparison of Figures 40 and 57 indicates that more turning was accomplished by the tandem blade than the plain blade, particularly at positive incidence angles.

Blade surface static pressure data (Figures 59 through 61) indicate very little diffusion on the aft blade and give no evidence of separation. The traverse charts indicated that some of the loss is the result of mixing between the forward blade wake and the suction-side boundary layer of the aft blade. This, together with results for TB3R, suggests a performance improvement with an increase in the tangential spacing of the forward and aft blades.

B3R (Figures 62 through 79)

Of the sections tested, the increase in efficiency with reduction in solidity, shown on Figure 62, is unique to B3R. Though these results include the effect of increased blade loading, they do not include increased end wall losses associated with the corresponding reductions in throat aspect ratio.

The β_2 curves (Figures 63 through 65) show a continual decrease in exit flow angle with both increasing incidence and decreasing solidity. Thus the 0.5 percent efficiency increase for $\sigma/\sigma_d = 0.85$ is accompanied by a 2° reduction in exit flow angle. In considering the C_{p2} data (Figures 66 through 68), note that mainstream values are negative in all cases, which implies static pressure recovery in the mixing process downstream of the traverse plane. The reduction in C_{p2} with increasing incidence can be attributed to reduced effective exit flow area. In particular, note the magnitude of change in C_{p2} as incidence is increased from $+5^\circ$ to $+10^\circ$ for both $\sigma/\sigma_d = 0.92$ and 0.85 . The corresponding surface pressure data (Figures 74, 75, 78, and 79) indicate a suction-side separation occurring farther upstream with $+10^\circ$ incidence (i.e., providing a smaller effective exit flow area).

The combination of negative reaction and relatively low throat aspect ratio, common to this section and those discussed below, resulted in an appreciable spanwise contraction effected by secondary flow development along the sidewalls. The magnitude of evaluated data for these sections must be qualified by this consideration. However, the sense of the apparent trends and, because of overall geometric similarity, the comparisons between B3R and TB3R are considered valid.

TB3R (Figures 80 through 111)

At turbine design flow conditions, Figures 80 and 81 show that, for the variations in axial overlap and tangential spacing tested, the most prominent effect on efficiency is due to increasing the axial overlap. This results in a reduction of about 2 percent in efficiency over the entire Mach no., incidence angle range. Here it is important to note the introduction of some divergence in the passage between the forward and aft blades as a result of maintaining the individual stagger angles while increasing the overlap. Reduction in tangential spacing has a relatively moderate detrimental effect (0.5%) over the test range. In terms of efficiency, the only improvement over the design configuration comes at negative incidence with a decrease in axial overlap. In comparison to B3R (Figure 62), which has identical vector diagram requirements, the tandem blade offers a substantial efficiency payoff at high positive incidence (2% at 10°) but imposes about a one percent penalty at all other angles tested.

Similar comparisons may be drawn from the exit flow angle data shown on Figures 82 through 86. The highest turning is achieved with the configuration having the smallest axial overlap, 82 being nearly 3° higher than for the design configuration and about 2° higher than for the plain blade (Figure 63). The configuration with increased tangential spacing also shows more turning capability, about 0.5° over the design configuration.

The exit static pressure profiles are nearly the same for all of the variations tested (Figures 87 through 91). Except at high positive incidence, the mainstream static pressure along the traverse line is near the far downstream value. Recall that, for the plain blade (Figure 66), this pressure is below the far downstream value by about five percent of the potential flow velocity head ($P_{T1} - P_{2\infty}$). Figures 92 through 111 show blade surface pressure data. There is no evidence of separation under any of the conditions tested; but most remarkable is the steepness of the adverse pressure gradient apparently sustained by the forward blade suction side at high positive incidence.

In summary of the results obtained for TB3R and B3R, it seems likely that a tandem blade can provide performance comparable to that of a plain blade while significantly reducing sensitivity to positive incidence for vector diagram requirements similar to those encountered here.

AB1R (Figures 112 through 116)

Testing of this blade section was limited to design solidity at -5° and 0° incidence because of severe flow separations. Although the efficiency data for negative incidence (Figure 112) look respectable, the surface pressure data (Figure 115) indicate the complications which were more clearly evident on the traverse charts. Pressure side separation leads to shocks within the blade passage for pressure ratios corresponding to ideal exit Mach numbers of the order of 0.8 and higher. With the incidence angle increased to near 0° , the same behavior is apparent (Figure 116) with the addition of a suction-side separation.

APPENDIX A

PROBE DESIGN AND CALIBRATION DATA

A five-hole conically tipped probe was designed for use in this test program with the objective of obtaining flow angle and static pressure data downstream of cascades, without compromising the accuracy of the total pressure measurement. Nomenclature relating to the probe calibration and dimensional data are given on Figure 117. The total included apex angle was set at 25° so as to avoid attachment of the probe shock at the highest Mach number required in the test program. It was concluded from Reference 6, that a larger angle would have reduced unnecessarily the incidence range over which measured total pressure errors are negligible.

The probe was calibrated, with both yaw and roll angles set to zero, over a Mach number range from 0.4 to 1.05 for pitch angles from -7.25° to $+8.00^\circ$. An attempt to obtain calibration data at higher Mach numbers was unsuccessful. All data were reduced in terms of correction factors for total pressure, flow angle, and static pressure as included in the list of definitions below.

- P_I , average indicated static pressure:

$$P_I \equiv \frac{1}{4} (P_{C1} + P_{C2} + P_{C3} + P_{C4})$$

- C_{TP} , total pressure correction factor:

$$C_{TP} \equiv \frac{P_T - P_{CO}}{P_{CO} - P_I}$$

- C_{FA} , flow angle correction factor:

$$C_{FA} \equiv \frac{P_{C1} - P_{C3}}{P_{CO} - P_I}$$

- C_{SP} , static pressure correction factor:

$$C_{SP} \equiv \frac{P_{CA} - P}{P_{CO} - P_I}$$

The total pressure error is negligible over the entire calibrated range, C_{TP} being less than 0.003 for $M = 0.4$ and less than 0.001 for $M = 1.0$. Angle correction factor data are shown on Figure 118 together with hand fitted curves defined by the following relations:

$$C_{FA} = \frac{1}{36.65} (\theta - 1.12) ; \quad M_I \leq 0.7$$

$$C_{FA} = \frac{1}{36.65} [\theta - 1.12 - 1.2 (M_I - 0.7)] ; \quad 0.7 < M_I < 0.9$$

The static pressure correction factor data were first plotted versus indicated pressure ratio (P_{CO}/P_I) with θ as a parameter. Hand fitted curves then were drawn so as to produce a consistent family of crossplotted curves covering the entire Mach number range. Each of the resulting C_{sp} vs. θ curves ($P_{CO}/P_{CA} = \text{constant}$) was represented by a polynomial of the following form:

$$C_{SP} = \sum_{i=0}^6 \alpha_i \theta^i$$

Polynomial coefficients for each parametric value of P_{CO}/P_I are given in Table IV, and the corresponding curves are shown in Figure 119. These curves provide 10 C_{sp} , P_{CO}/P_I points for a given pitch angle. A static pressure correction factor may be determined satisfactorily through a fifth-order polynomial fit of this set of points. Polynomial curves generated in this manner for each of the pitch angles set during calibration are presented in Figures 120 and 121 together with the corresponding calibration data.

APPENDIX B

DEFINITION OF SYMBOLS

AB1R	alternate stage one rotor hub section identification
AW	axial width of blade section (inch)
B1R	stage one rotor rub section identification
B3R	stage three rotor hub section identification
C_{FA}	probe flow angle correction factor, $(P_{C1} - P_{C3}) / (P_{CO} - P_I)$
C_{P2}	exit static pressure coefficient, $(P_2 - P_{2\infty}) / (P_{T1} - P_{2\infty})$
C_{PS}	blade surface static pressure coefficient, $(P_{T1} - P) / (P_{T1} - P_{2\infty})$
C_{SF}	cascade scale factor, e.g. t/t_d
C_{SP}	probe static pressure correction factor, $(P_I - P) / (P_{CO} - P_I)$
C_{TP}	probe total pressure correction factor, $(P_T - P_{CO}) / (P_{CO} - P_I)$
d_o	blade passage width (throat) at trailing edge (inch)
e_{ax}	axial overlap between forward and aft blades (inch)
e_t	tangential spacing between forward and aft blades (inch)
i	incidence angle, $\beta_1 - \beta_{1d}$
M	Mach number
M_I	probe-indicated Mach number from P_{CO} / P_I
n_p	number of passages in cascade
N1R	stage one stator hub section identification
N2R	stage two stator hub section identification
P	static pressure (psia)
P_T	total pressure (psia)
P_{C1}	(i = 0, 1, 2, 3, 4) pressures sensed by probe (psia)
P_I	probe indicated static pressure (psia), average of P_{C1} , P_{C2} , P_{C3} , and P_{C4}
ΔP_T	total pressure loss (psia), $P_{T1} - P_{T2}$
RH	cascade blade span (inch)
R_e	Reynold's number
t	blade section to blade section tangential spacing (inch)
TB3R	tandem stage three rotor hub section identification
TN2R	tandem stage two stator hub section identification

V	gas flow speed (ft/sec)
X	axial distance (inch)
y	tangential distance (inch)
α_i	(i = 1, 2, 3, 4, 5, 6) polynomial coefficients
γ	ratio of specific heats
γ^0	blade chord angle with respect to axial (degrees)
β	gas flow angle with respect to axial (degrees)
$\delta\eta$	uncertainty in efficiency
η	cascade efficiency
θ	gas flow angle with respect to probe axis (degrees)
ρ	gas density (lb _m /ft ³)
σ	blade solidity, chord/t
ϕ	blade mean line camber angle (degrees)

Subscripts

0	ideal exit flow condition, from $P_{T1}/P_{2\infty}$
1	condition at station 1, uniform flow upstream of cascade
2	condition at station 2, along traverse line downstream of cascade
2∞	far downstream condition
a	aft blade
d	turbine design value
f	forward blade

REFERENCES

1. Evans, D.C., "Investigation of a Highly Loaded Multistage Fan Drive Turbine," Report for Task I - "Vector Diagram Study," NASA CR-1862, July, 1971.
2. Evans, D.C. and Wolfmeyer, G.W., "Highly Loaded Multistage Fan Drive Turbine - Plain Blade Configuration Design," NASA CR-1964, February, 1972.
3. Evans, D.C. and Wolfmeyer, G.W., "Highly Loaded Multistage Fan Drive Turbine - Tandem Blade Configuration Design," NASA CR-2097, August, 1972.
4. Livesey, J.L., "The Behavior of Transverse Cylindrical and Forward Facing Total Pressure Probes in Transverse Total Pressure Gradients," J.A.S., Vol. 23, No. 10, October, 1956, pp. 949-955.
5. Bueckner, H.F. and Schnackel, H.C., "The Calculation of Incompressible Flow Through Turbine Cascades," paper presented at ASME 1959 Annual Meeting, Session: Power IV, copies available at Engineering Society Library, United Engineering Center, N.Y., N.Y.
6. Gracey, William, "Wind-Tunnel Investigation of a Number of Total-Pressure Tubes at High Angles of Attack - Subsonic, Transonic, and Supersonic Speeds," NACA Report 1303, 1957.

Table I. Comparative Vector Diagram Requirements - Stage
One Rotor Hub Sections.

Parameter	B1R	AB1R
Inlet flow angle, β_1 (degrees)	57.1	57.9
Gas turning angle, $\Delta\beta$ (degrees)	116.1	114.9
Reaction, R_x	0.068	-0.180
Exit swirl angle, Γ (degrees)	50.0	46.0
Relative inlet Mach no., M_{R1}	0.824	0.927
Relative exit Mach no., M_{R2}	0.871	0.788
Loading factor*, $gJ\Delta h/2U^2$	2.832	2.832
<p>* Δh is stage energy extraction (Btu/lb_m) and U is wheel speed (ft/sec)</p>		

Table II. Cascade Geometric Data.

Identification Code	C _{SF}	d _o /t	σ/σ _d	RH/d _o	e _t /t	e _{ax} /AW	AW/t	β ₁	φ	γ _o	γ _f	γ _a	η _p	Re × 10 ⁻⁵	Re/Re _d
N1R	1.1445	0.503	1.00	7.95	---	---	1.139	0	66.8	40.5	---	---	12	1.39	0.44
	1.1445	0.503	0.90	7.16	---	---	1.025	0	66.8	41.3	---	---	10	---	---
	1.1445	0.503	0.80	6.36	---	---	0.911	0	66.8	43.0	---	---	9	---	---
B1R	2.8324	0.534	1.00	5.01	---	---	1.732	55.0	112.4	8.6	---	---	14	1.94	1.15
	2.8324	0.534	0.92	4.61	---	---	1.593	55.0	112.4	9.4	---	---	12	---	---
	2.8324	0.534	0.85	4.26	---	---	1.472	55.0	112.4	10.7	---	---	12	---	---
N2R	2.9626	0.491	1.00	5.31	---	---	1.765	49.3	108.8	22.7	---	---	12	1.92	1.47
	2.9626	0.491	0.90	4.78	---	---	1.589	49.3	108.8	23.2	---	---	10	---	---
	2.9626	0.491	0.80	4.25	---	---	1.412	49.3	108.8	25.0	---	---	9	---	---
TN2R	2.9626	0.491	1.00	5.31	0.100	0.102	1.770	49.3	113.7	16.1	-31.2	38.0	12	1.92	1.47
B3R	2.0154	0.828	1.00	4.80	---	---	2.457	45.5	75.9	-7.0	---	---	17	1.72	1.75
	2.0154	0.828	0.92	4.42	---	---	2.260	45.5	75.9	-7.0	---	---	15	---	---
	2.0154	0.828	0.85	4.08	---	---	2.088	45.5	75.9	-7.0	---	---	14	---	---
TB3R	2.0154	0.828	1.00	4.80	0.158	0.094	2.459	45.5	75.5	-1.2	-30.2	6.0	17	1.72	1.75
	2.0154	0.828	1.00	4.80	0.158	0.048	2.568	45.5	75.5	-1.2	-30.2	6.0	17	---	---
	2.0154	0.828	1.00	4.80	0.158	0.158	2.323	45.5	75.5	-1.2	-30.2	6.0	17	---	---
	2.0154	0.828	1.00	4.80	0.098	0.094	2.459	45.5	75.5	-2.5	-30.2	6.0	17	---	---
	2.0154	0.828	1.00	4.80	0.198	0.094	2.459	45.5	75.5	-0.2	-30.2	6.0	17	---	---
AB1R	2.8780	0.559	1.00	5.07	---	---	1.860	57.9	110.7	5.4	---	---	16	1.87	1.19
	2.8780	0.559	0.92	4.66	---	---	1.711	57.9	110.7	6.2	---	---	14	---	---
	2.8780	0.559	0.95	4.31	---	---	1.581	57.9	110.7	7.3	---	---	13	---	---

Note: All angles given in degrees.

Table III. Relative Uncertainty in Calculated Efficiency.*

$\frac{\delta\eta}{\eta}$ for $M_{2\infty} =$		SOURCE
0.5	1.0	
0.0010	0.0008	reading of X-Y chart
0.0007	0.0007	potentiometer
0.0001	0.0001	ΔP transducer
0.0007	0.0001	$P_{2\infty}$ transducer
0.0008	0.0003	P_{T1} transducer
<p>* Estimations based on an efficiency of 0.96 and a triangular wake whose base is 25 percent of the blade spacing.</p>		

Table IV. Probe Calibration, Polynomial Coefficients for Static Pressure Correction Factor.

$$C_{sp} = \sum_{i=0}^6 \alpha_i \theta^i; \quad P_{co}/P_I = \text{constant}$$

P_{co}/P_I	$a_0 \times 10$	$a_1 \times 10^3$	$a_2 \times 10^3$	$a_3 \times 10^5$	$a_4 \times 10^5$	$a_5 \times 10^7$	$a_6 \times 10^7$
1.100	0.8577	0.9840	0.4055	0.1634	0.1310	---	---
1.250	0.8893	1.3461	0.4505	0.4808	0.1710	---	---
1.400	0.9553	1.6857	0.5186	0.6556	0.2120	---	---
1.500	1.0562	1.7289	0.5936	0.5333	0.2404	---	---
1.550	1.1587	1.7596	0.6885	0.5325	0.3034	---	---
1.600	1.3393	1.6511	1.0023	1.0203	0.9215	0.7663	0.4821
1.625	1.4810	1.7487	1.2612	1.4602	1.3315	1.3206	0.7281
1.650	1.6598	2.2203	1.4908	3.0062	1.6429	2.8456	0.9534
1.675	1.9091	3.4461	1.8503	5.9405	2.1681	5.2789	1.3224
1.700	2.2472	5.5409	2.5463	11.489	3.5450	10.534	2.3932

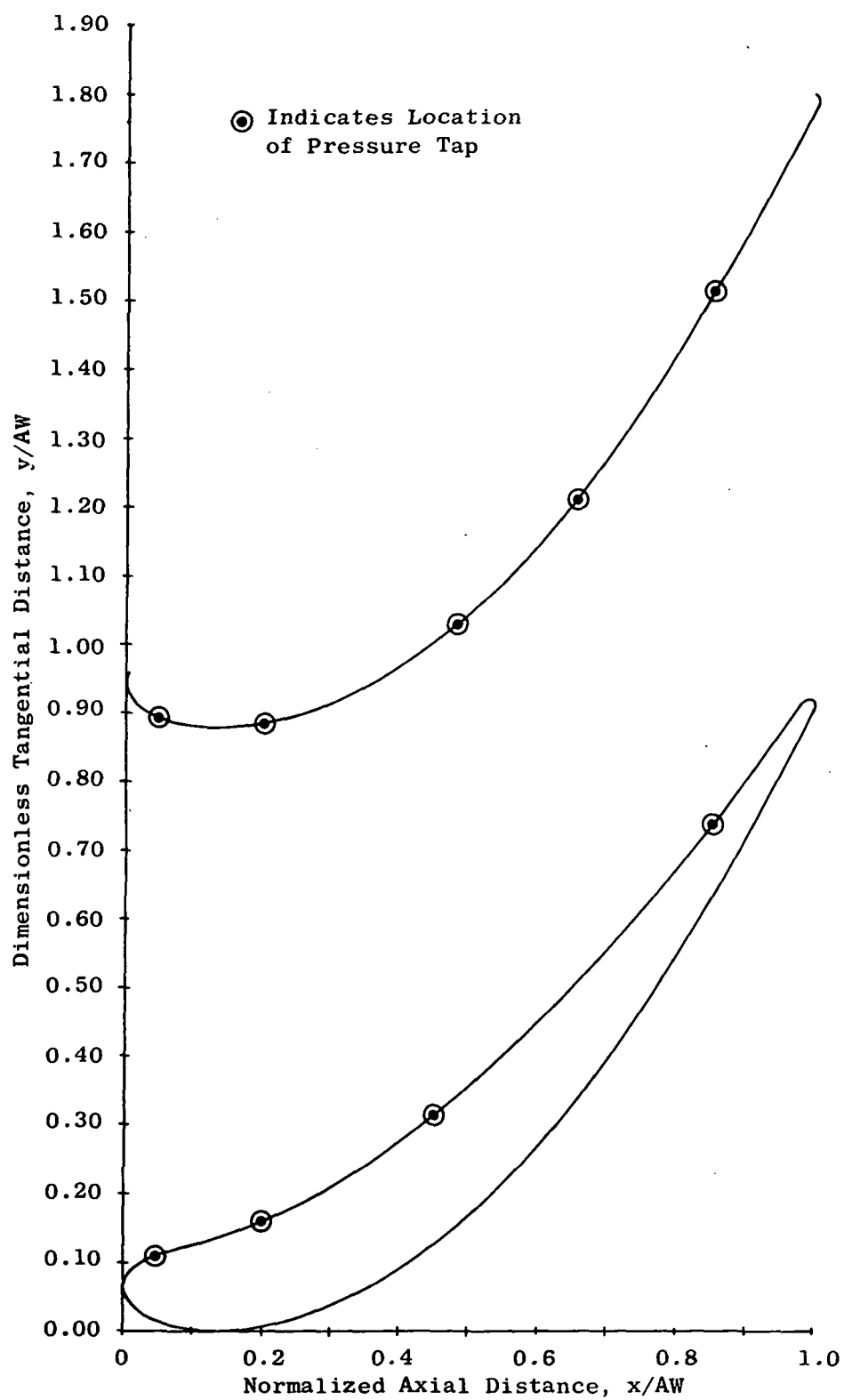


Figure 1. Flowpath, N1R in Turbine Design Configuration.

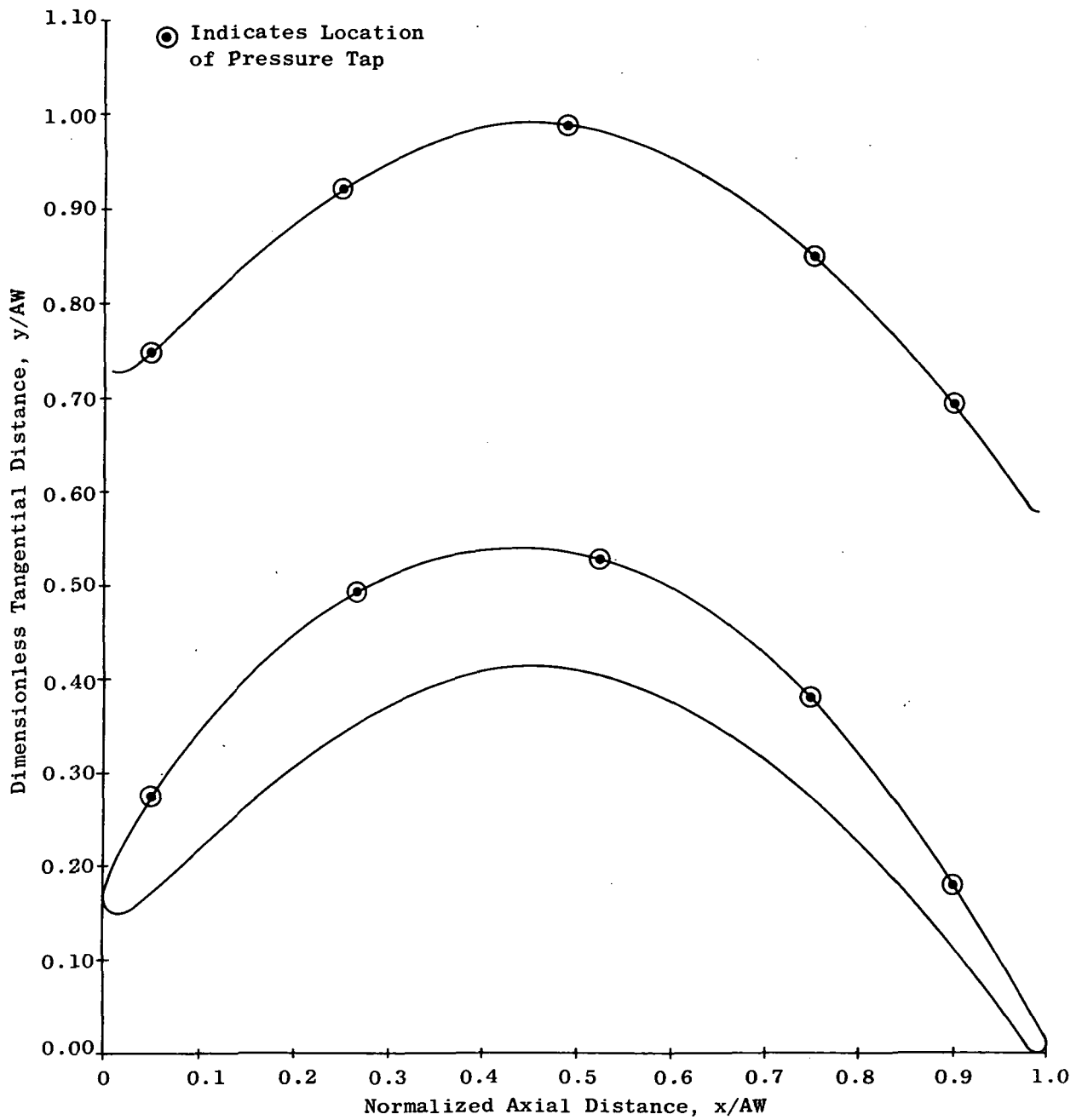


Figure 2. Flowpath, BlR in Turbine Design Configuration.

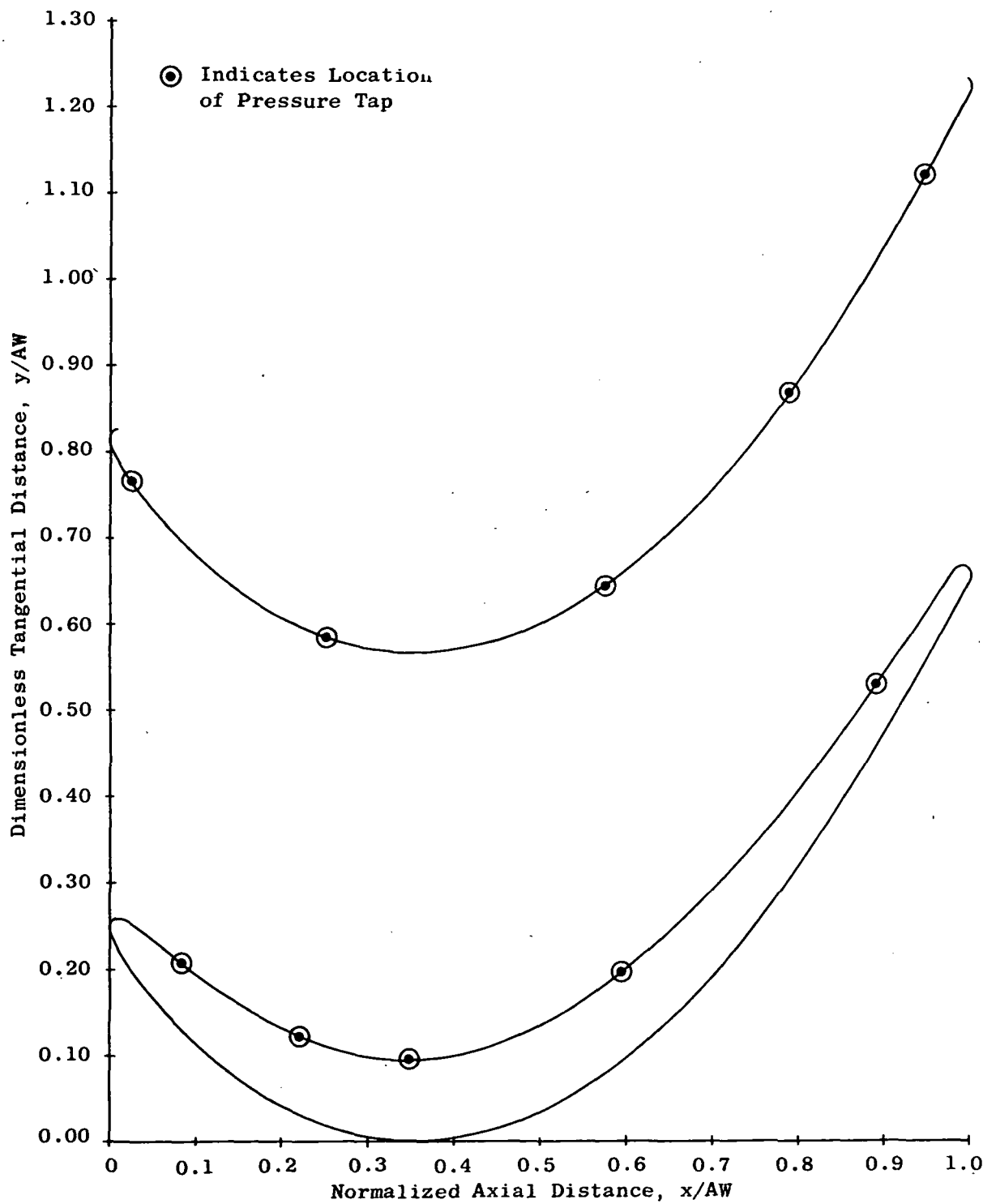


Figure 3. Flowpath, N2R in Turbine Design Configuration.

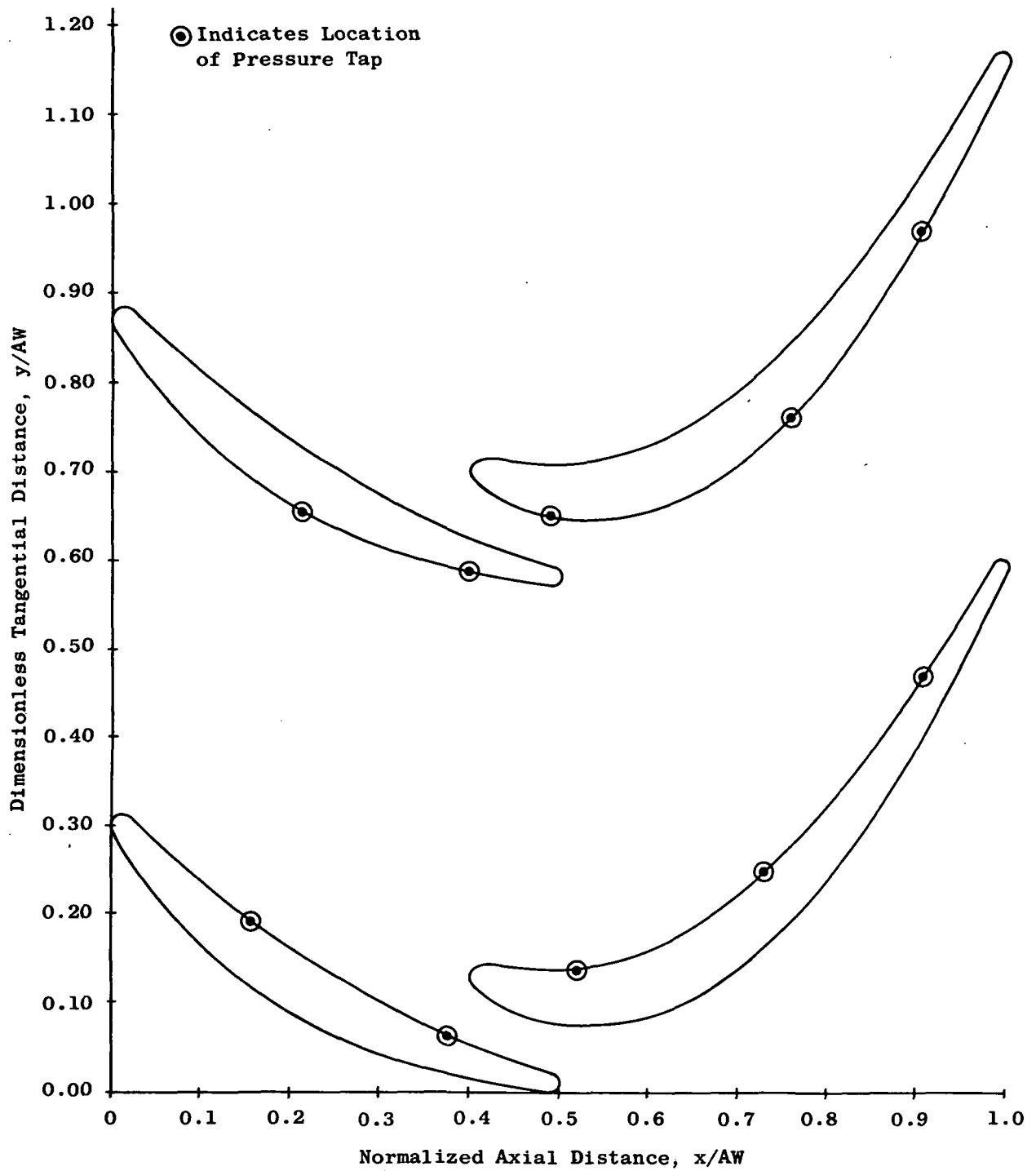


Figure 4. Flowpath, TN2R in Turbine Design Configuration.

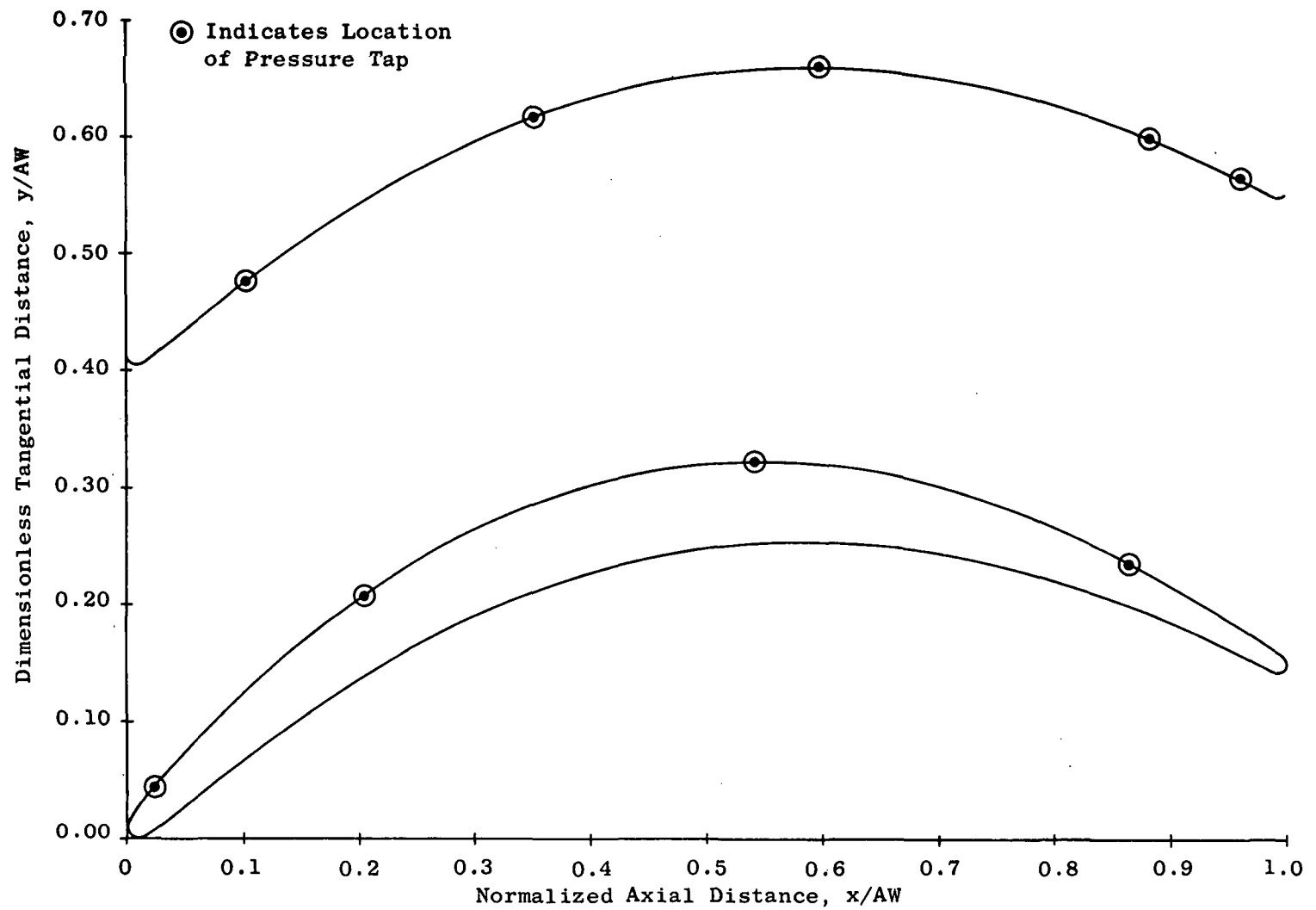


Figure 5. Flowpath, B3R in Turbine Design Configuration.

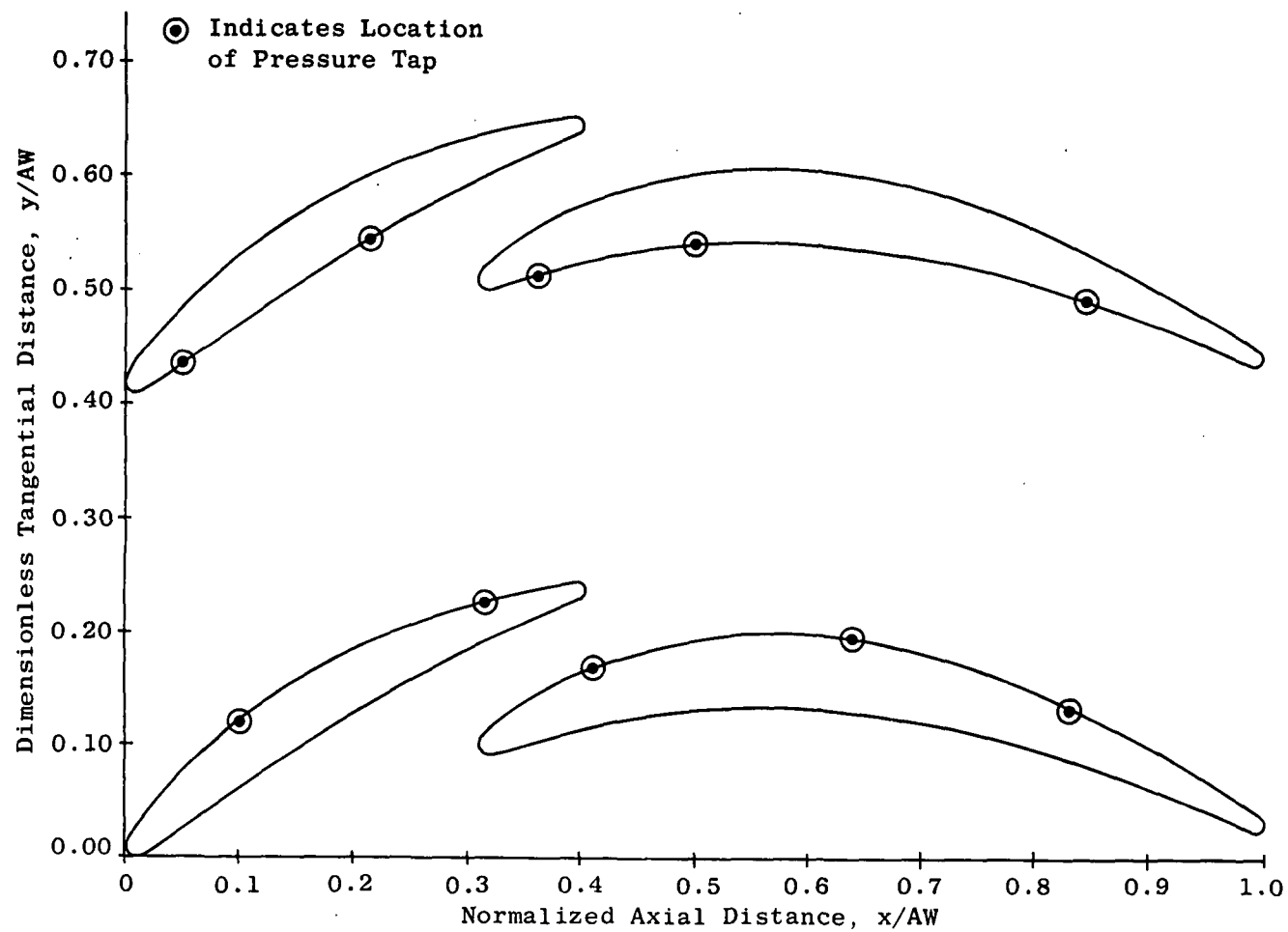


Figure 6. Flowpath, TB3R in Turbine Design Configuration.

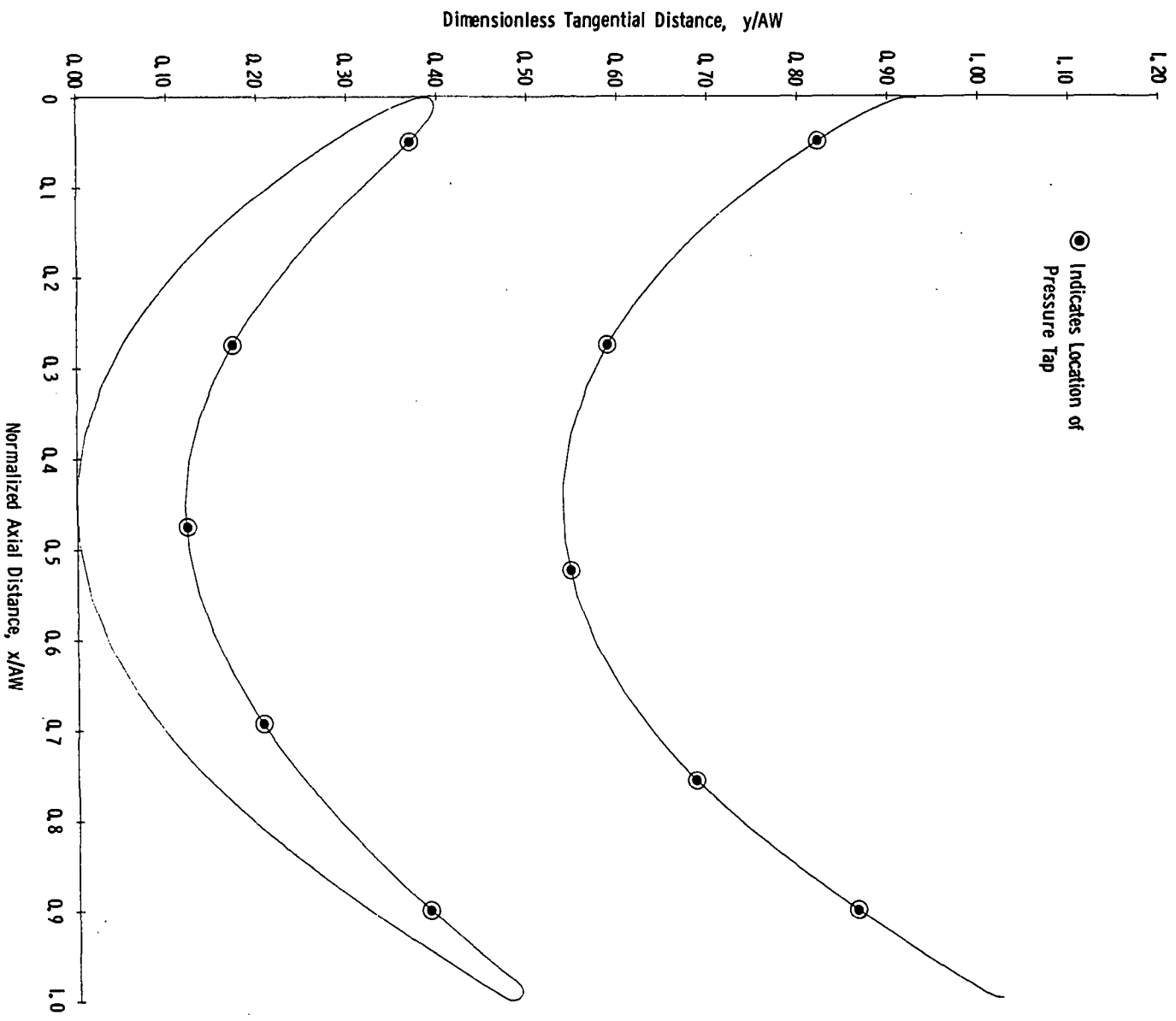
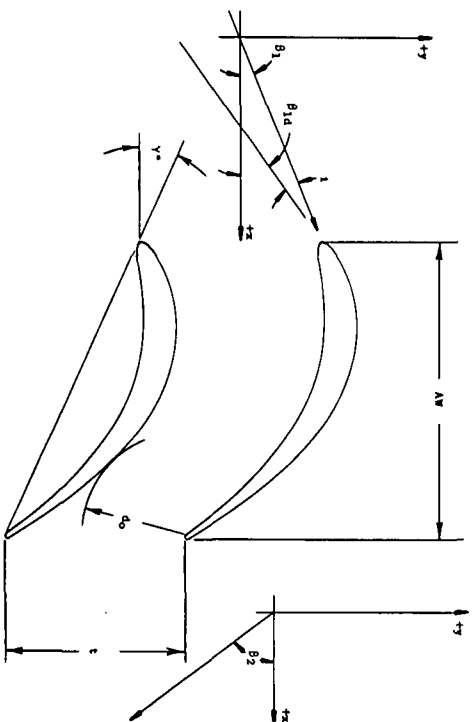
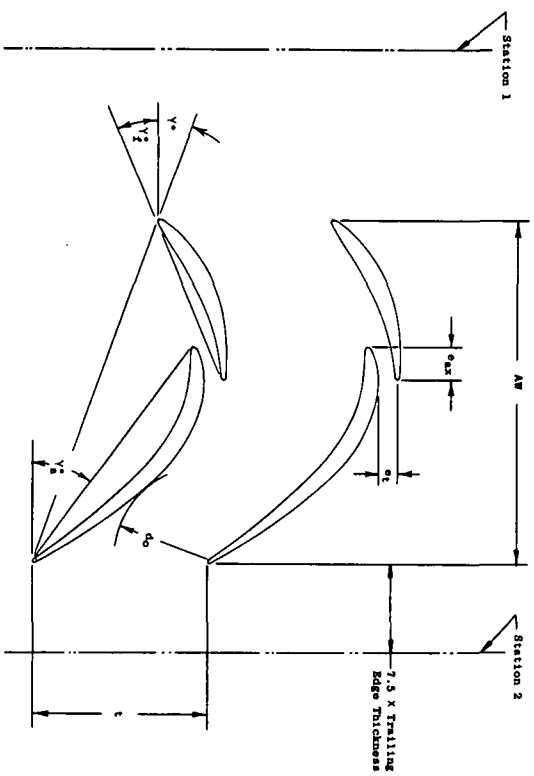


Figure 7. Flowpath, ABIR in Turbine Design Configuration.



a). Plain Blade



b). Tandem Blade

Figure 8. Cascade Nomenclature.

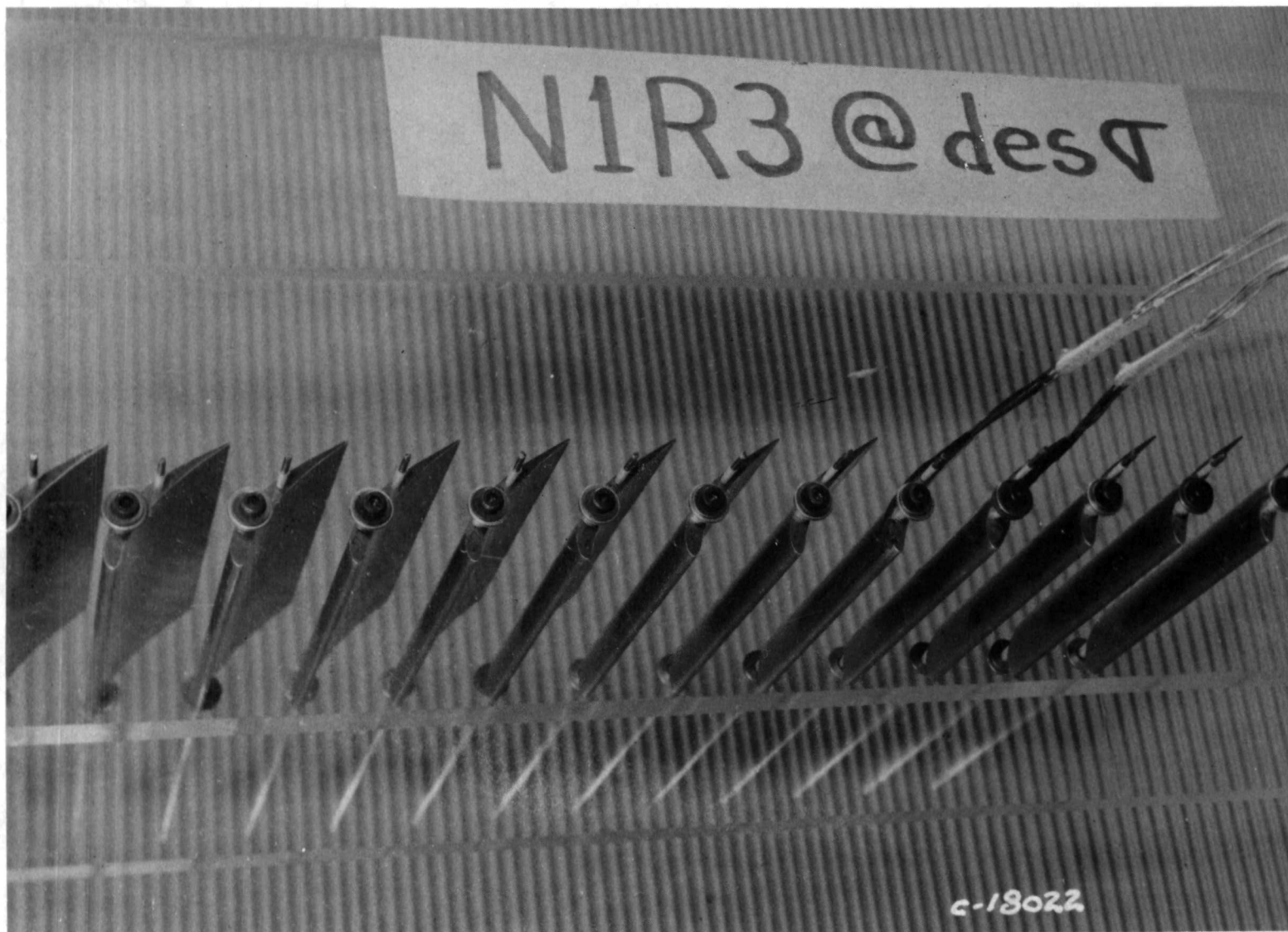


Figure 9. Cascade Photograph, N1R Turbine Design Configuration.

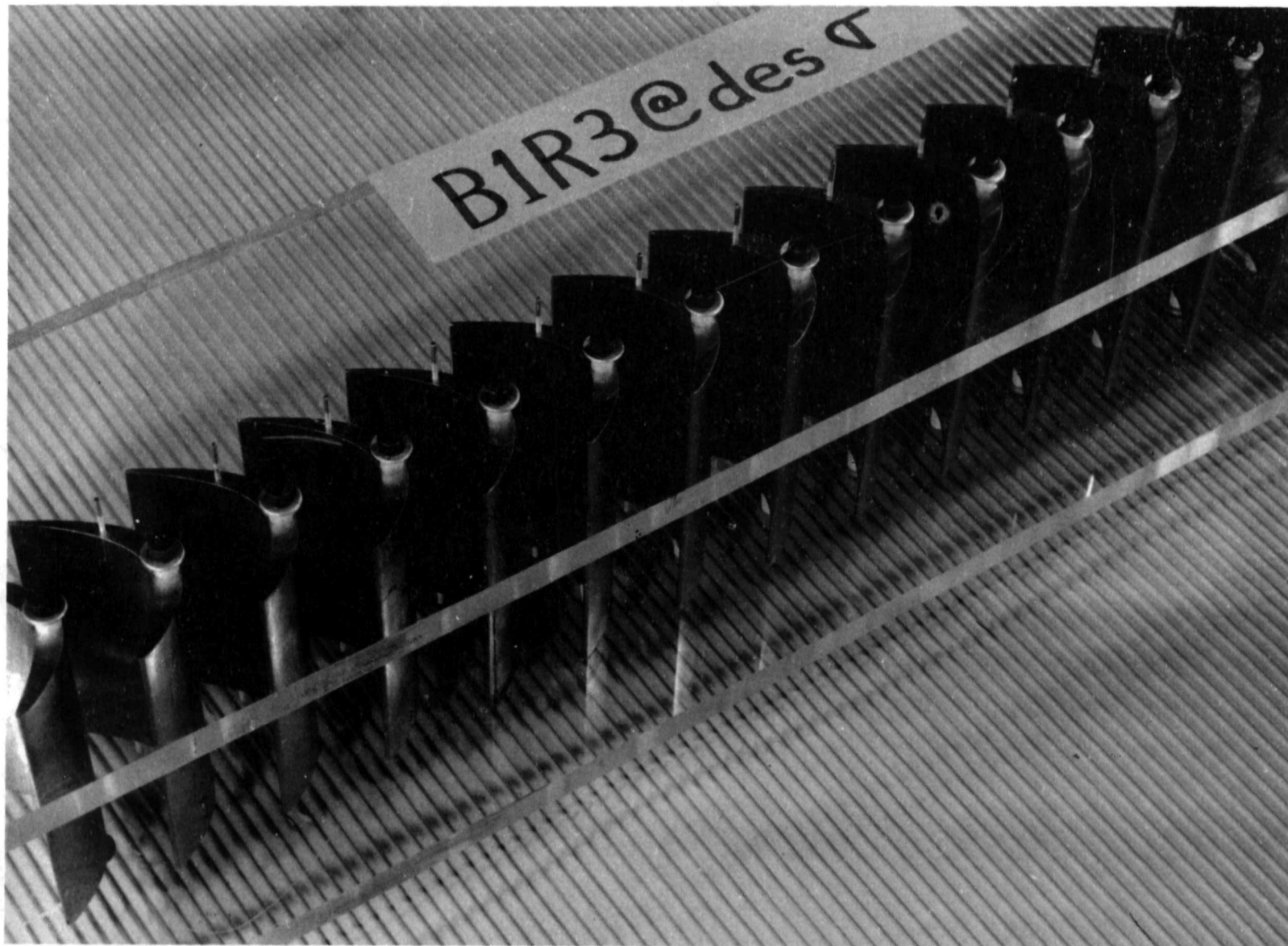


Figure 10. Cascade Photograph, B1R Turbine Design Configuration.

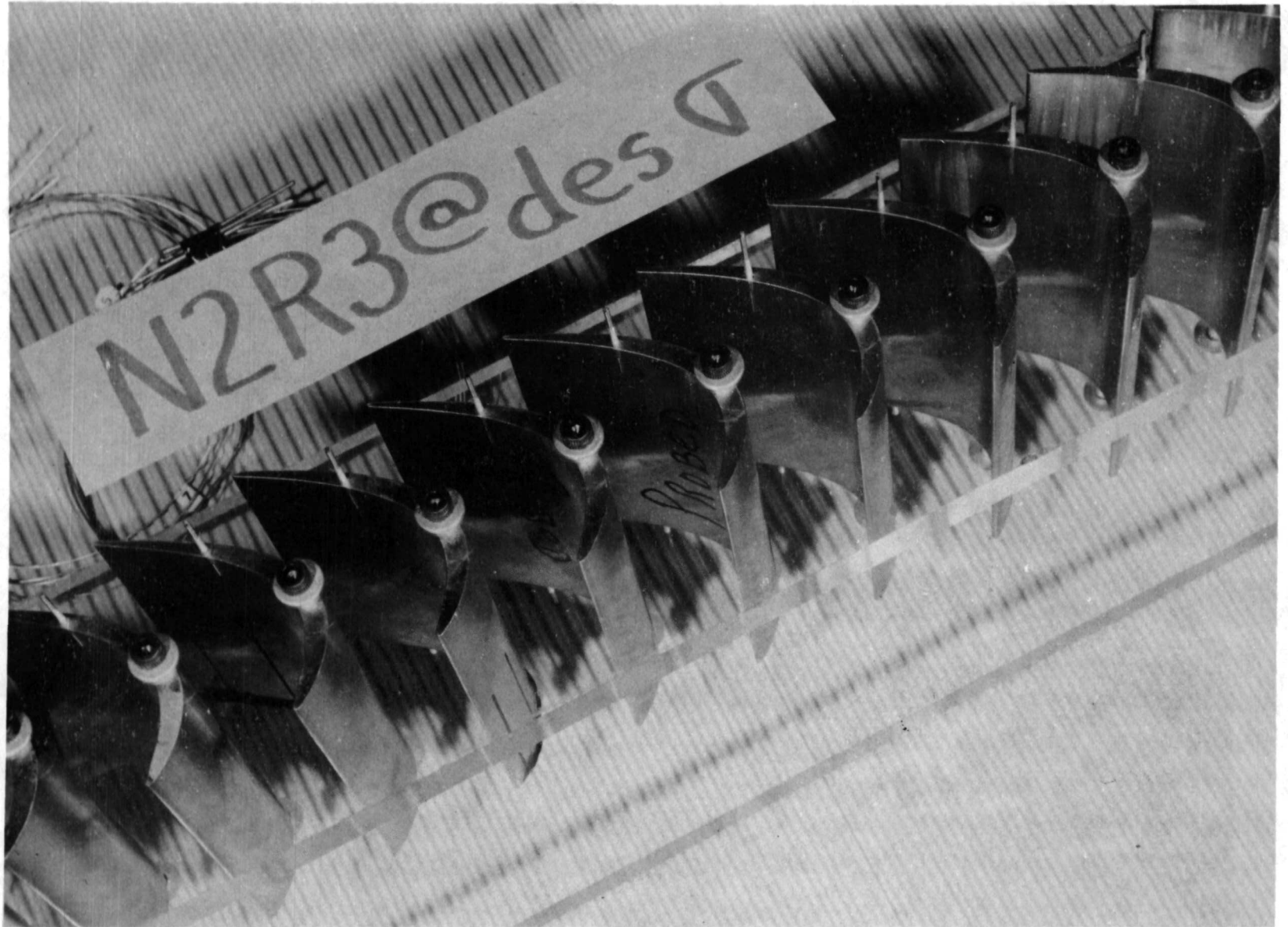


Figure 11. Cascade Photograph, N2R Turbine Design Configuration.

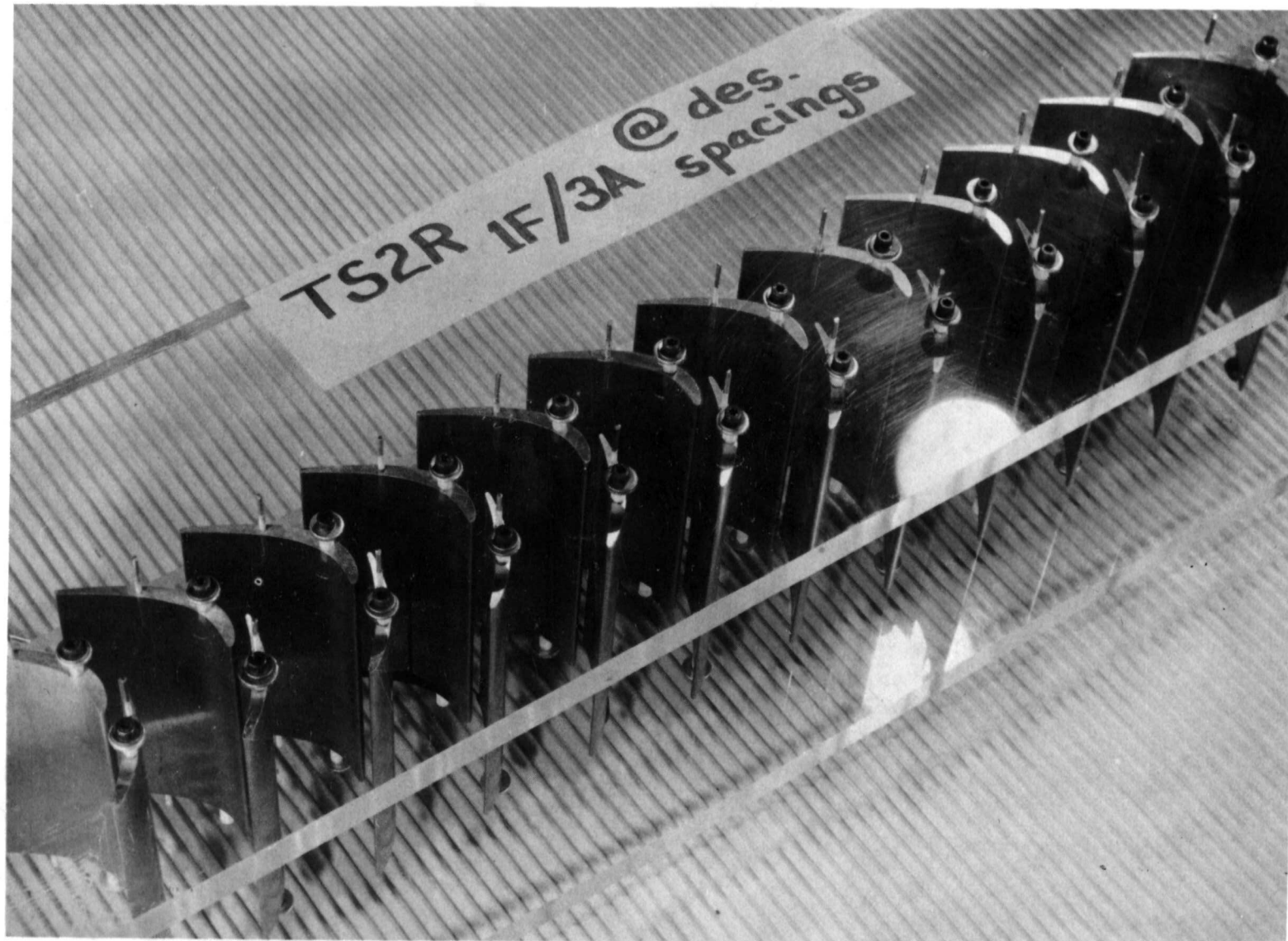


Figure 12. Cascade Photograph, TN2R Turbine Design Configuration.

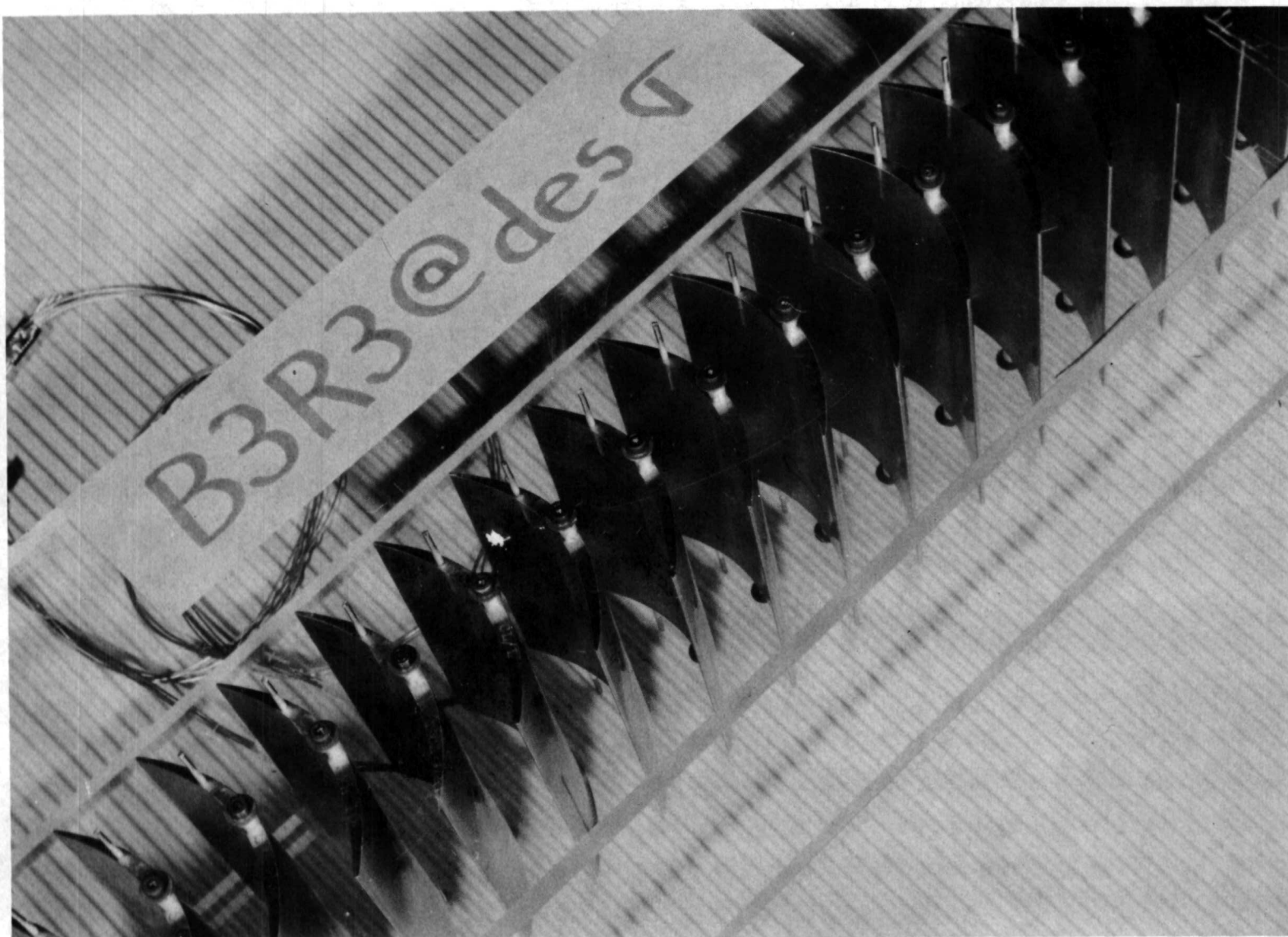


Figure 13. Cascade Photograph, B3R Turbine Design Configuration.



Figure 14. Cascade Photograph, TB3R Turbine Design Configuration.

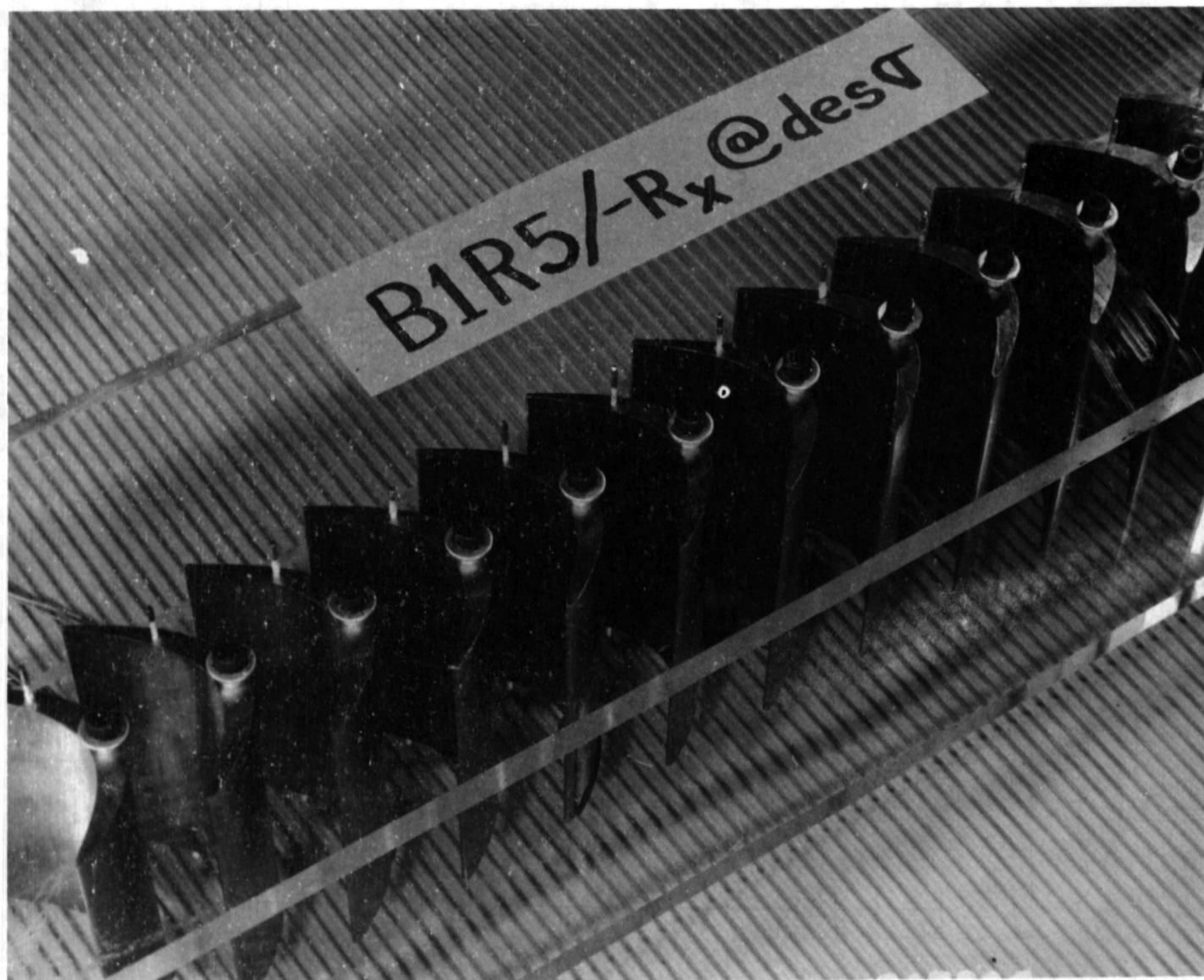


Figure 15. Cascade Photograph, AB1R Turbine Design Configuration.

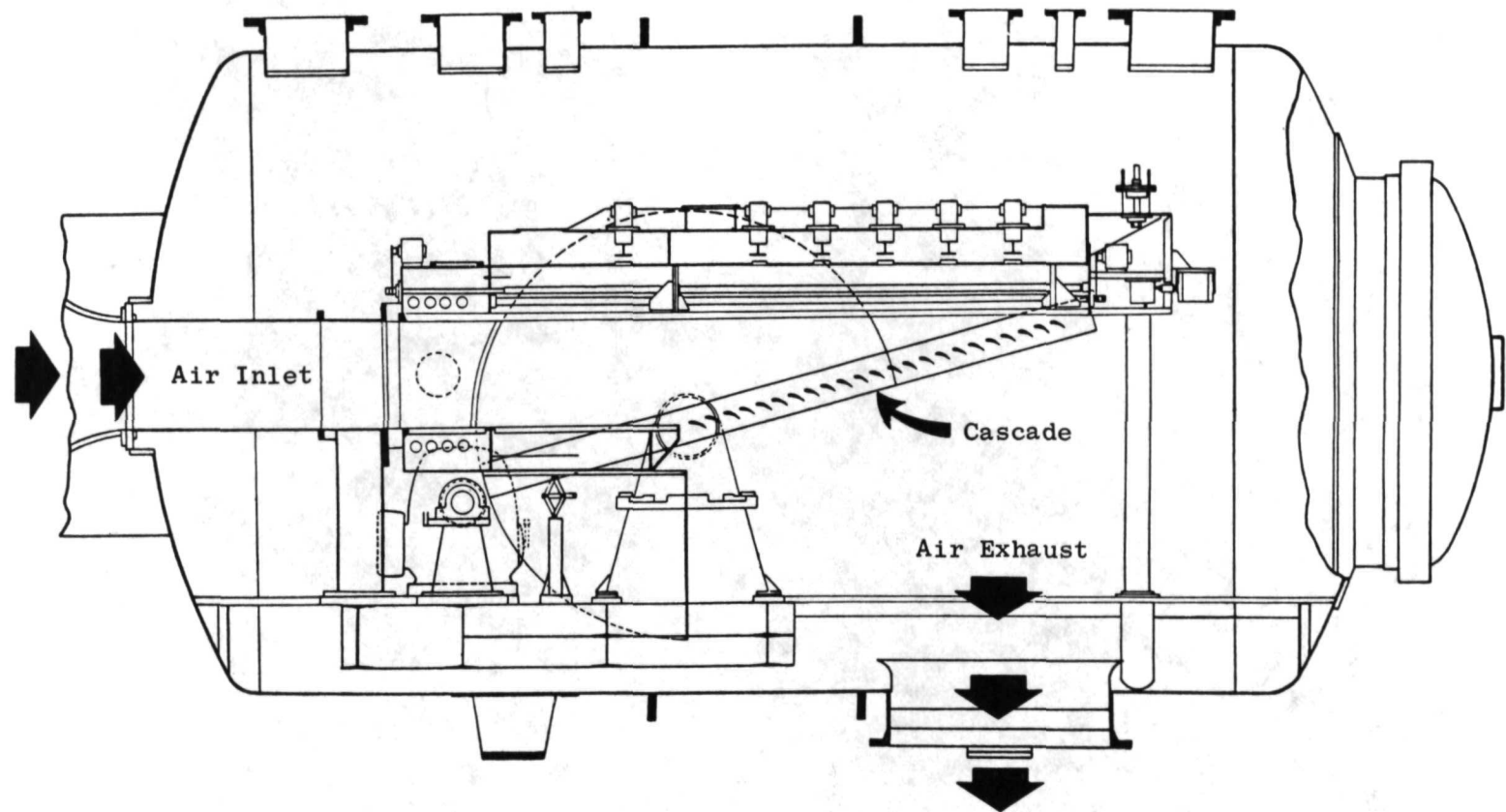


Figure 16. Cascade Tunnel Schematic.

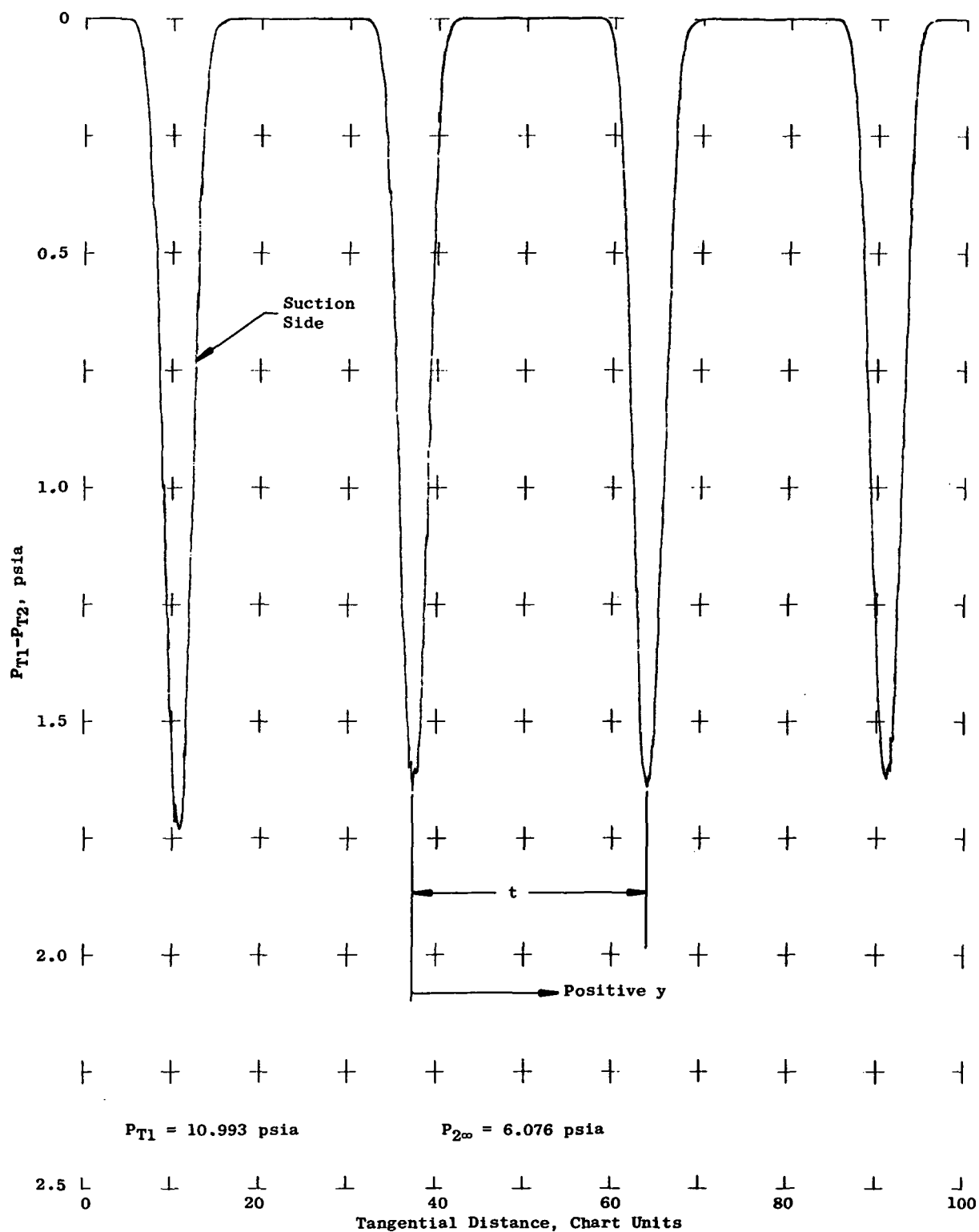


Figure 17. Typical Traverse Chart.

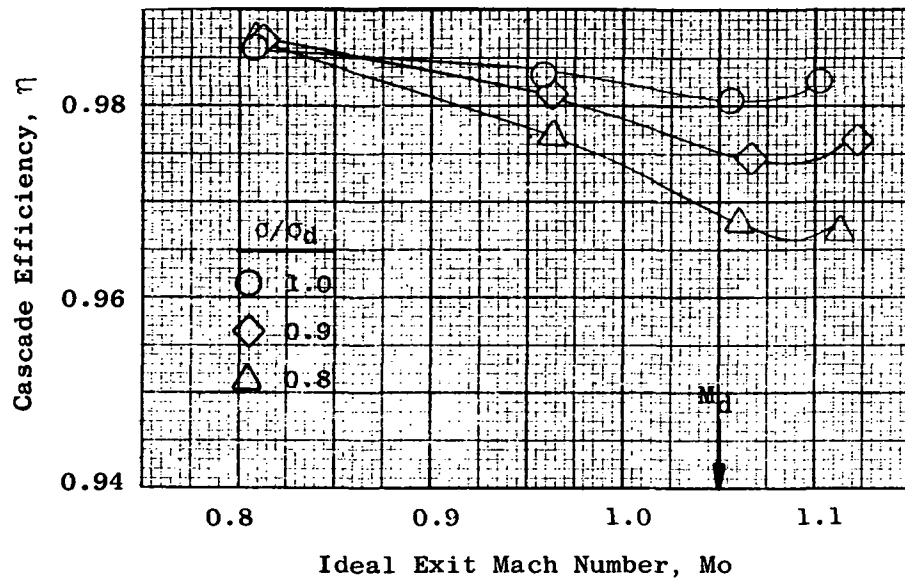


Figure 18. Cascade Efficiency Vs. Mach Number, $N1R$,
 $i = 0^\circ$.

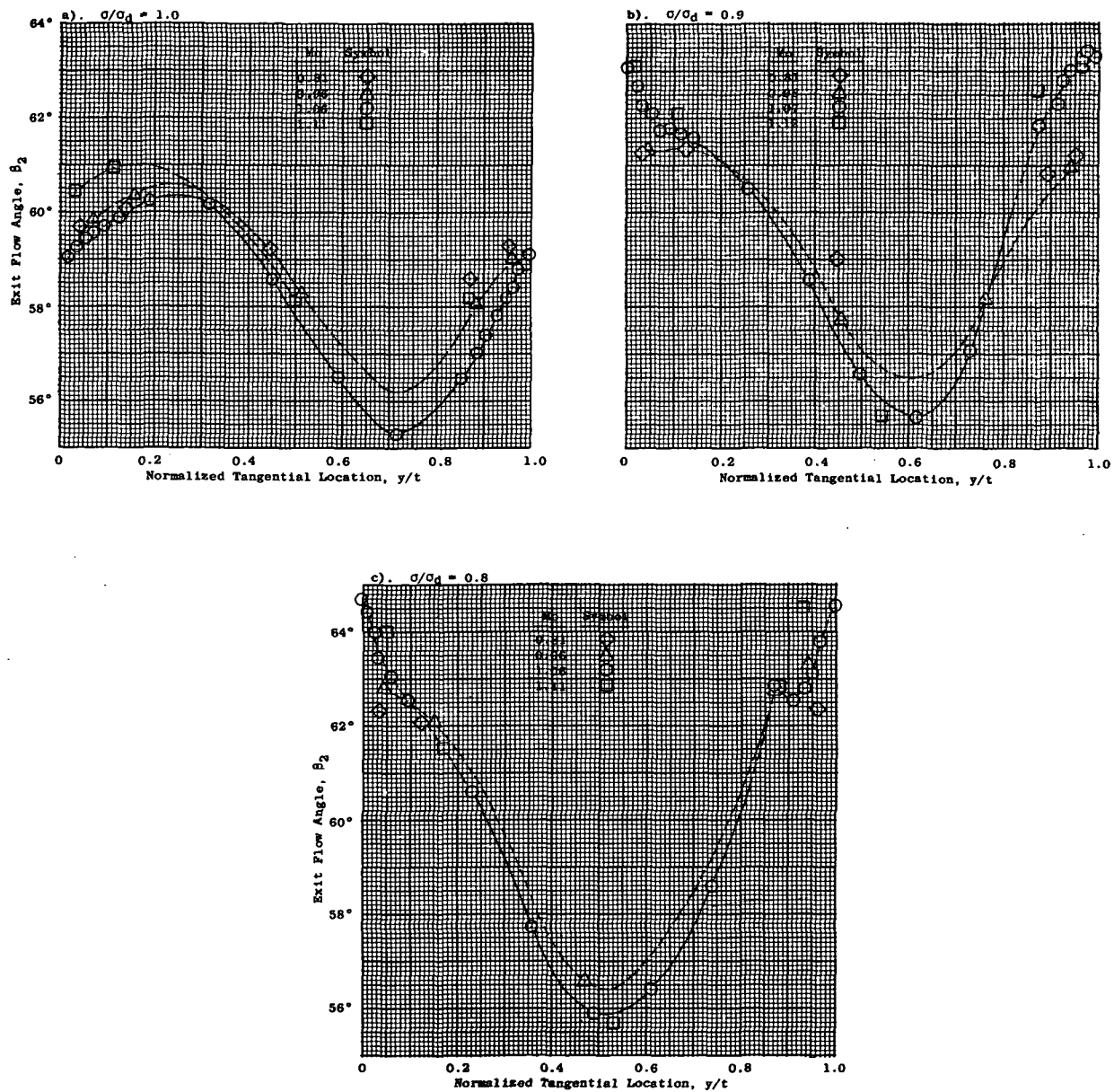


Figure 19. Exit Flow Angle Vs. Normalized Tangential Location, NlR , $i = 0^\circ$.

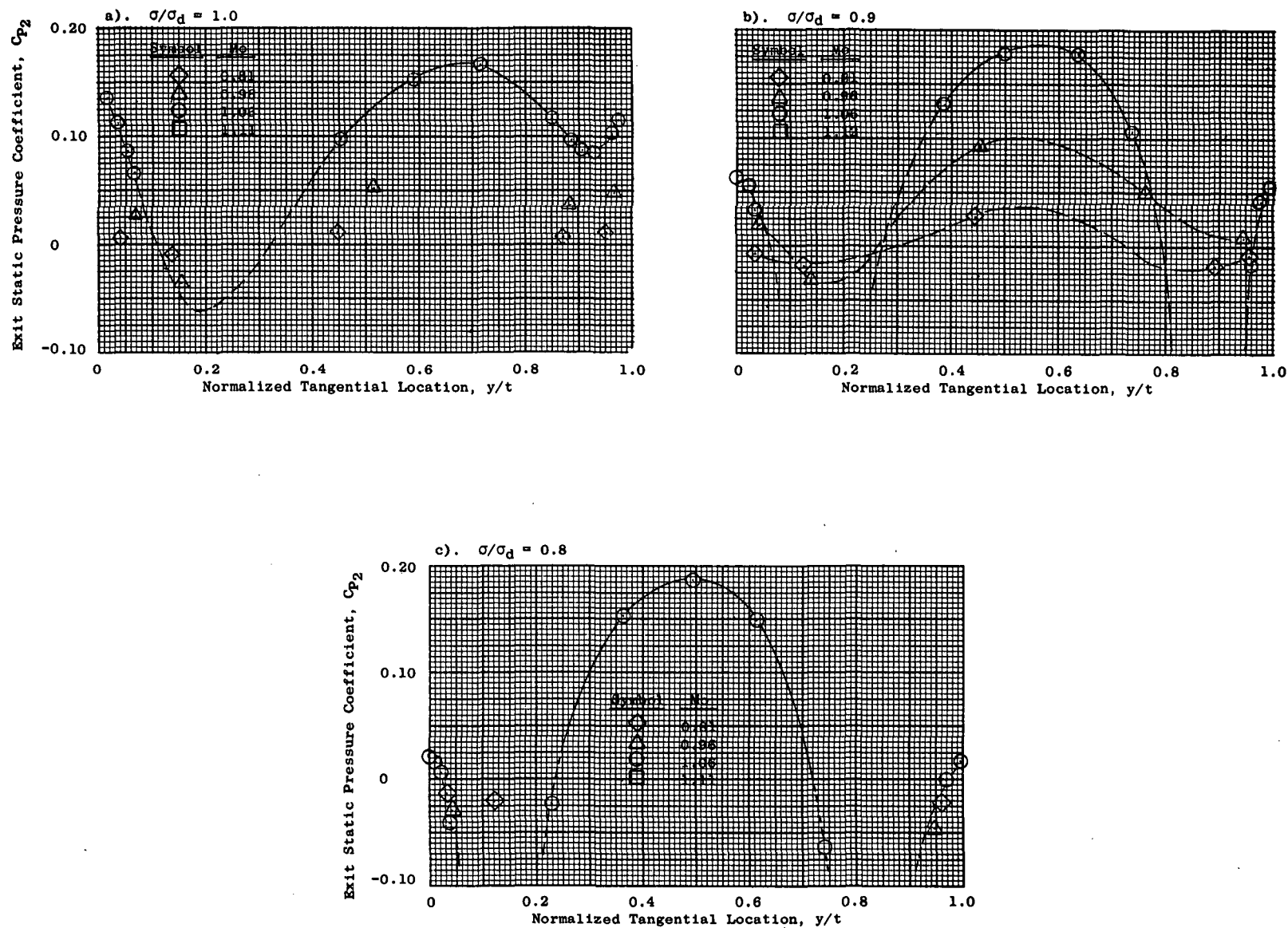


Figure 20. Exit Static Pressure Coefficient Vs. Normalized Tangential Location, NlR , $i = 0^\circ$.

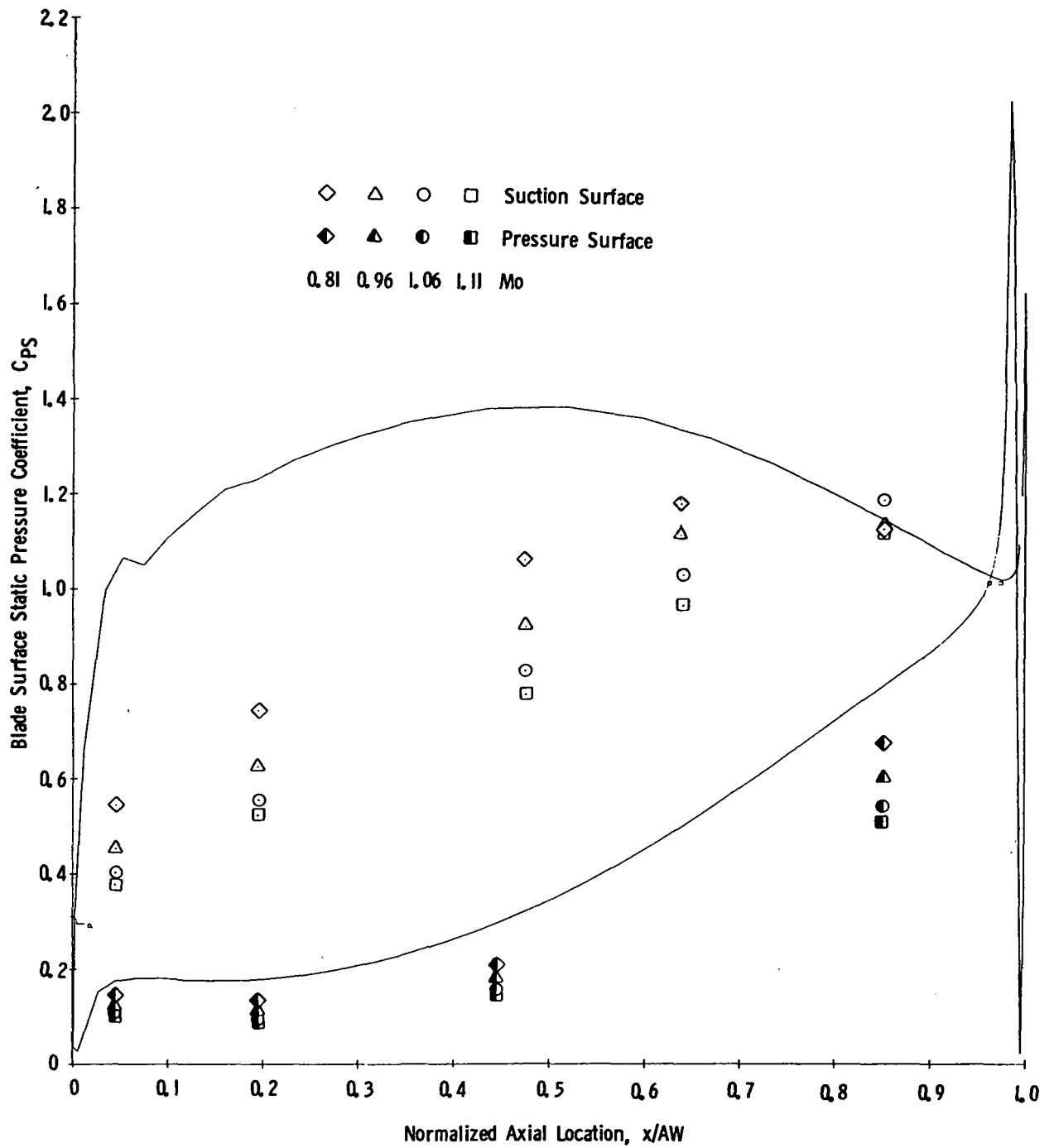


Figure 21. Blade Surface Static Pressure Coefficient Vs. Normalized Axial Location, NlR , $\sigma/\sigma_d = 1.0$, $i = 0^\circ$.

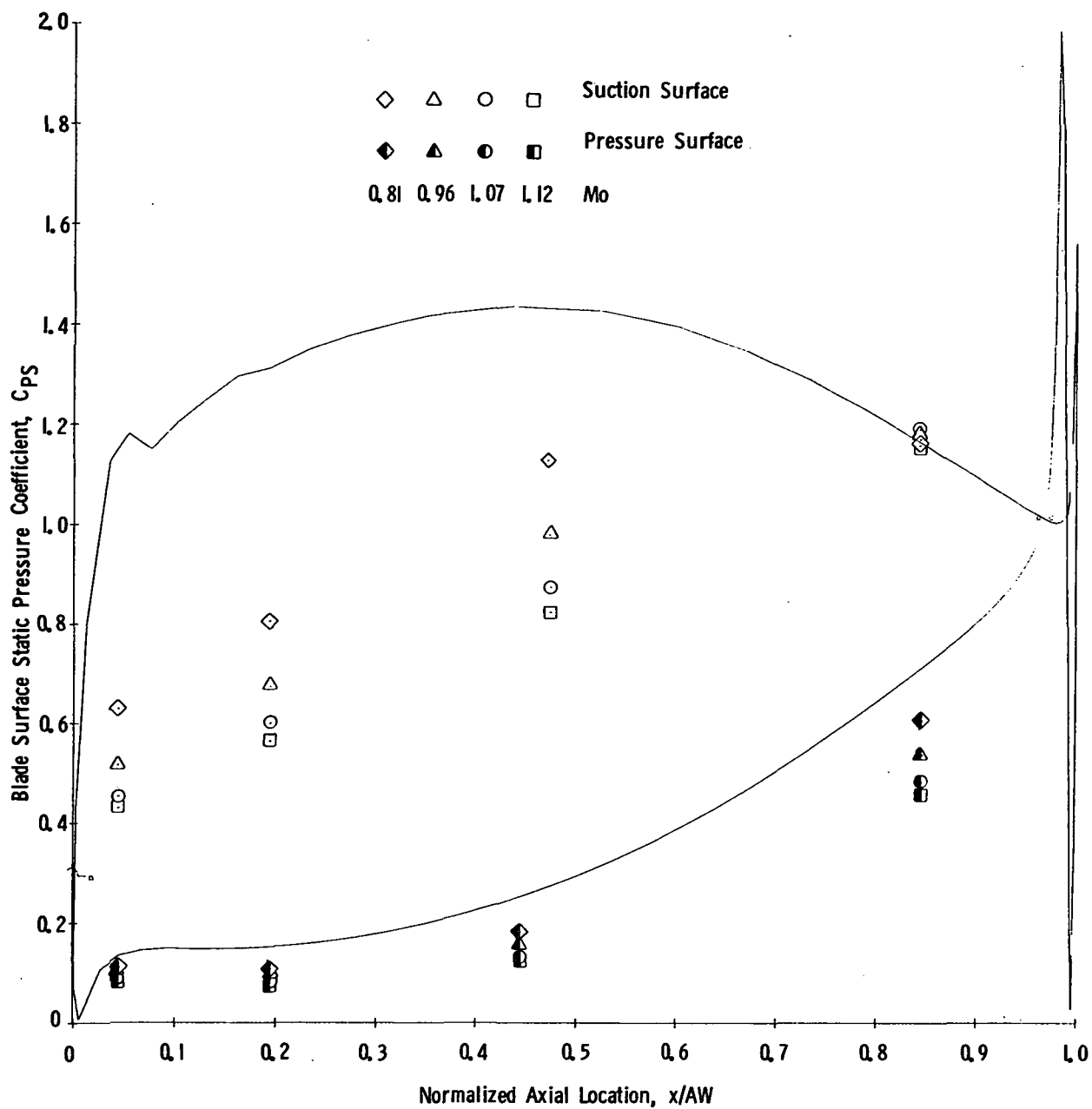


Figure 22. Blade Surface Static Pressure Coefficient Vs. Normalized Axial Location, N1R, $\sigma/\sigma_d = 0.9$, $i = 0^\circ$.

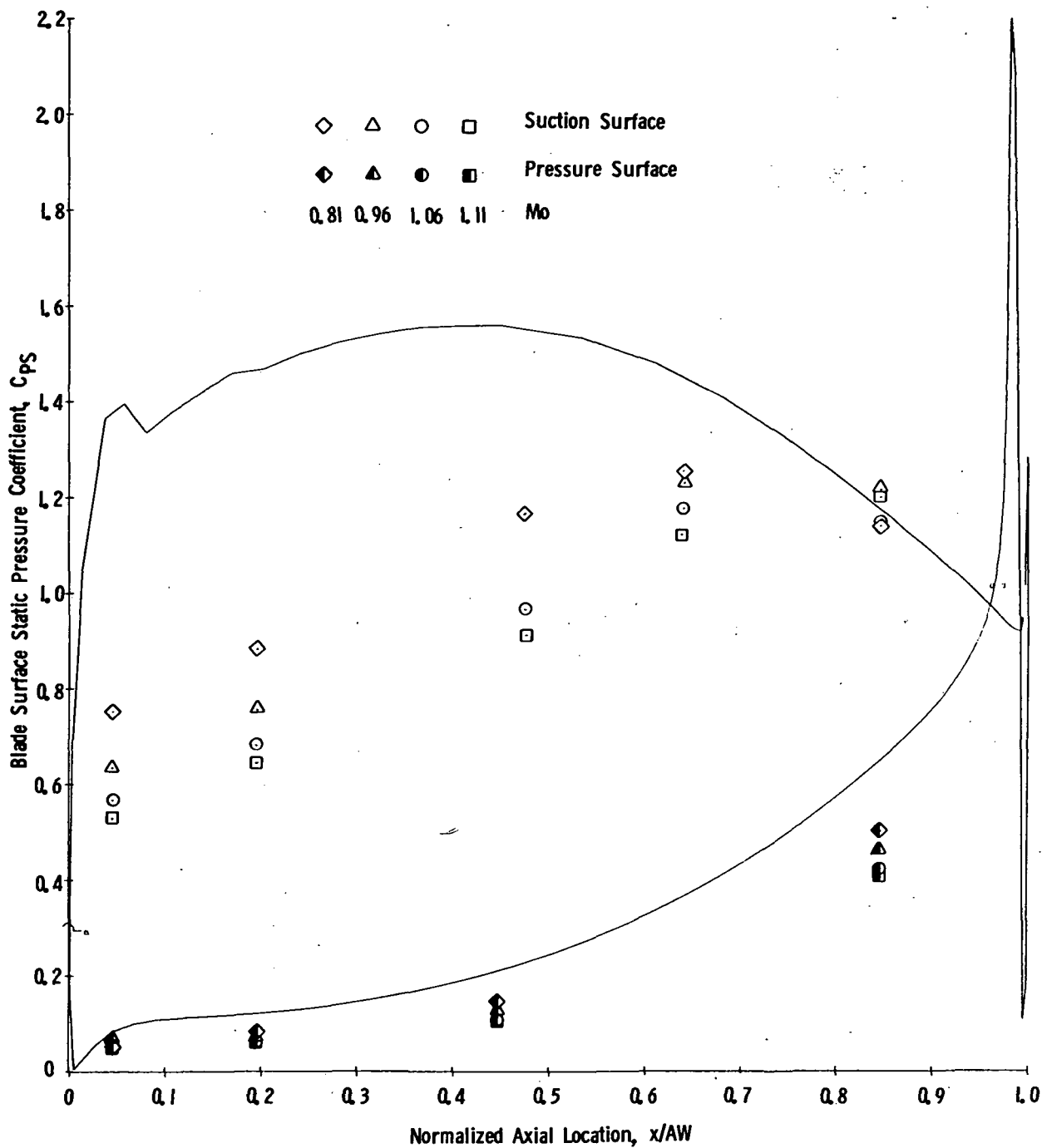


Figure 23. Blade Surface Static Pressure Coefficient Vs. Normalized Axial Location, NlR , $\sigma/\sigma_d = 0.8$, $i = 0^\circ$.

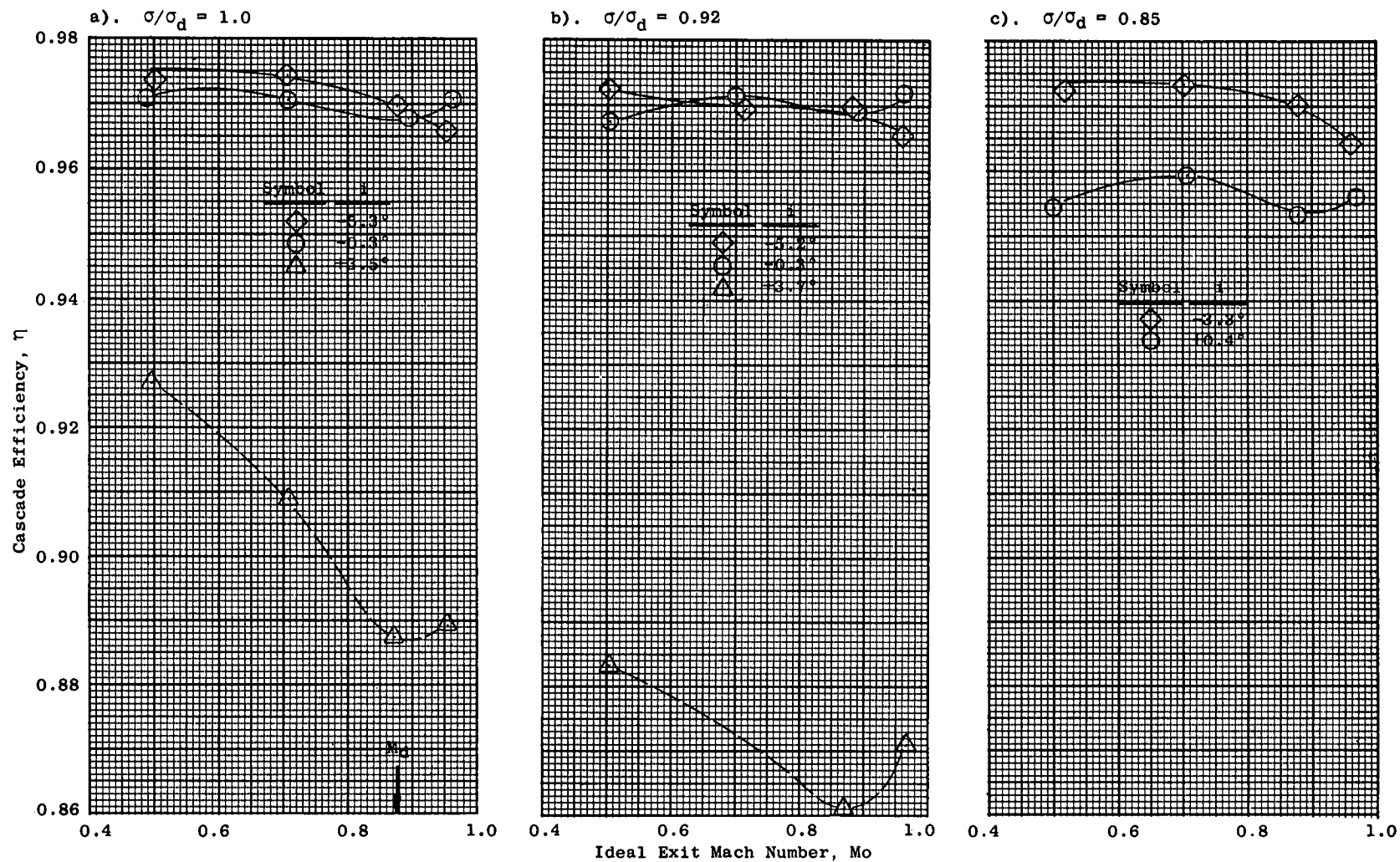


Figure 24. Cascade Efficiency Vs. Mach Number, BlR.

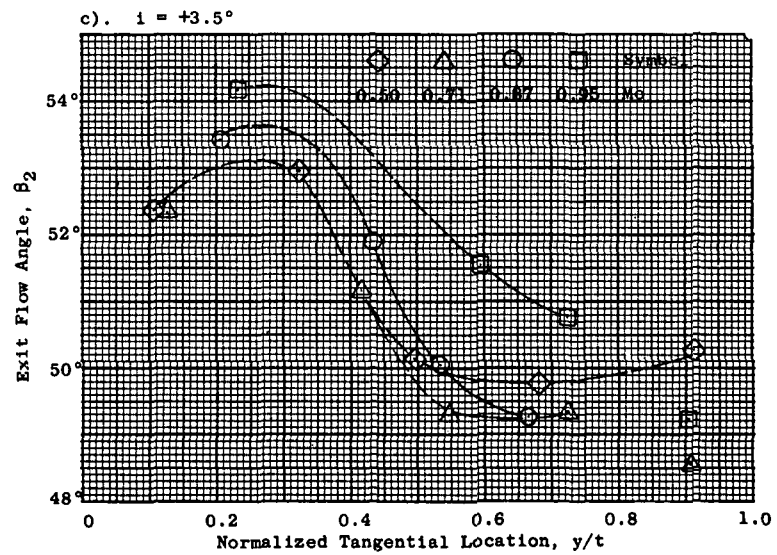
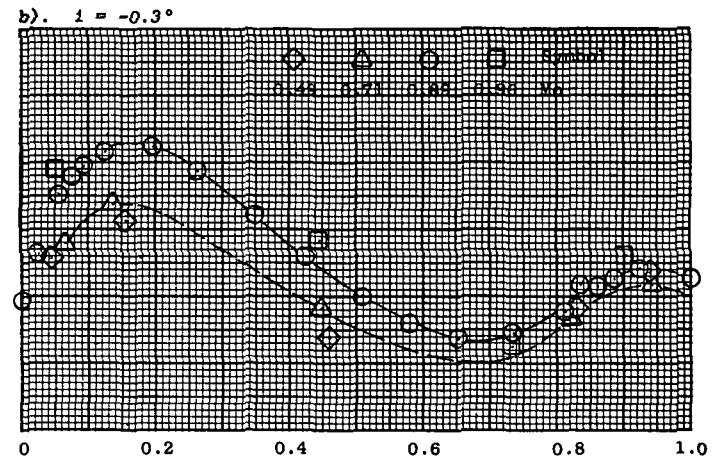
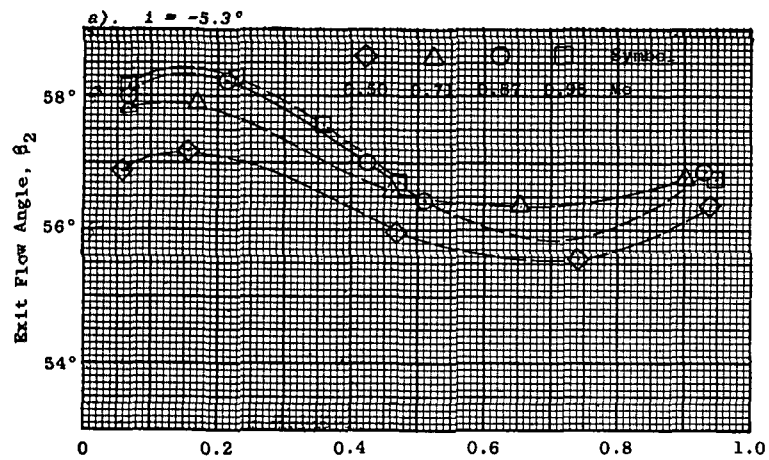


Figure 25. Exit Flow Angle Vs. Normalized Tangential Location, B/R , $\sigma/\sigma_d = 1.0$.

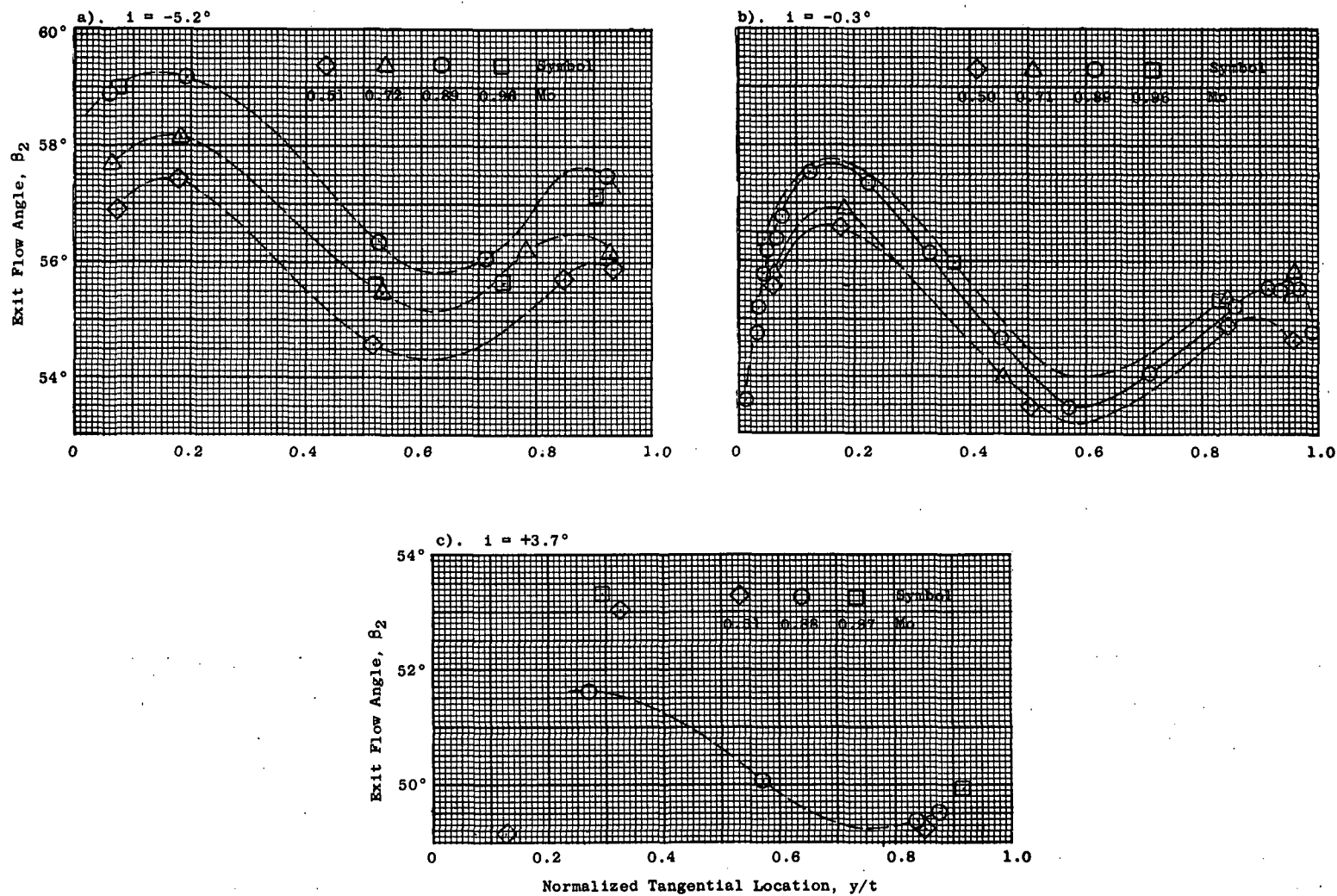


Figure 26. Exit Flow Angle Vs. Normalized Tangential Location, BlR, $\sigma/\sigma_d = 0.92$.

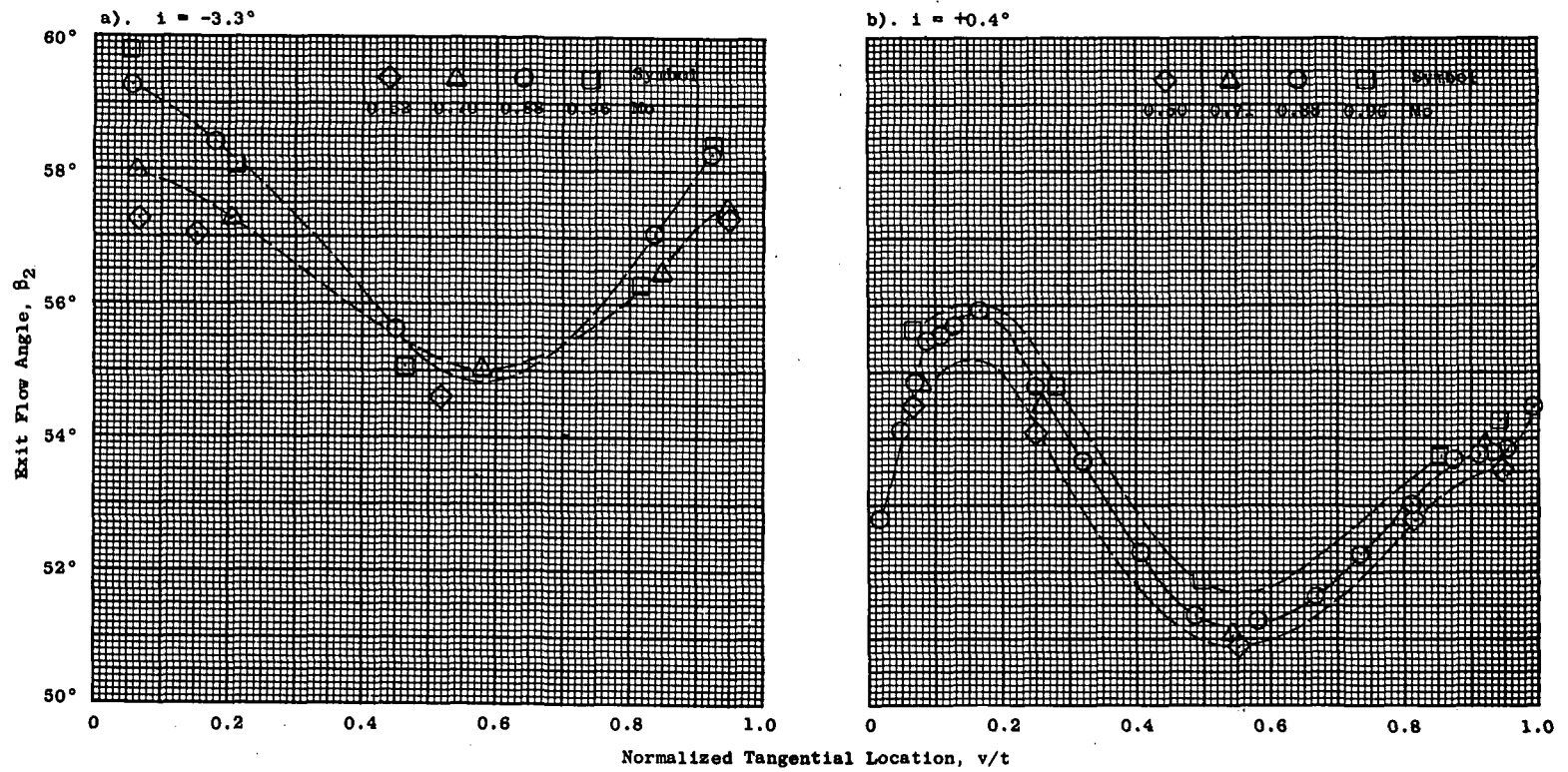


Figure 27. Exit Flow Angle Vs. Normalized Tangential Location, $B1R$, $\sigma/\sigma_d = 0.85$.

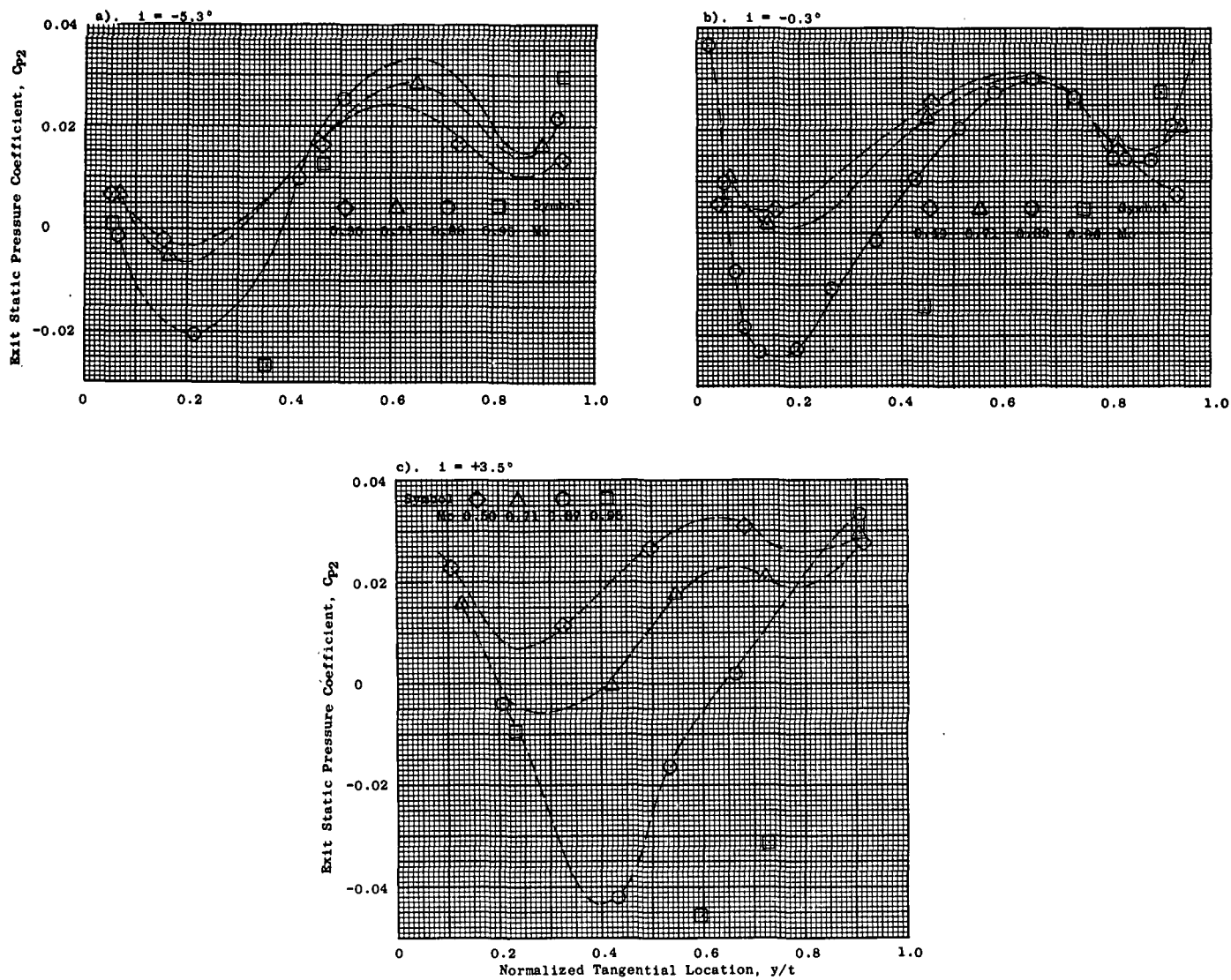


Figure 28. Exit Static Pressure Coefficient Vs. Normalized Tangential Location, B1R, $\sigma/\sigma_d = 1.0$.

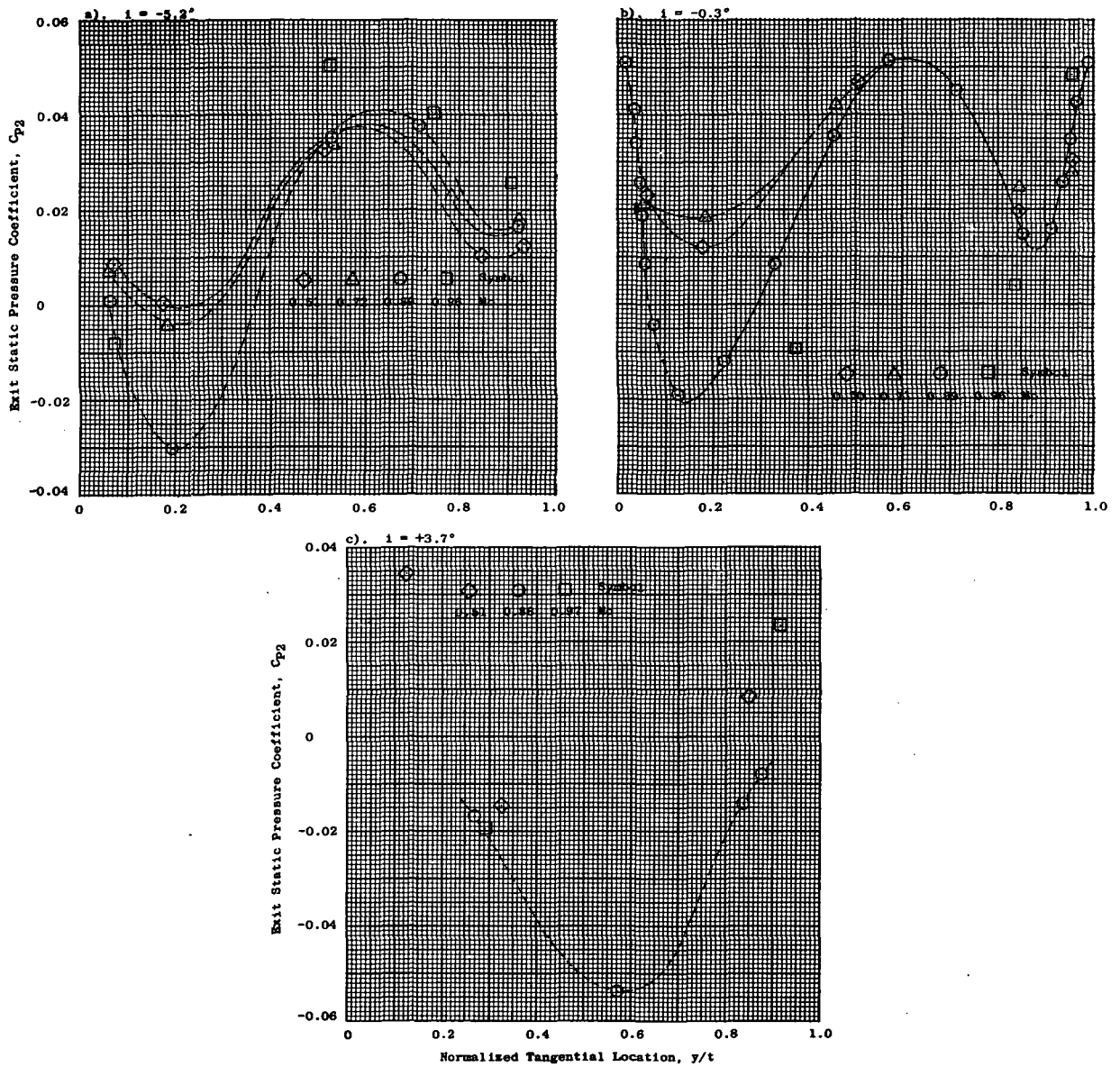


Figure 29. Exit Static Pressure Coefficient Vs. Normalized Tangential Location, BlR, $\sigma/\sigma_d = 0.92$.

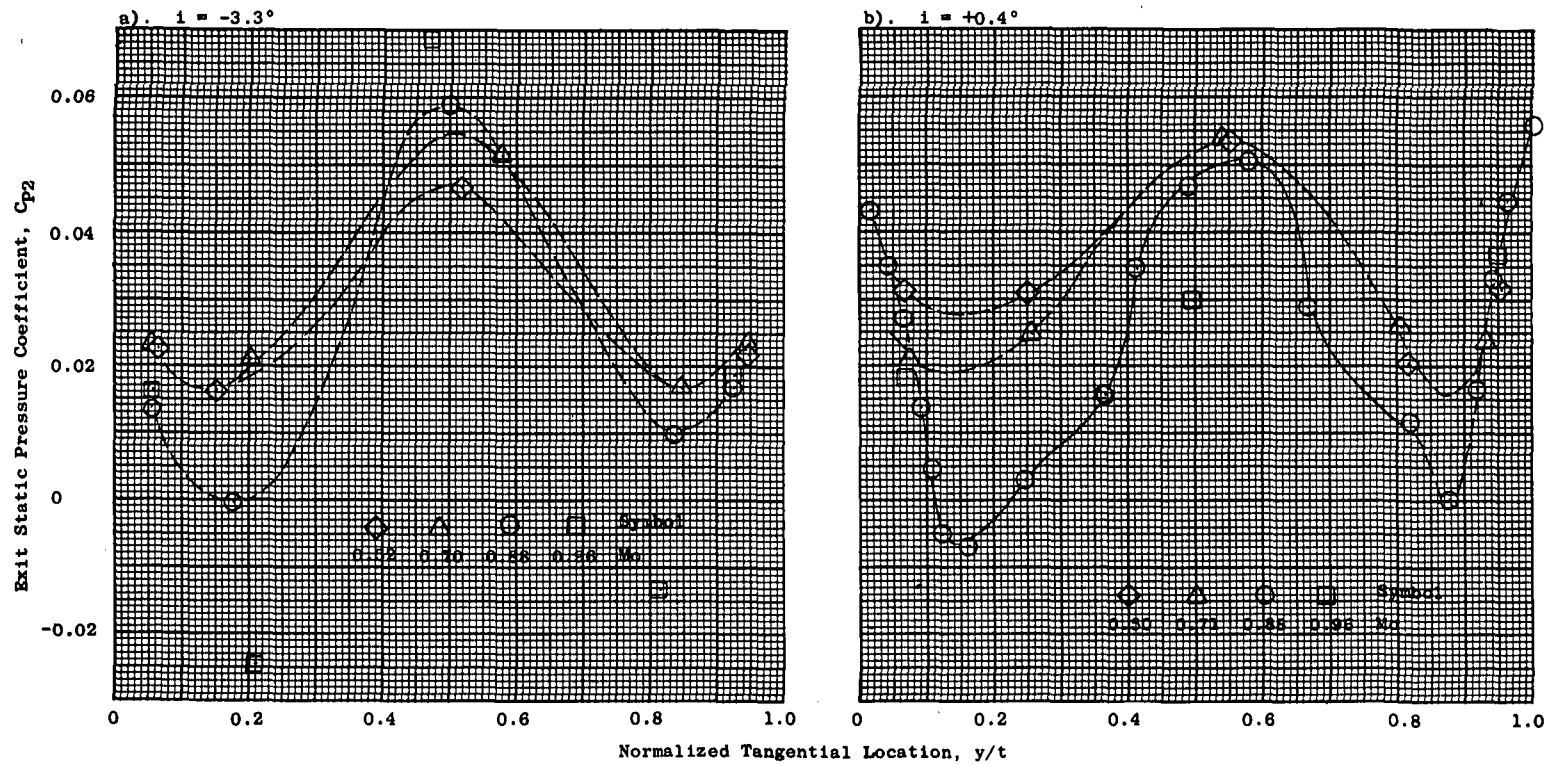


Figure 30. Exit Static Pressure Coefficient Vs. Normalized Tangential Location, B1R,
 $\sigma/\sigma_d = 0.85$.

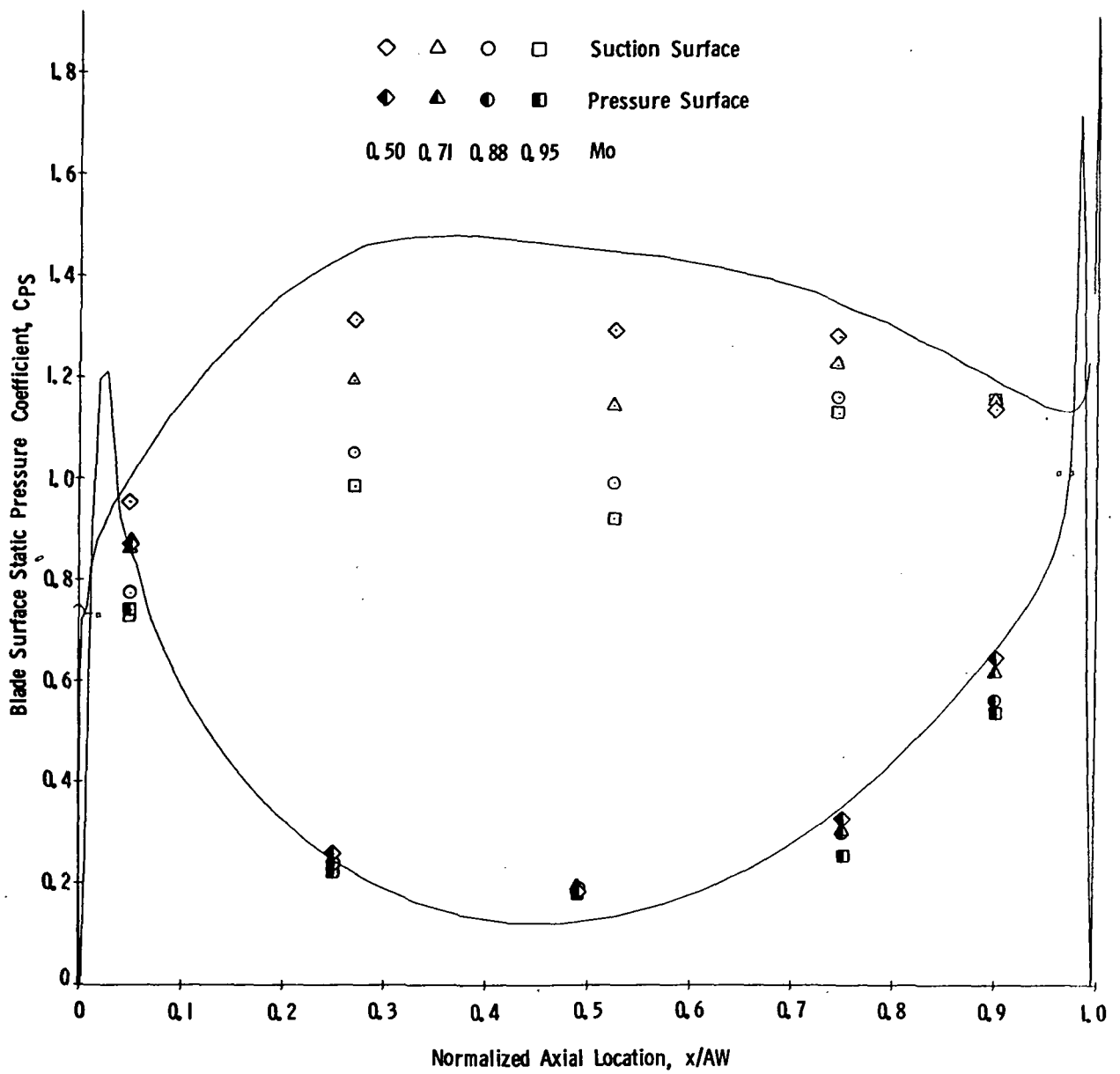


Figure 31. Blade Surface Static Pressure Coefficient Vs. Normalized Axial Location, BlR, $\sigma/\sigma_d = 1.0$, $i = -5.3^\circ$.

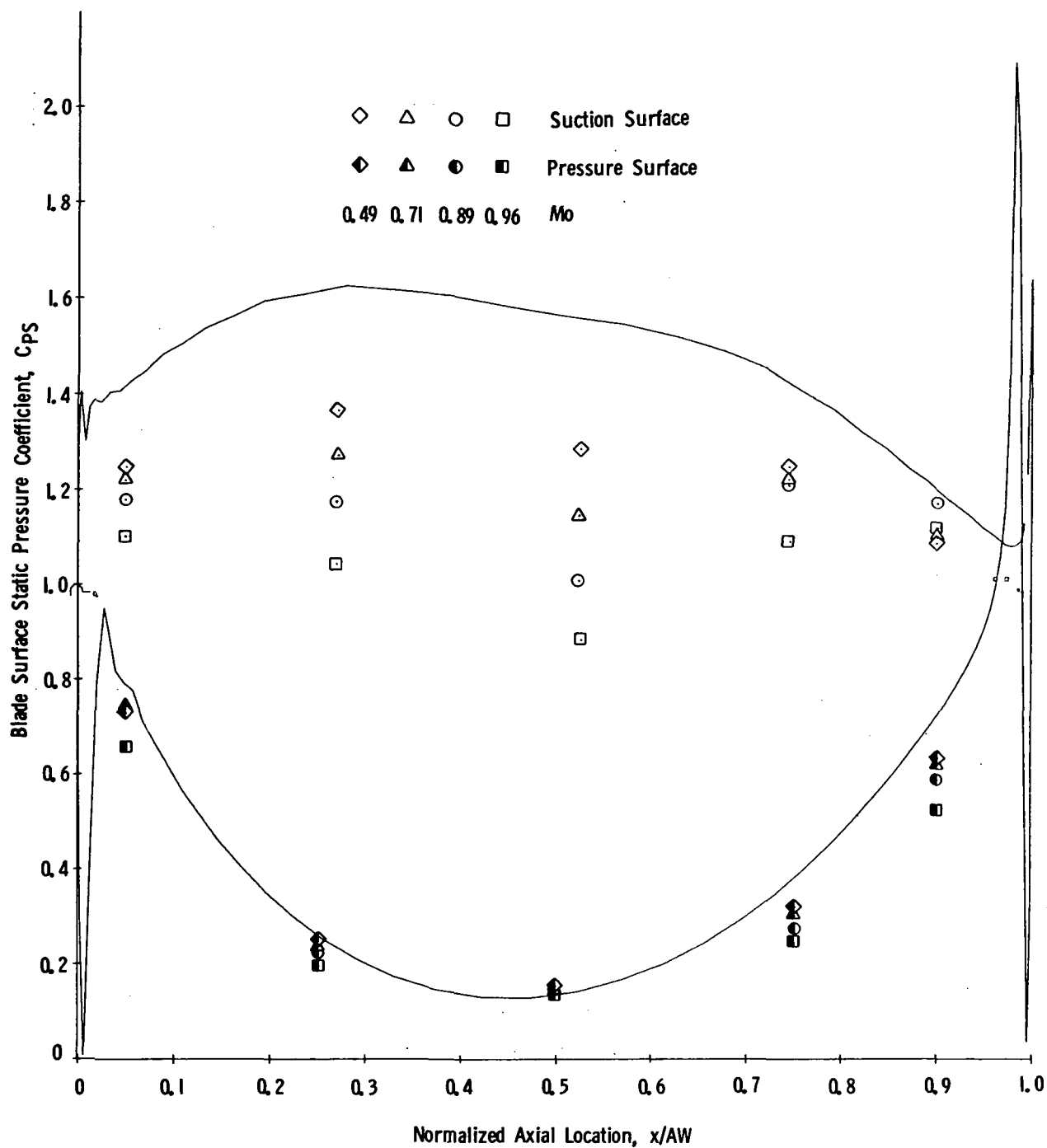


Figure 32. Blade Surface Static Pressure Coefficient Vs. Normalized Axial Location, BlR, $\sigma/\sigma_d = 1.0$, $i = -0.3^\circ$.

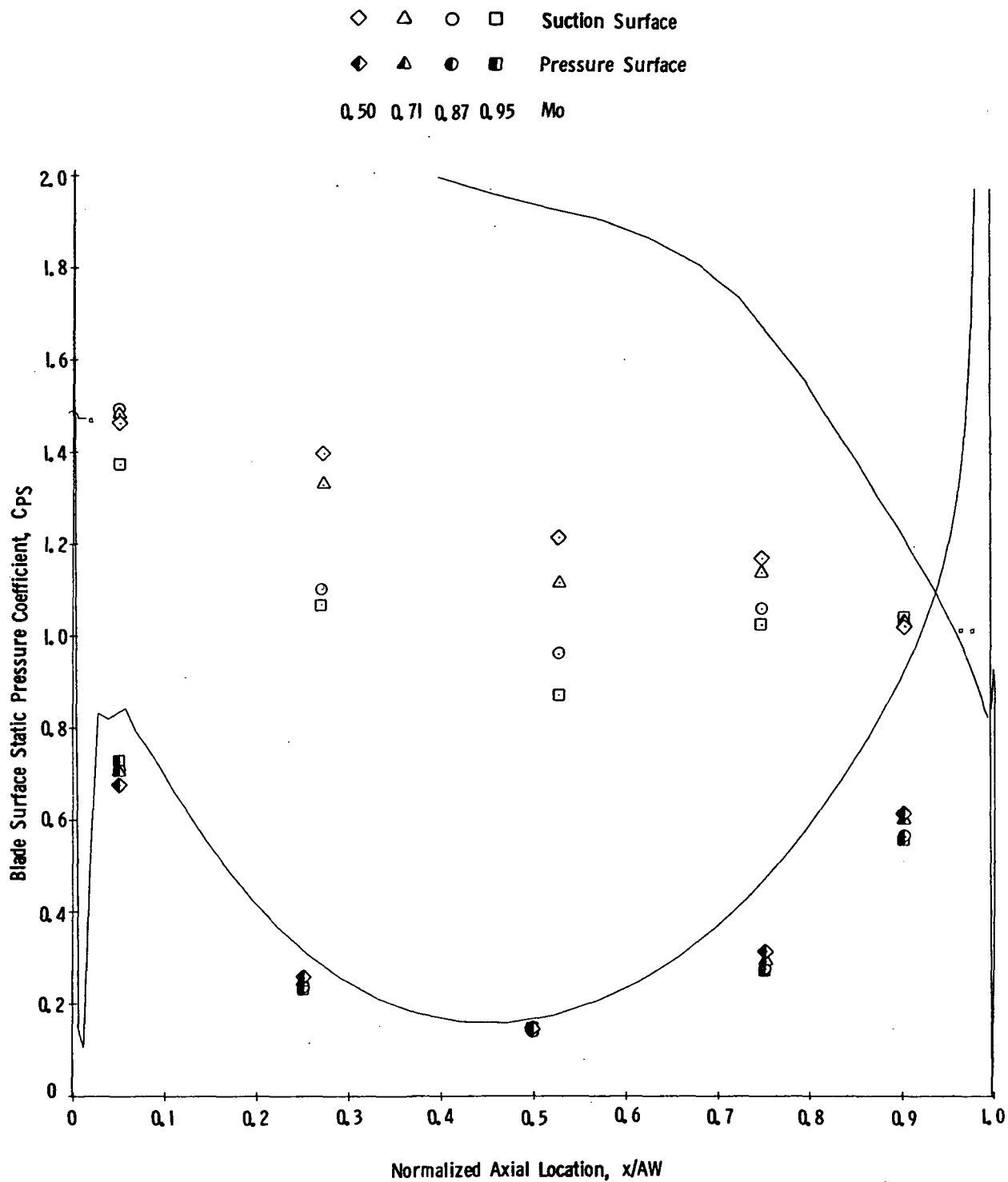


Figure 33. Blade Surface Static Pressure Coefficient Vs. Normalized Axial Location, BlR, $\sigma/\sigma_d = 1.0$, $i = 3.5^\circ$.

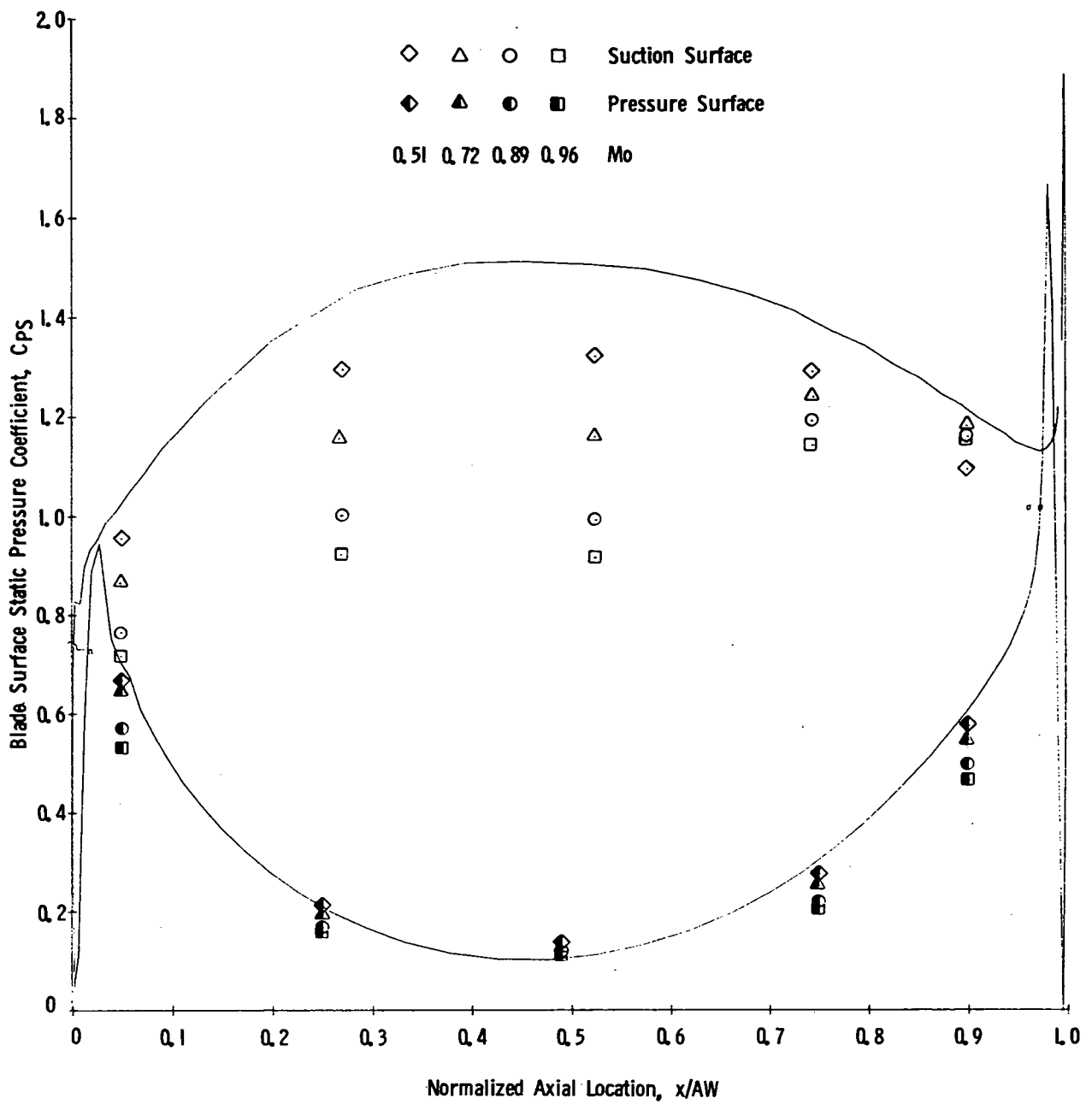


Figure 34. Blade Surface Static Pressure Coefficient Vs. Normalized Axial Location, B1R, $\sigma/\sigma_d = 0.92$, $i = -5.2^\circ$.

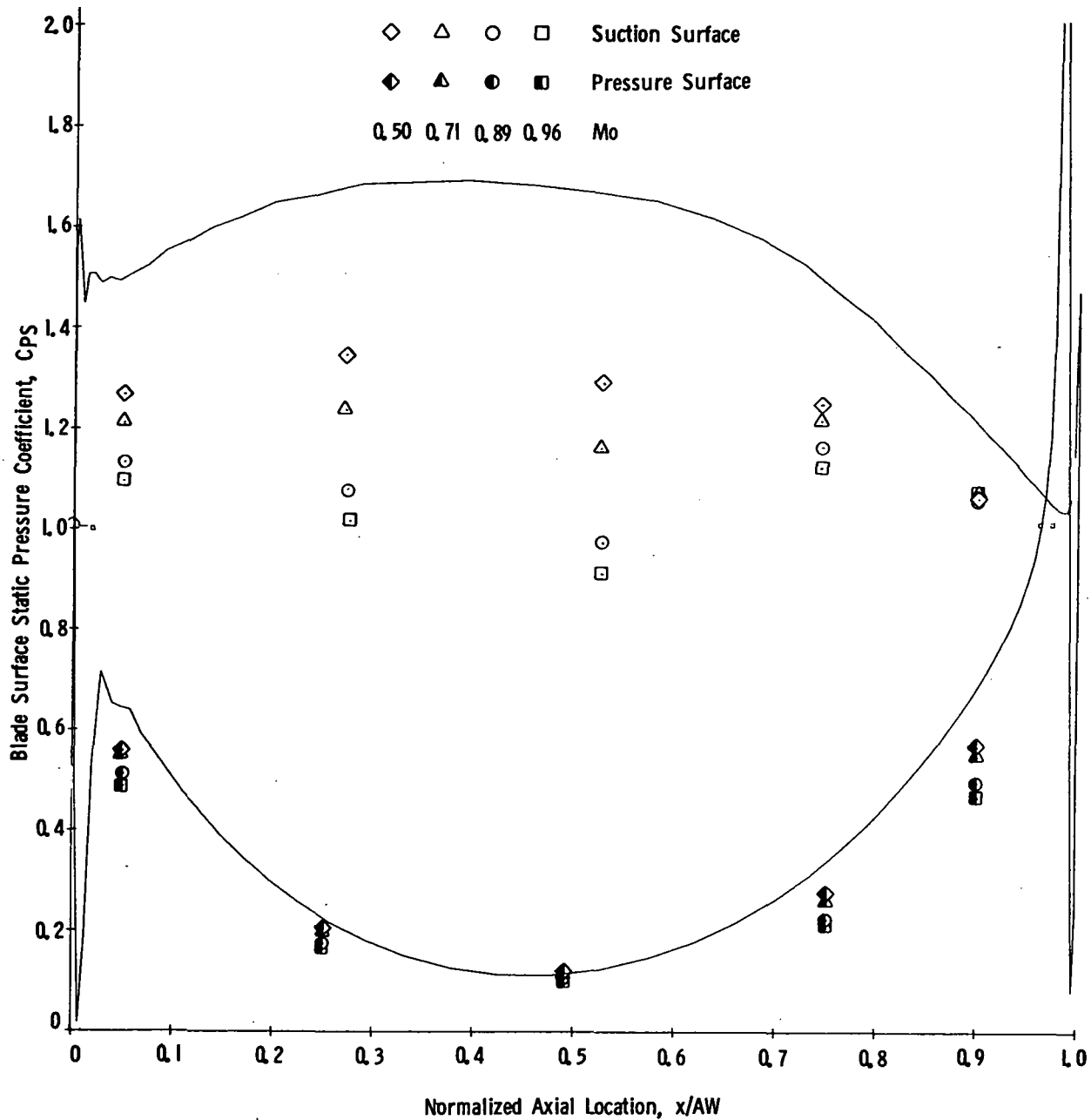


Figure 35. Blade Surface Static Pressure Coefficient Vs. Normalized Axial Location, BlR , $\sigma/\sigma_d = 0.92$, $i = -0.3^\circ$.

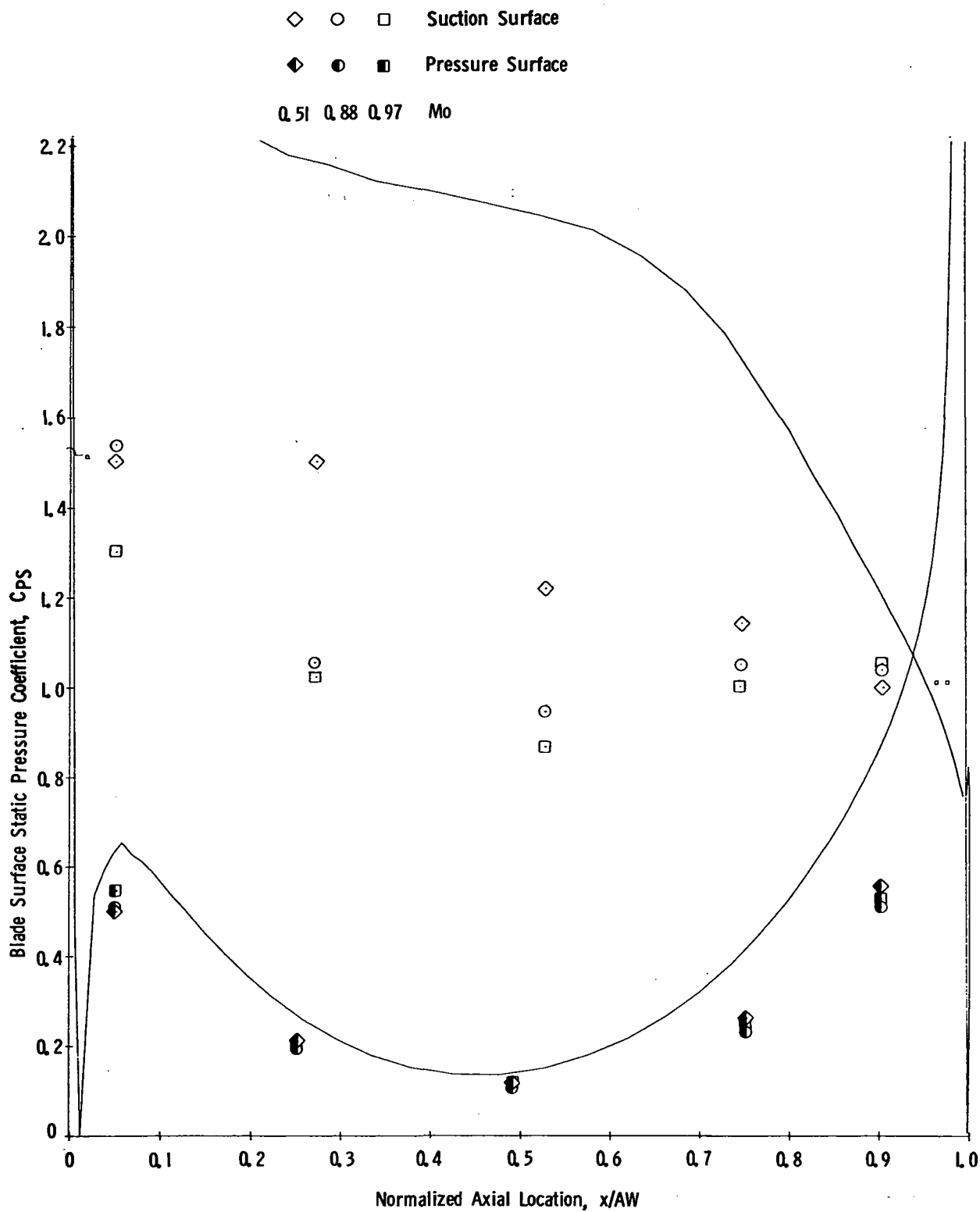


Figure 36. Blade Surface Static Pressure Coefficient Vs. Normalized Axial Location, B1R, $\sigma/\sigma_d = 0.92$, $i = 3.7^\circ$.

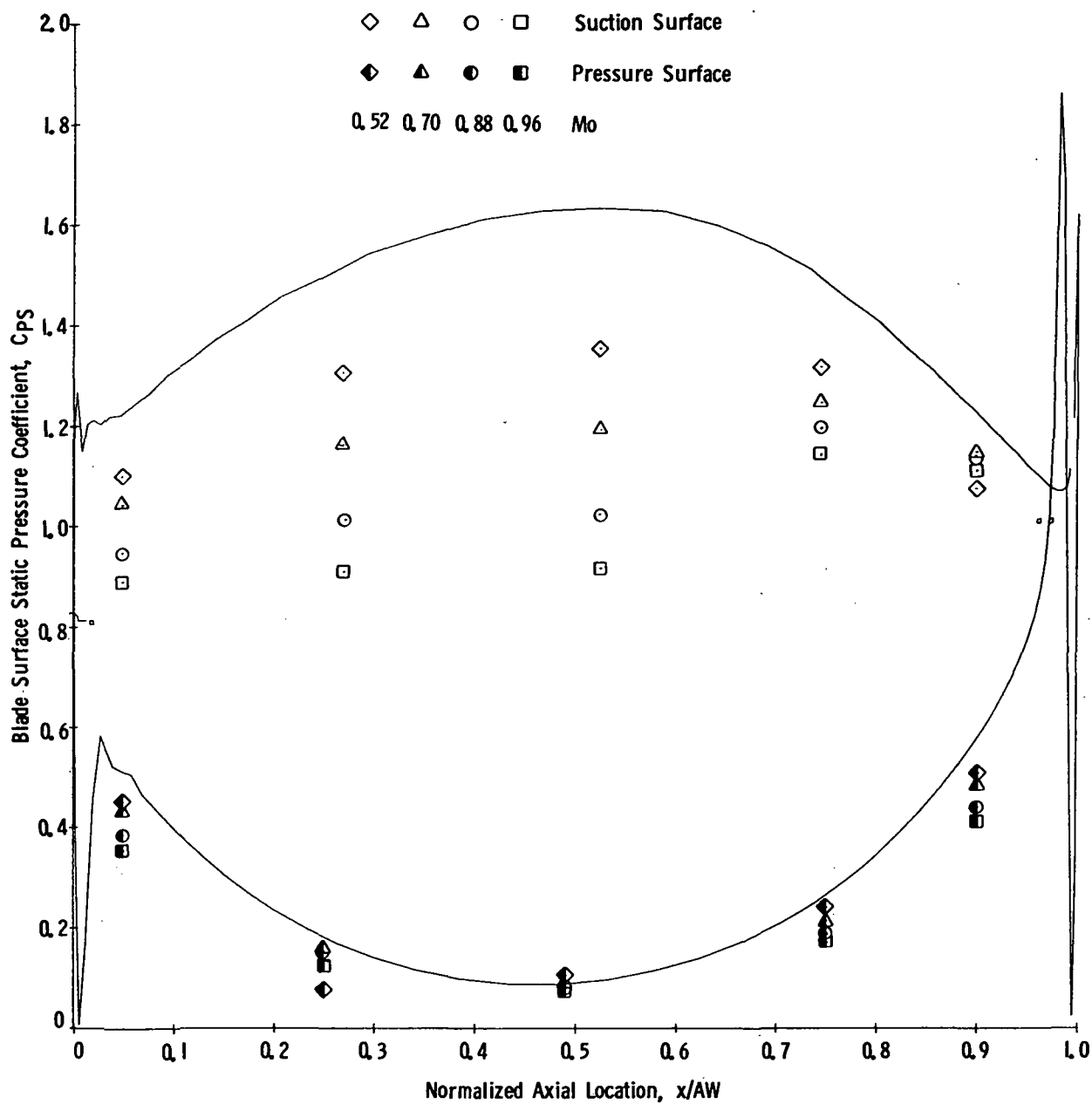


Figure 37. Blade Surface Static Pressure Coefficient Vs. Normalized Axial Location, $B1R$, $\sigma/\sigma_d = 0.85$, $i = -3.3^\circ$.

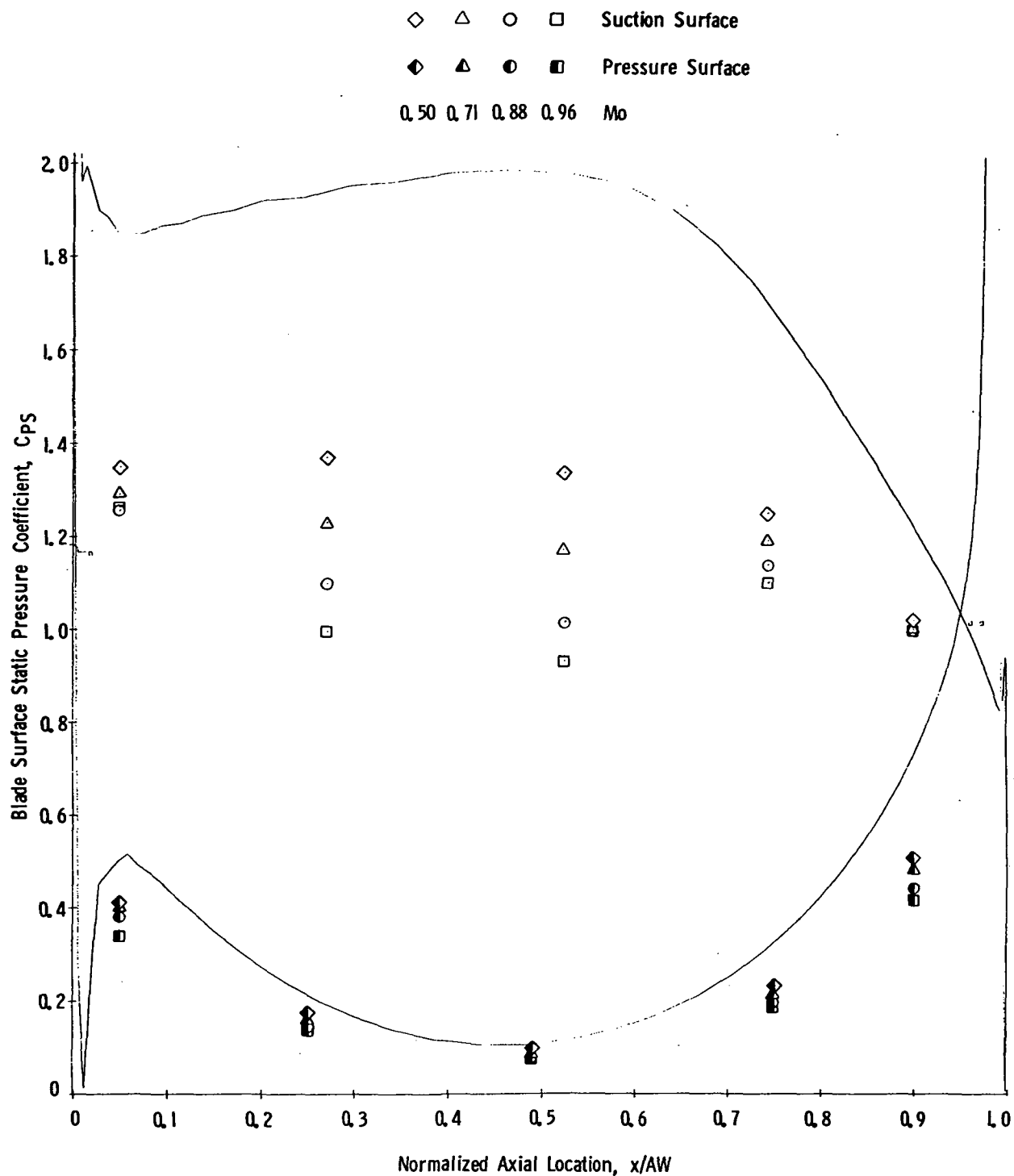


Figure 38. Blade Surface Static Pressure Coefficient Vs. Normalized Axial Location, BlR, $\sigma/\sigma_d = 0.85$, $i = 0.5^\circ$.

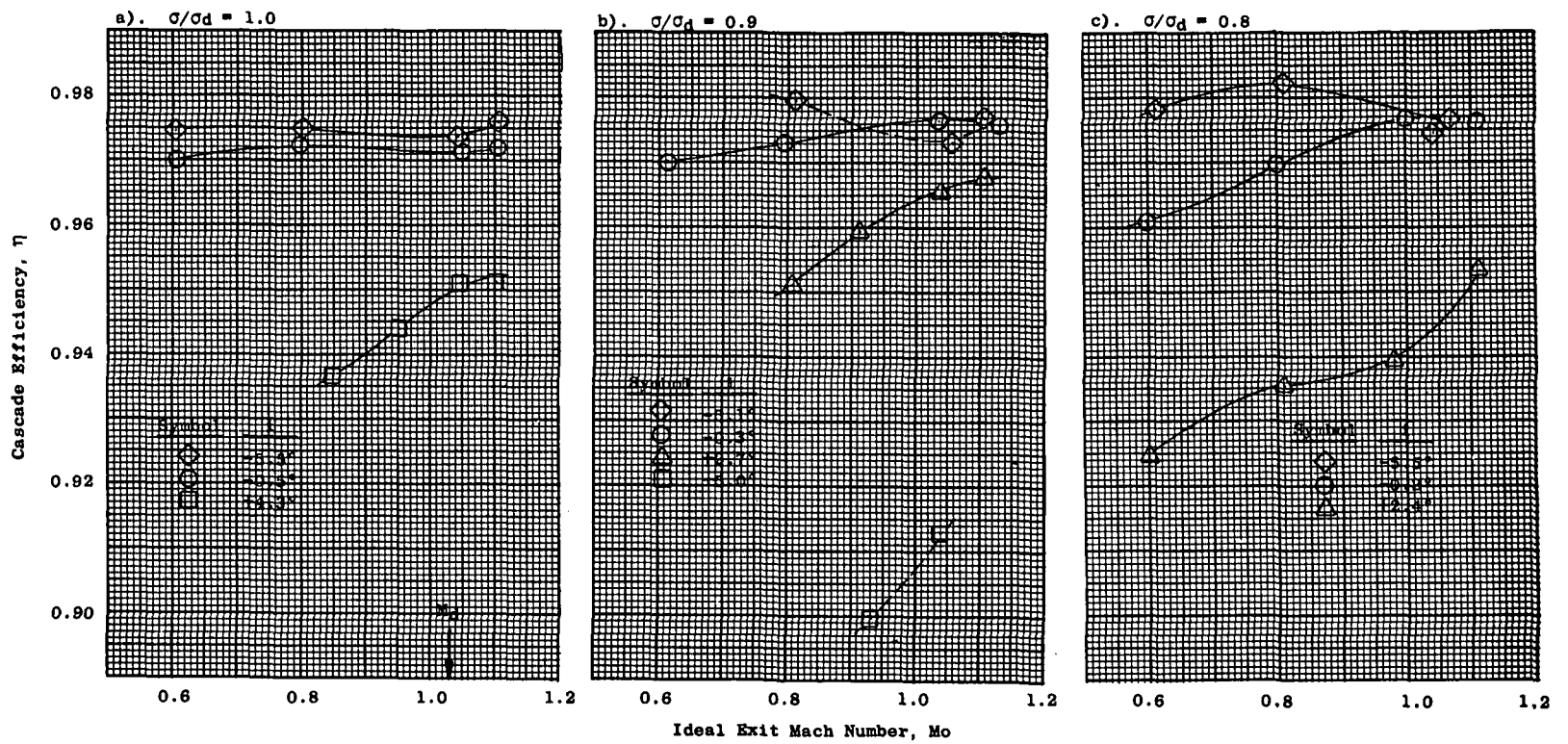


Figure 39. Cascade Efficiency Vs. Mach Number, N2R.

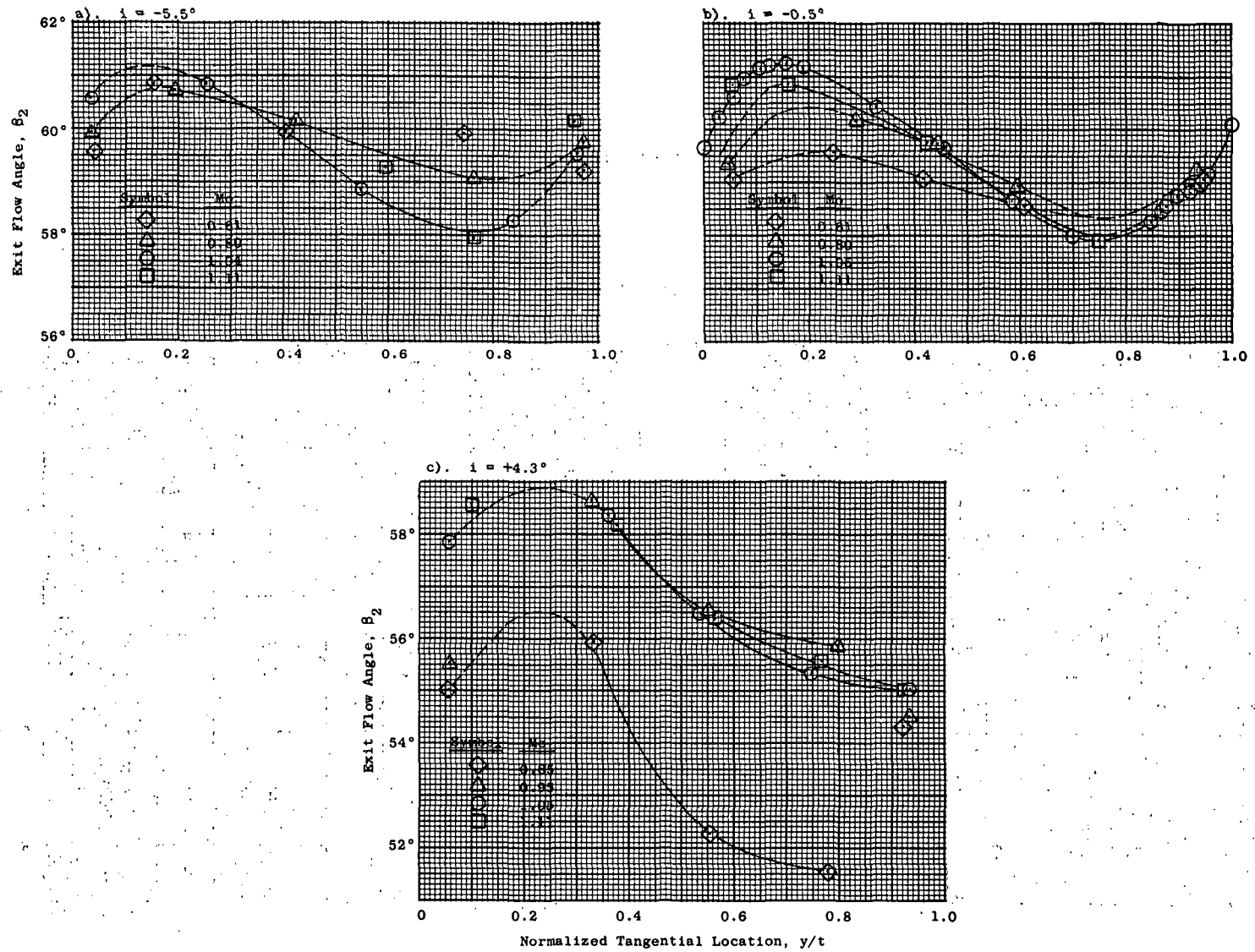


Figure 40. Exit Flow Angle Vs. Normalized Tangential Location, N2R, $\sigma/\sigma_d = 1.0$.

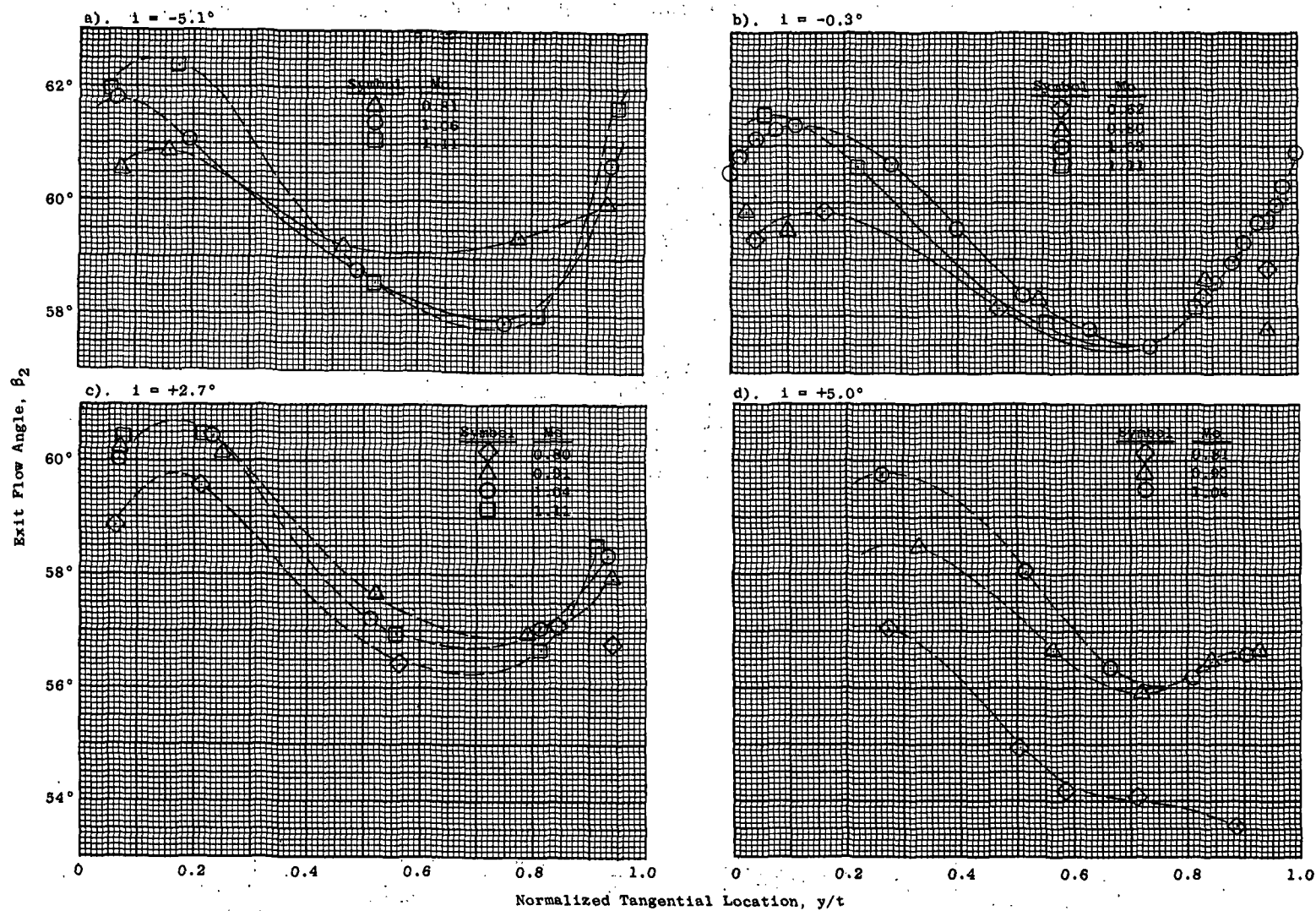


Figure 41. Exit Flow Angle Vs. Normalized Tangential Location, N_{2R} , $\sigma/\sigma_d = 0.9$.

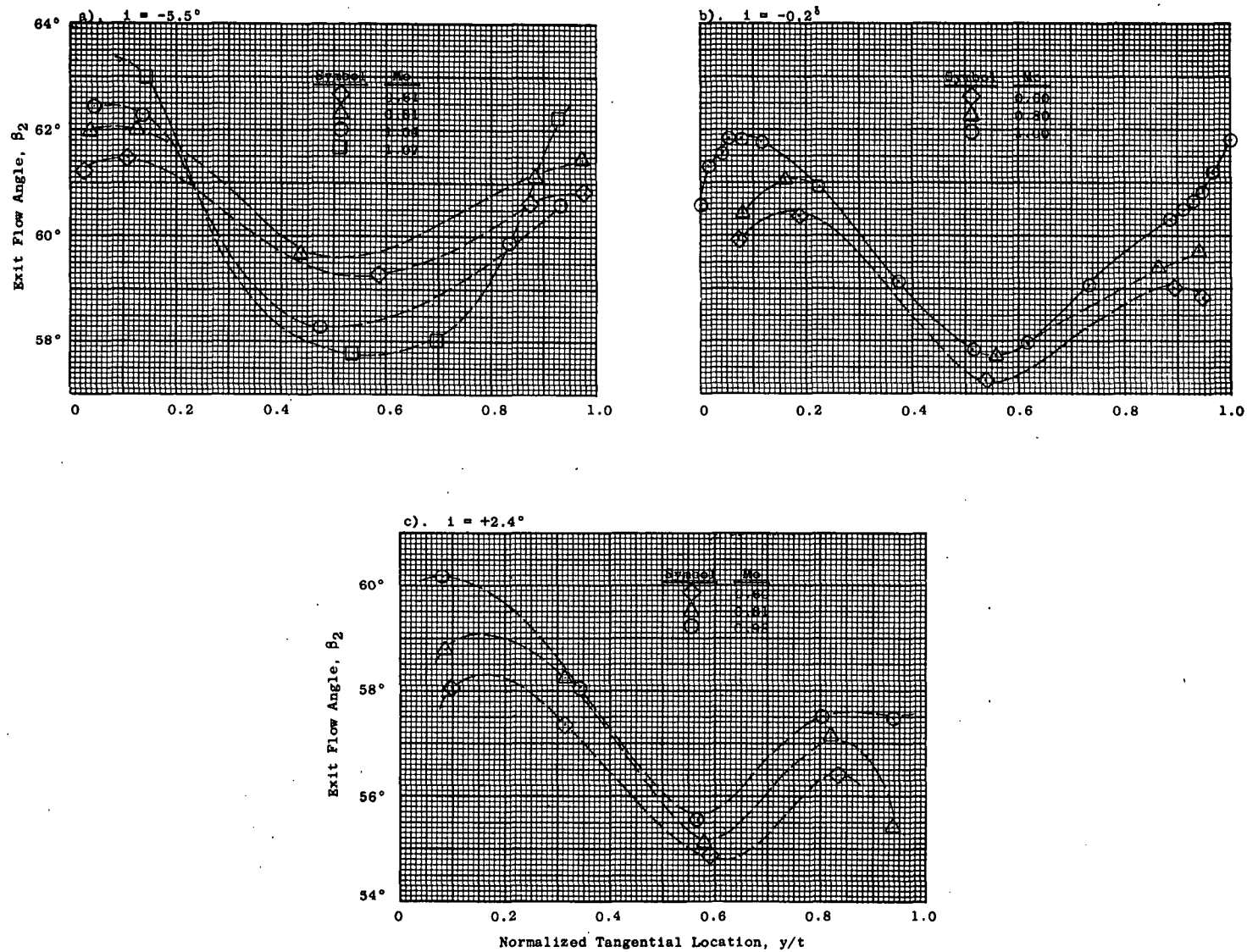


Figure 42. Exit Flow Angle Vs. Normalized Tangential Location, N2R, $\sigma/\sigma_d = 0.8$.

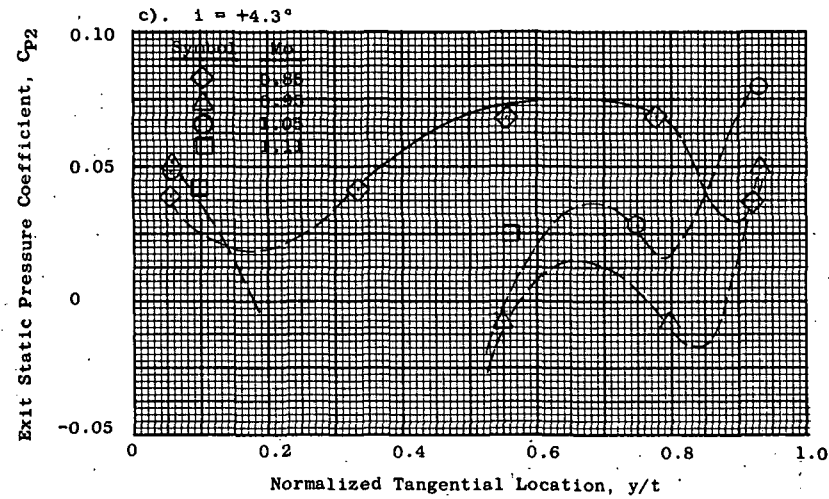
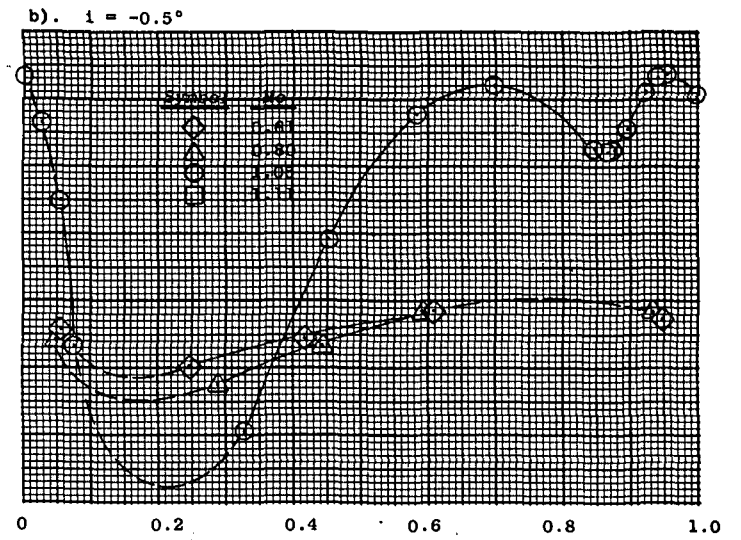
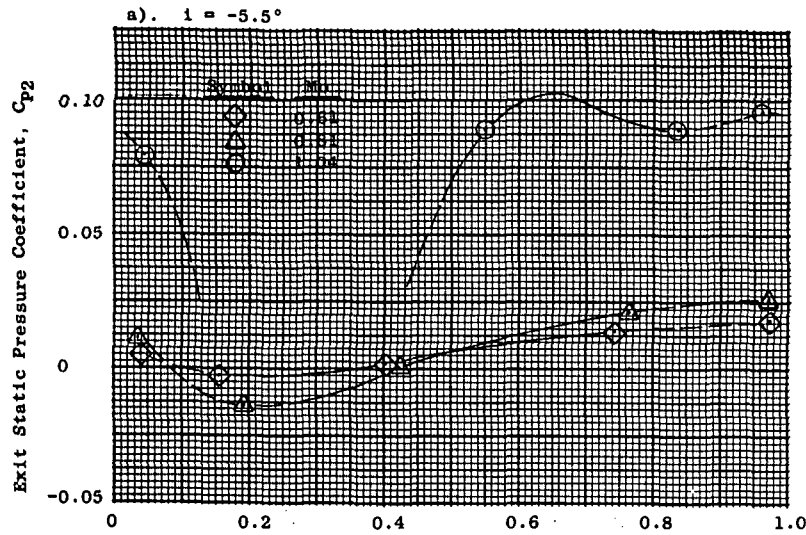


Figure 43. Exit Static Pressure Coefficient Vs. Normalized Tangential Location, N2R, $\sigma/\sigma_d = 1.0$.

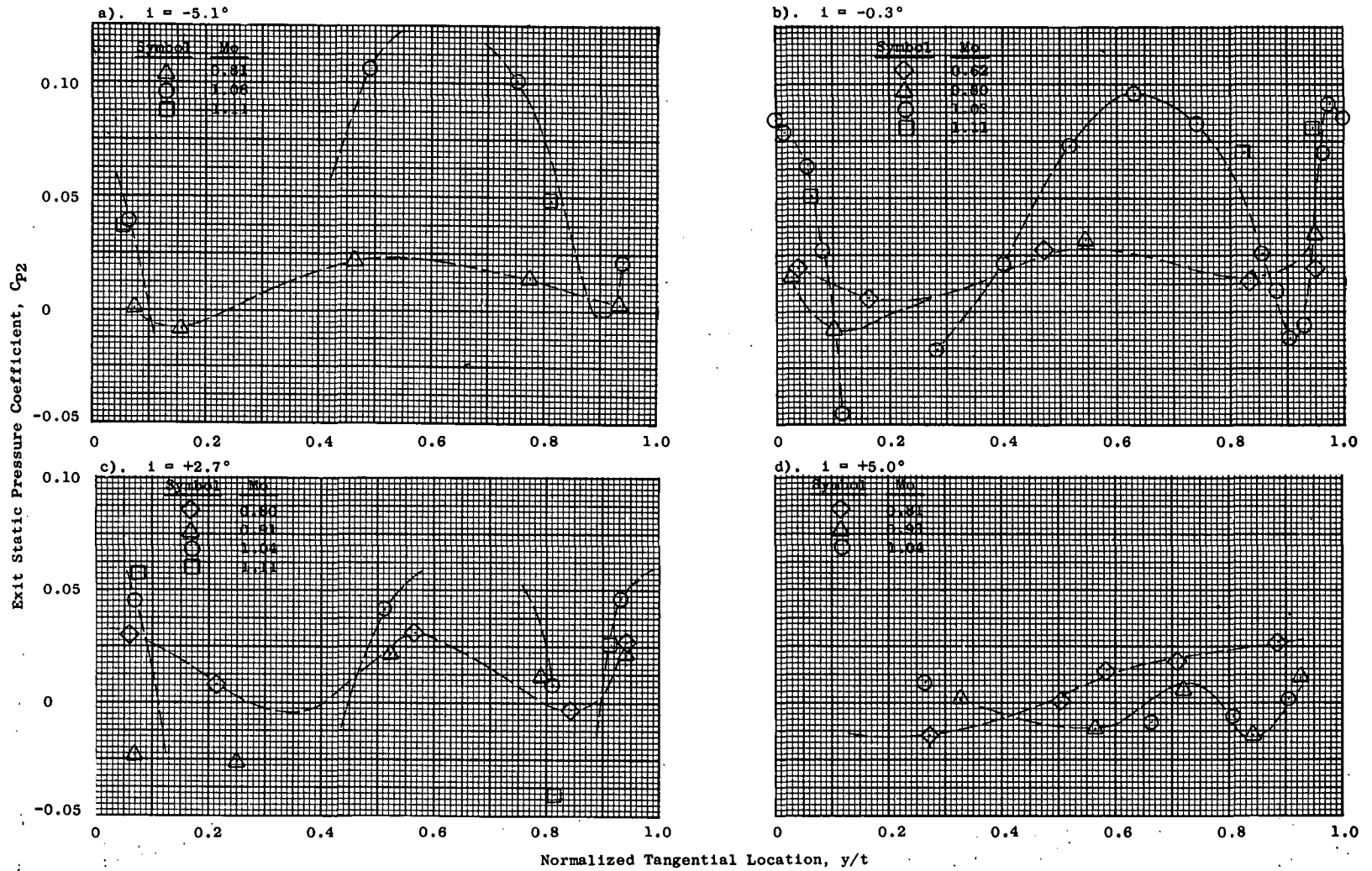


Figure 44. Exit Static Pressure Coefficient Vs. Normalized Tangential Location, N2R, $\sigma/\sigma_d = 0.9$.

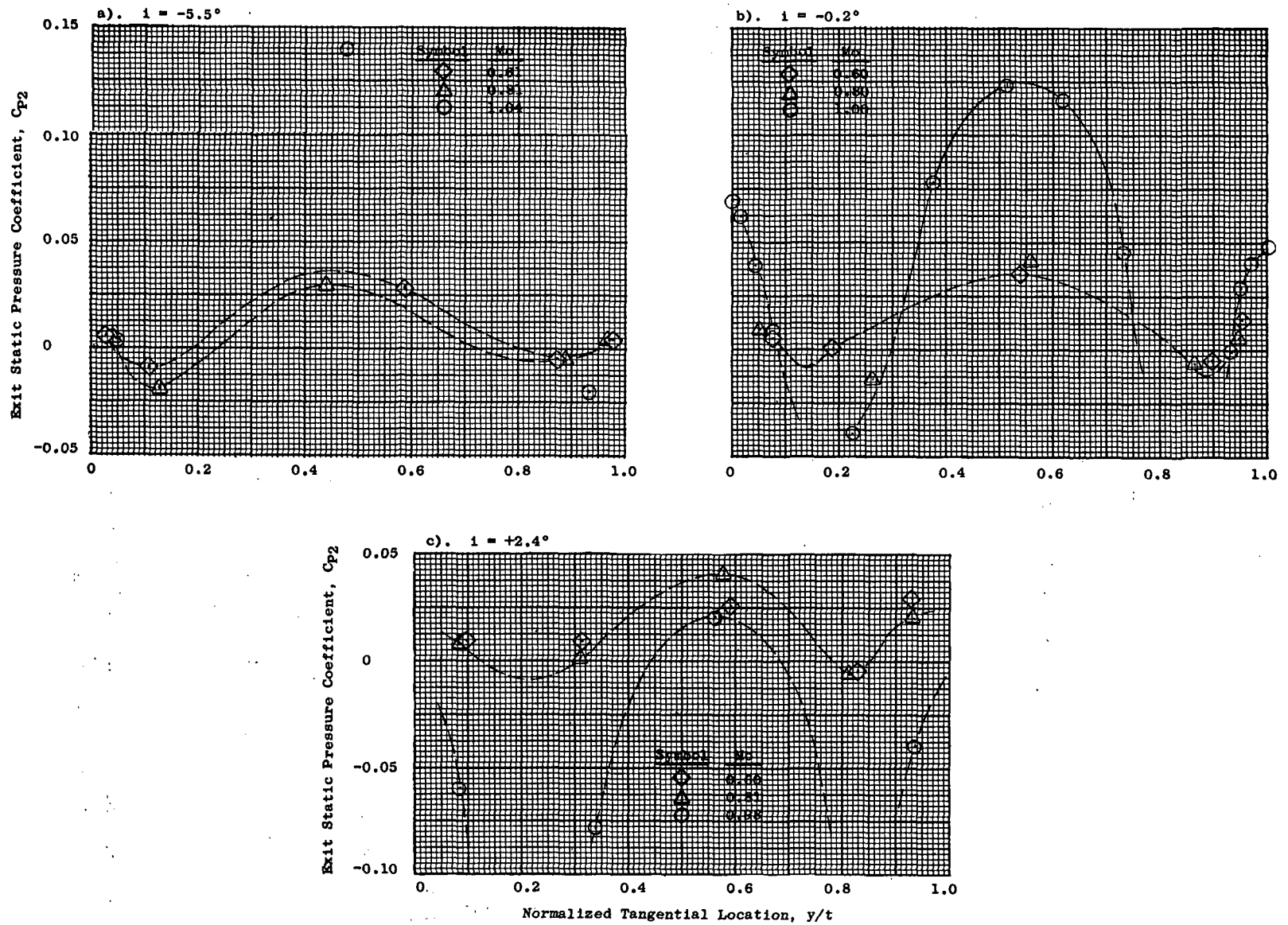


Figure 45. Exit Static Pressure Coefficient Vs. Normalized Tangential Location, N2R, $\sigma/\sigma_d = 0.8$.

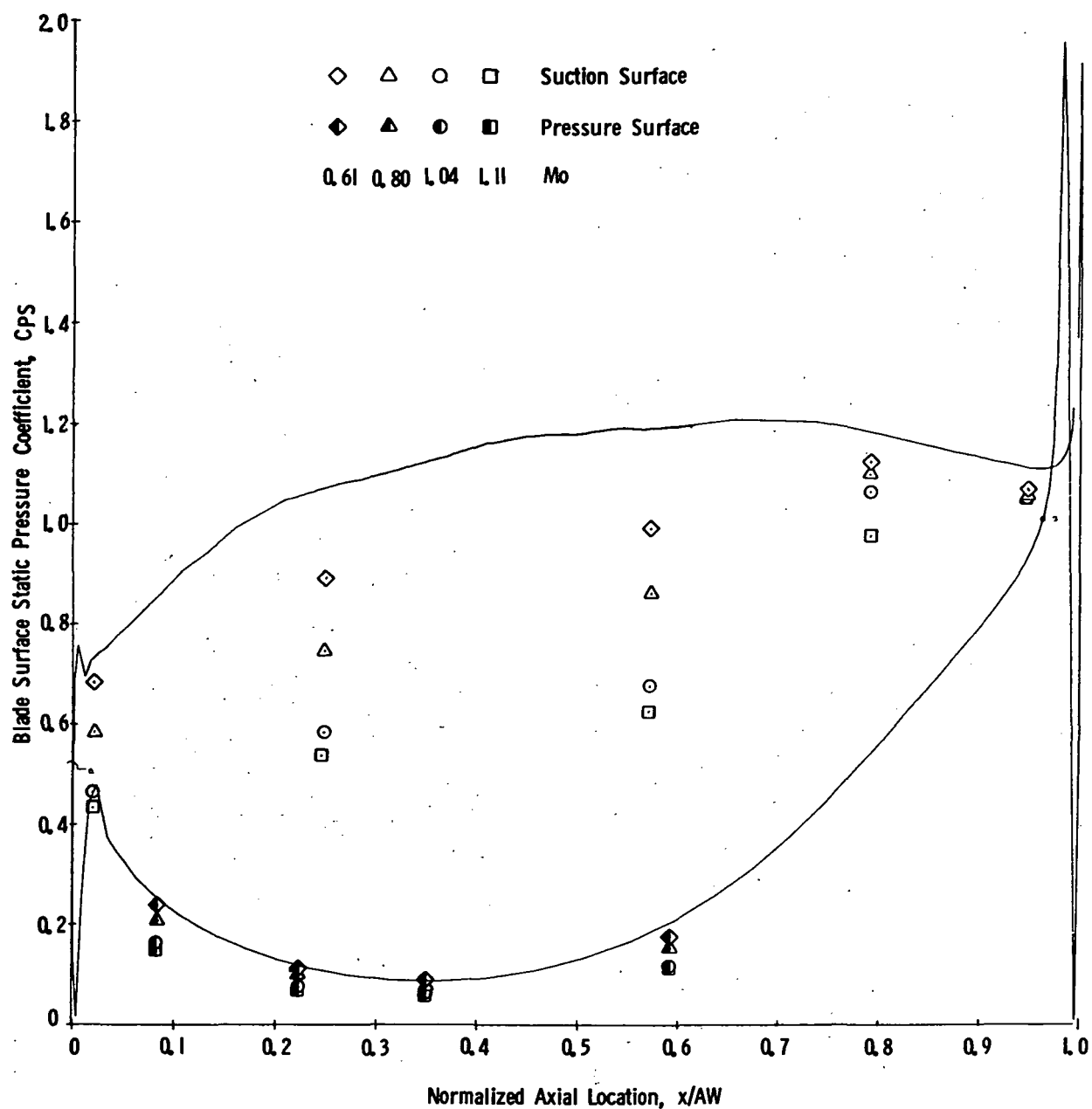


Figure 46. Blade Surface Static Pressure Coefficient Vs. Normalized Axial Location, N2R, $\sigma/\sigma_d = 1.0$, $i = -5.5^\circ$.

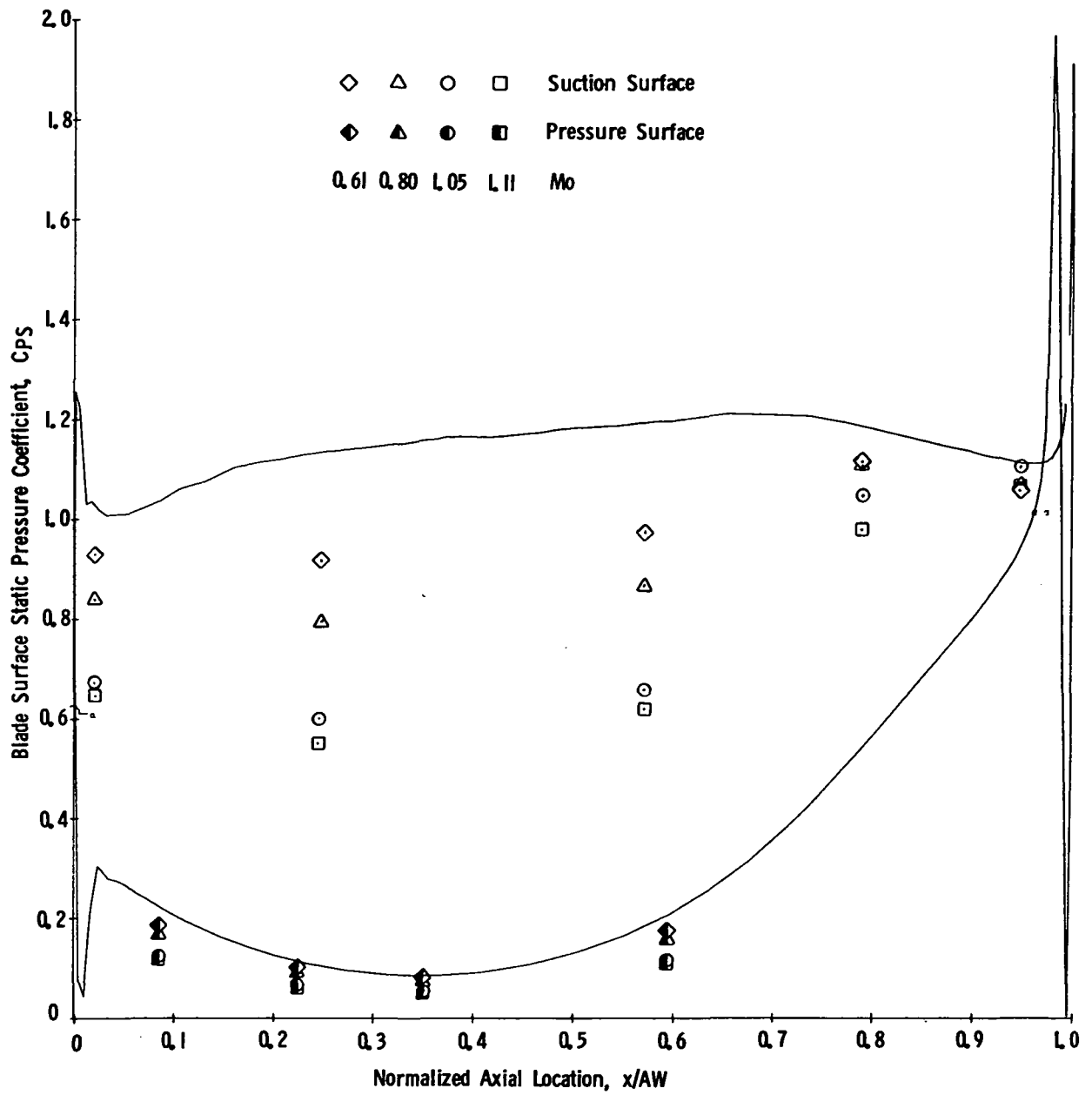


Figure 47. Blade Surface Static Pressure Coefficient Vs. Normalized Axial Location, N2R, $\sigma/\sigma_d = 1.0$, $i = -0.5^\circ$.

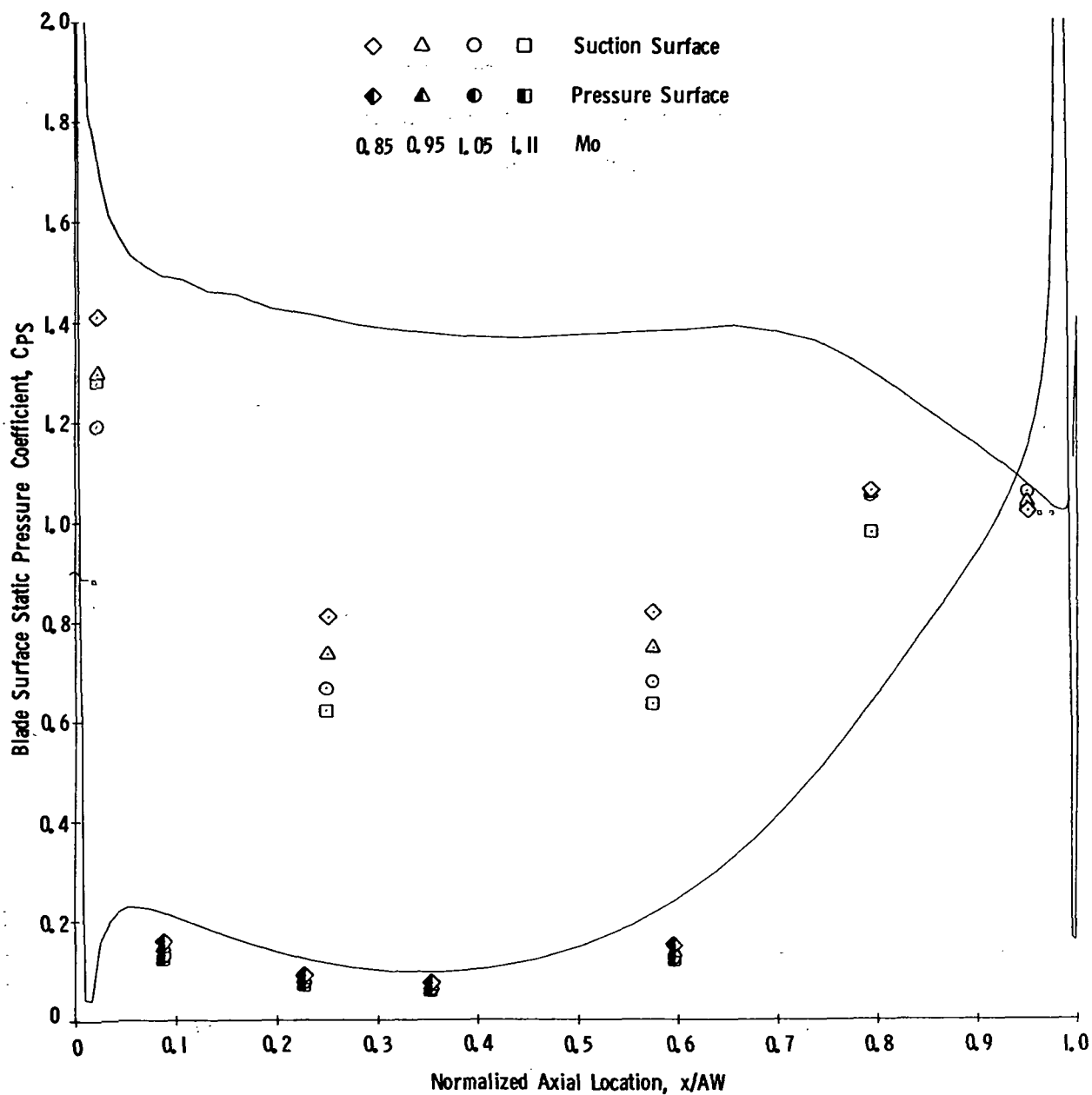


Figure 48. Blade Surface Static Pressure Coefficient Vs. Normalized Axial Location, N2R, $\sigma/\sigma_d = 1.0$, $i = 4.3^\circ$.

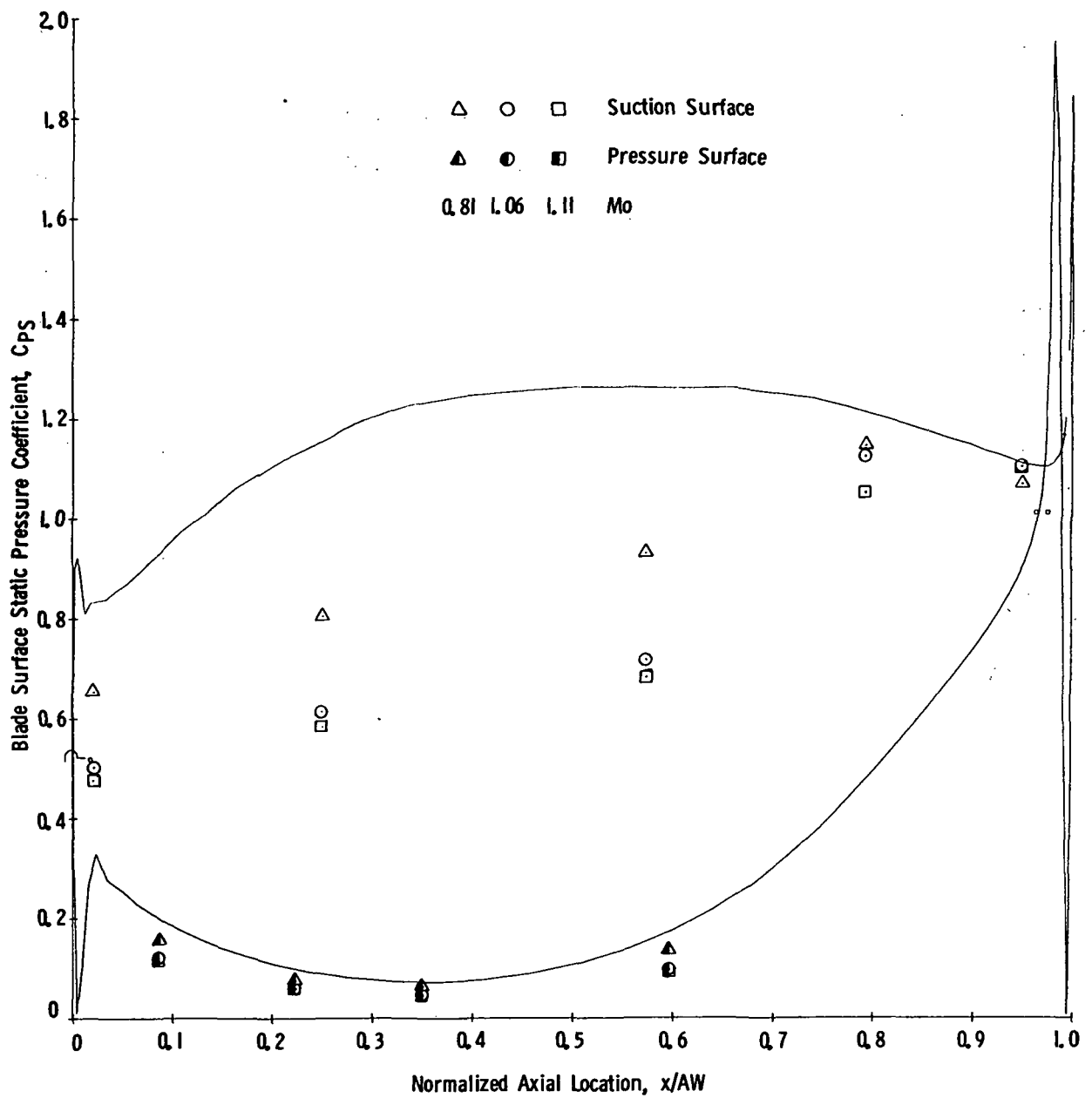


Figure 49. Blade Surface Static Pressure Coefficient Vs. Normalized Axial Location, N2R, $\sigma/\sigma_d = 0.9$, $i = -5.1^\circ$.

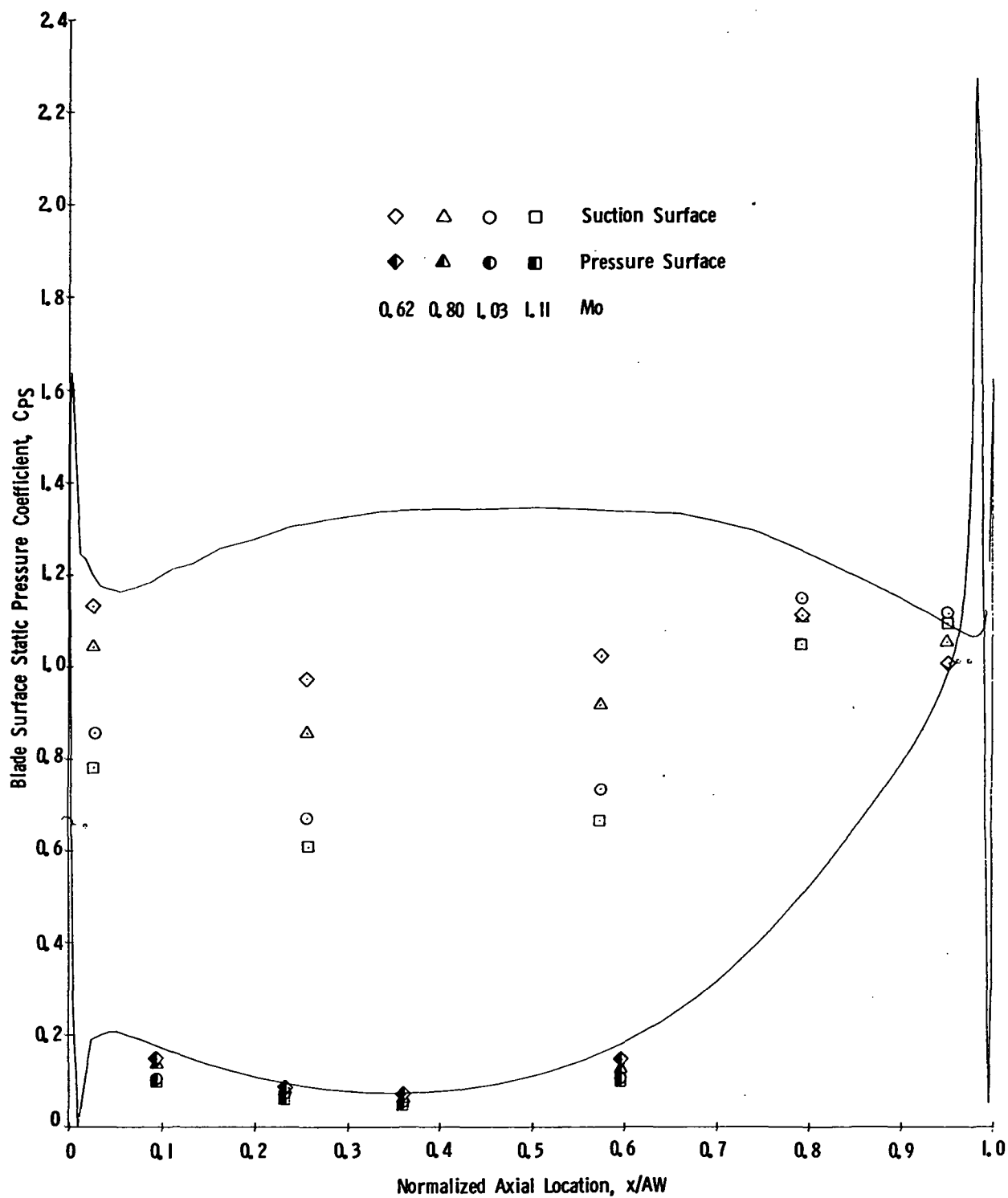


Figure 50. Blade Surface Static Pressure Coefficient Vs. Normalized Axial Location, N2R, $\sigma/\sigma_d = 0.9$, $i = -0.3^\circ$.

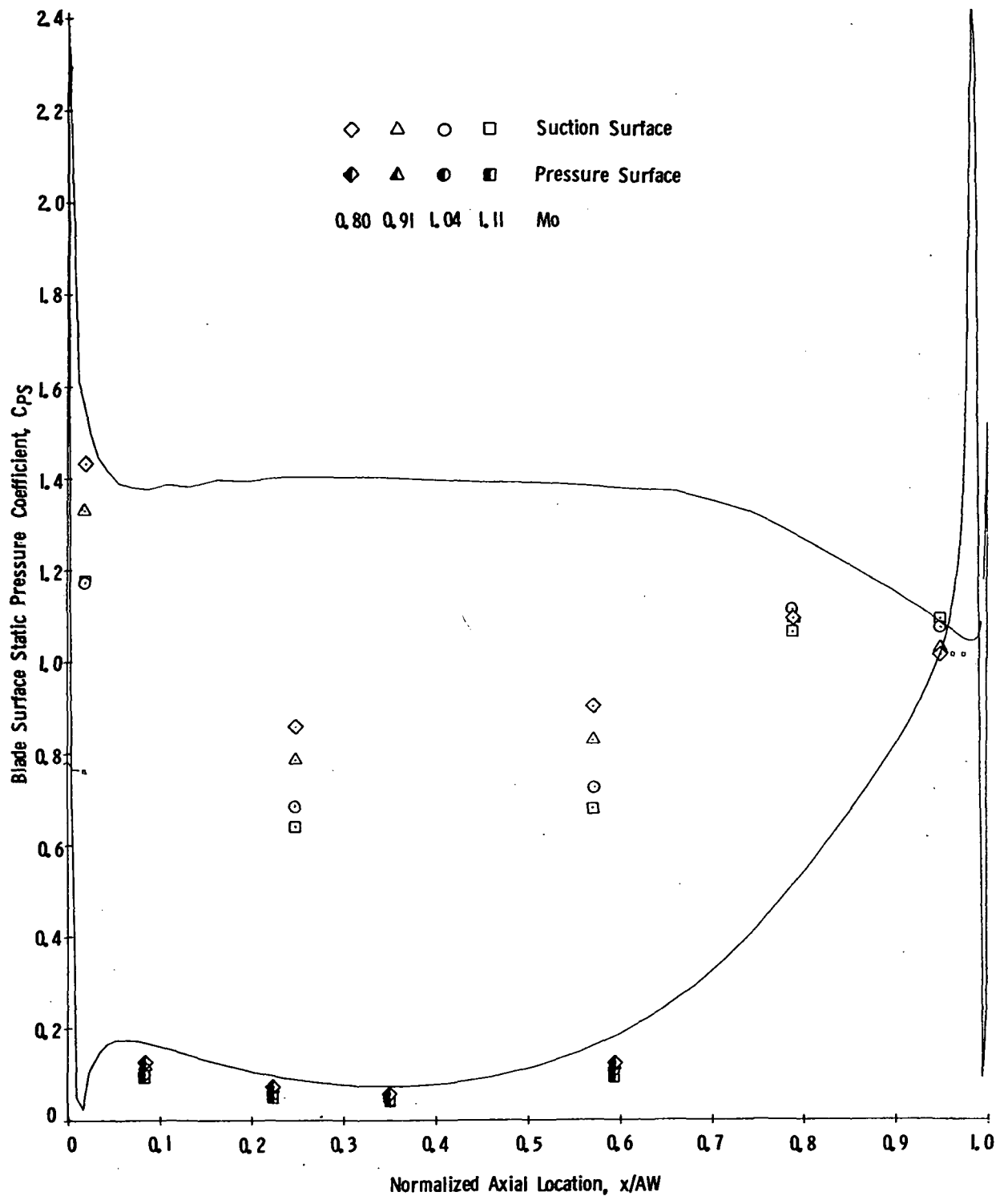


Figure 51. Blade Surface Static Pressure Coefficient Vs. Normalized Axial Location, N2R, $\sigma/\sigma_d = 0.9$, $i = 2.7^\circ$.

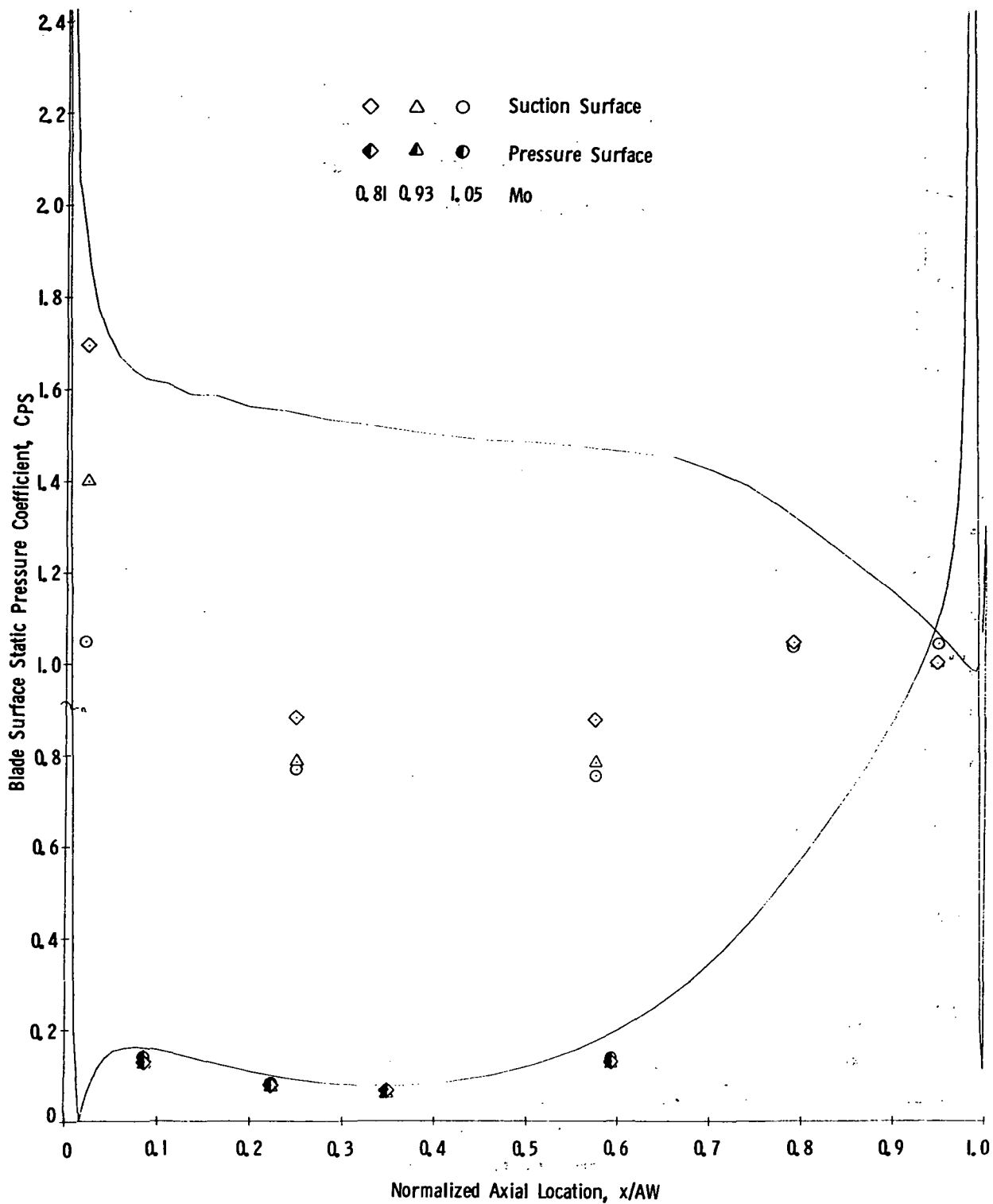


Figure 52. Blade Surface Static Pressure Coefficient Vs. Normalized Axial Location, N2R, $\sigma/\sigma_d = 0.9$, $i = 5.0^\circ$.

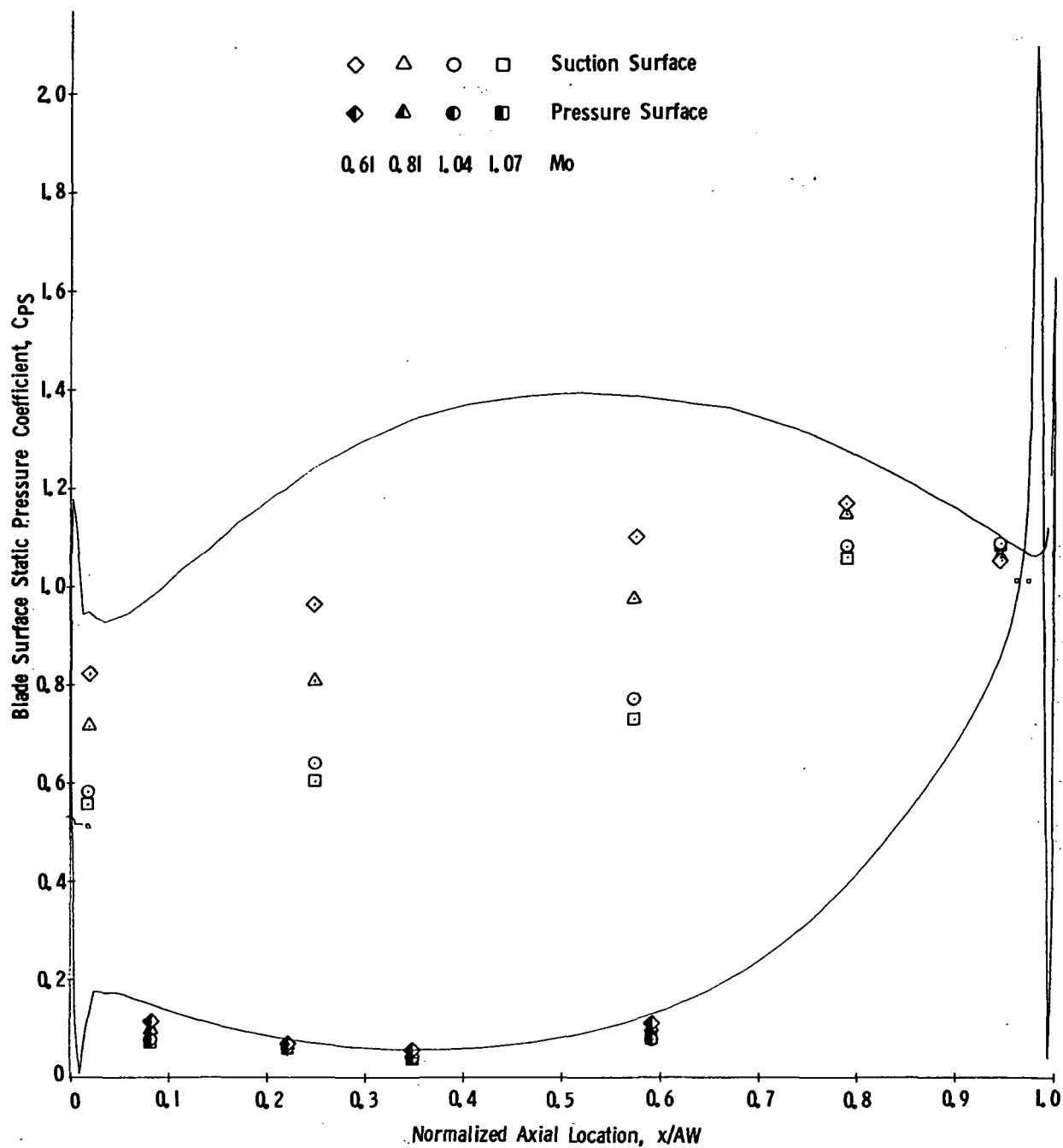


Figure 53. Blade Surface Static Pressure Coefficient Vs. Normalized Axial Location, N2R, $\sigma/\sigma_d = 0.8$, $i = -5.5^\circ$.

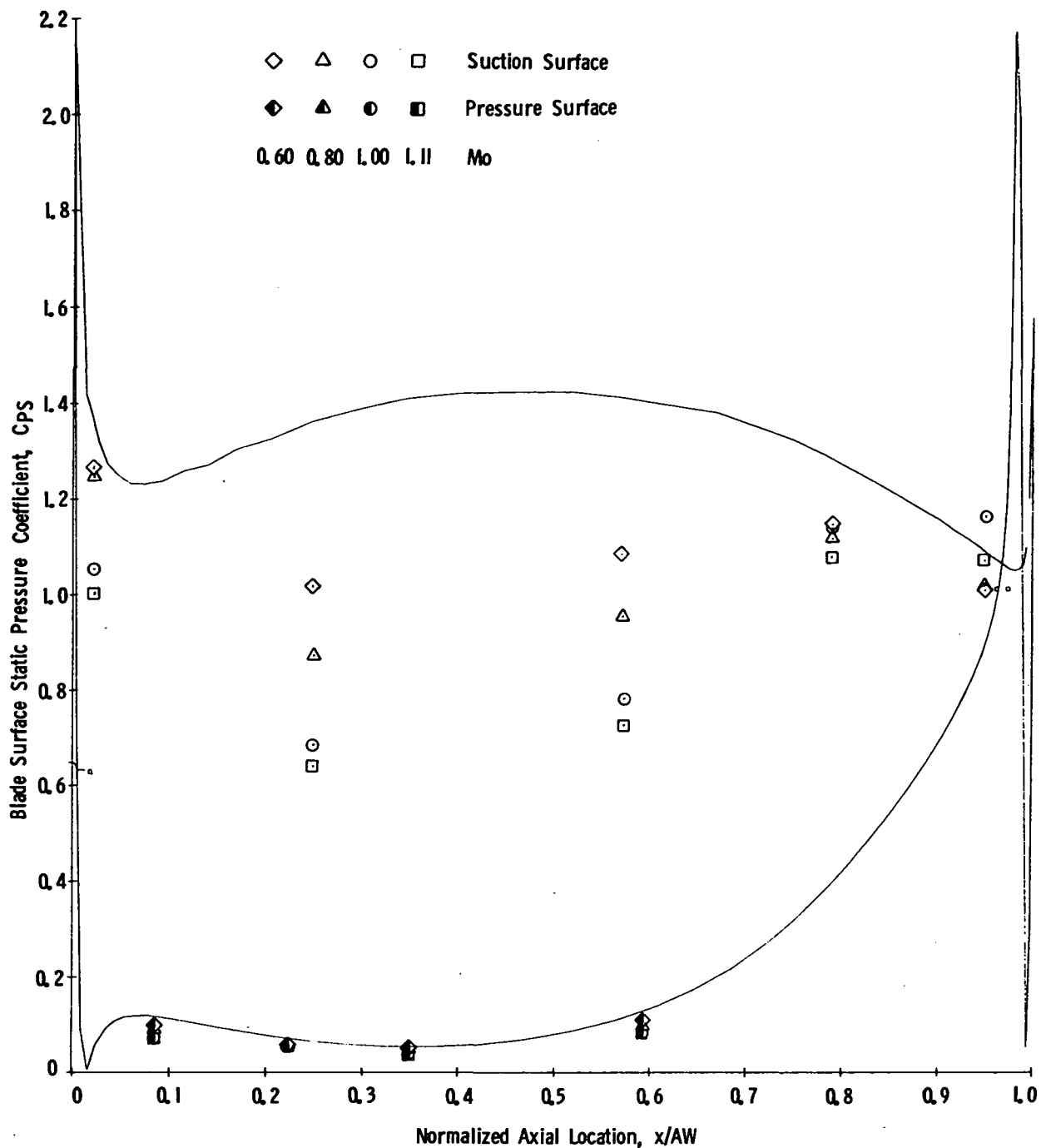


Figure 54. Blade Surface Static Pressure Coefficient Vs. Normalized Axial Location, N2R, $\sigma/\sigma_d = 0.8$, $i = -0.2^\circ$.

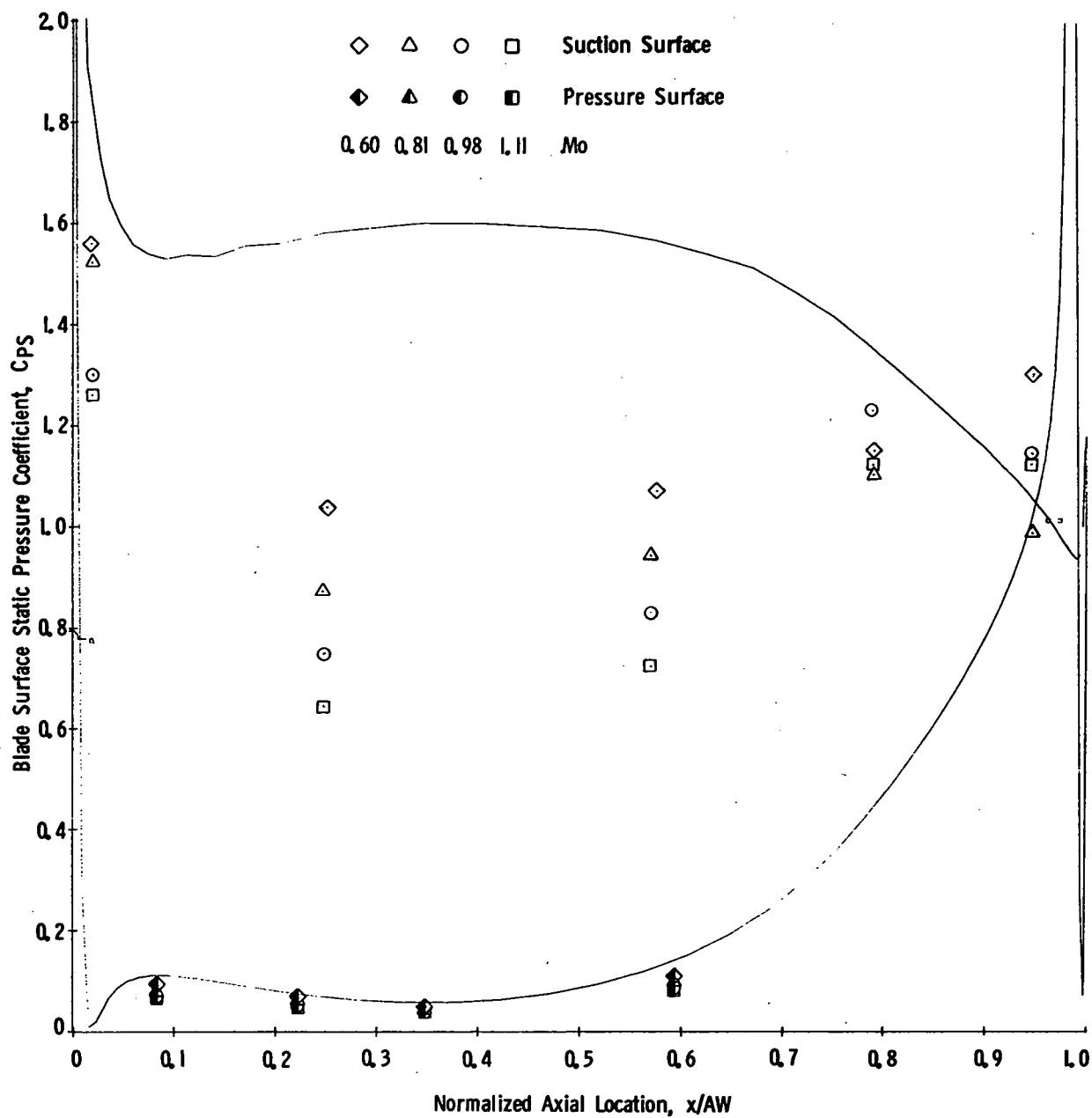


Figure 55. Blade Surface Static Pressure Coefficient Vs. Normalized Axial Location, N2R, $\sigma/\sigma_d = 0.8$, $i = 2.4^\circ$.

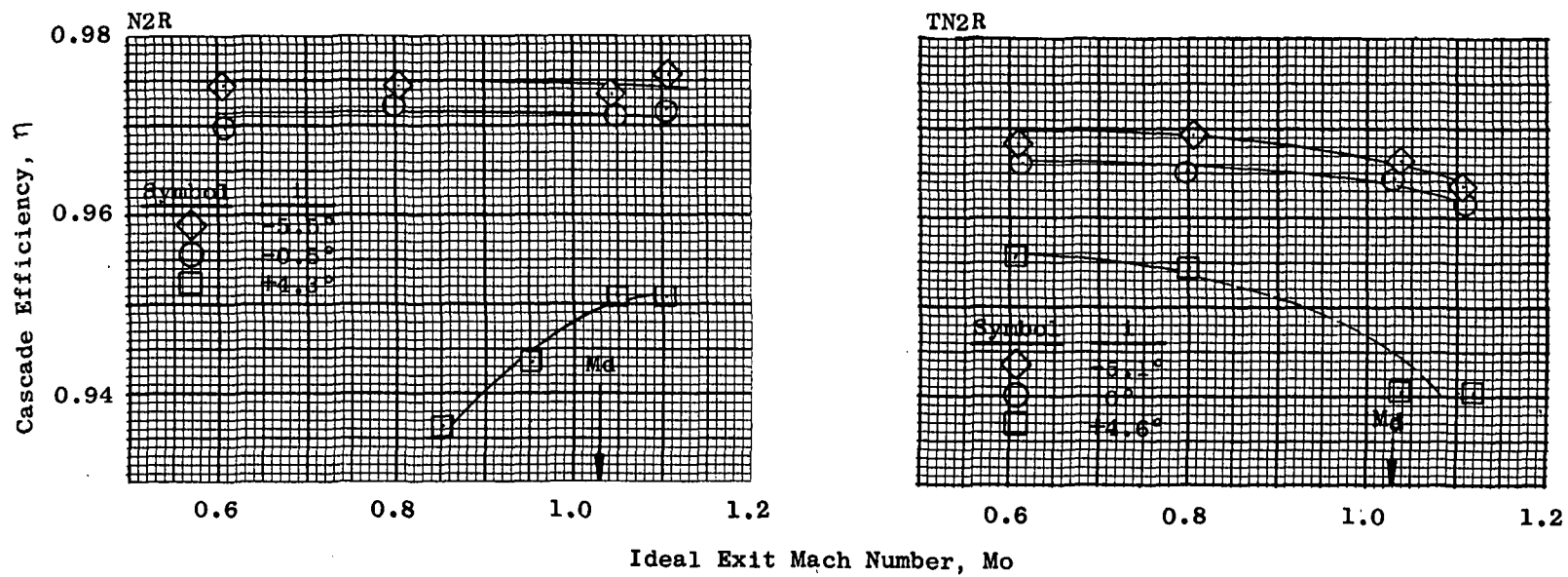


Figure 56. Cascade Efficiency Vs. Mach Number, TN2R with N2R at $\sigma/\sigma_d = 1.0$.

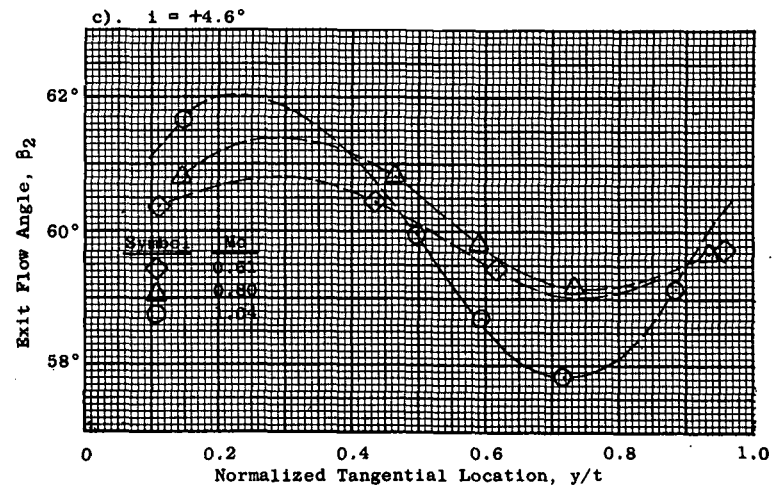
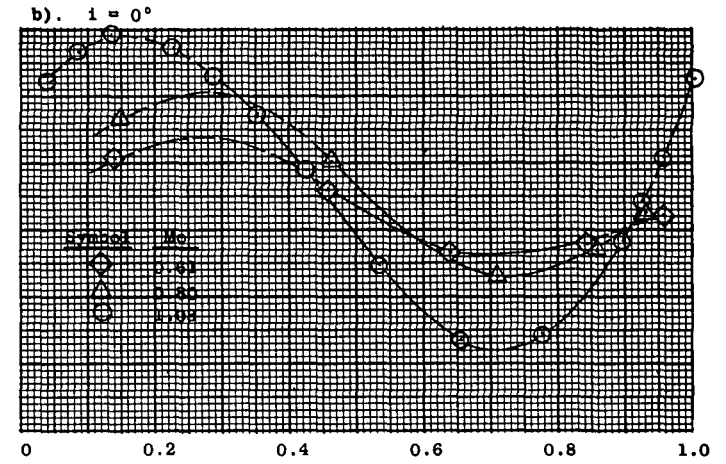
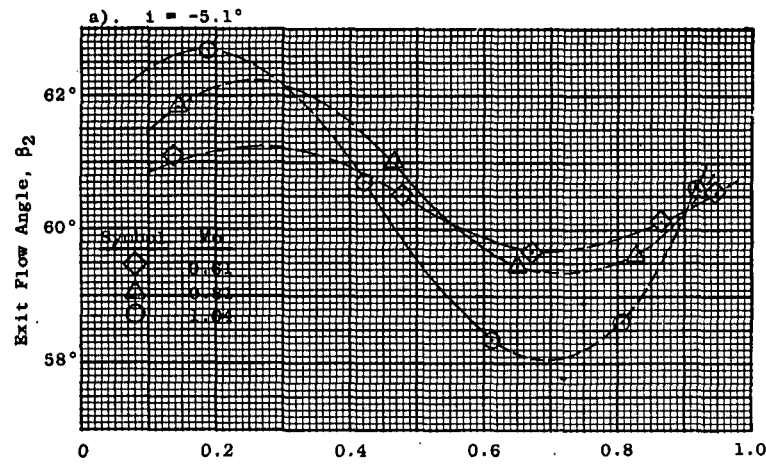


Figure 57. Exit Flow Angle Vs. Normalized Tangential Location, TN2R Turbine Design Configuration.

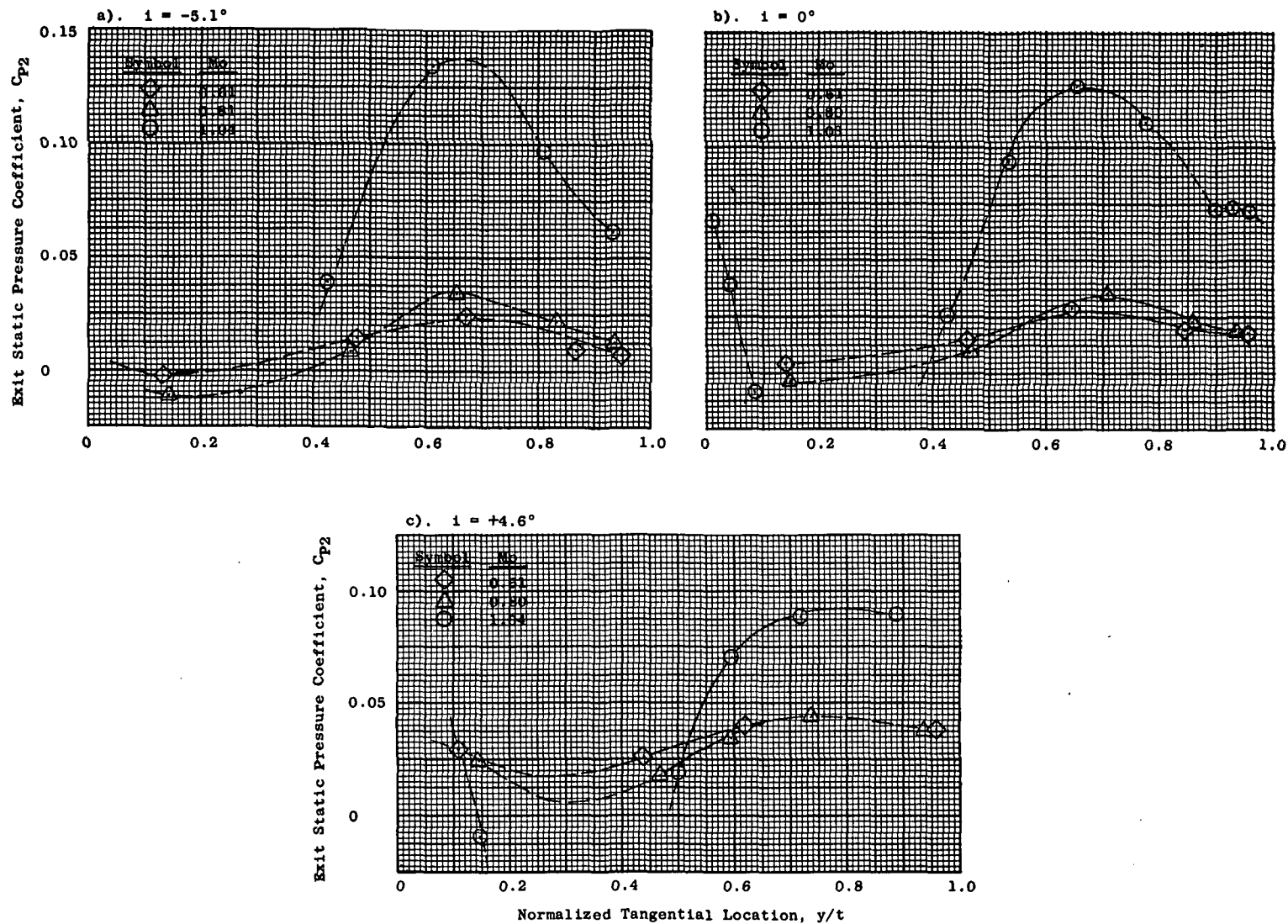


Figure 58. Exit Static Pressure Coefficient Vs. Normalized Tangential Location, TN2R Turbine Design Configuration.

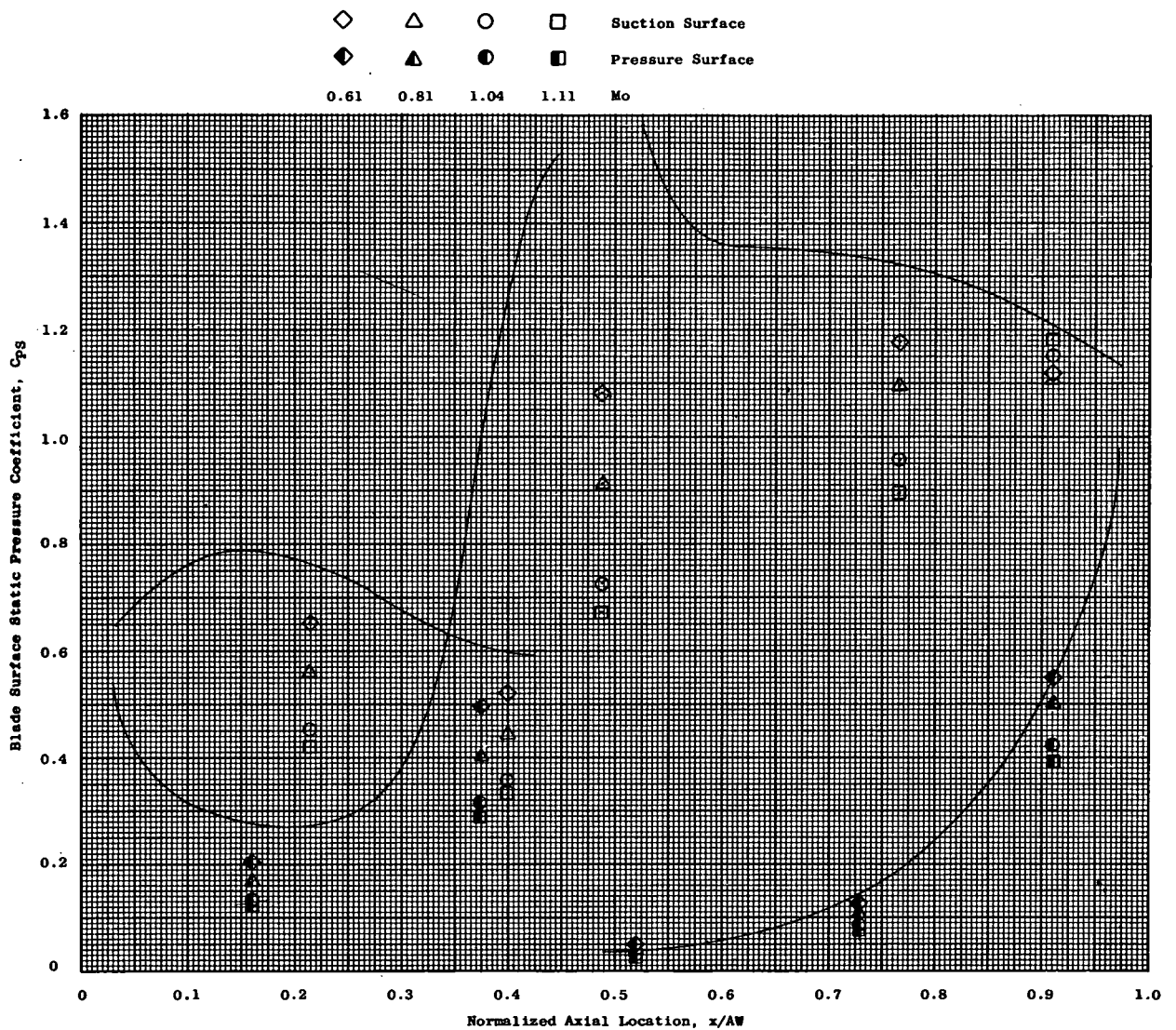


Figure 59. Blade Surface Static Pressure Coefficient Vs. Normalized Axial Location, TN2R Turbine Design Configuration, $i = -5.1^\circ$.

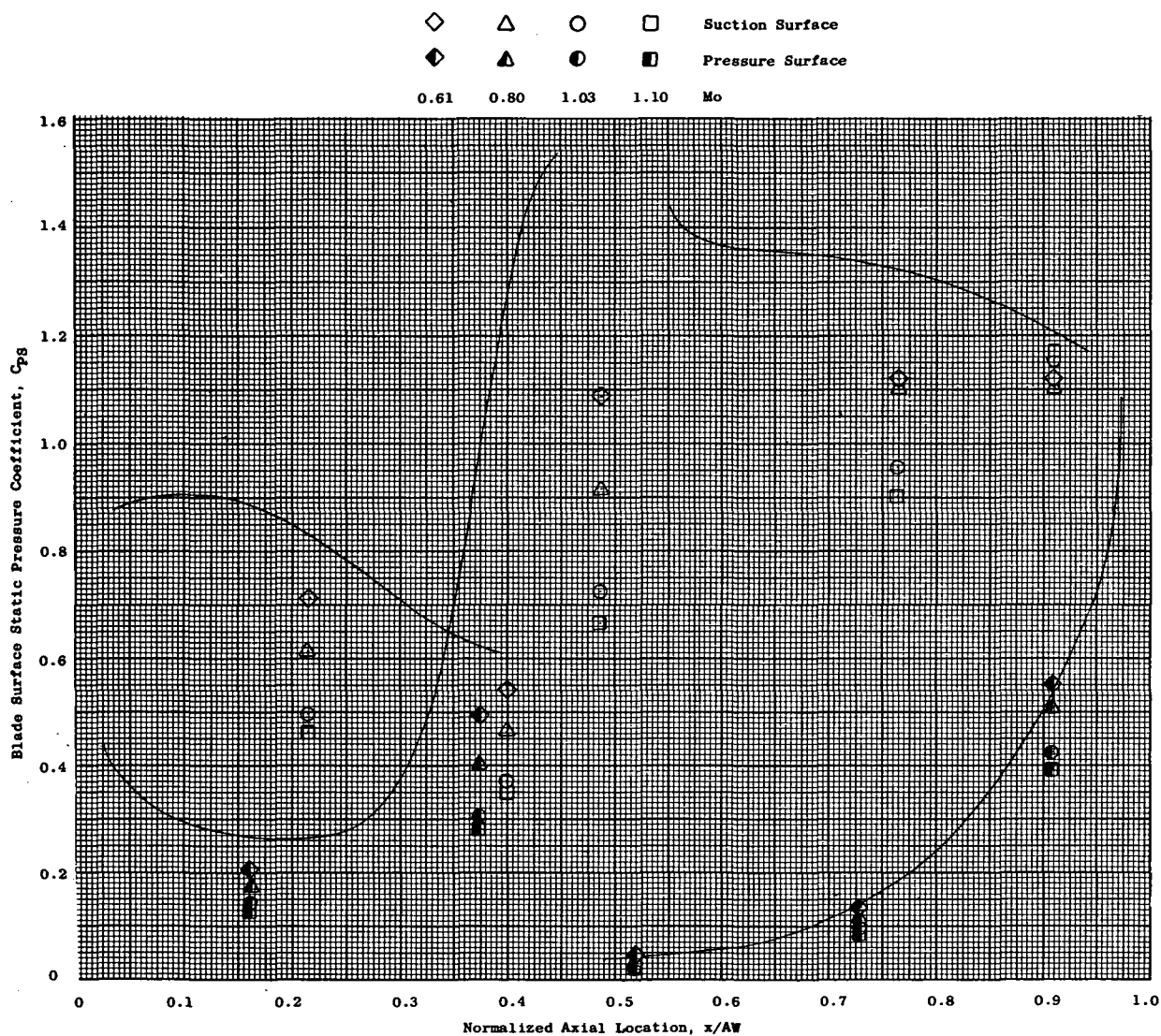


Figure 60. Blade Surface Static Pressure Coefficient Vs. Normalized Axial Location, TN2R Turbine Design Configuration, $i = 0^\circ$.

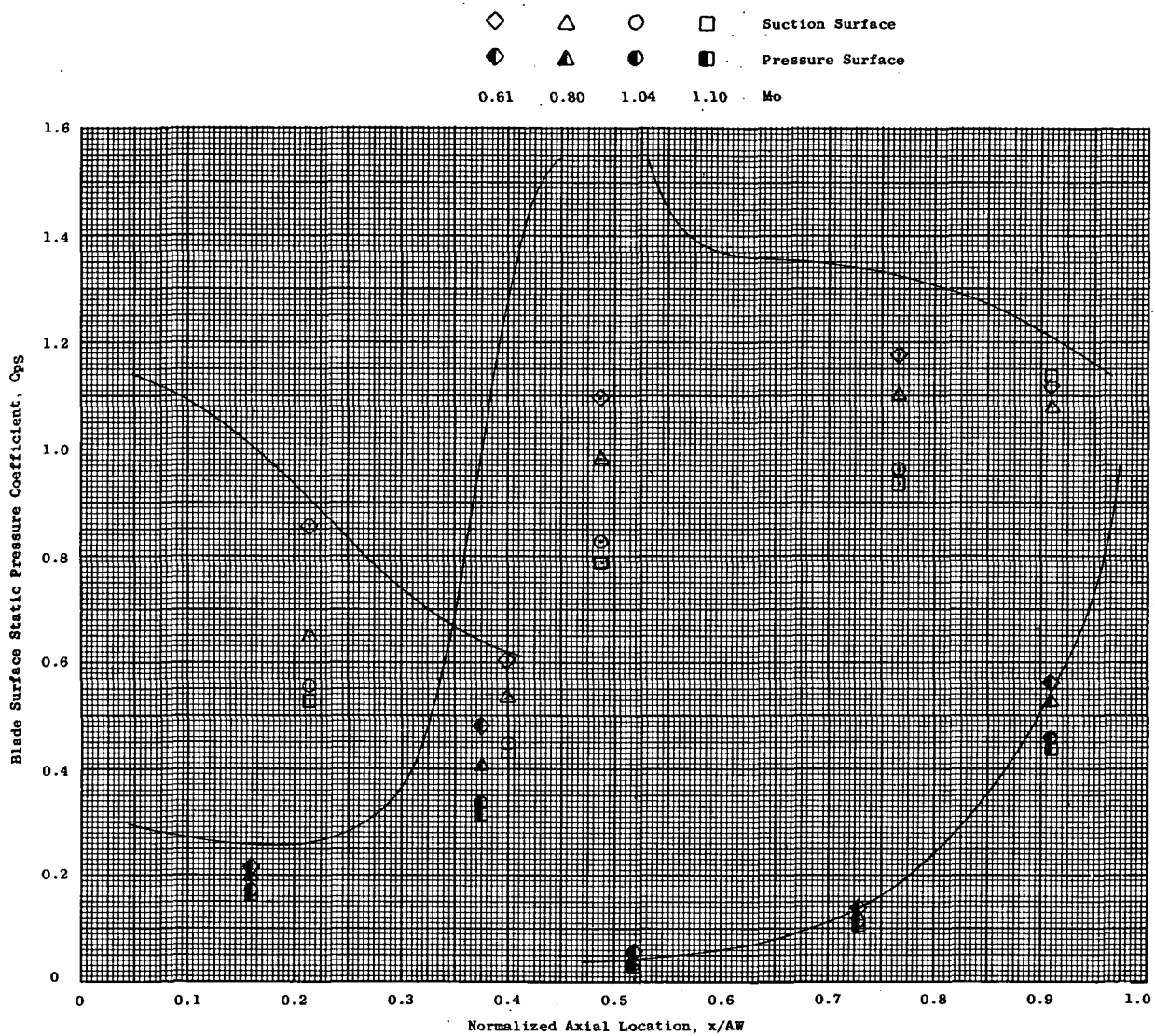


Figure 61. Blade Surface Static Pressure Coefficient Vs. Normalized Axial Location, TN2R Turbine Design Configuration, $i = 4.6^\circ$.

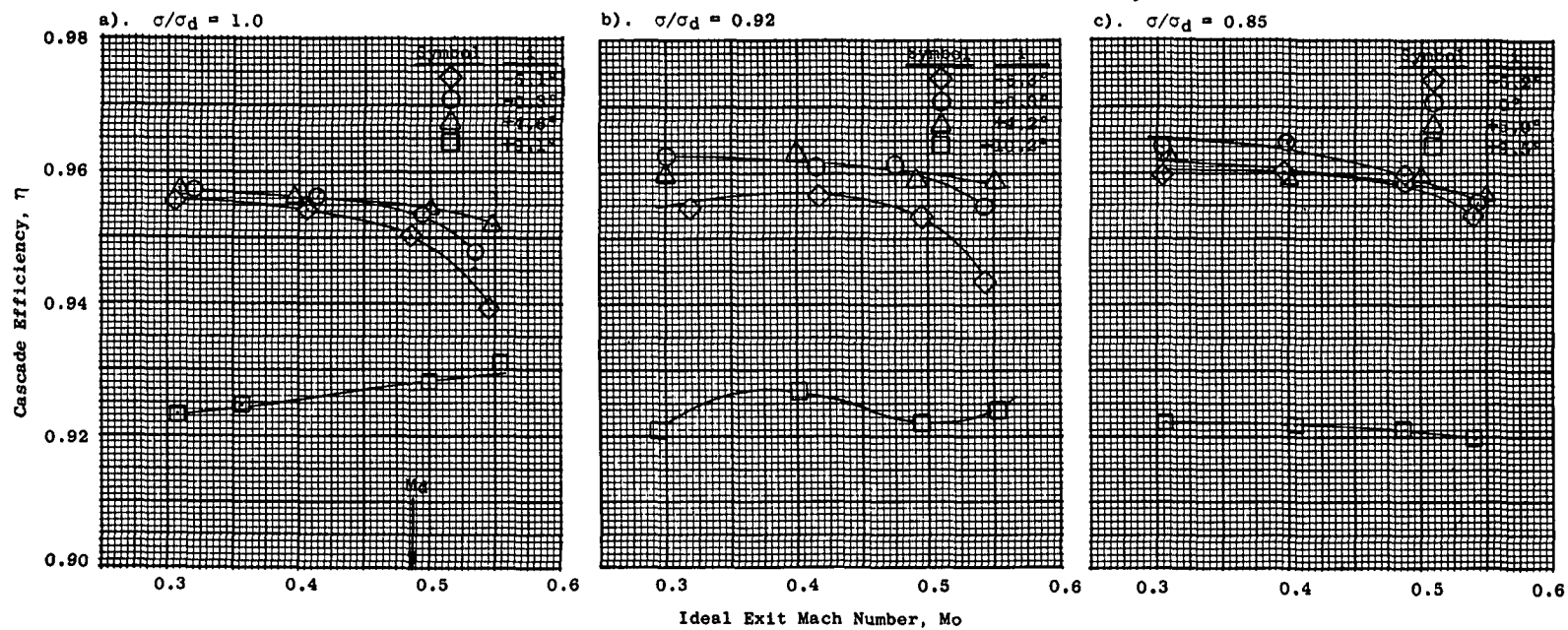


Figure 62. Cascade Efficiency Vs. Mach Number, B3R.

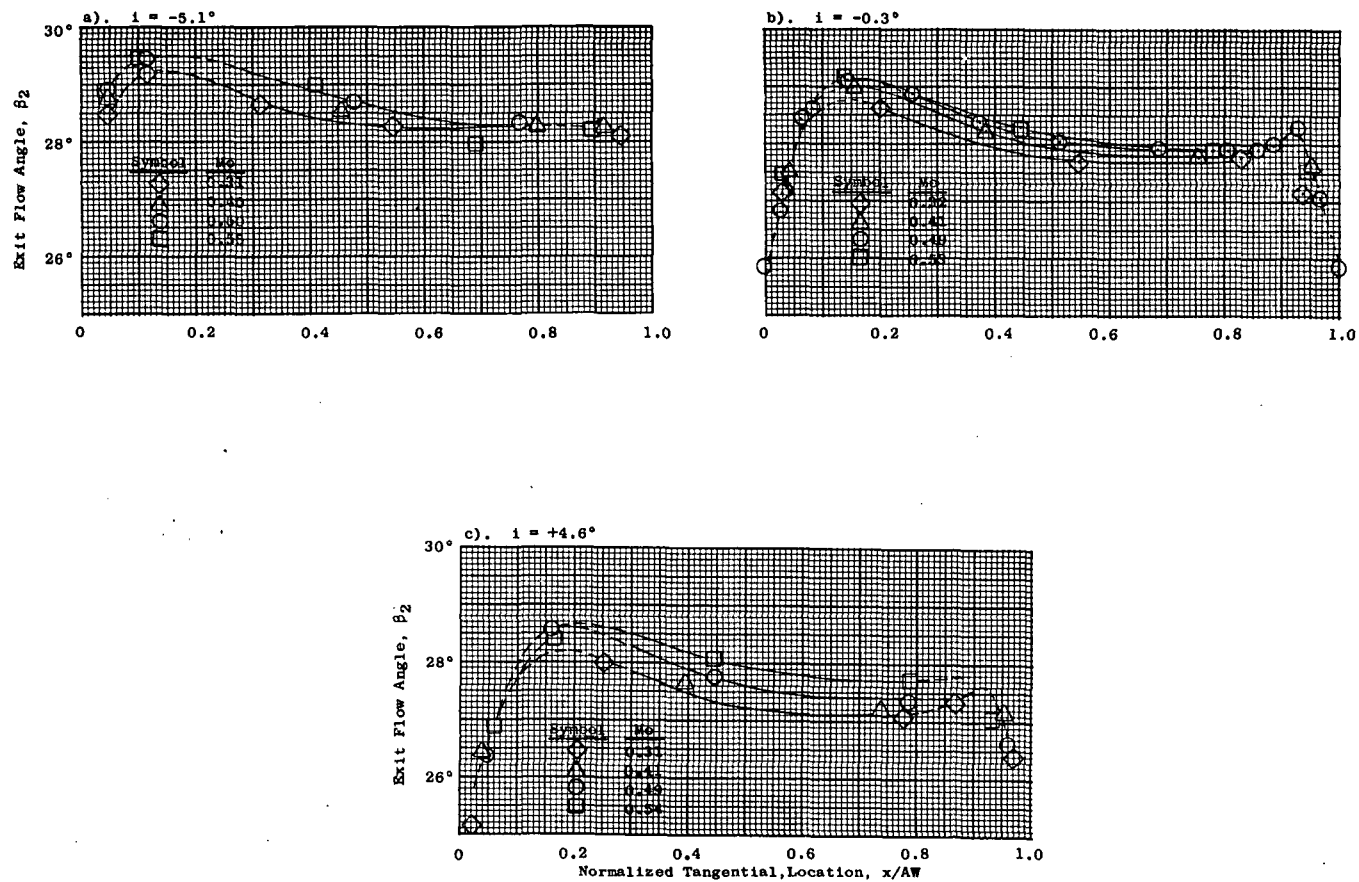


Figure 63. Exit Flow Angle Vs. Normalized Tangential Location, B3R, $\sigma/\sigma_d = 1.0$.

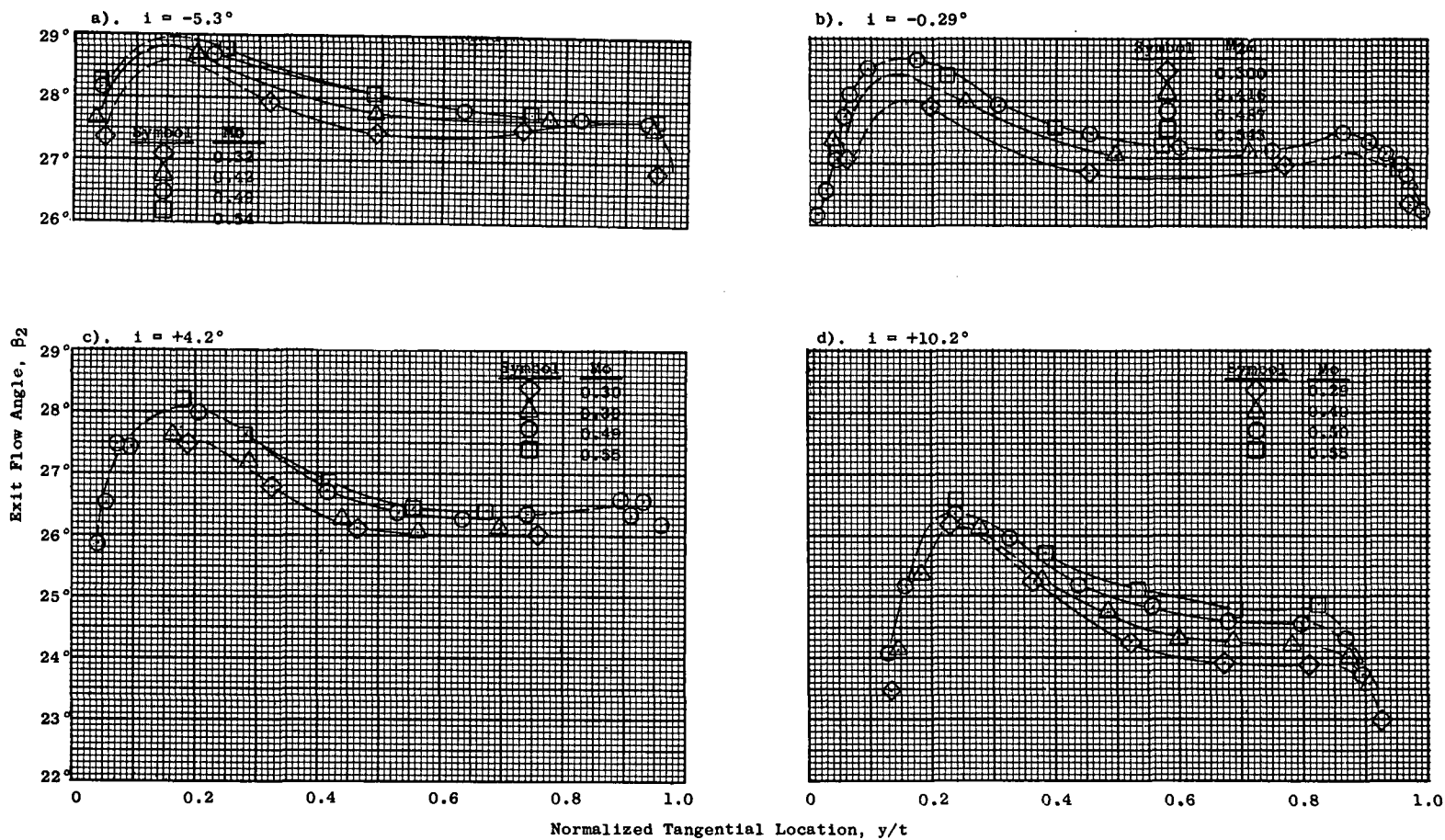


Figure 64. Exit Flow Angle Vs. Normalized Tangential Location, B3R, $\sigma/\sigma_d = 0.92$.

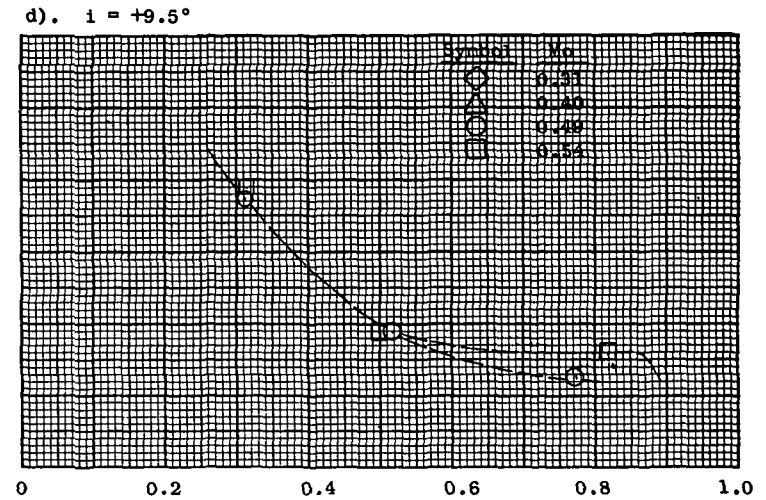
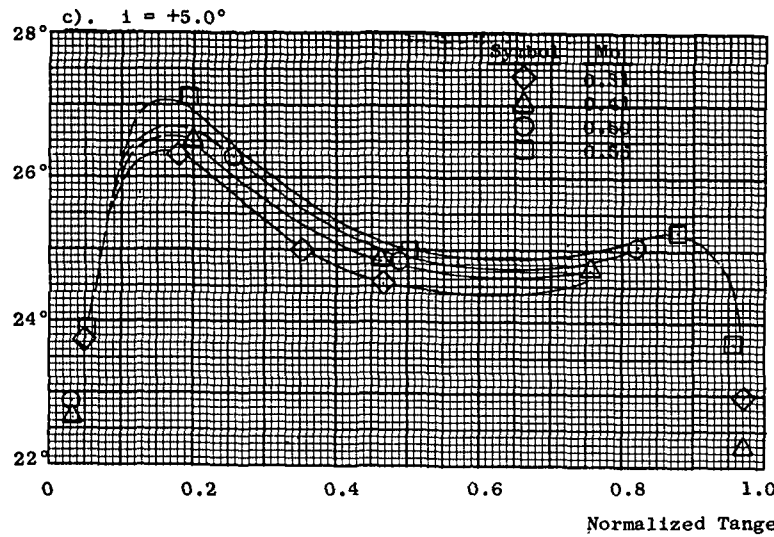
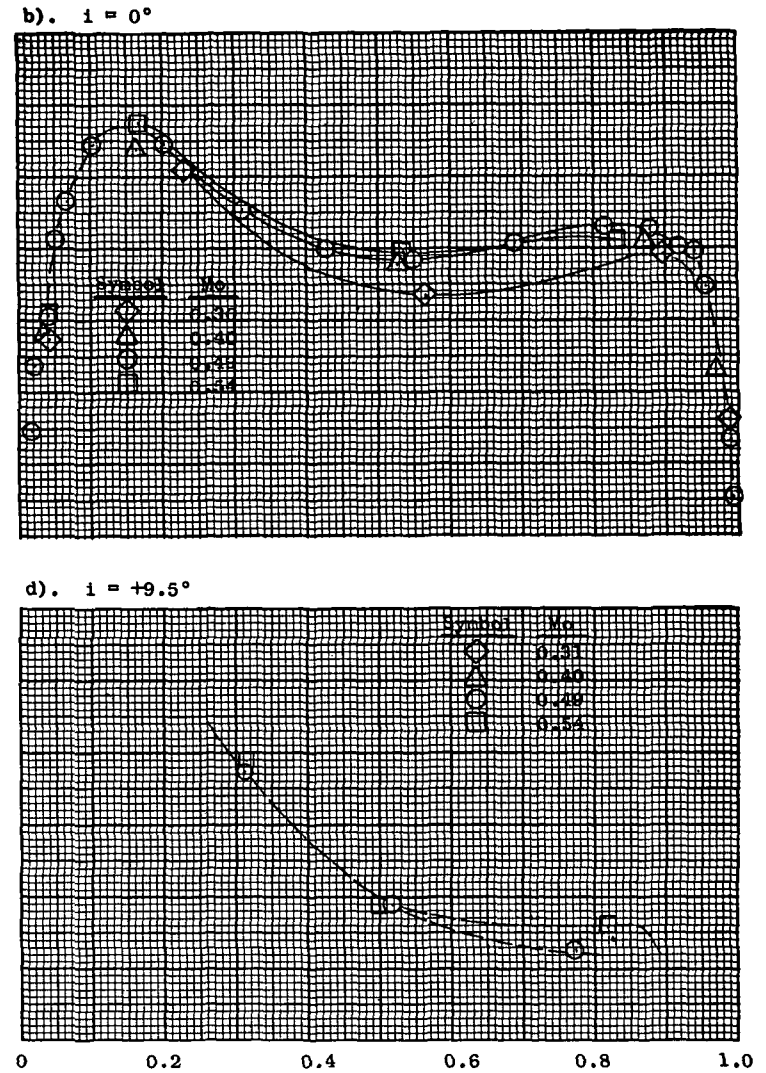
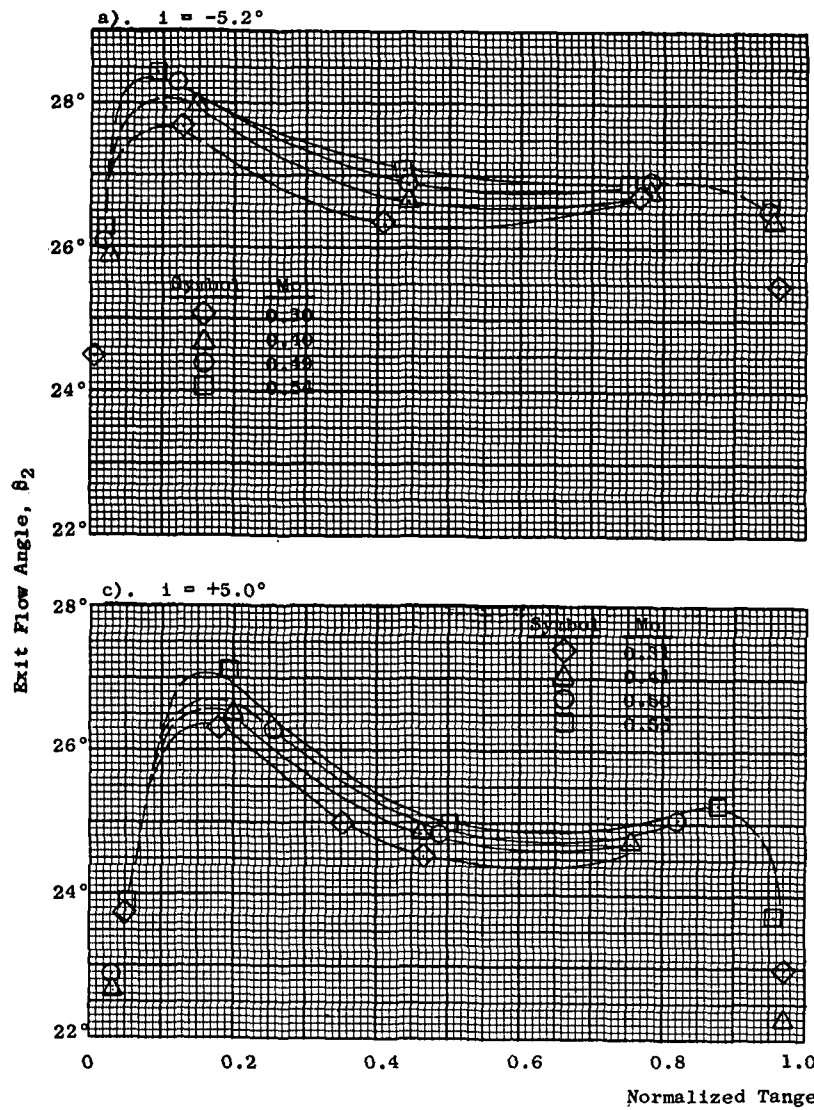


Figure 65. Exit Flow Angle Vs. Normalized Tangential Location, B3R, $\sigma/\sigma_d = 0.85$.

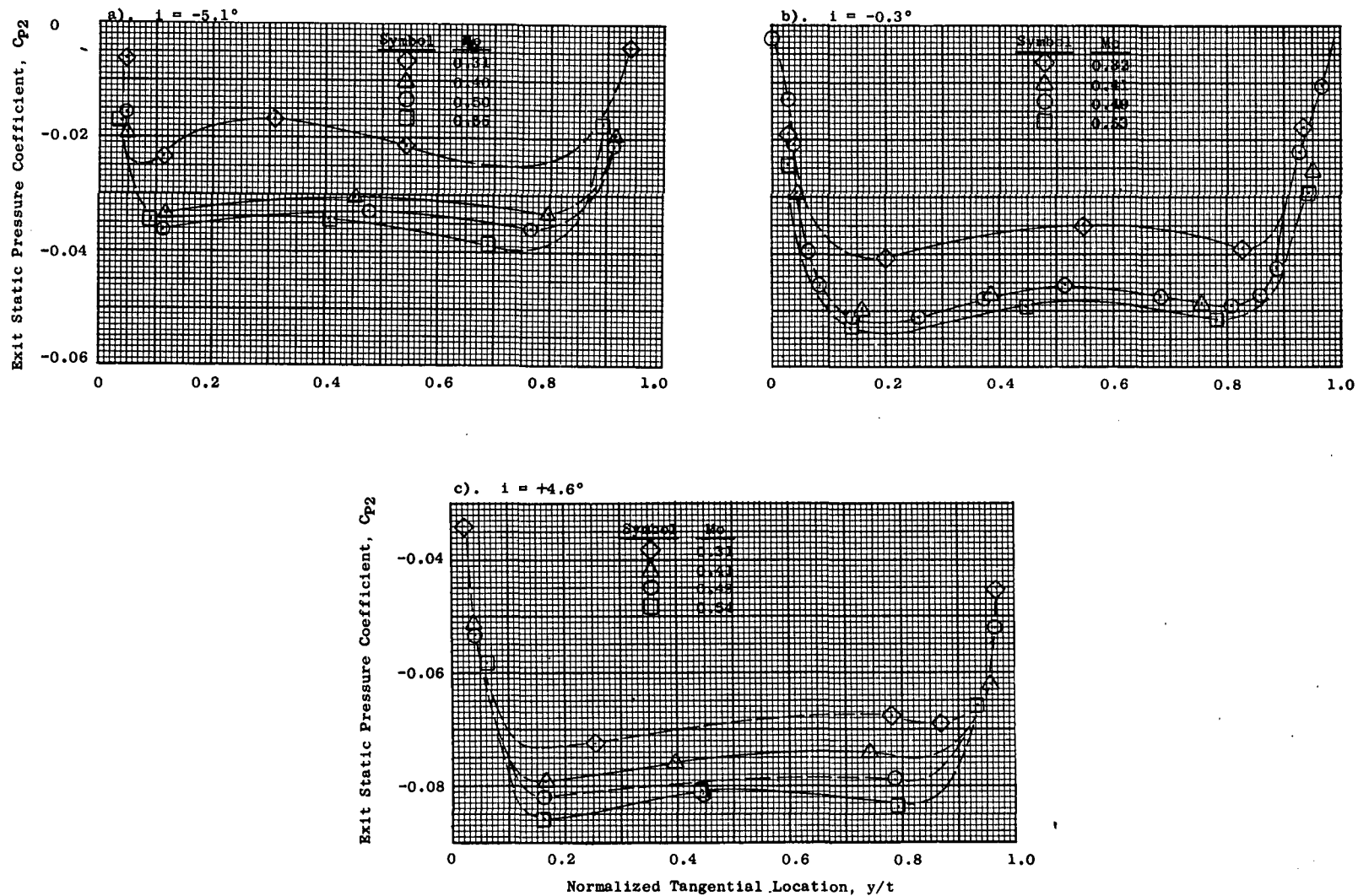


Figure 66. Exit Static Pressure Coefficient Vs. Normalized Tangential Location, B3R, $\sigma/\sigma_d = 1.0$.

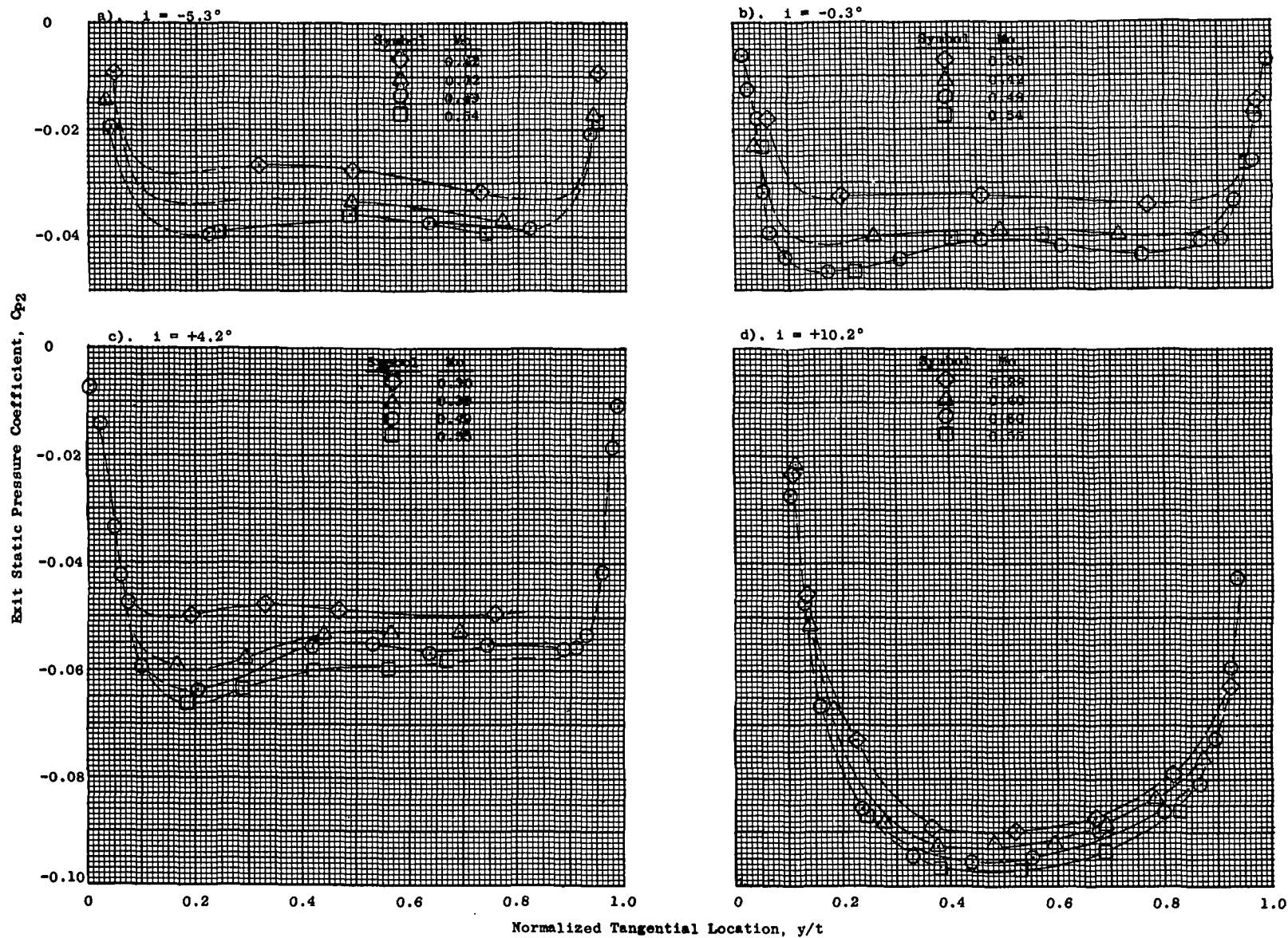


Figure 67. Exit Static Pressure Coefficient Vs. Normalized Tangential Location, B3R, $\sigma/\sigma_d = 0.92$.

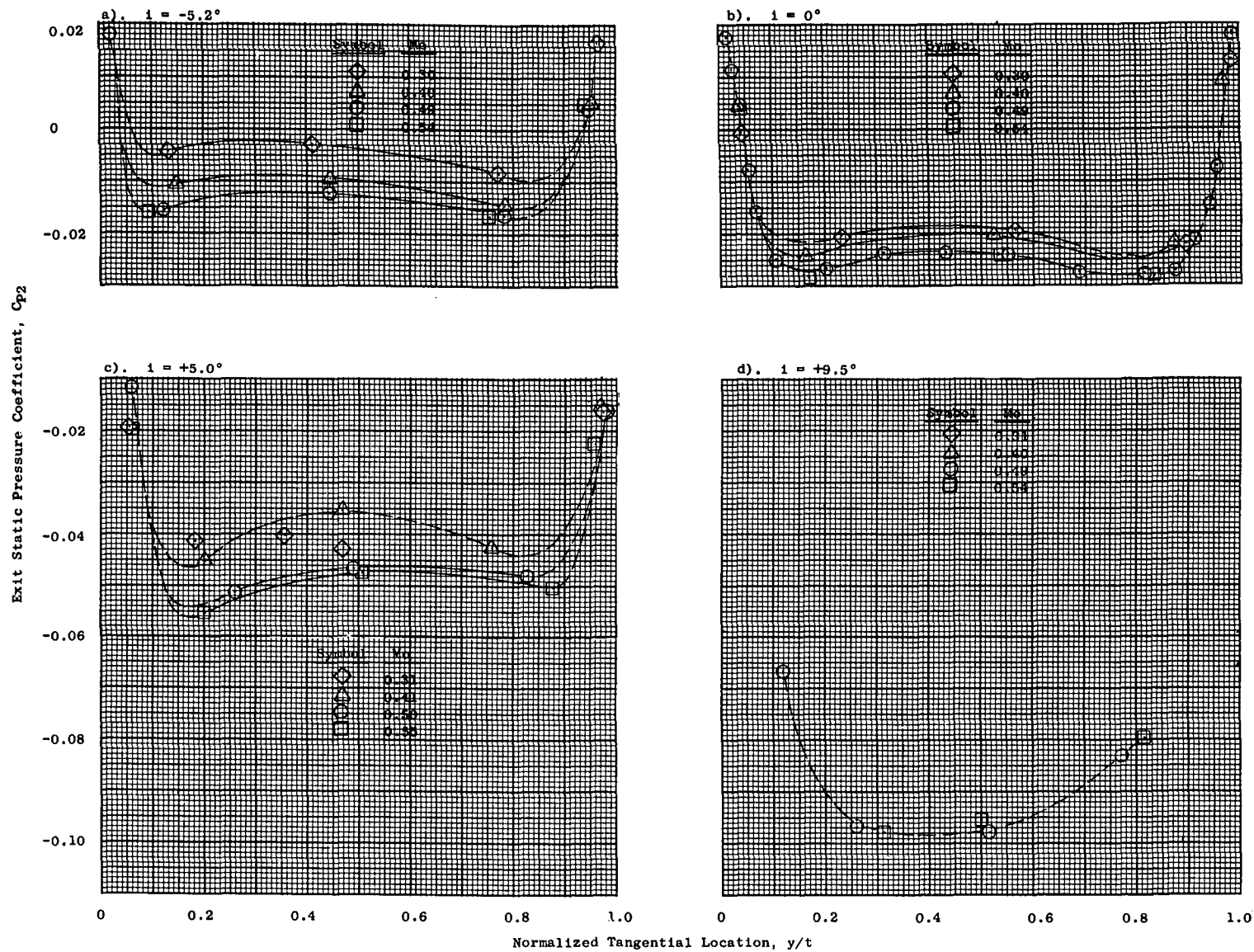


Figure 68. Exit Static Pressure Coefficient Vs. Normalized Tangential Location, B3R, $\sigma/\sigma_d = 0.85$.

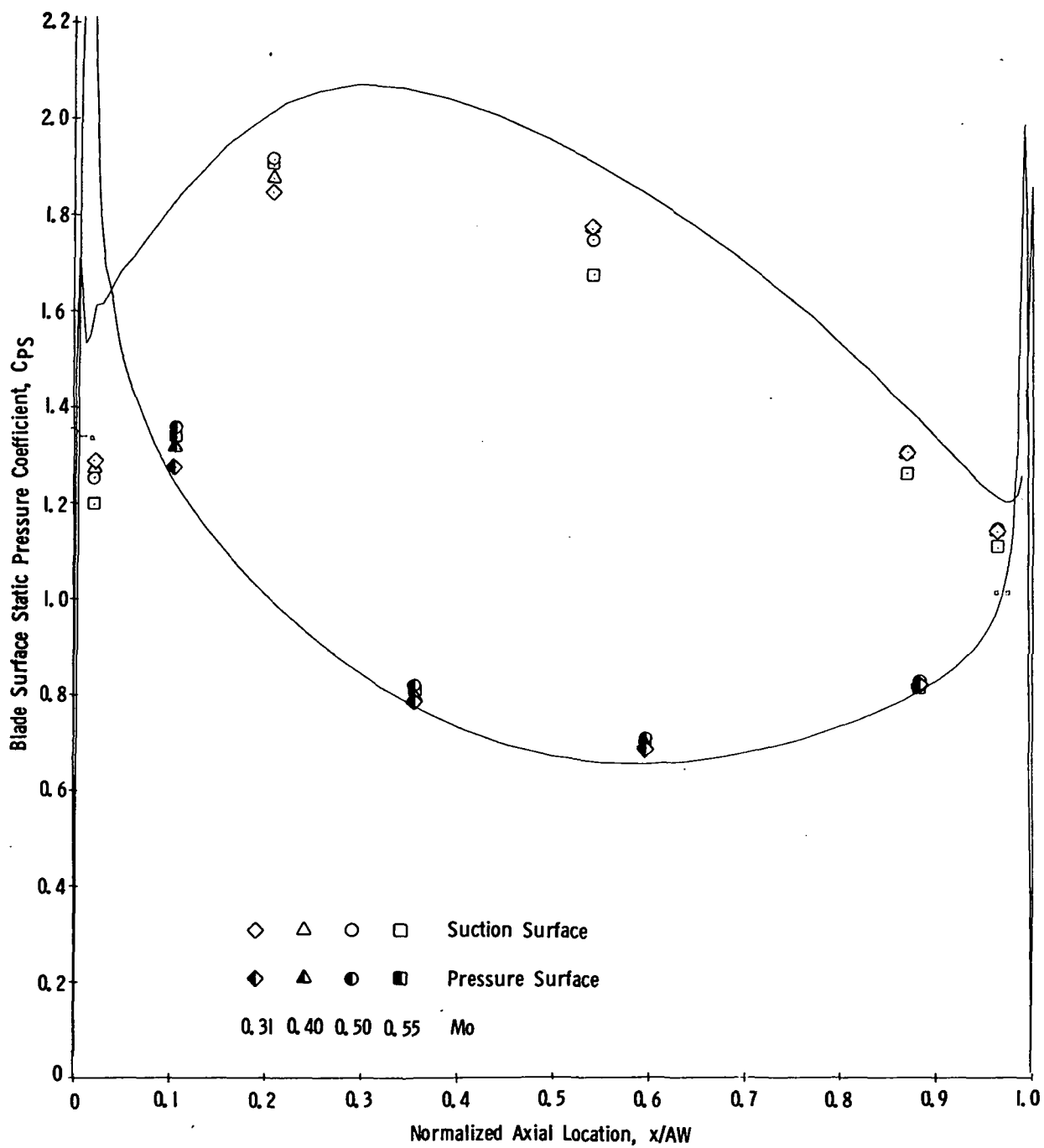


Figure 69. Blade Surface Static Pressure Coefficient Vs. Normalized Axial Location, B3R, $\sigma/\sigma_d = 1.0$, $i = -5.1^\circ$.

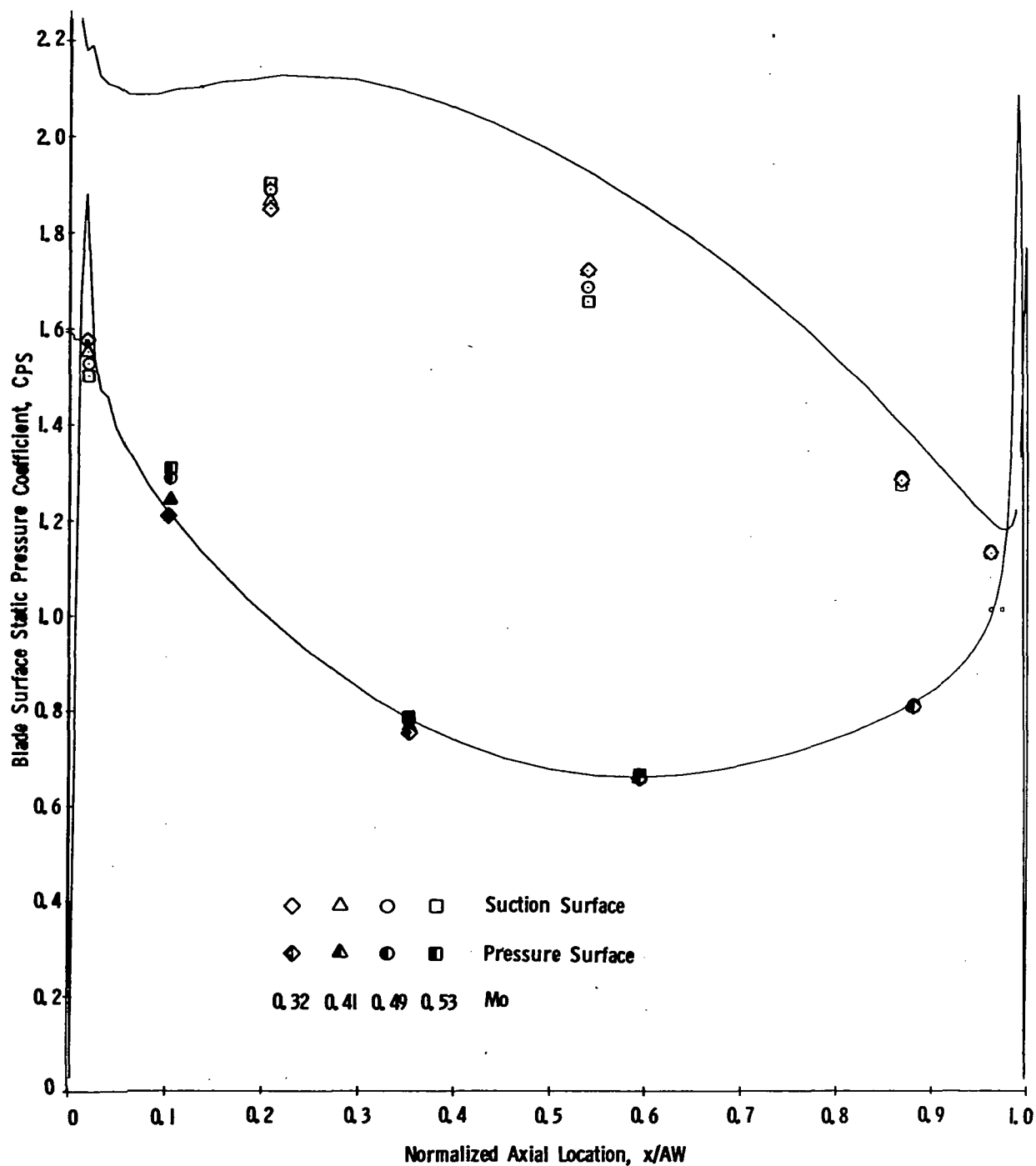


Figure 70. Blade Surface Static Pressure Coefficient Vs. Normalized Axial Location, B3R, $\sigma/\sigma_d = 1.0$, $i = -0.3^\circ$.

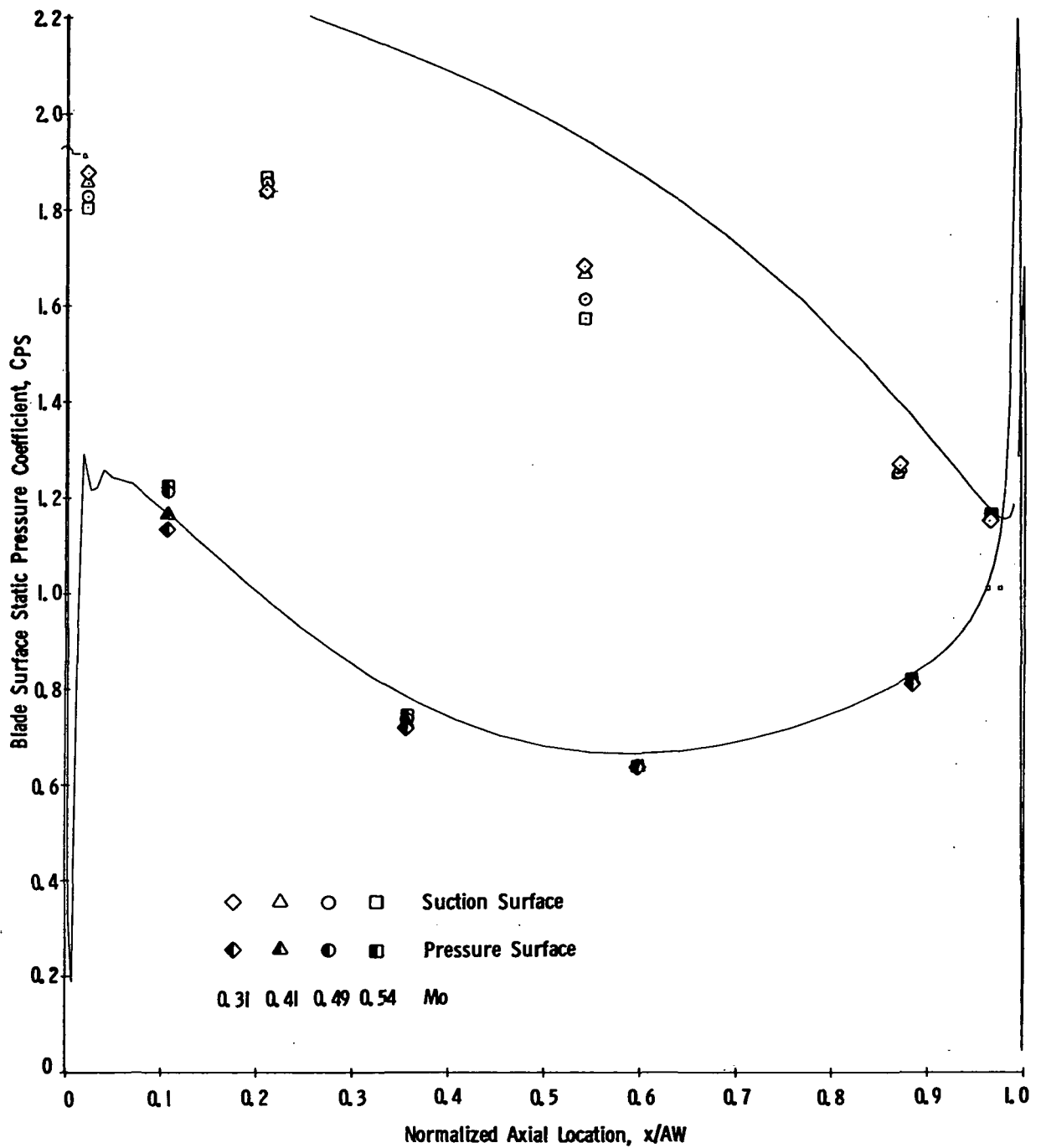


Figure 71. Blade Surface Static Pressure Coefficient Vs. Normalized Axial Location, B3R, $\sigma/\sigma_d = 1.0$, $i = 4.6^\circ$.

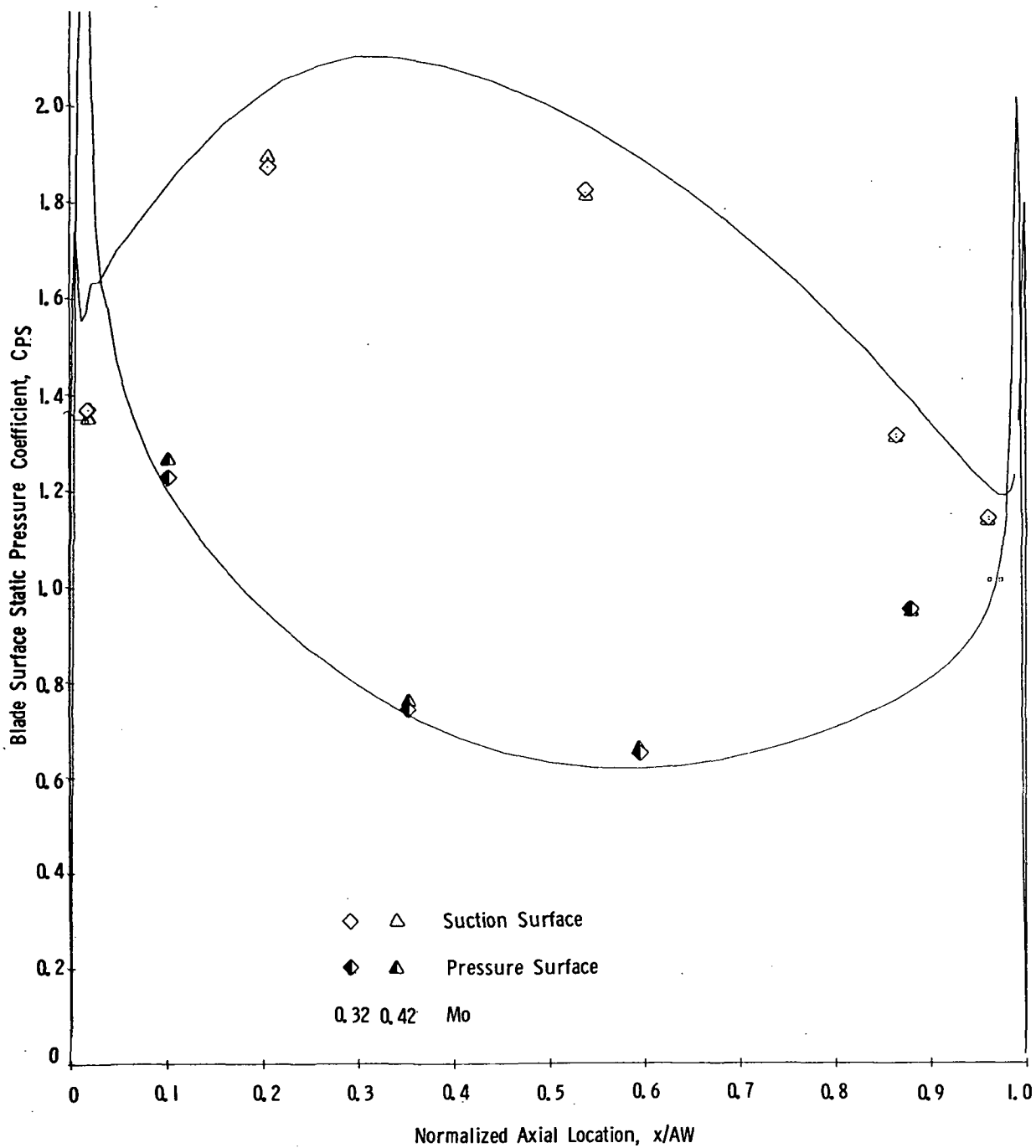


Figure 72. Blade Surface Static Pressure Coefficient Vs. Normalized Axial Location, B3R, $\sigma/\sigma_d = 0.92$, $i = -5.3^\circ$.

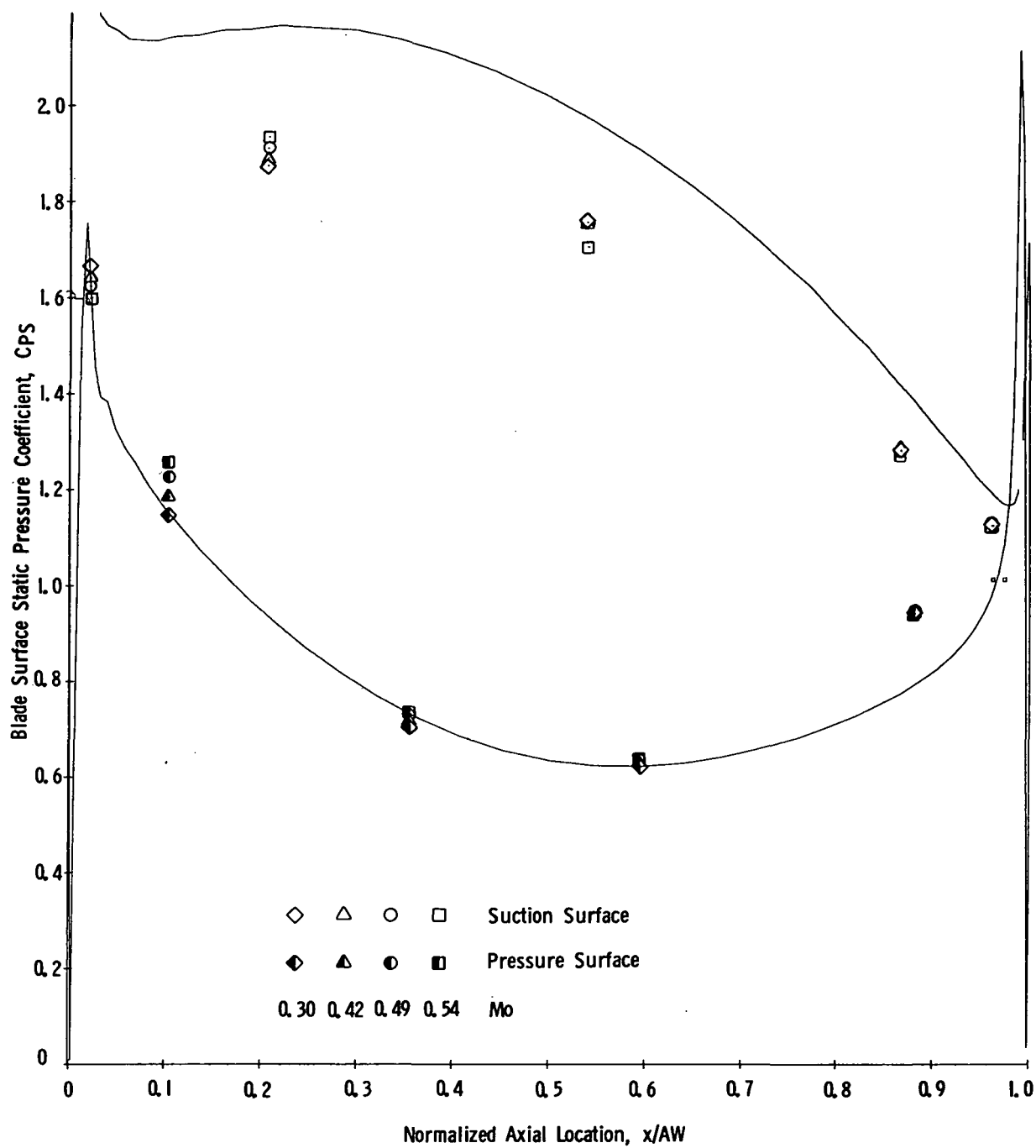


Figure 73. Blade Surface Static Pressure Coefficient Vs. Normalized Axial Location, B3R, $\sigma/\sigma_d = 0.92$, $i = -0.3^\circ$.

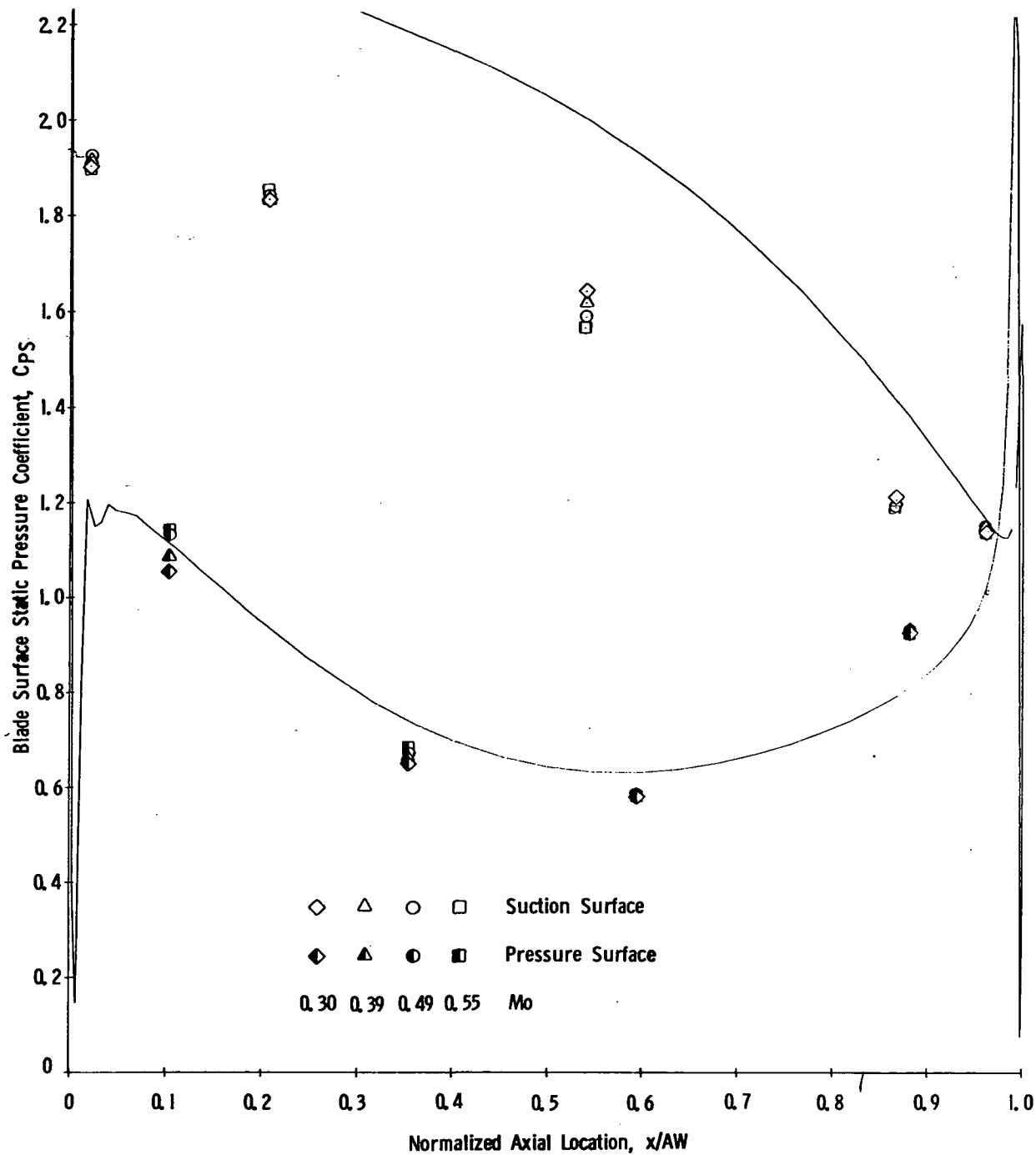


Figure 74. Blade Surface Static Pressure Coefficient Vs. Normalized Axial Location, B3R, $\sigma/\sigma_d = 0.92$, $i = 4.2^\circ$.

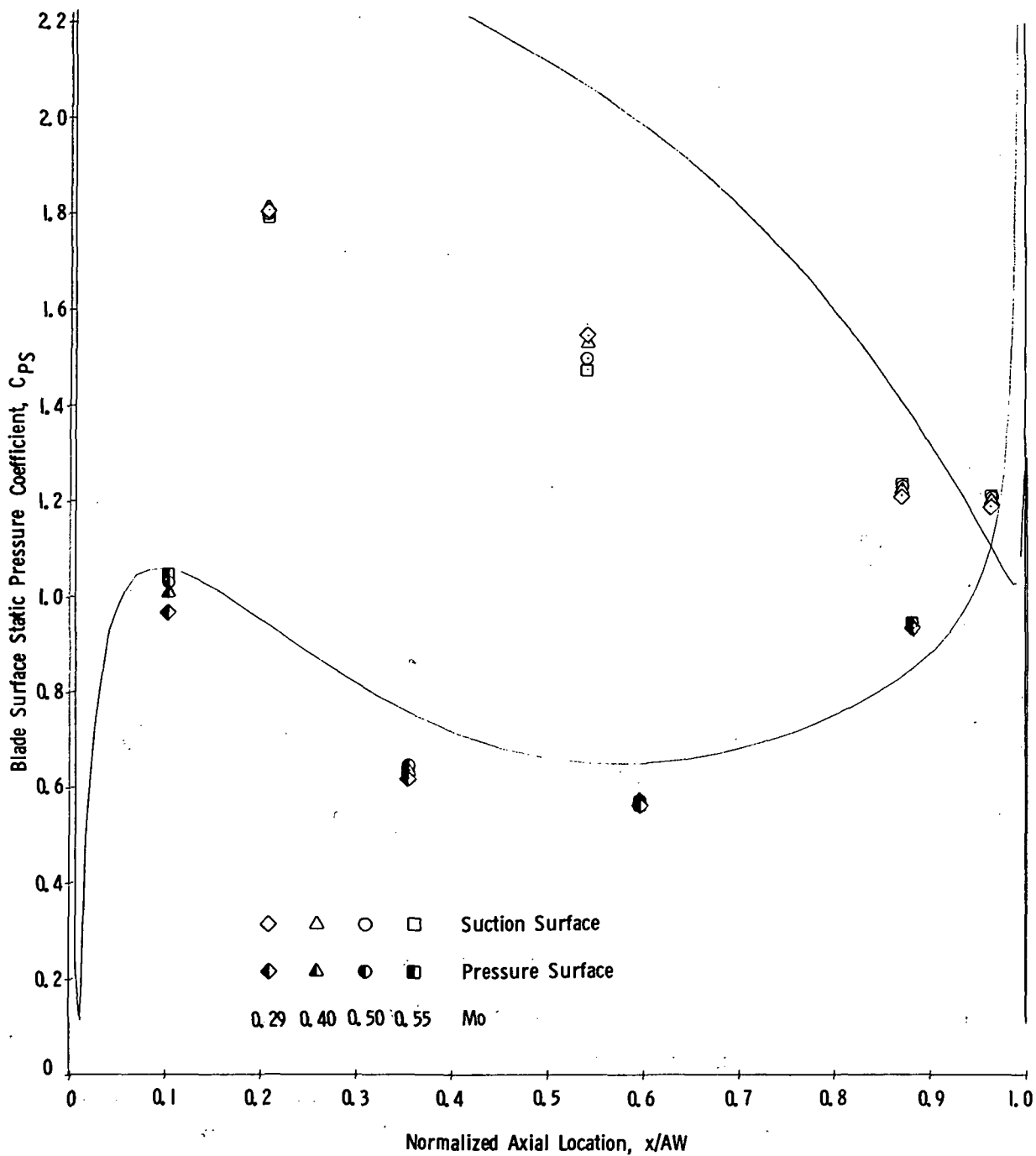


Figure 75. Blade Surface Static Pressure Coefficient Vs. Normalized Axial Location, B3R, $\sigma/\sigma_d = 0.92$, $i = 10.2^\circ$.

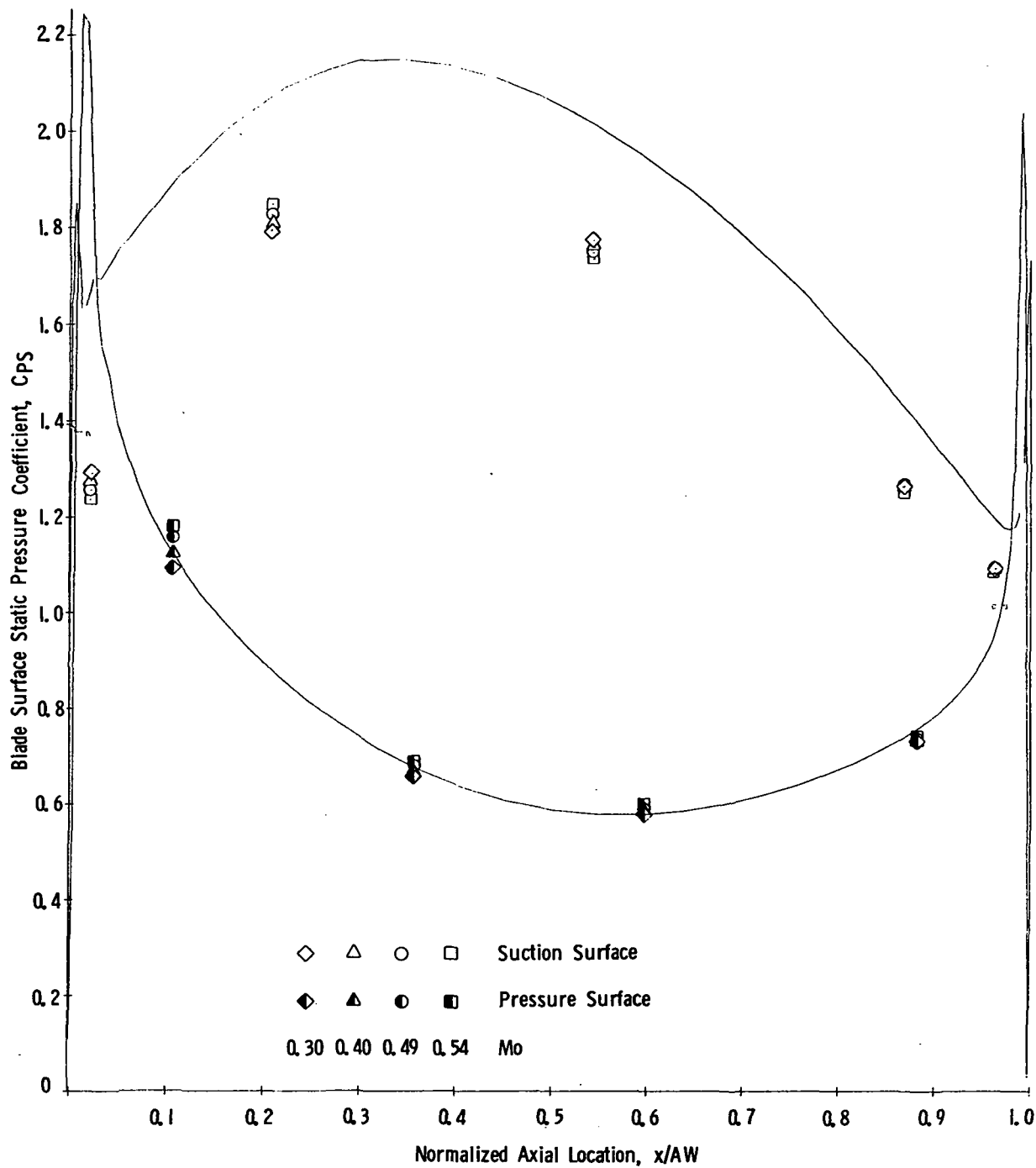


Figure 76. Blade Surface Static Pressure Coefficient Vs. Normalized Axial Location, B3R, $\sigma/\sigma_d = 0.85$, $i = -5.2^\circ$.

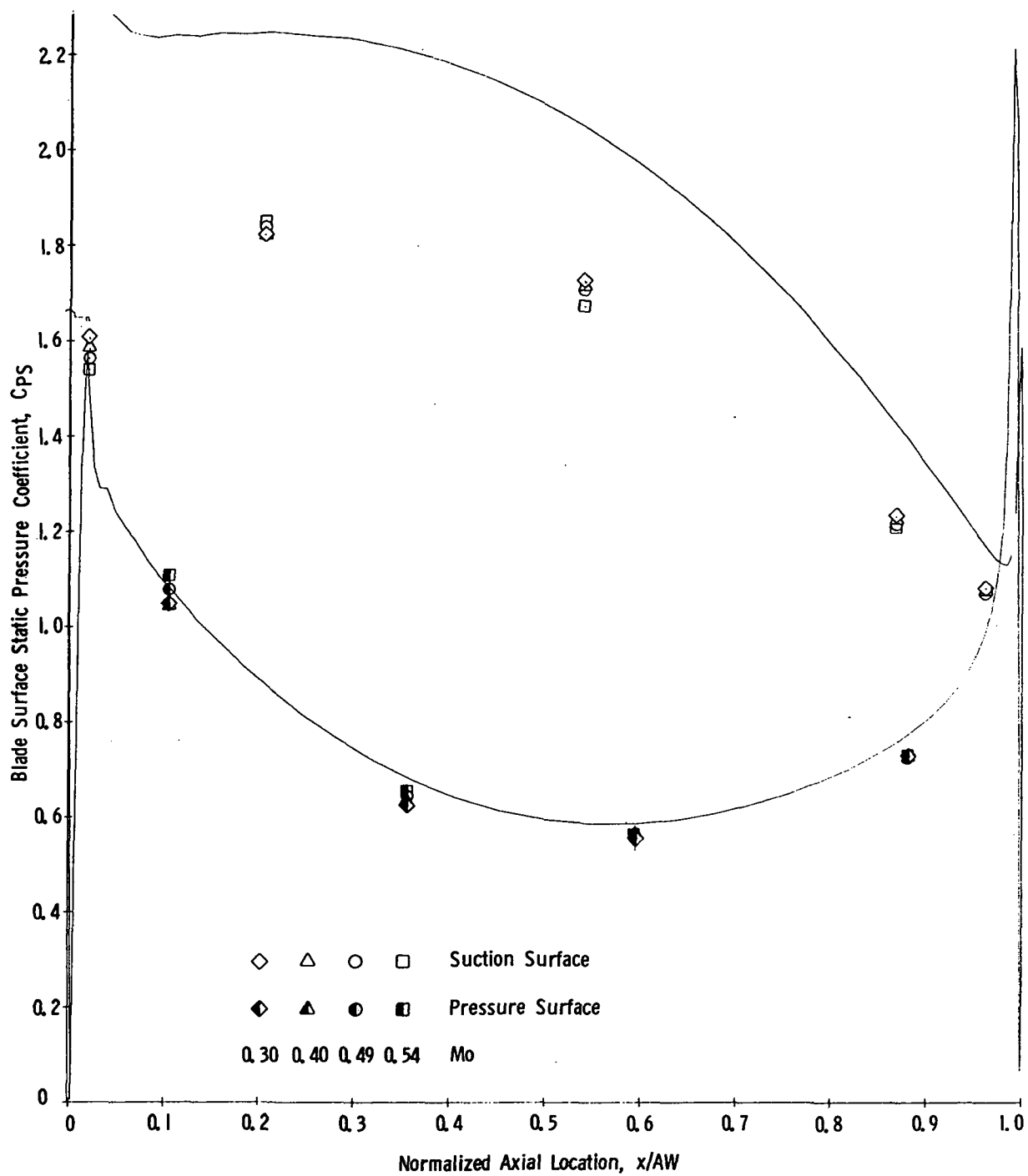


Figure 77. Blade Surface Static Pressure Coefficient Vs. Normalized Axial Location, B3R, $\sigma/\sigma_d = 0.85$, $i = 0^\circ$.

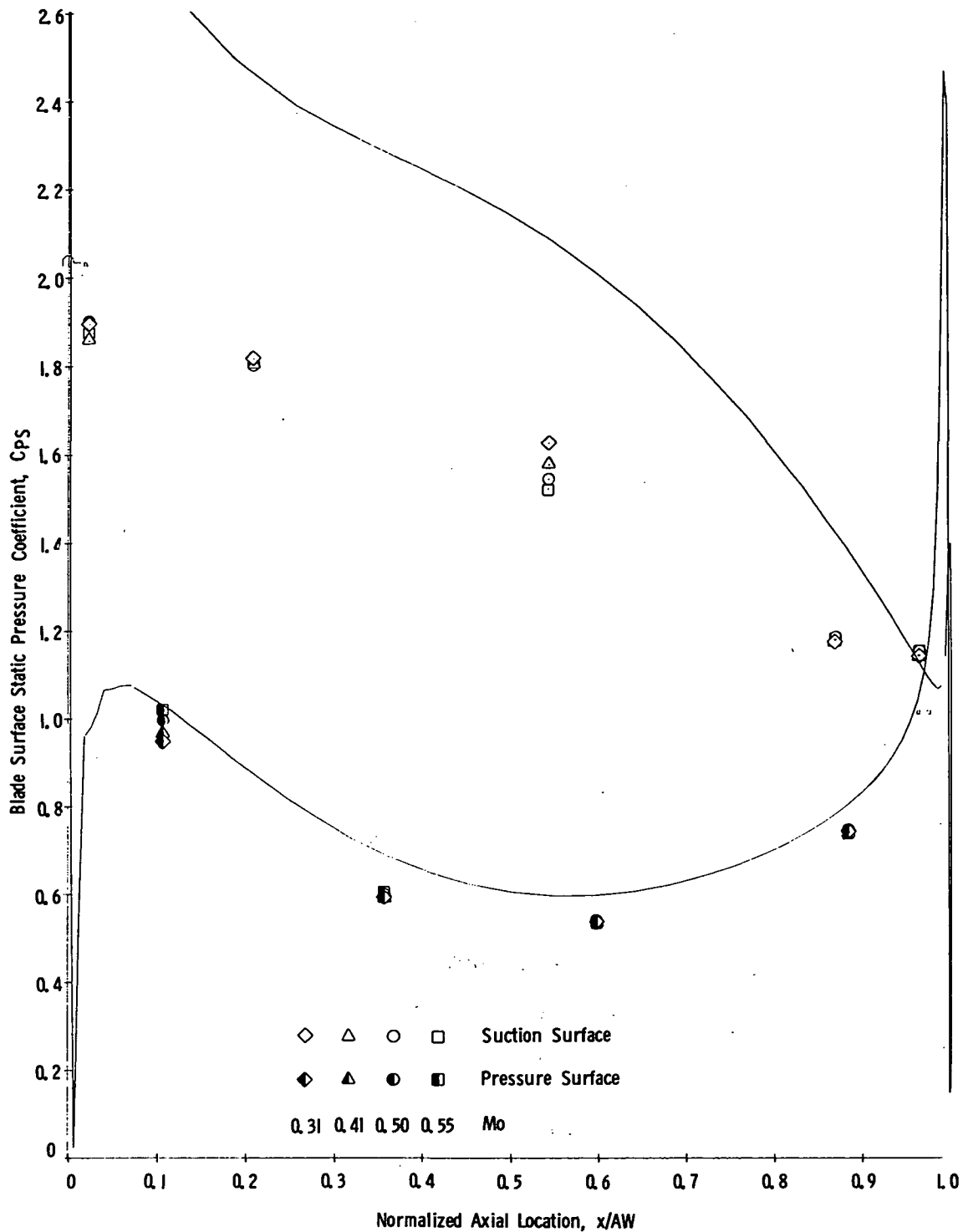


Figure 78. Blade Surface Static Pressure Coefficient Vs. Normalized Axial Location, B3R, $\sigma/\sigma_d = 0.85$, $i = 5.0^\circ$.

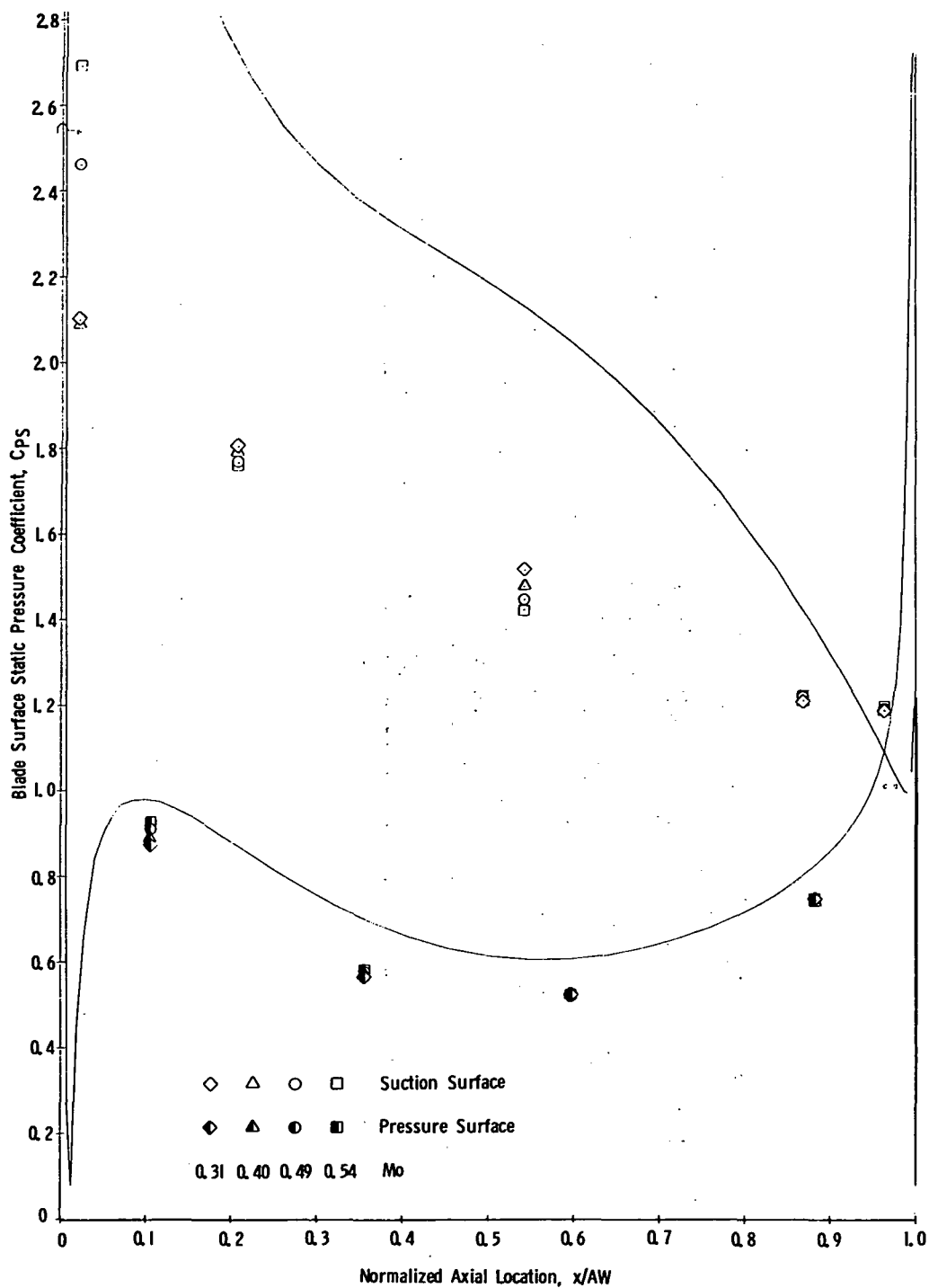


Figure 79. Blade Surface Static Pressure Coefficient Vs. Normalized Axial Location, B3R, $\sigma/\sigma_d = 0.85$, $i = 9.5^\circ$.

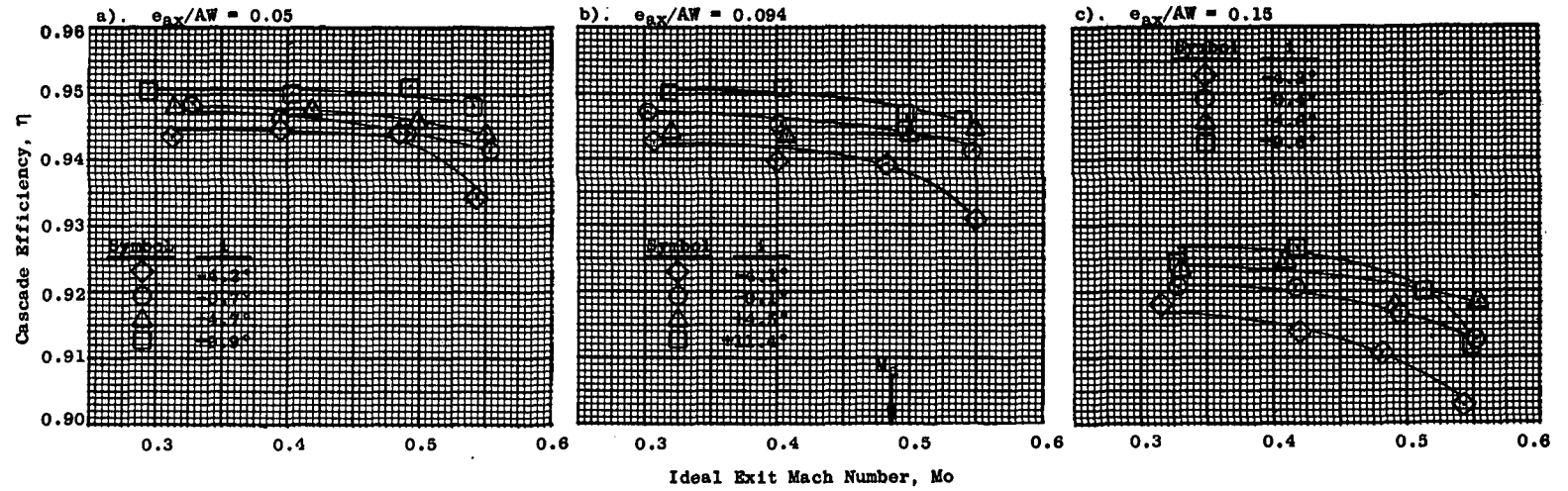


Figure 80. Cascade Efficiency Vs. Mach Number, TB3R at Turbine Design e_t .

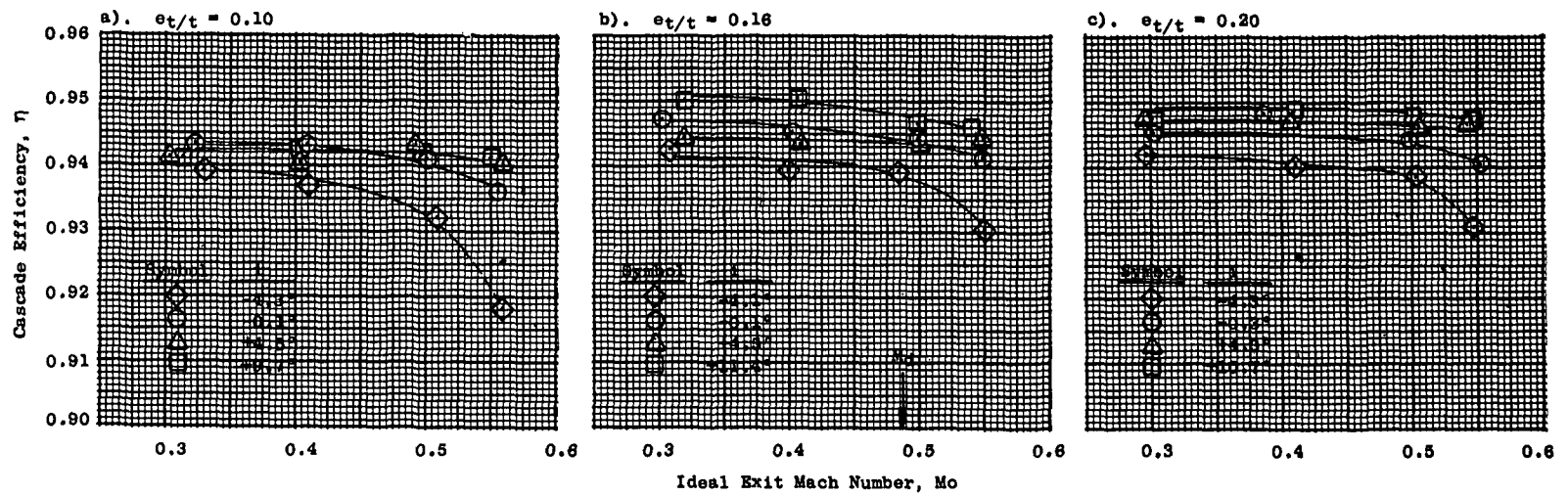


Figure 81. Cascade Efficiency Vs. Mach Number, TB3R at Turbine Design e_{ax} .

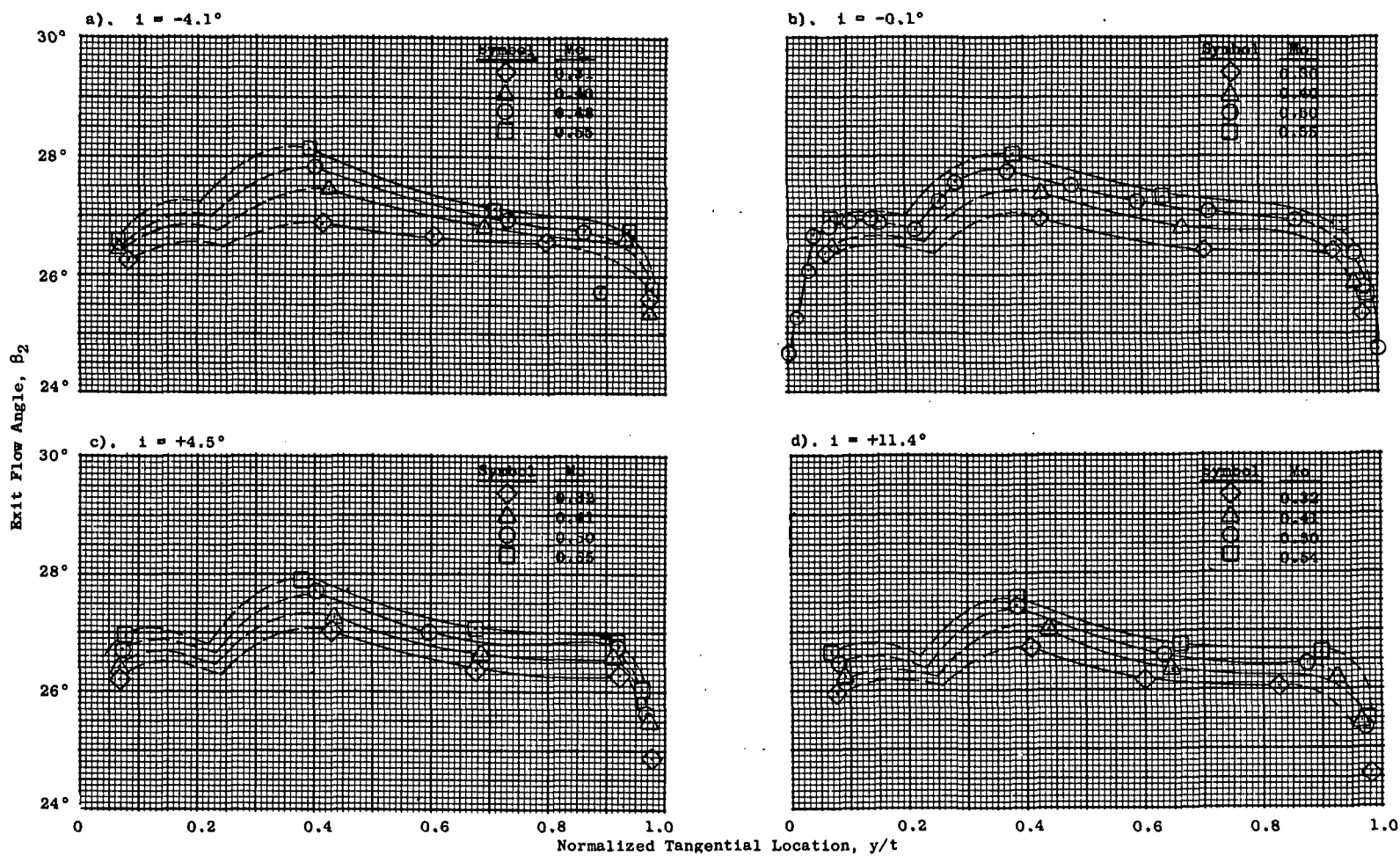


Figure 82. Exit Flow Angle Vs. Normalized Tangential Location, TB3R Turbine Design Configuration.

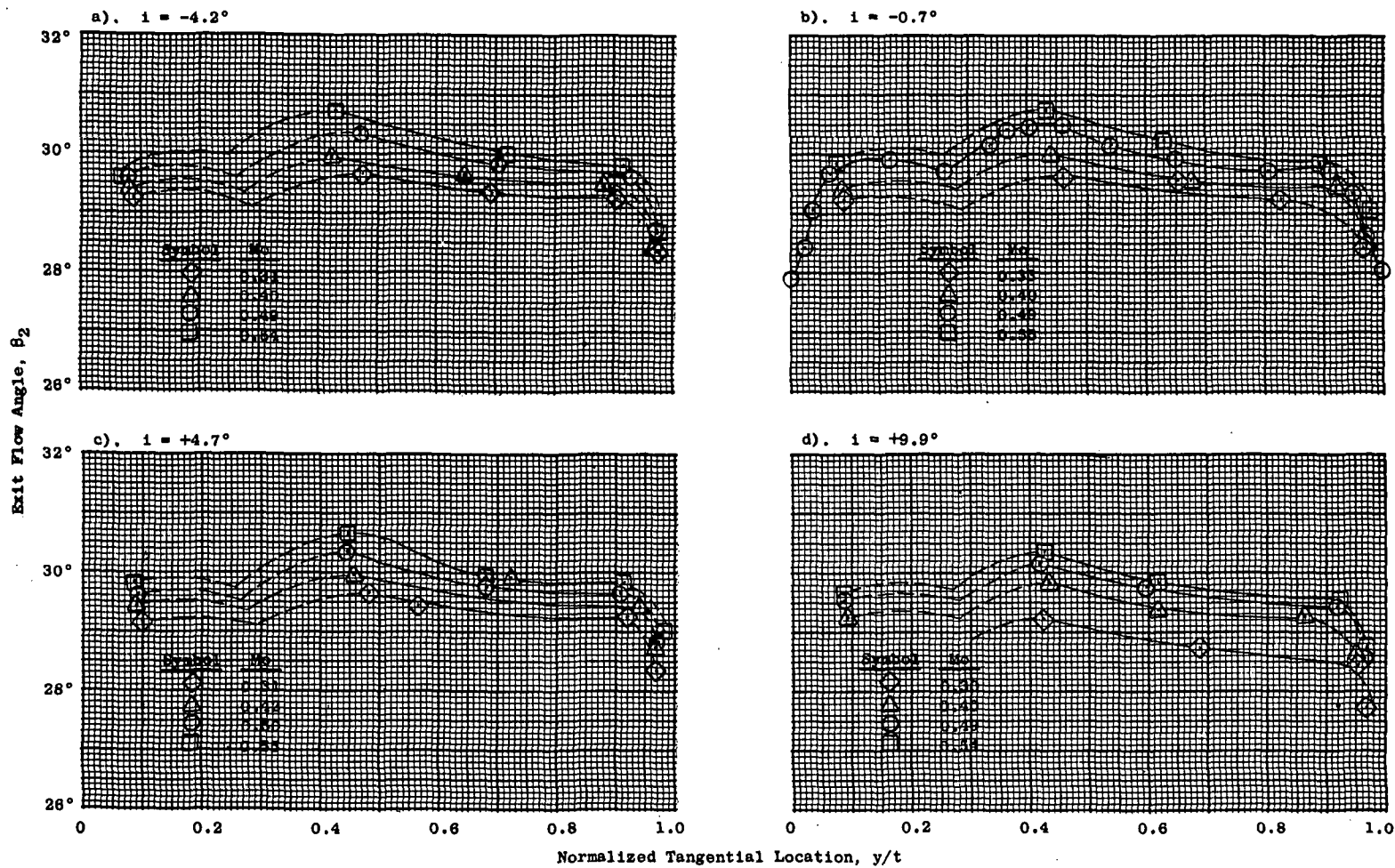


Figure 83. Exit Flow Angle Vs. Normalized Tangential Location, TB3R, e_{ax} Reduced.

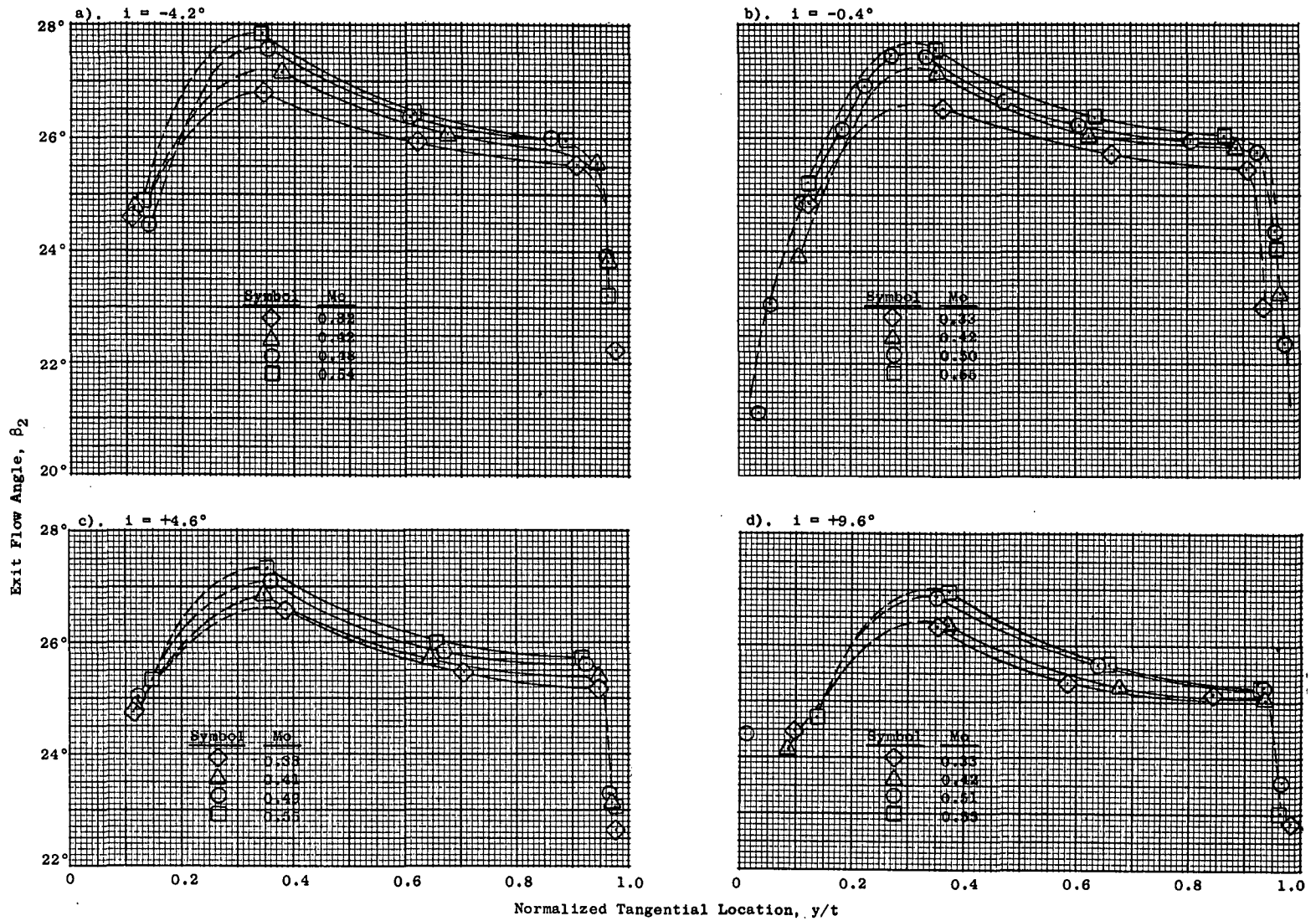


Figure 84. Exit Flow Angle Vs. Normalized Tangential Location, TB3R, e_{ax} Increased.

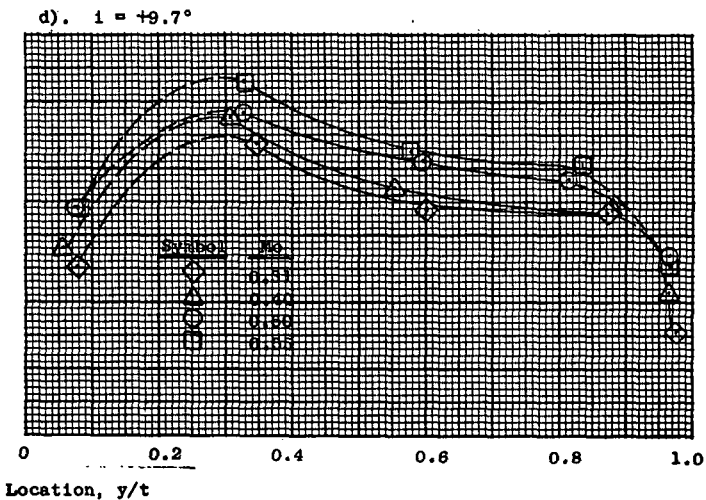
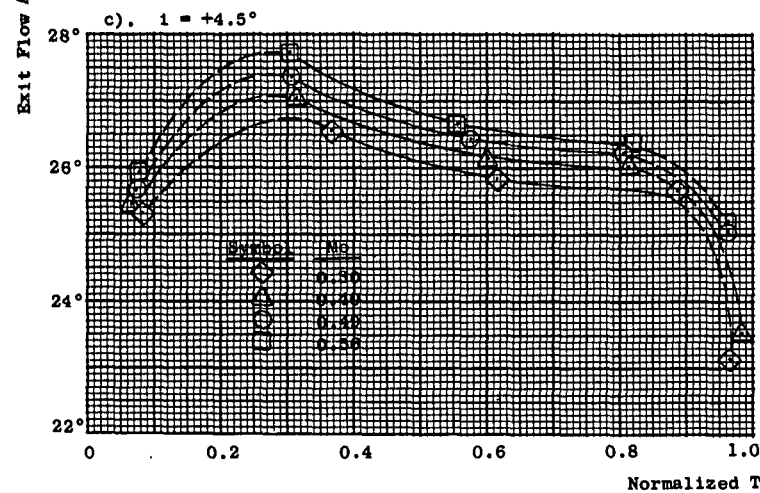
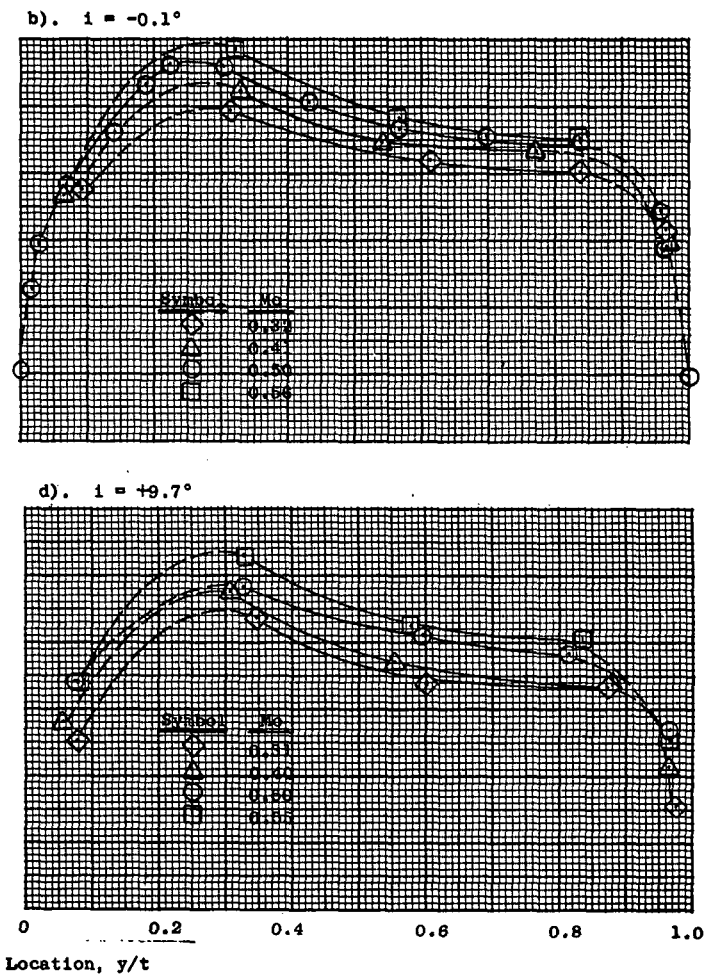
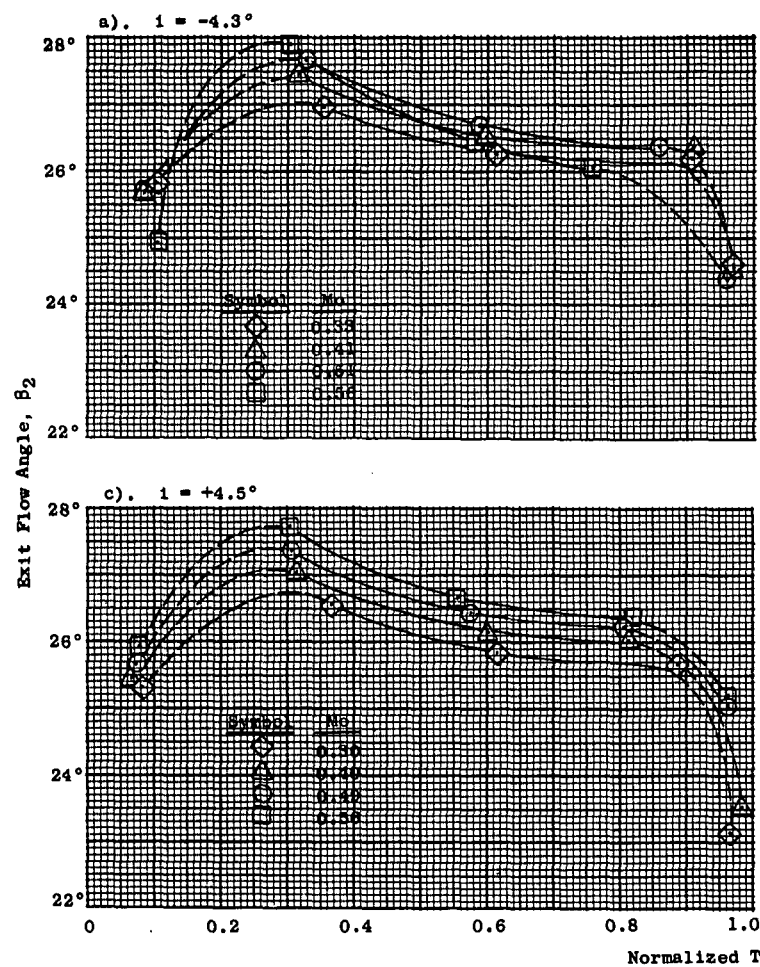


Figure 85. Exit Flow Angle Vs. Normalized Tangential Location, TB3R, e_t Reduced.

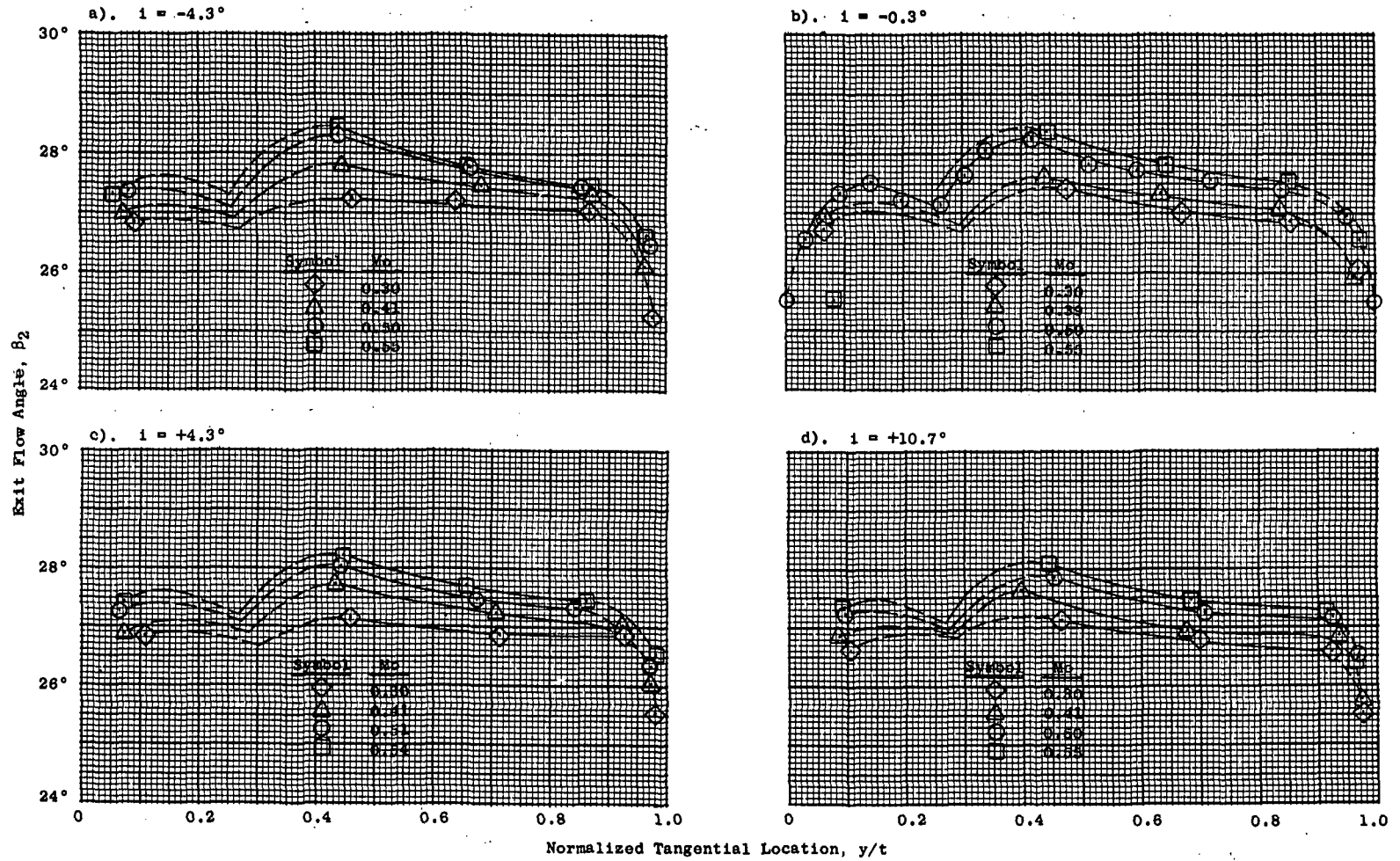


Figure 86. Exit Flow Angle Vs. Normalized Tangential Location, TB3R, e_t Increased.

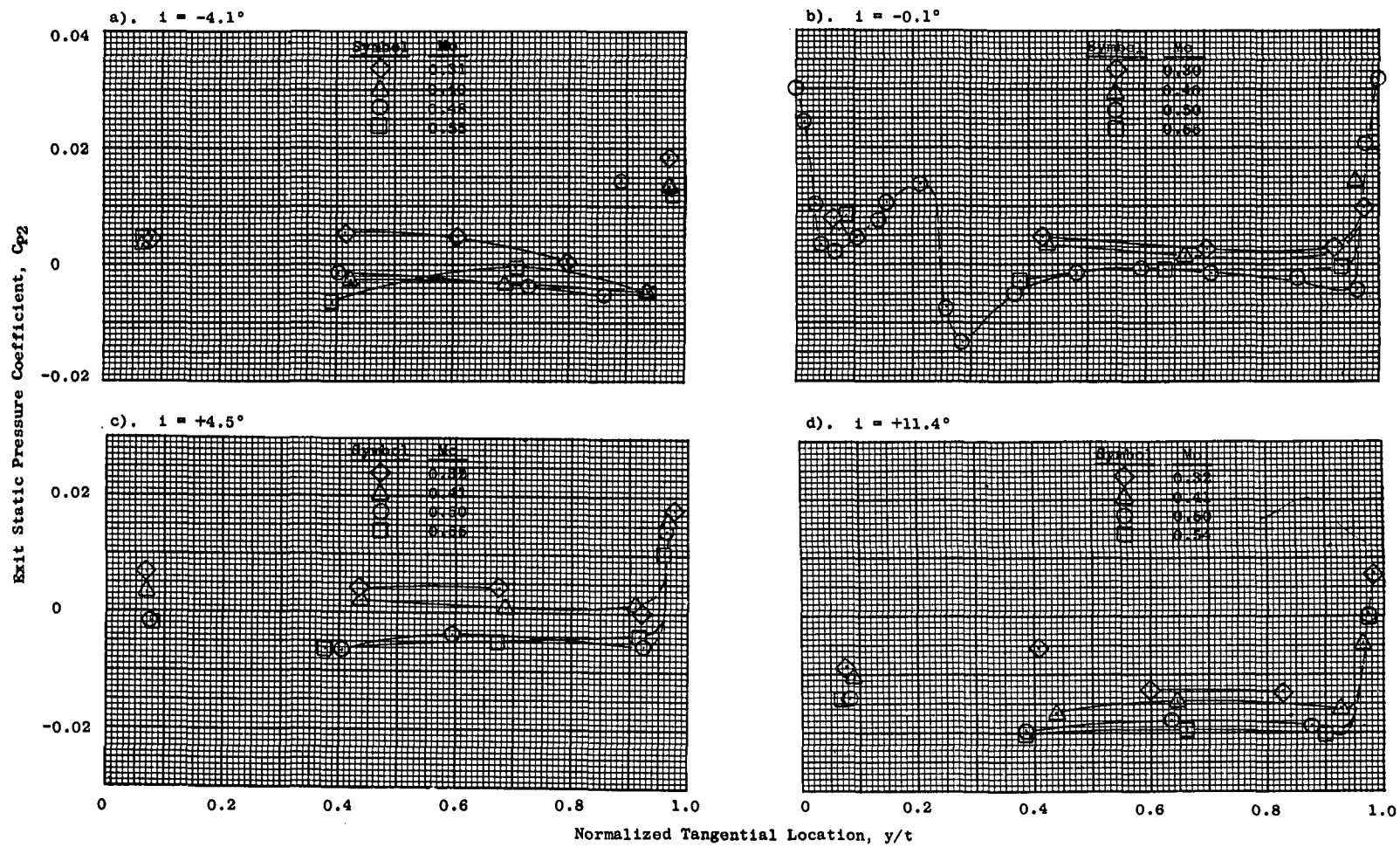


Figure 87. Exit Static Pressure Coefficient Vs. Normalized Tangential Location, TB3R Turbine Design Configuration.

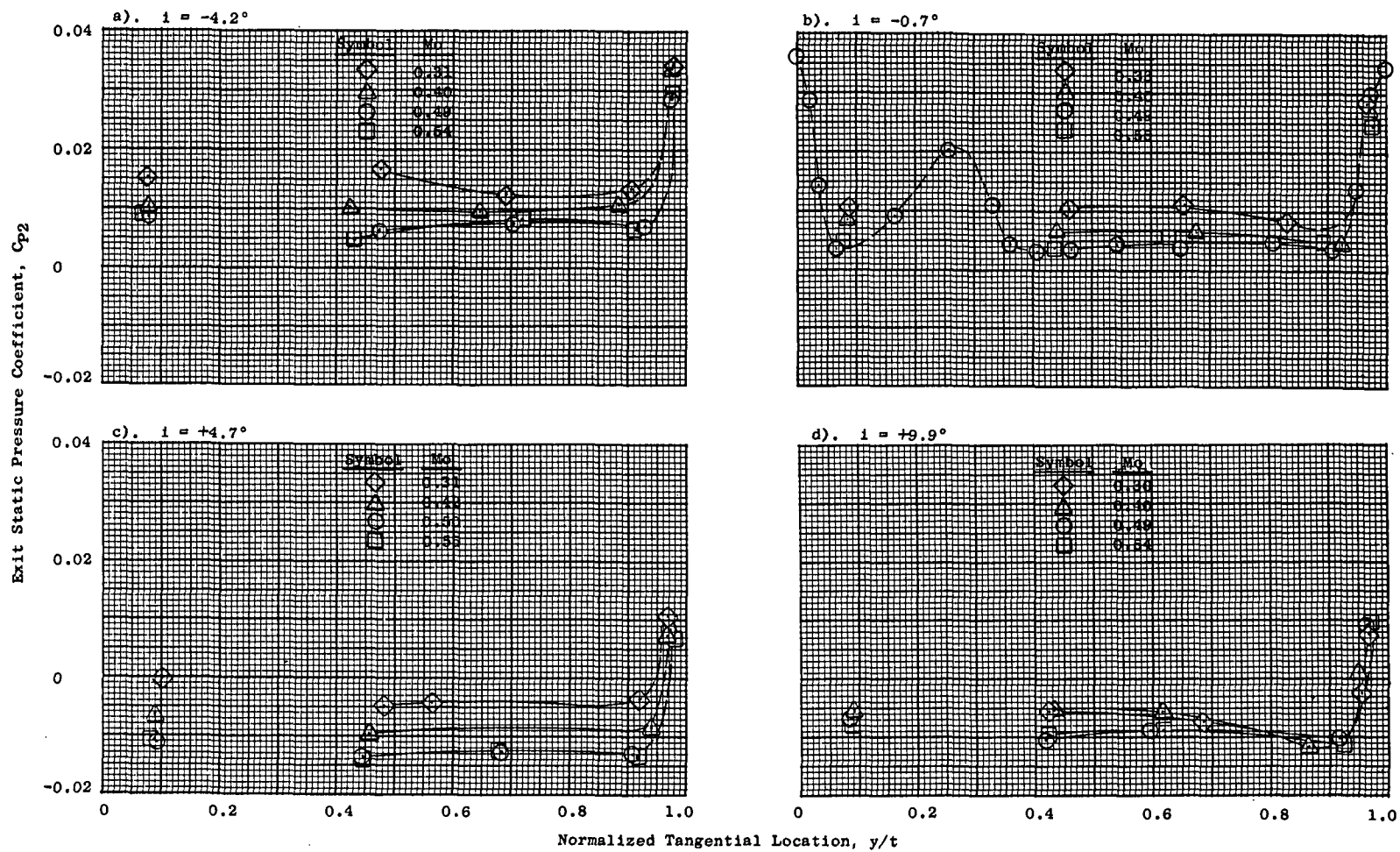


Figure 88. Exit Static Pressure Coefficient Vs. Normalized Tangential Location, TB3R, e_{ax} Reduced.

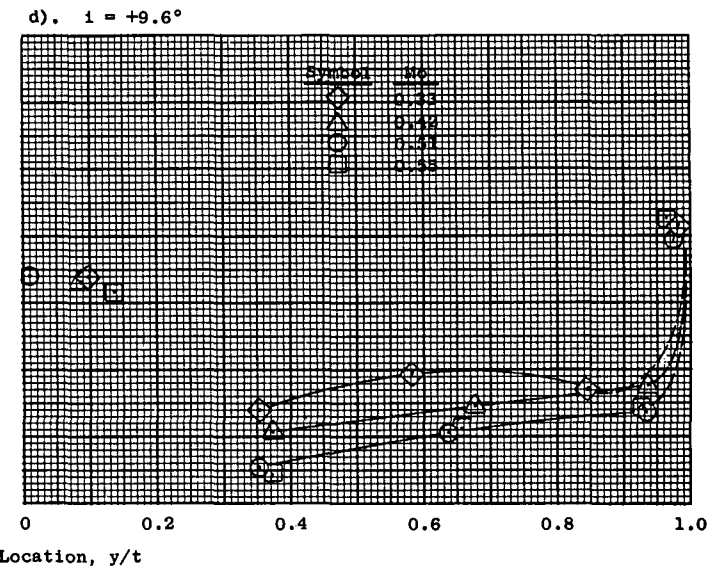
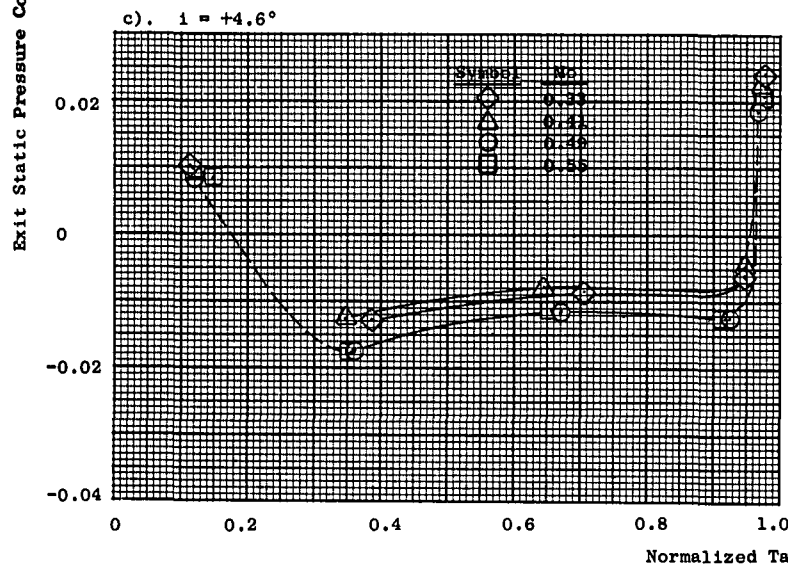
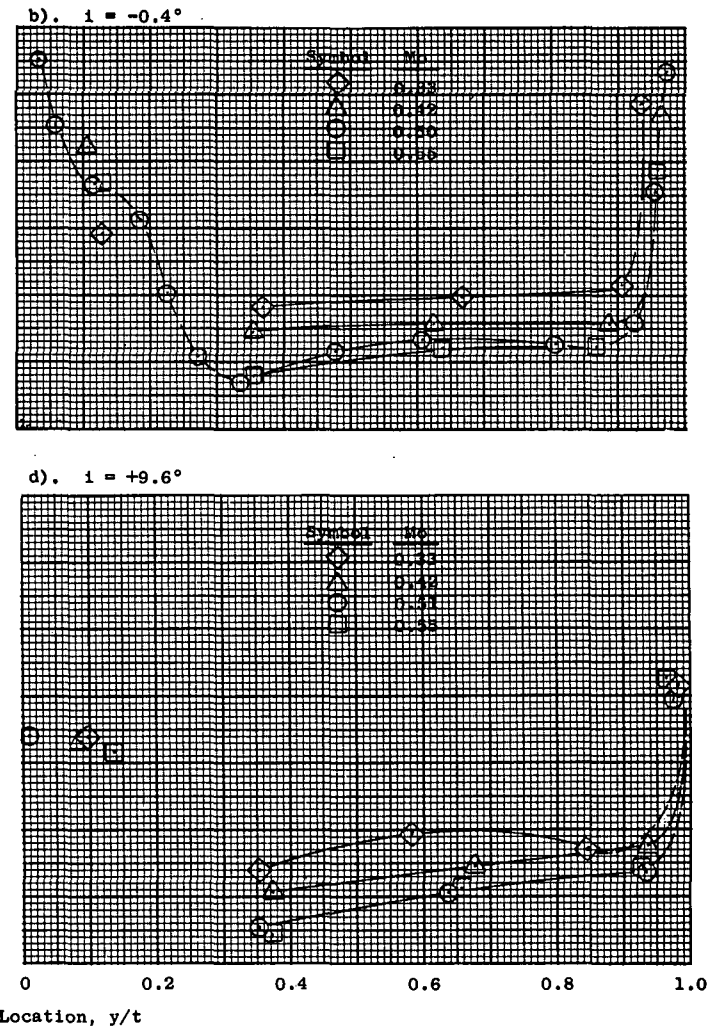
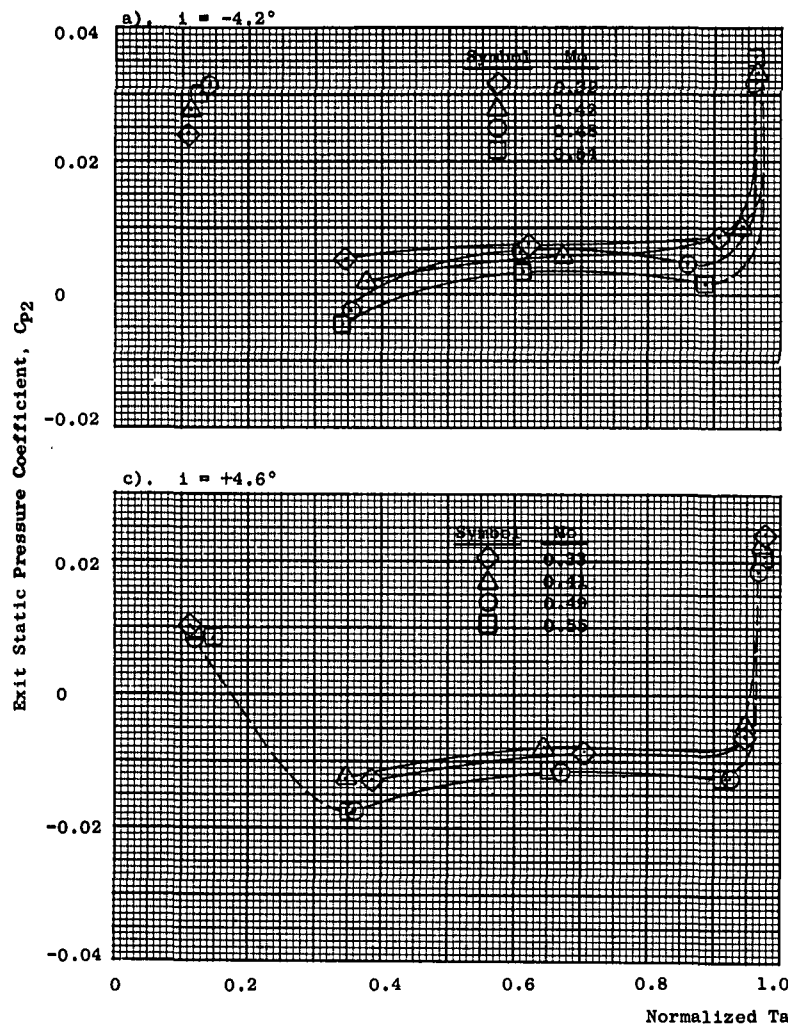


Figure 89. Exit Static Pressure Coefficient Vs. Normalized Tangential Location, TB3R, e_{ax} Increased.

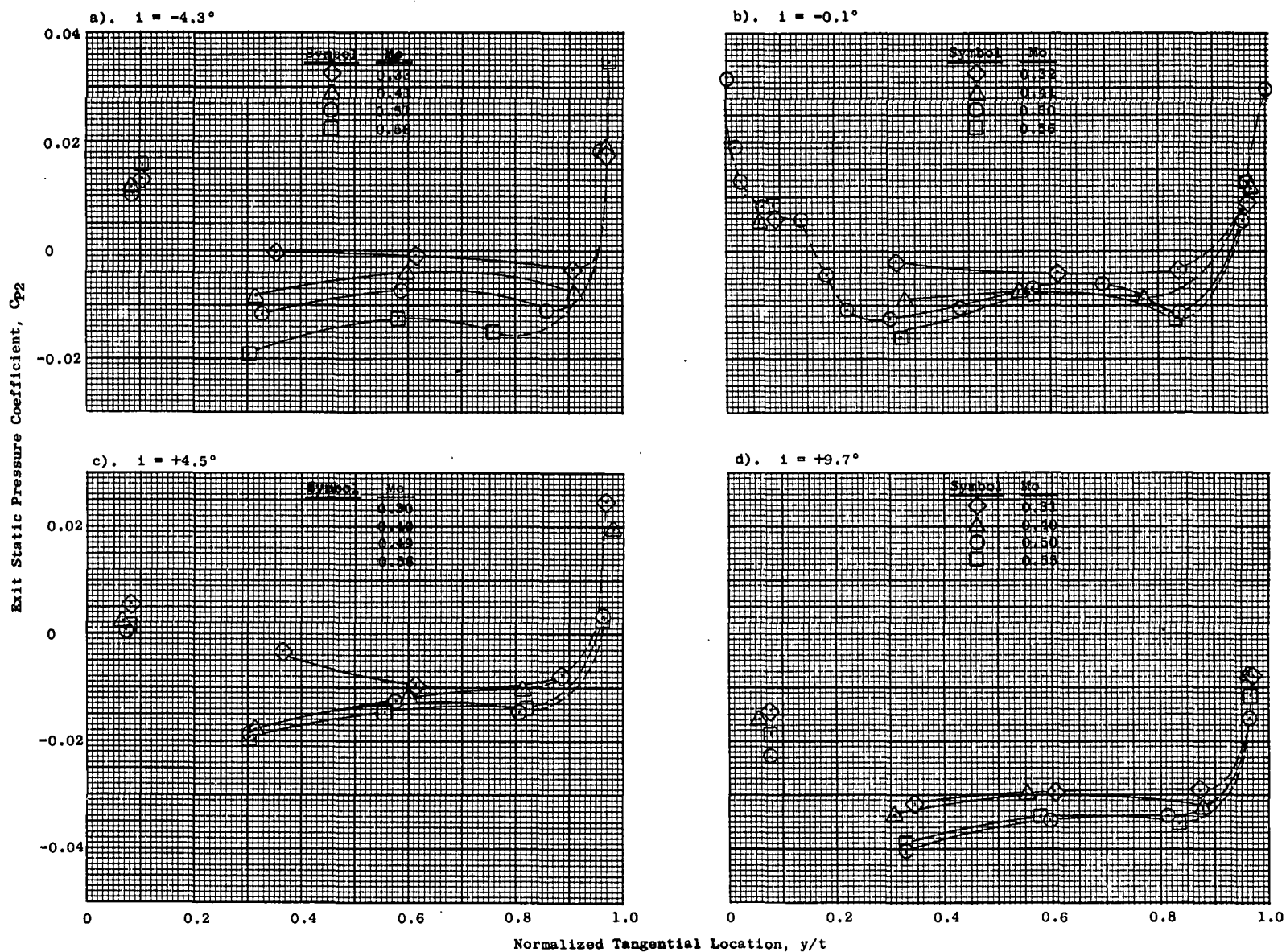


Figure 90. Exit Static Pressure Coefficient Vs. Normalized Tangential Location, TB3R, e_t Reduced.

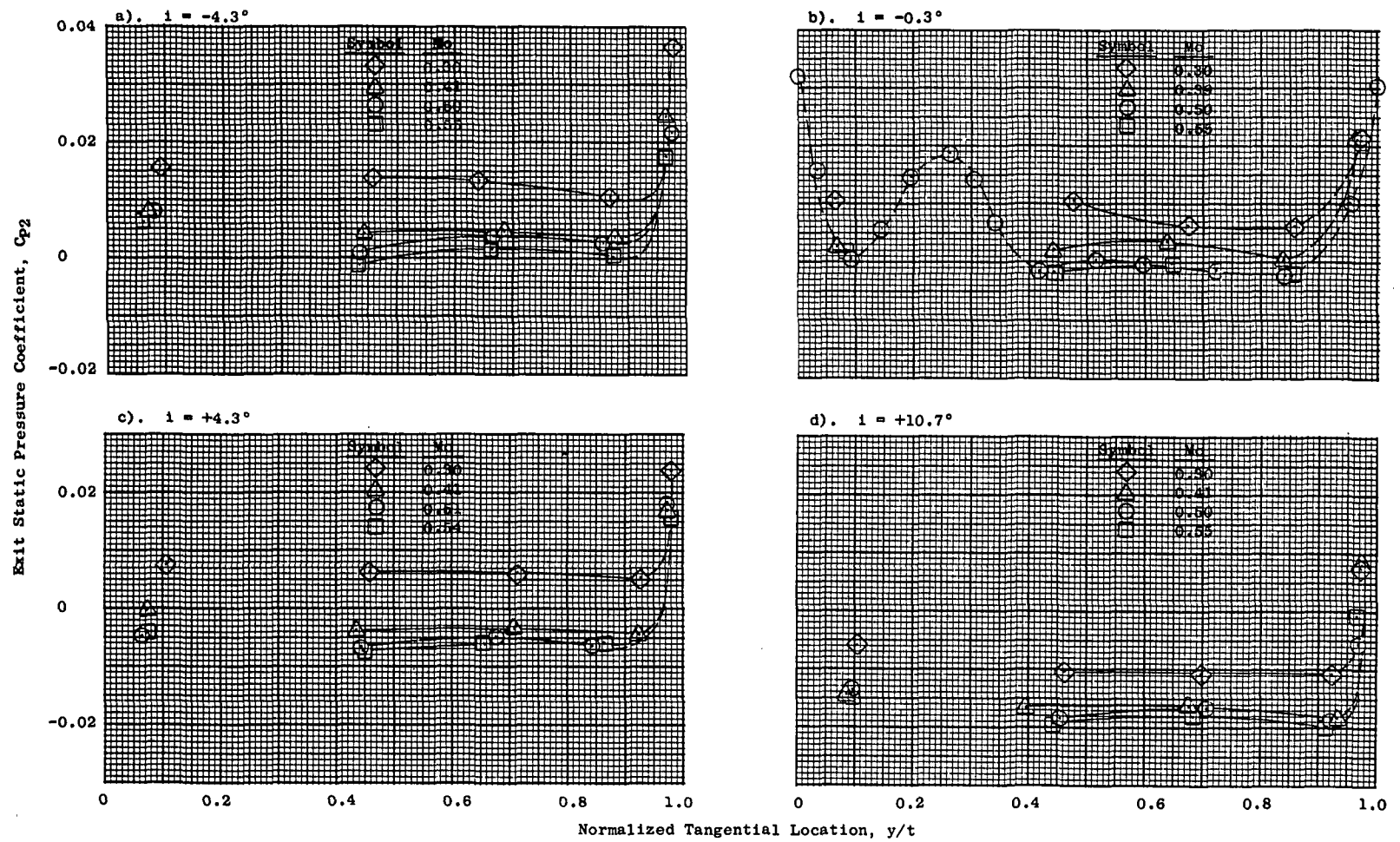


Figure 91. Exit Static Pressure Coefficient Vs. Normalized Tangential Location, TB3R, e_t Reduced.

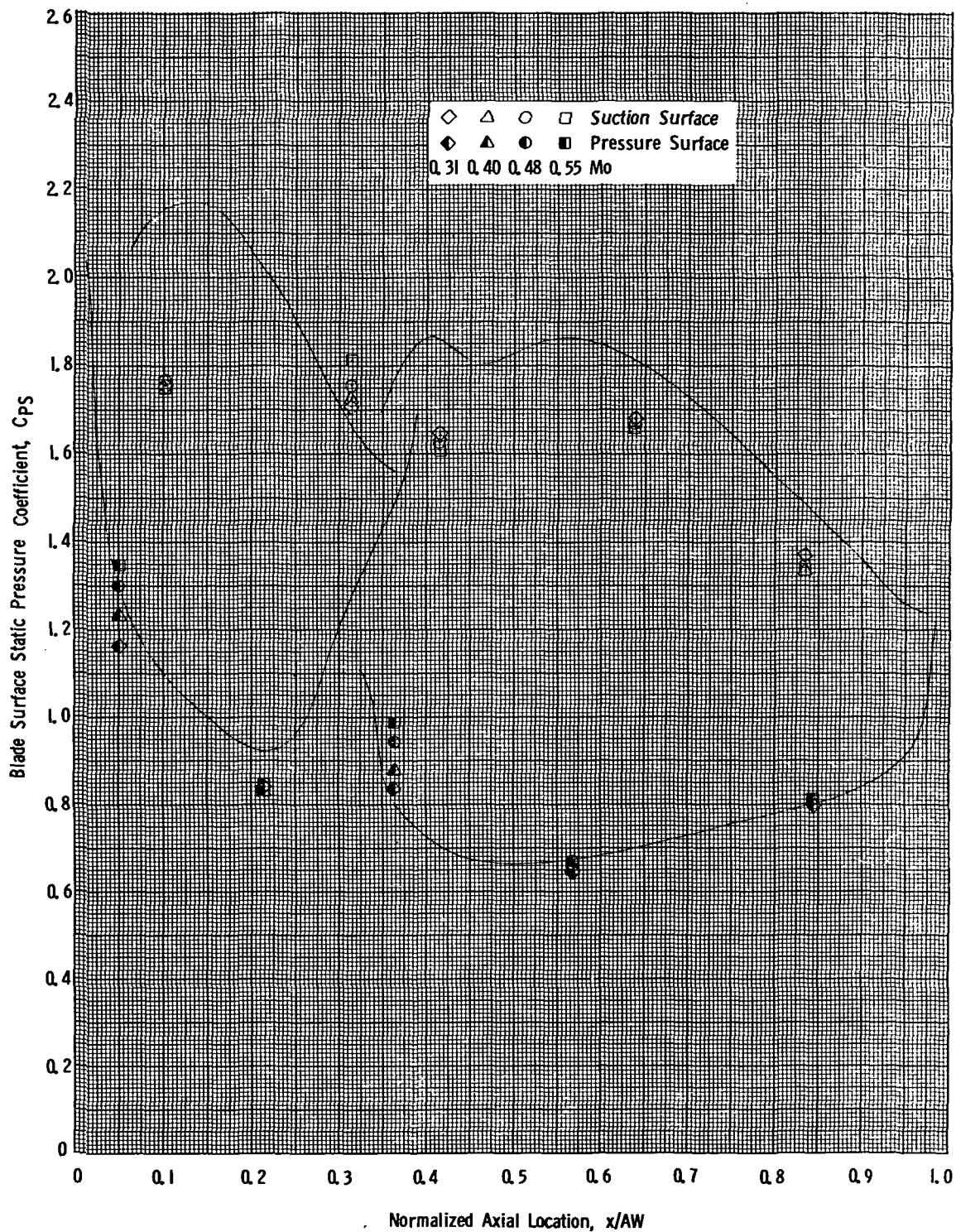


Figure 92. Blade Surface Static Pressure Coefficient Vs. Normalized Axial Location, TB3R Turbine Design Configuration, $i = -4.1^\circ$.

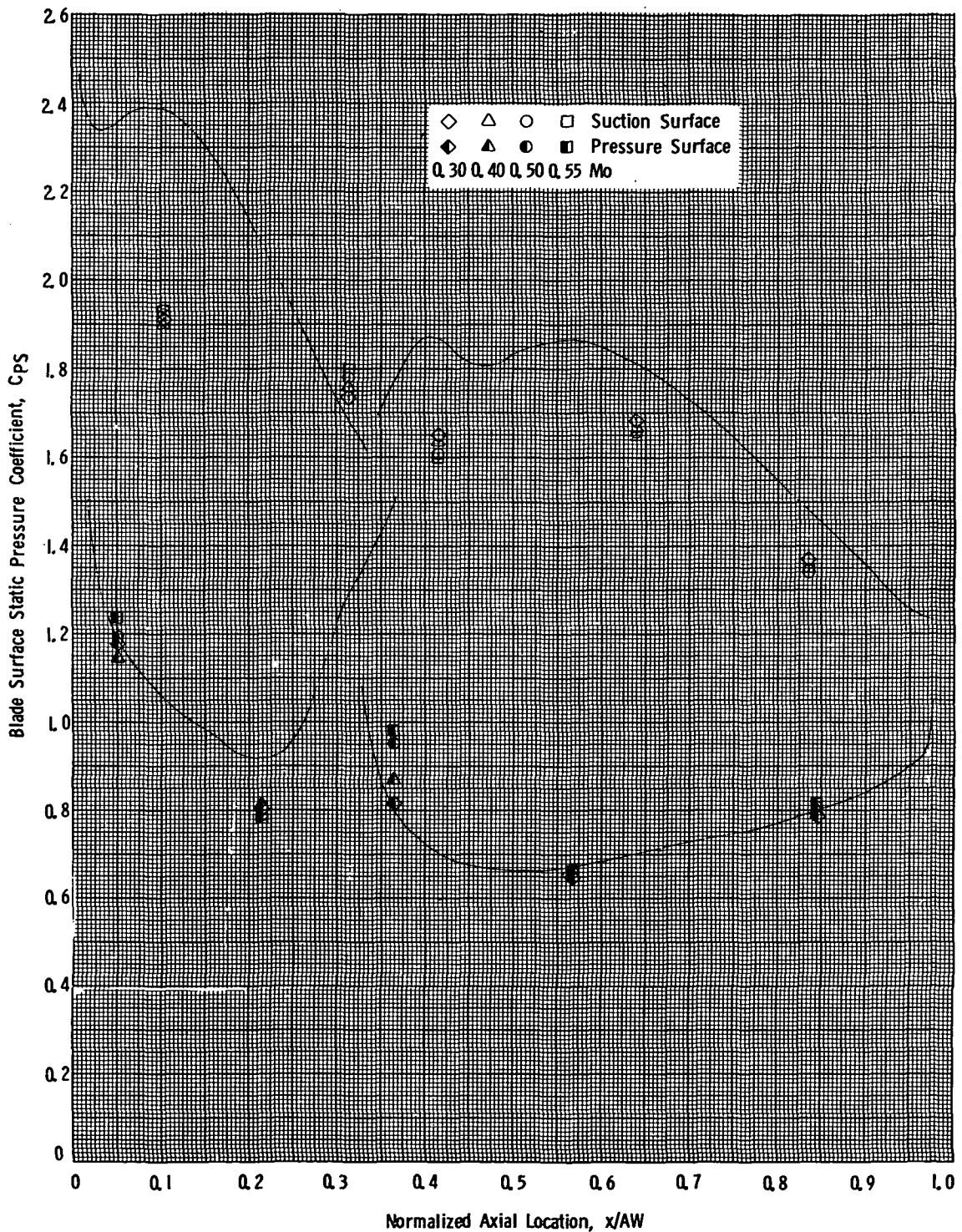


Figure 93. Blade Surface Static Pressure Coefficient Vs. Normalized Axial Location, TB3R Turbine Design Configuration, $i = -0.1^\circ$.

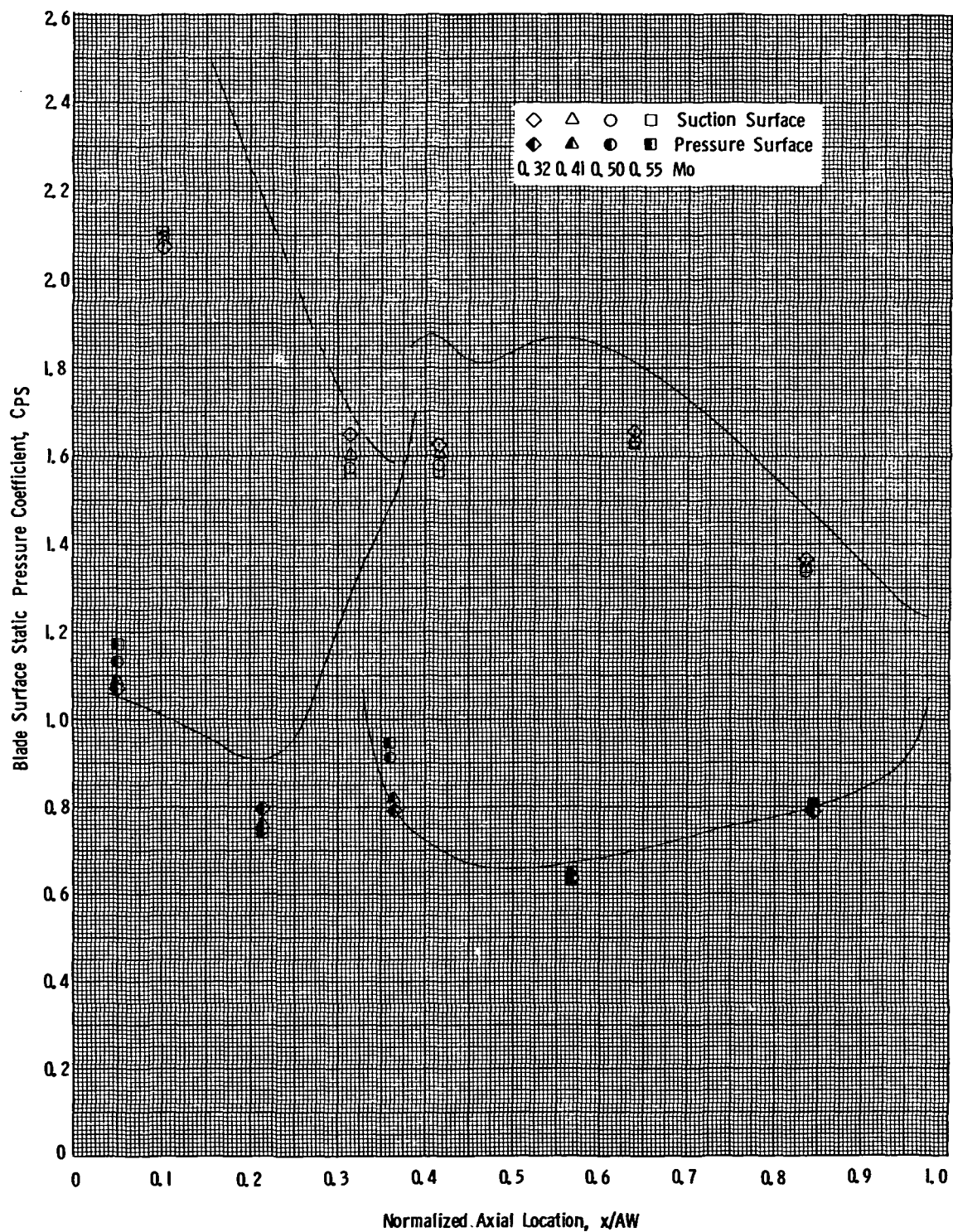


Figure 94. Blade Surface Static Pressure Coefficient Vs. Normalized Axial Location, TB3R Turbine Design Configuration, $i = 4.5^\circ$.

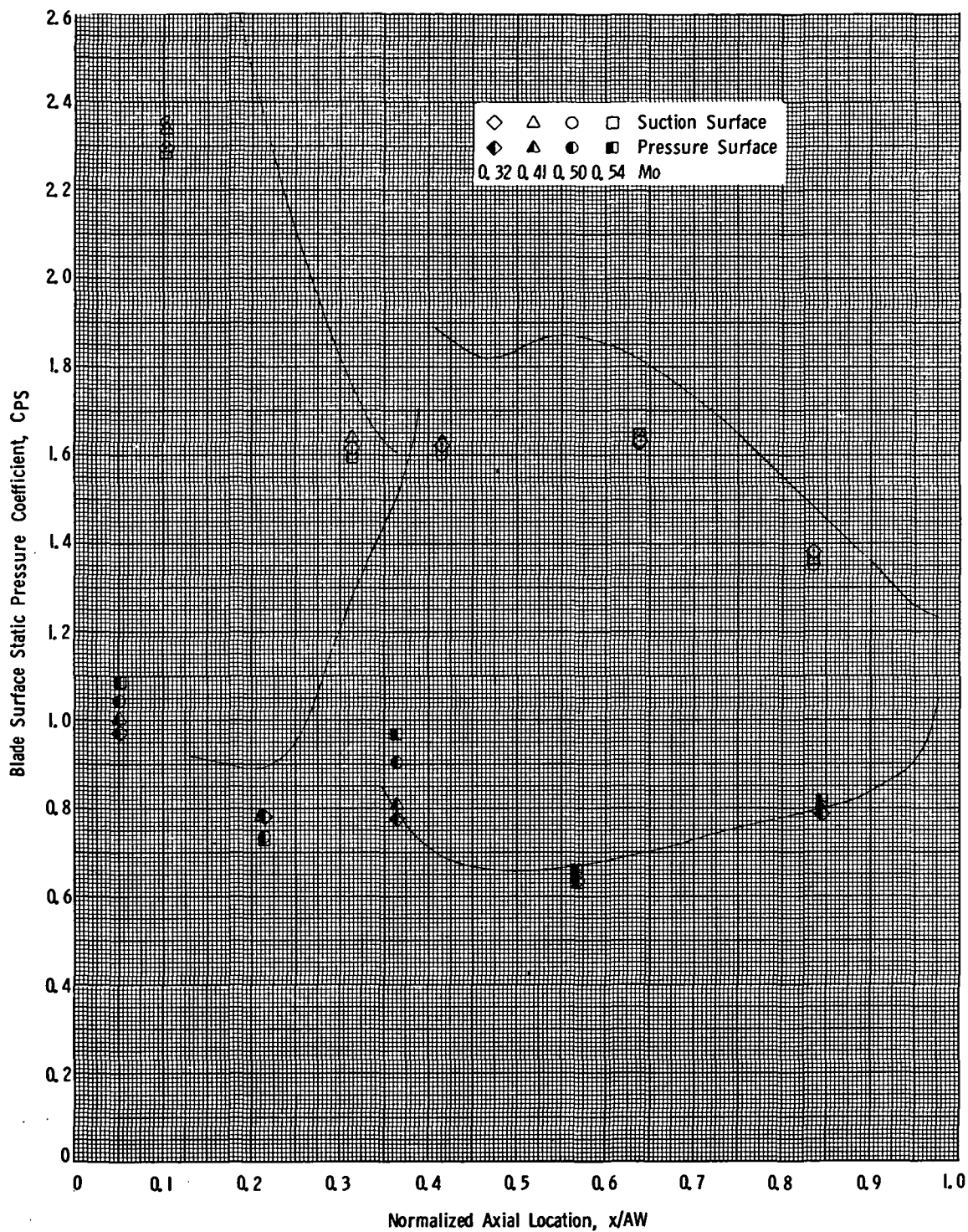


Figure 95. Blade Surface Static Pressure Coefficient Vs. Normalized Axial Location, TB3R Turbine Design Configuration, $i = 11.4^\circ$.

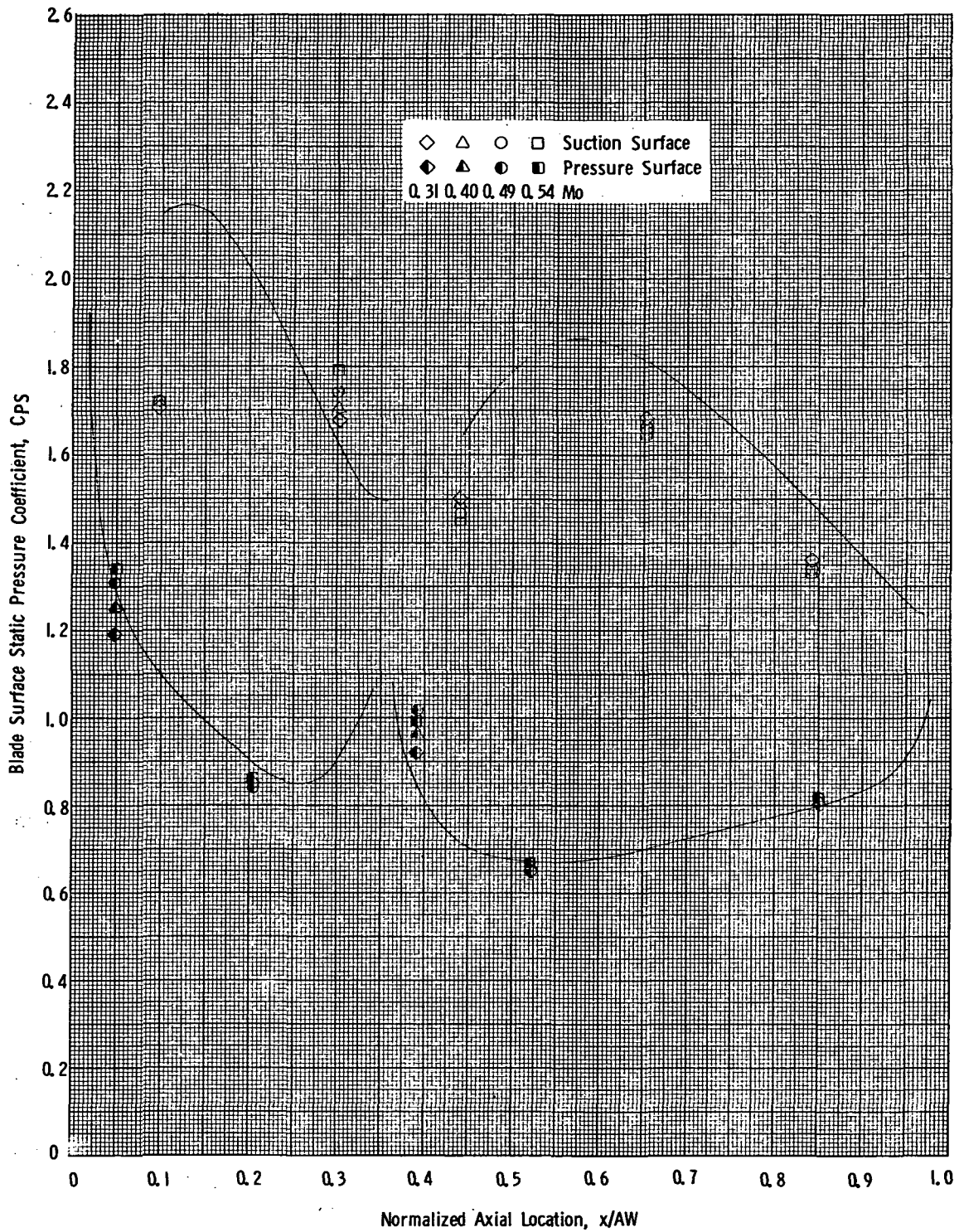


Figure 96. Blade Surface Static Pressure Coefficient Vs. Normalized Axial Location, TB3R, e_{ax} Reduced, $i = -4.2^\circ$.

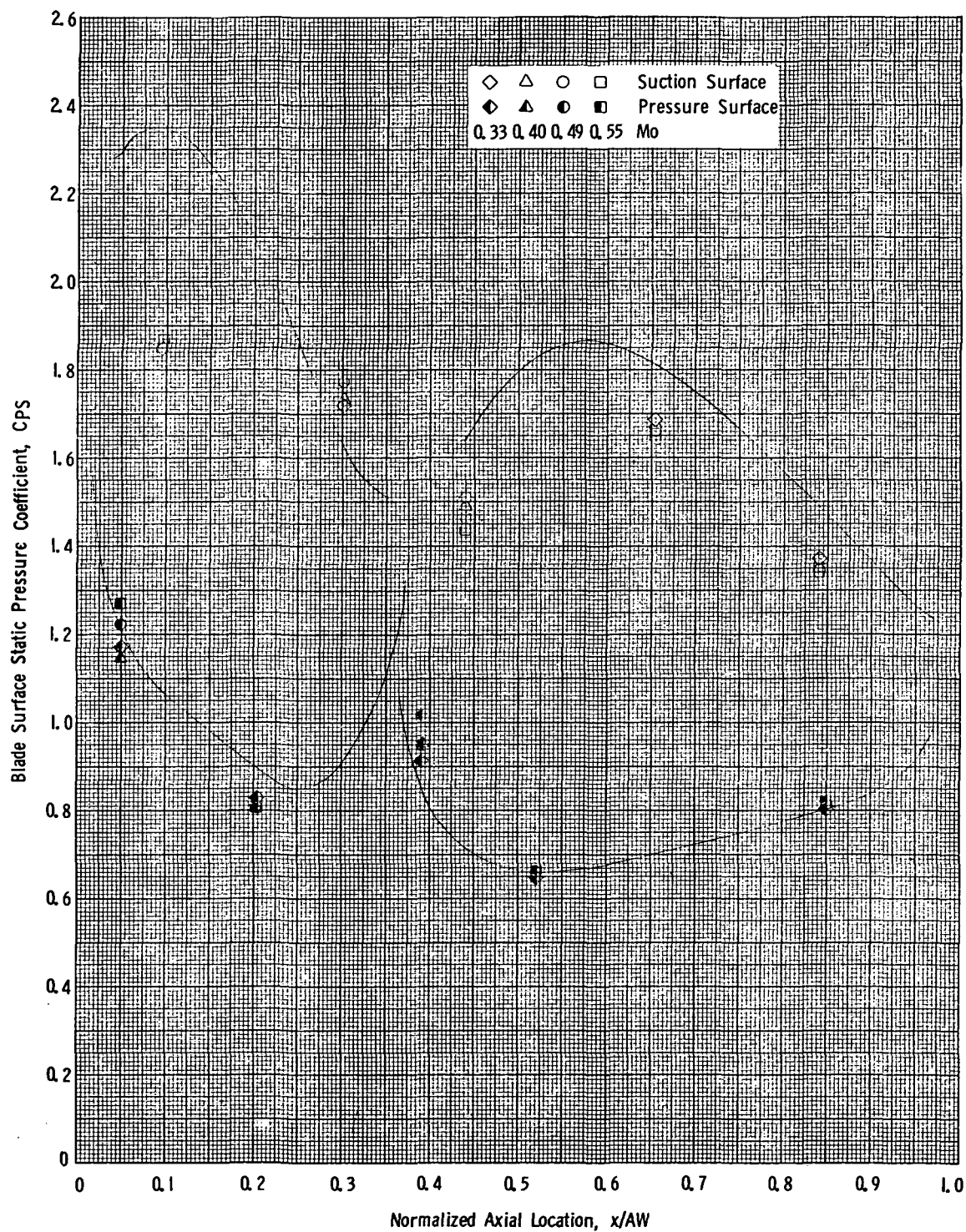


Figure 97. Blade Surface Static Pressure Coefficient Vs. Normalized Axial Location, TB3R, e_{ax} Reduced, $i = -0.7^\circ$.

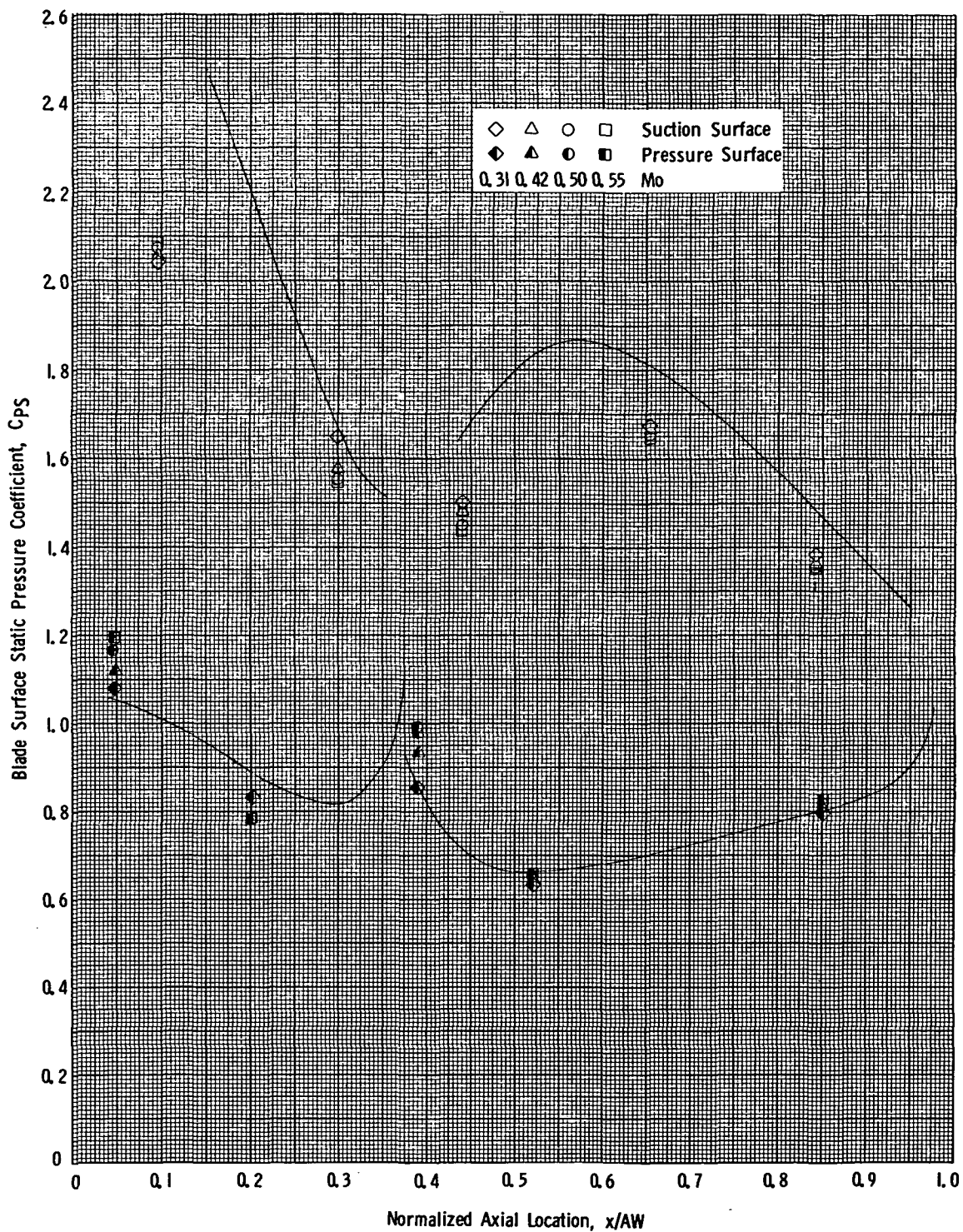


Figure 98. Blade Surface Static Pressure Coefficient Vs. Normalized Axial Location, TB3R, e_{ax} Reduced, $i = 4.7^\circ$.

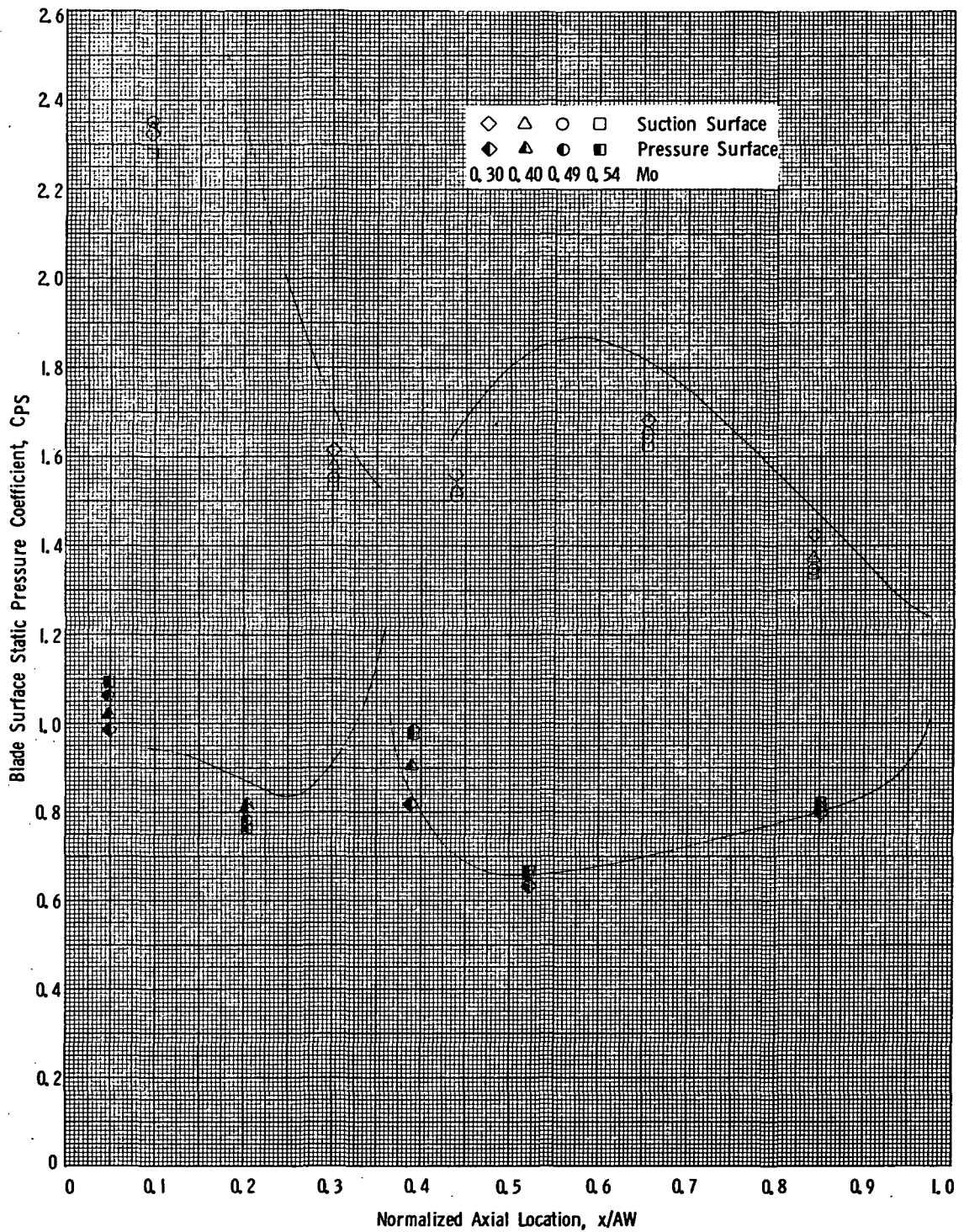


Figure 99. Blade Surface Static Pressure Coefficient Vs. Normalized Axial Location, TB3R, e_{ax} Reduced, $i = 9.9^\circ$.

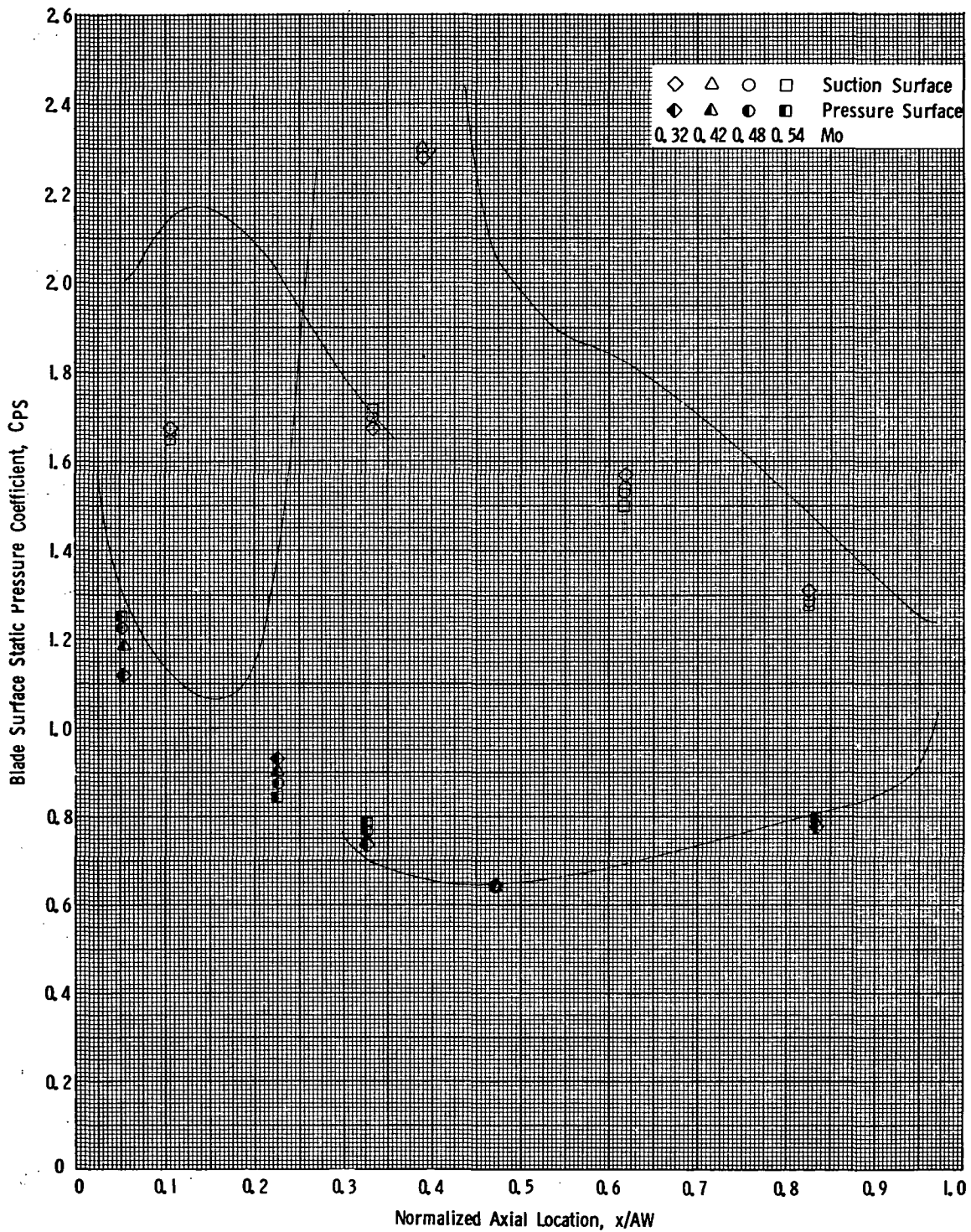


Figure 100. Blade Surface Static Pressure Coefficient Vs. Normalized Axial Location, TB3R, e_{ax} Increased, $i = -4.2^\circ$.

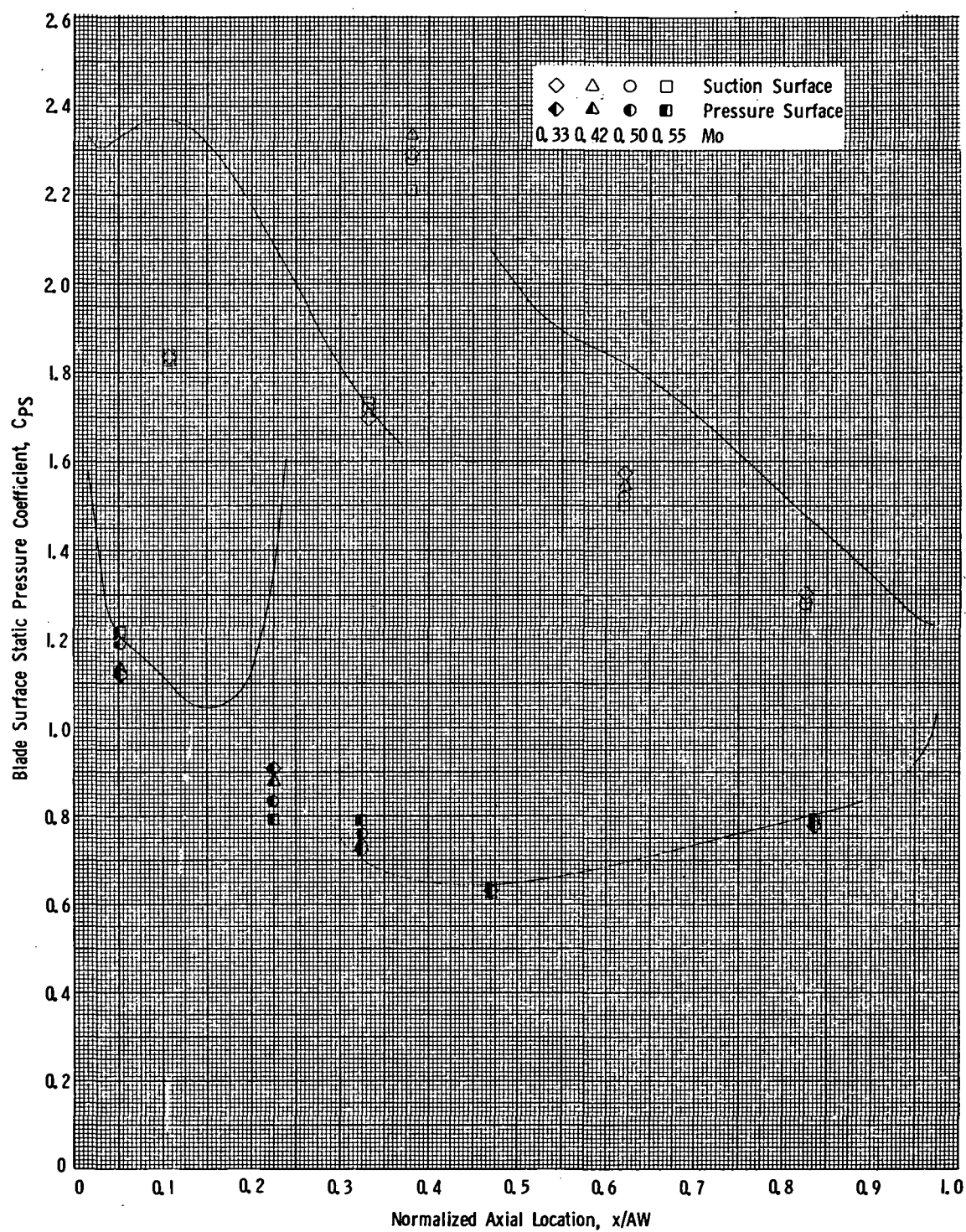


Figure 101. Blade Surface Static Pressure Coefficient Vs. Normalized Axial Location, TB3R, e_{ax} Increased; $i = -0.4^\circ$.

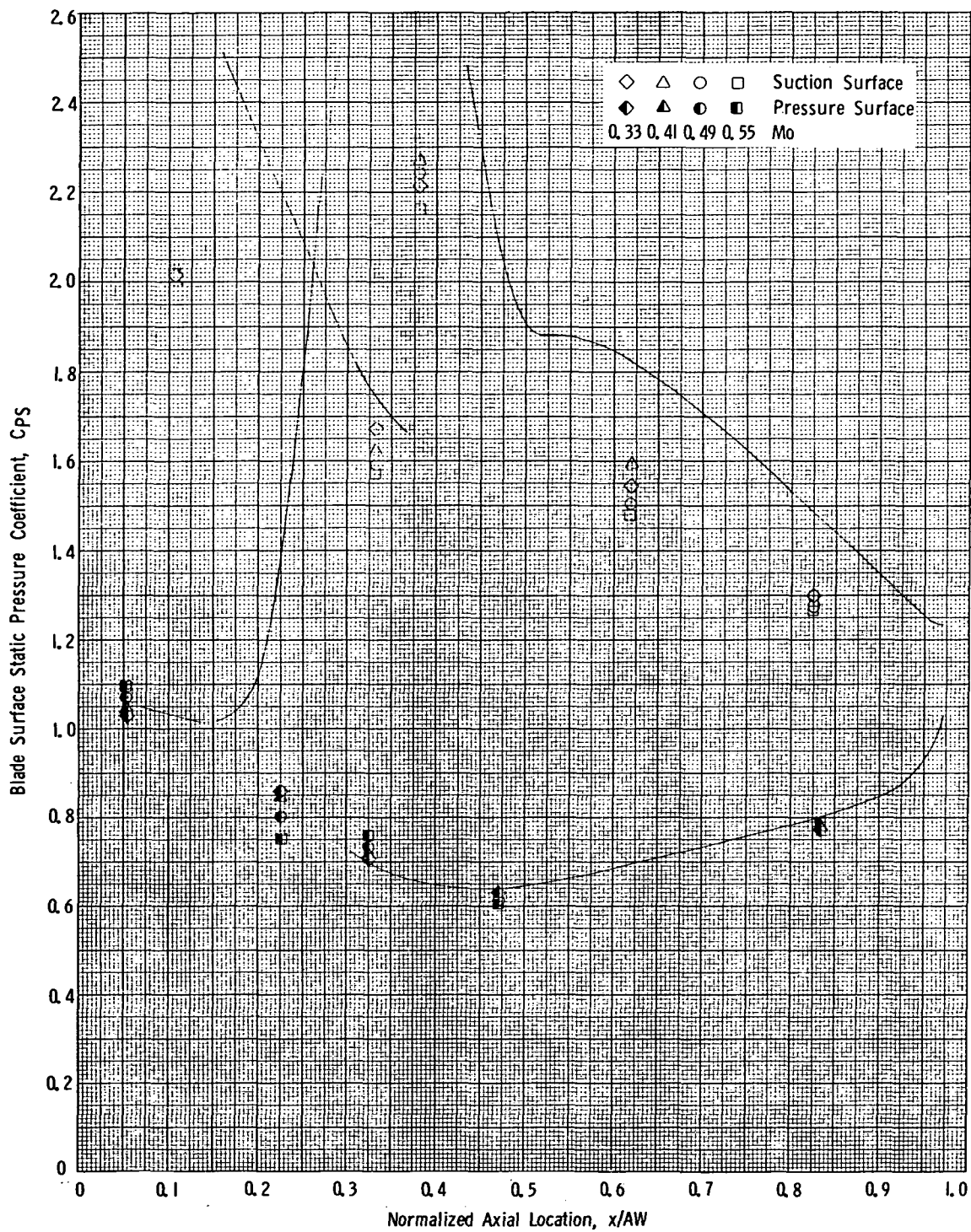


Figure 102. Blade Surface Static Pressure Coefficient Vs. Normalized Axial Location, TB3R, e_{ax} Increased, $i = 4.6^\circ$.

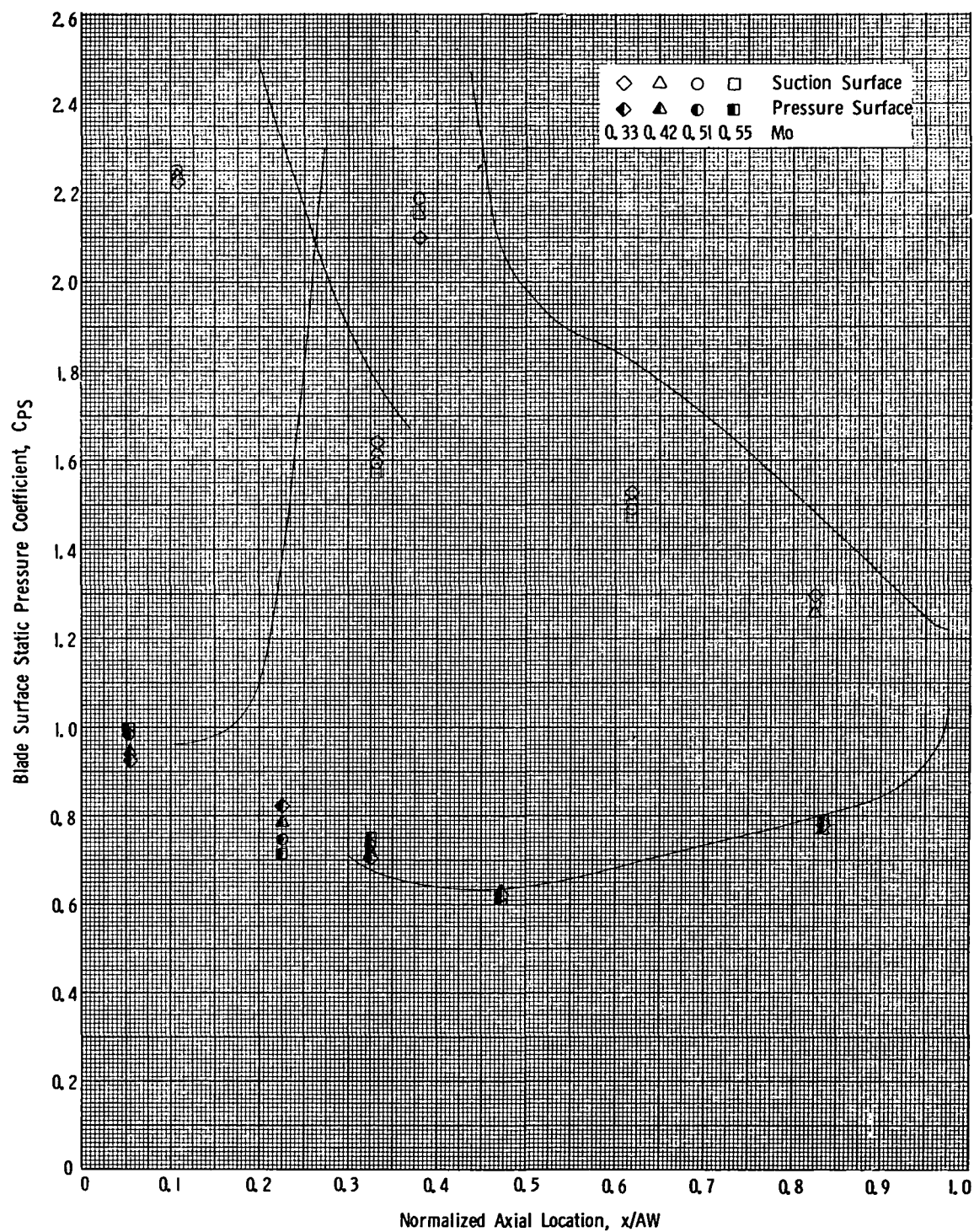


Figure 103. Blade Surface Static Pressure Coefficient Vs. Normalized Axial Location, TB3R, e_{ax} Increased, $i = 9.6^\circ$.

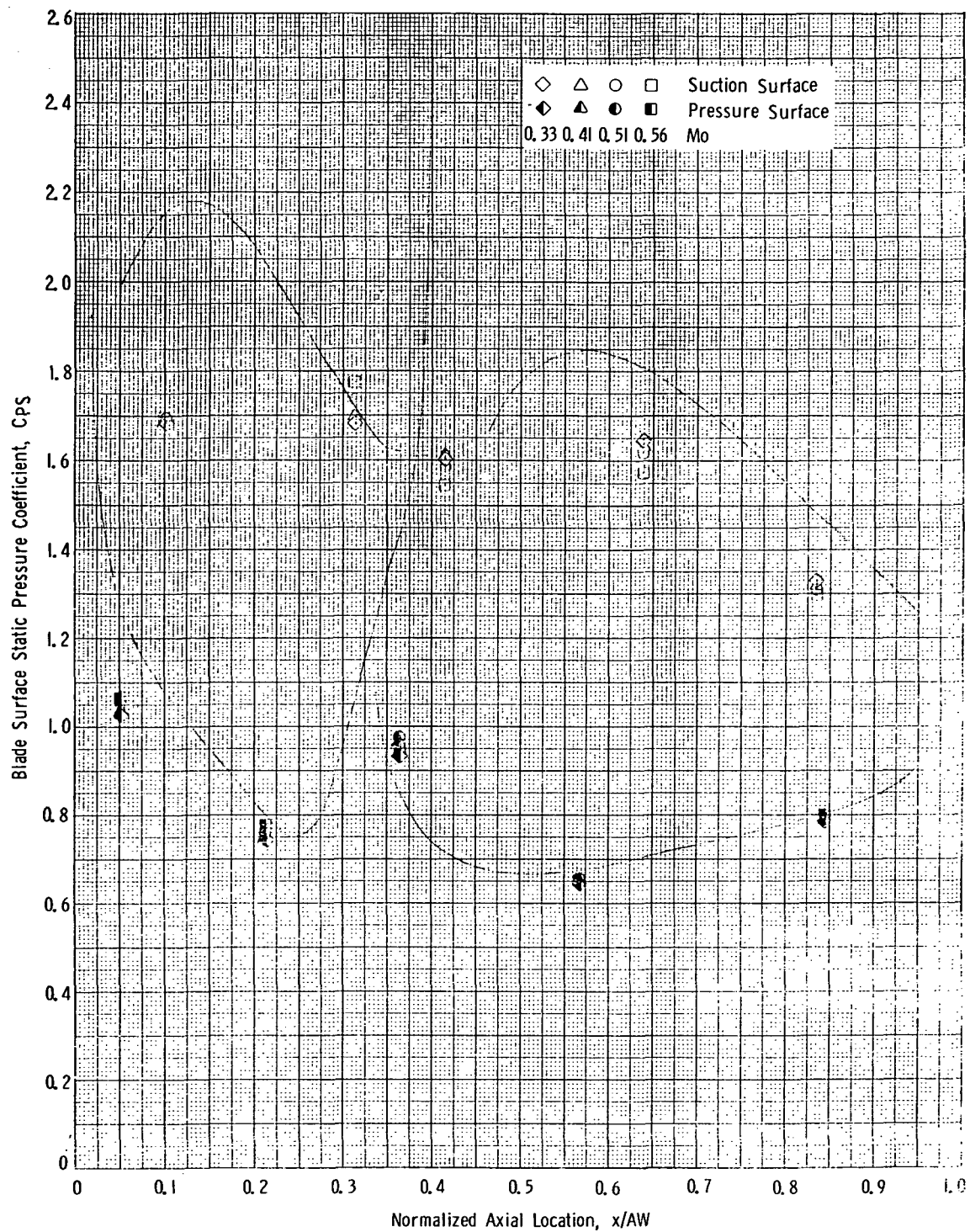


Figure 104. Blade Surface Static Pressure Coefficient Vs. Normalized Axial Location, TB3R, e_t Reduced, $i = -4.3^\circ$.

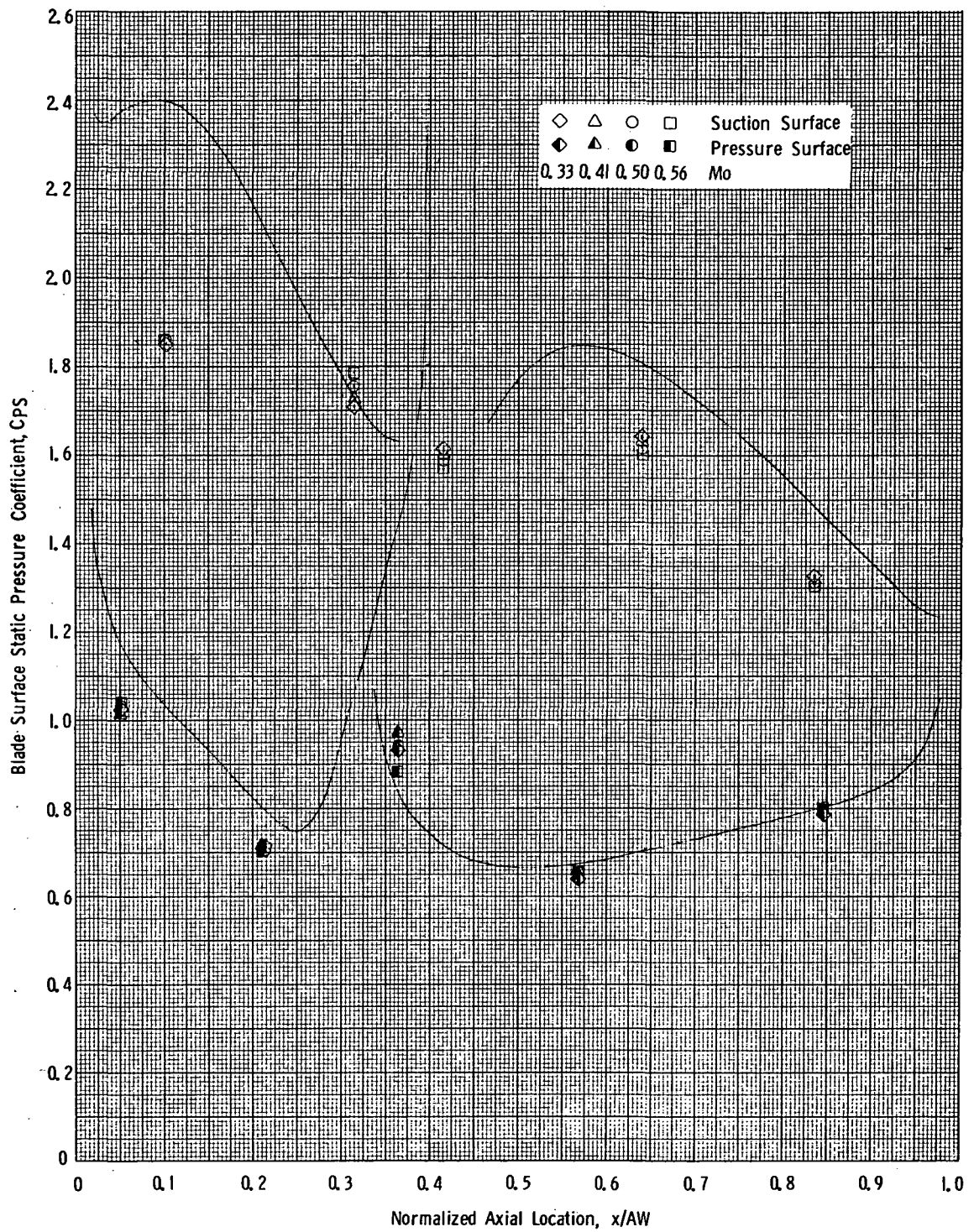


Figure 105. Blade Surface Static Pressure Coefficient Vs. Normalized Axial Location, TB3R, e_t Reduced, $i = -0.1^\circ$.

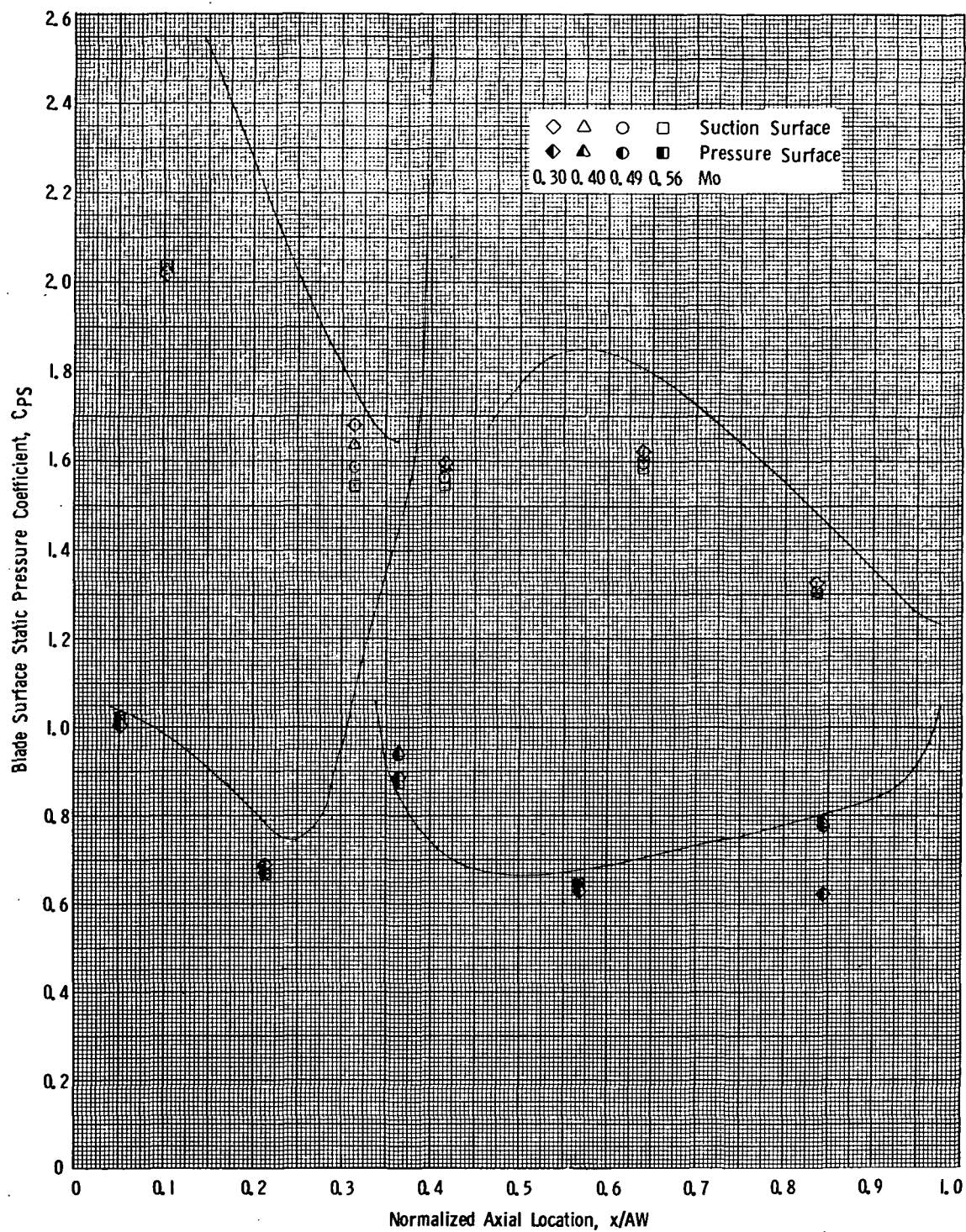


Figure 106. Blade Surface Static Pressure Coefficient Vs. Normalized Axial Location, TB3R, e_t Reduced, $i = 4.5^\circ$.

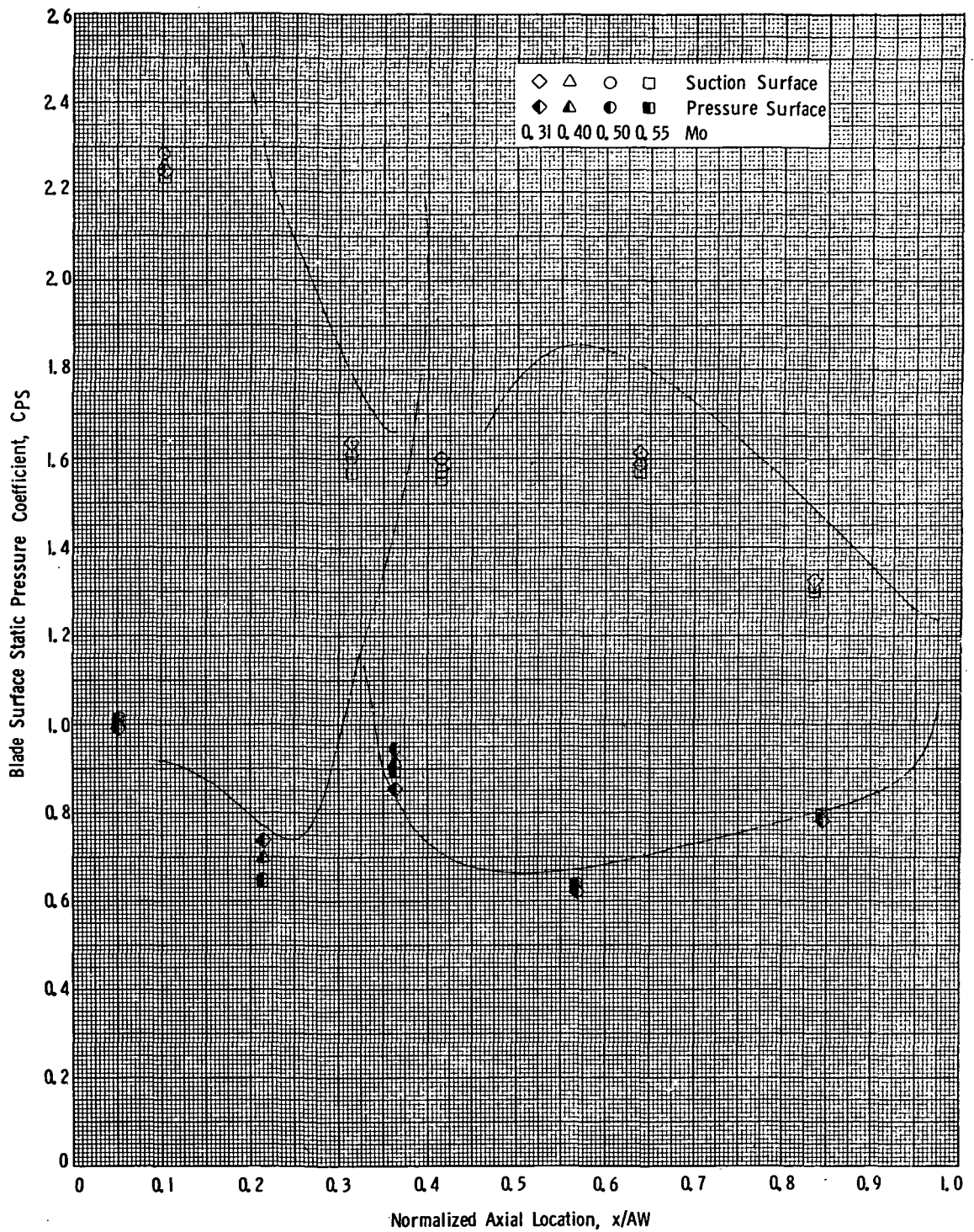


Figure 107. Blade Surface Static Pressure Coefficient Vs. Normalized Axial Location, TB3R, e_t Reduced, $i = 9.7^\circ$.

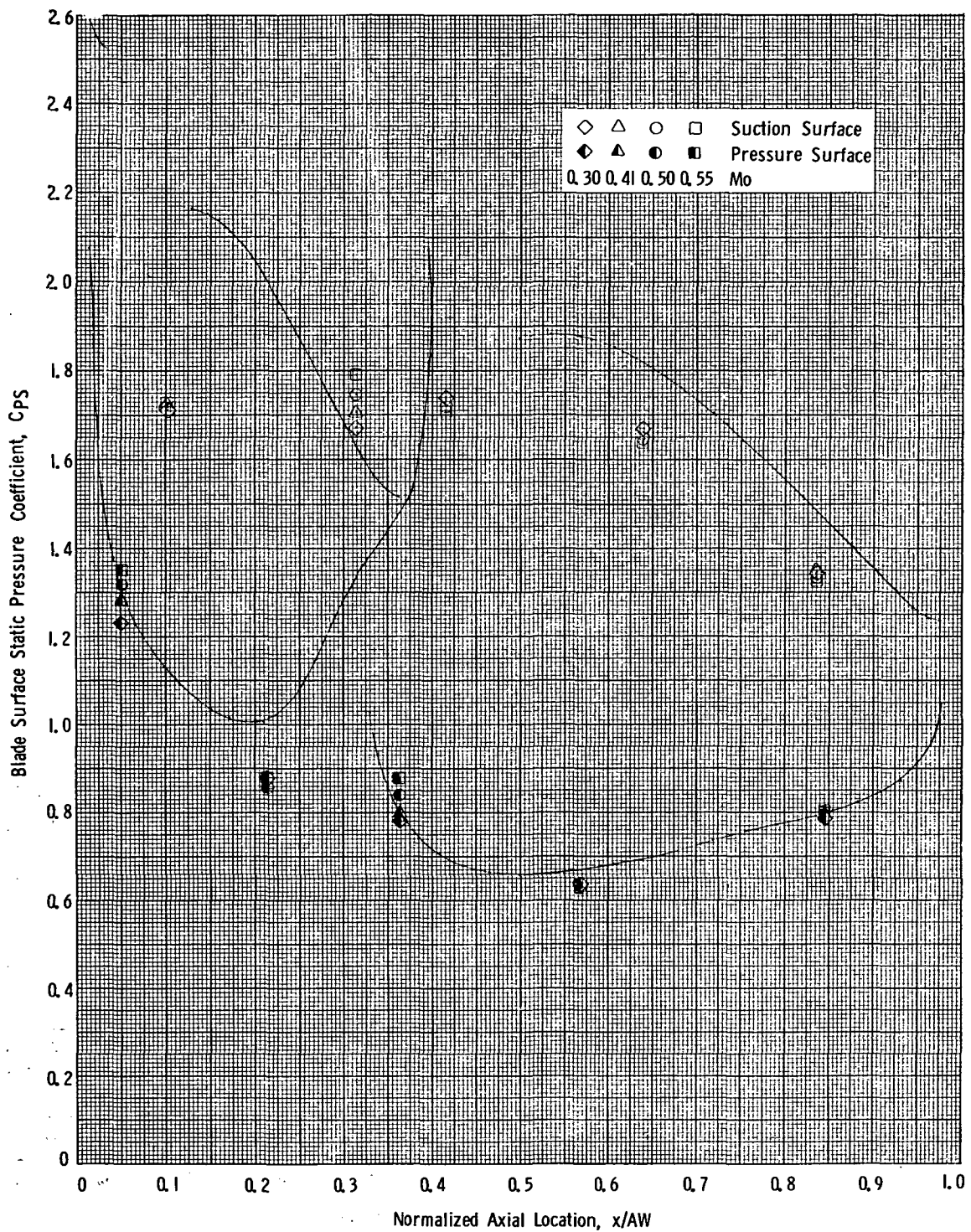


Figure 108. Blade Surface Static Pressure Coefficient Vs. Normalized Axial Location, TB3R, e_t Increased, $i = -4.3^\circ$.

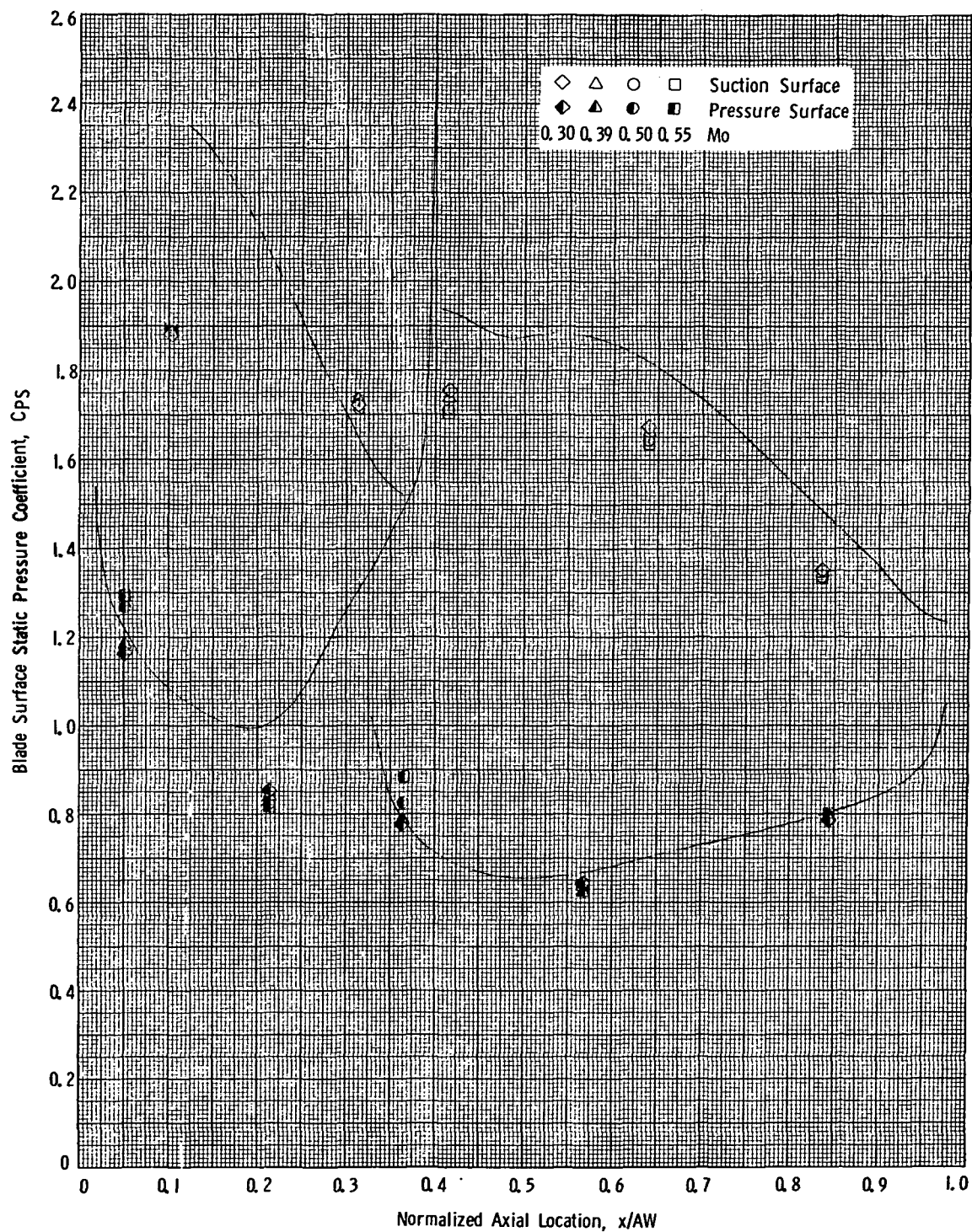


Figure 109. Blade Surface Static Pressure Coefficient Vs. Normalized Axial Location, TB3R, e_t Increased, $i = -0.3^\circ$.

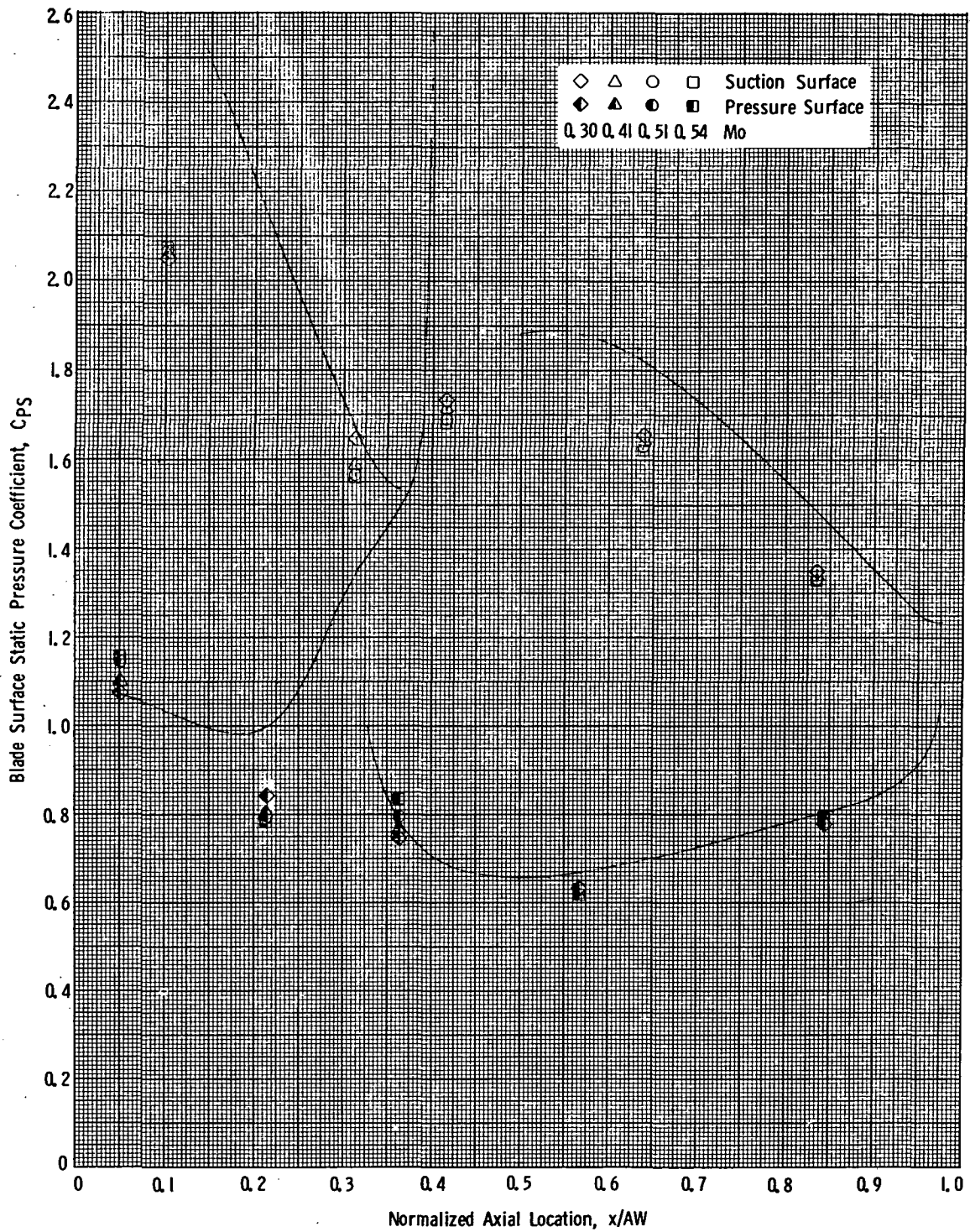


Figure 110. Blade Surface Static Pressure Coefficient Vs. Normalized Axial Location, TB3R, e_t Increased, $i = 4.3^\circ$.

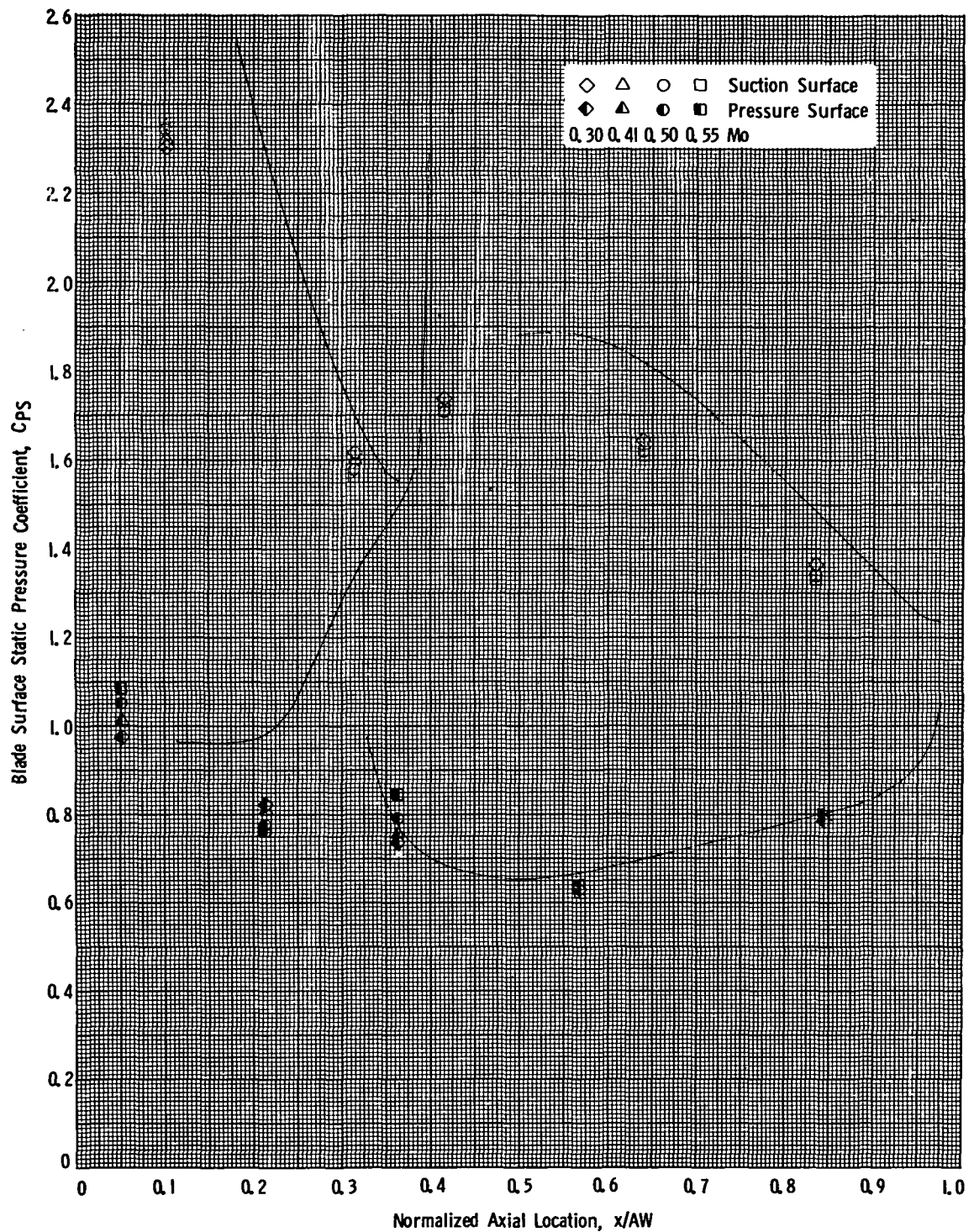


Figure 111. Blade Surface Static Pressure Coefficient Vs. Normalized Axial Location, TB3R, e_t Increased, $i = 10.7^\circ$.

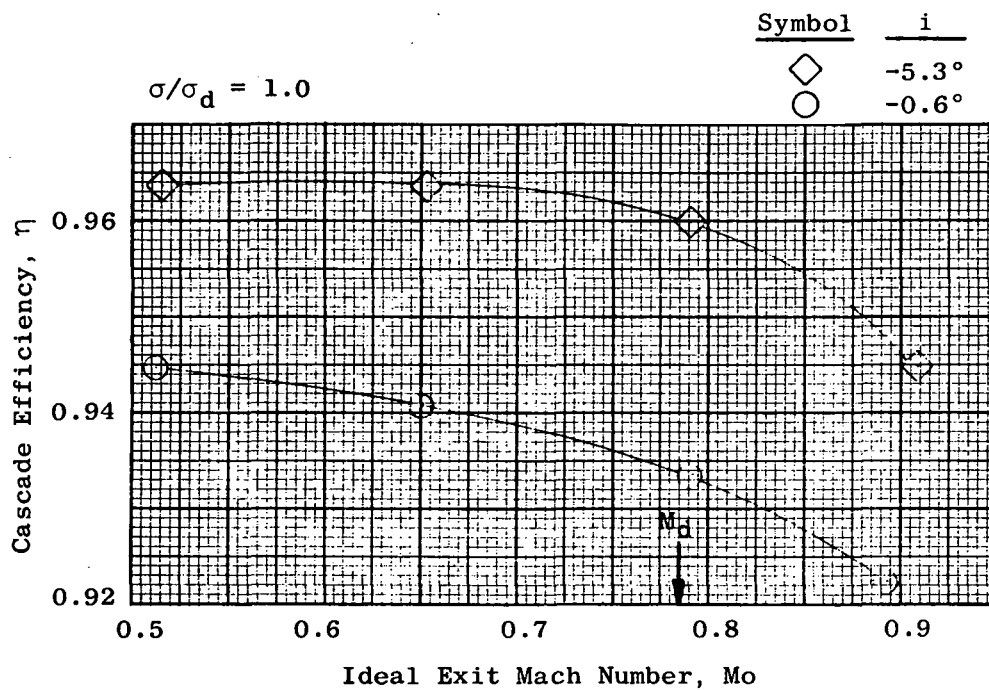


Figure 112. Cascade Efficiency Vs. Mach Number, AB1R.

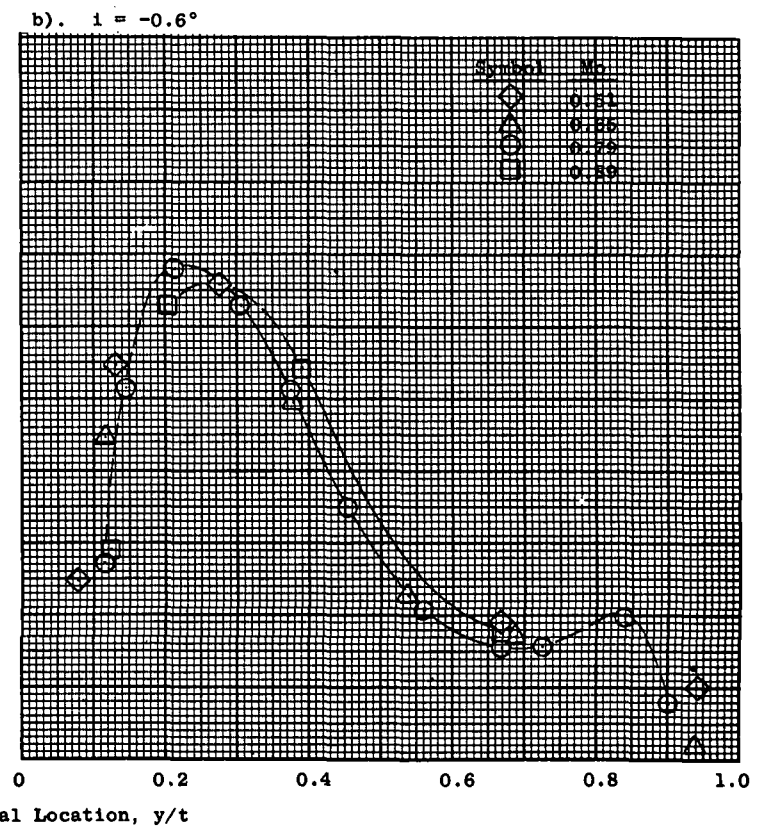
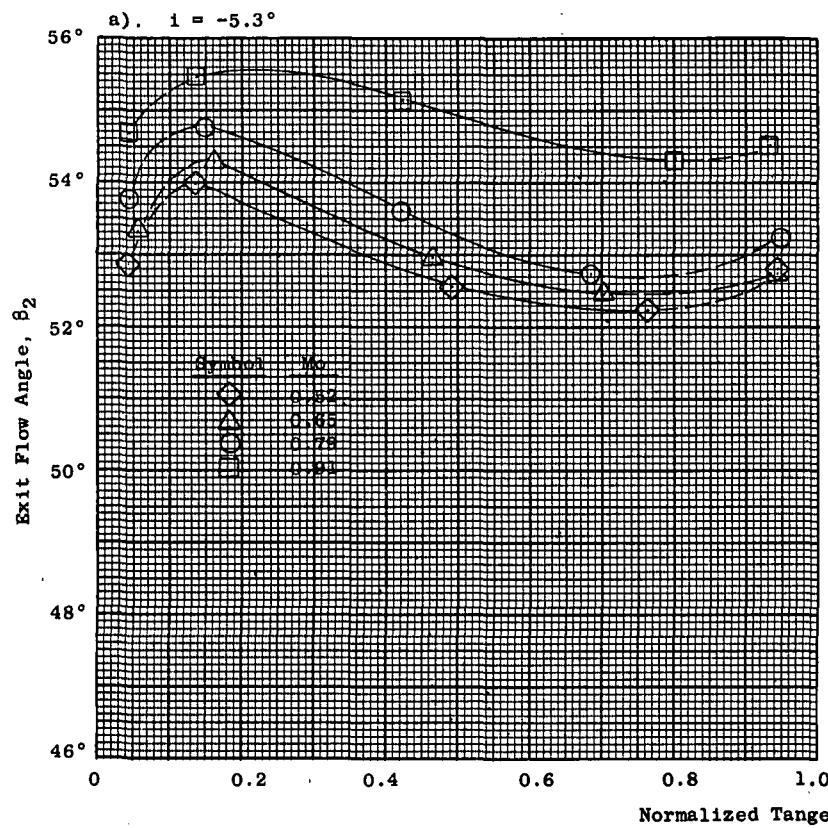


Figure 113. Exit Flow Angle Vs, Normalized Tangential Location, AB1R.

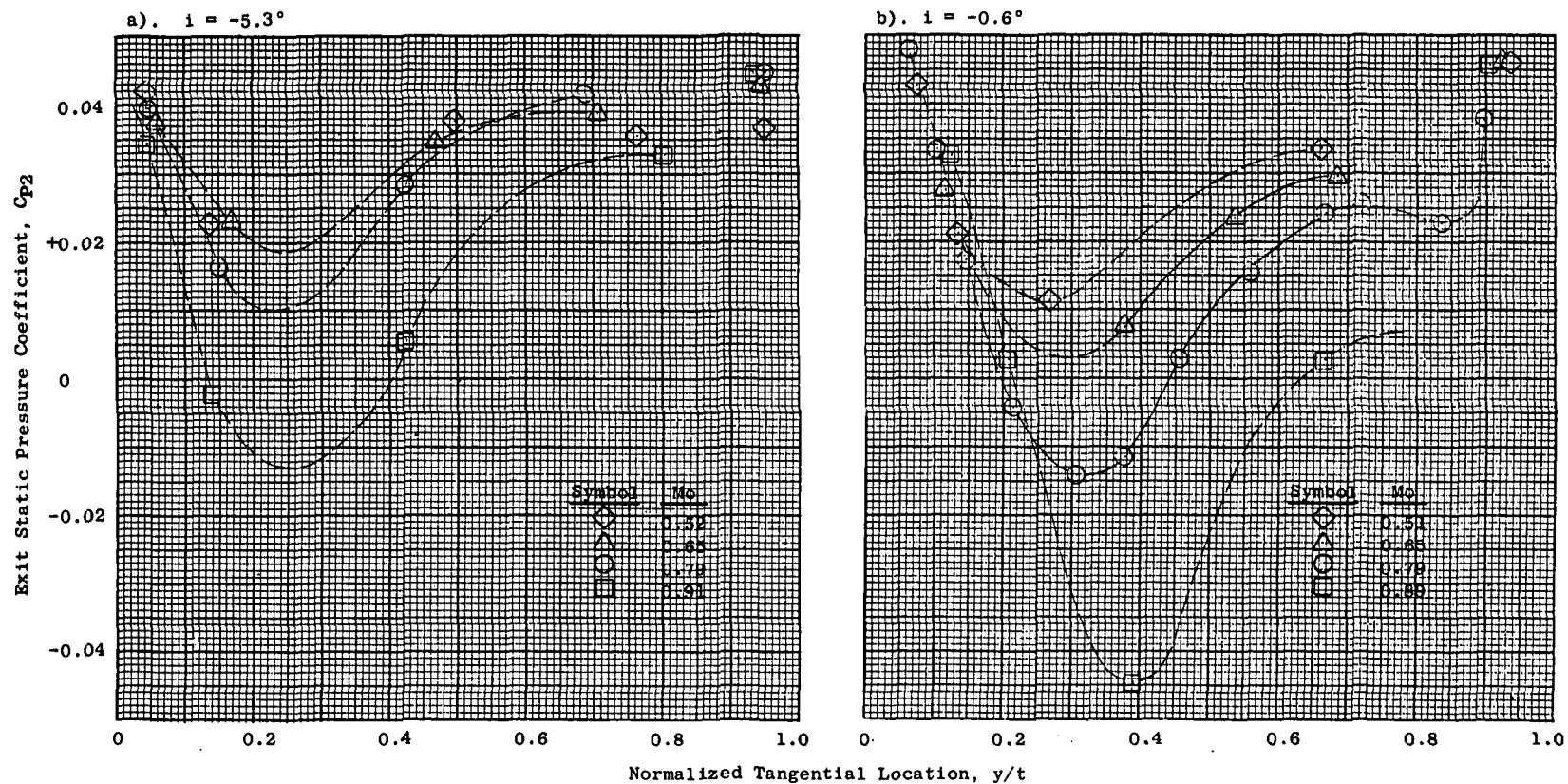


Figure 114. Exit Static Pressure Coefficient Vs. Normalized Tangential Location, AB1R.

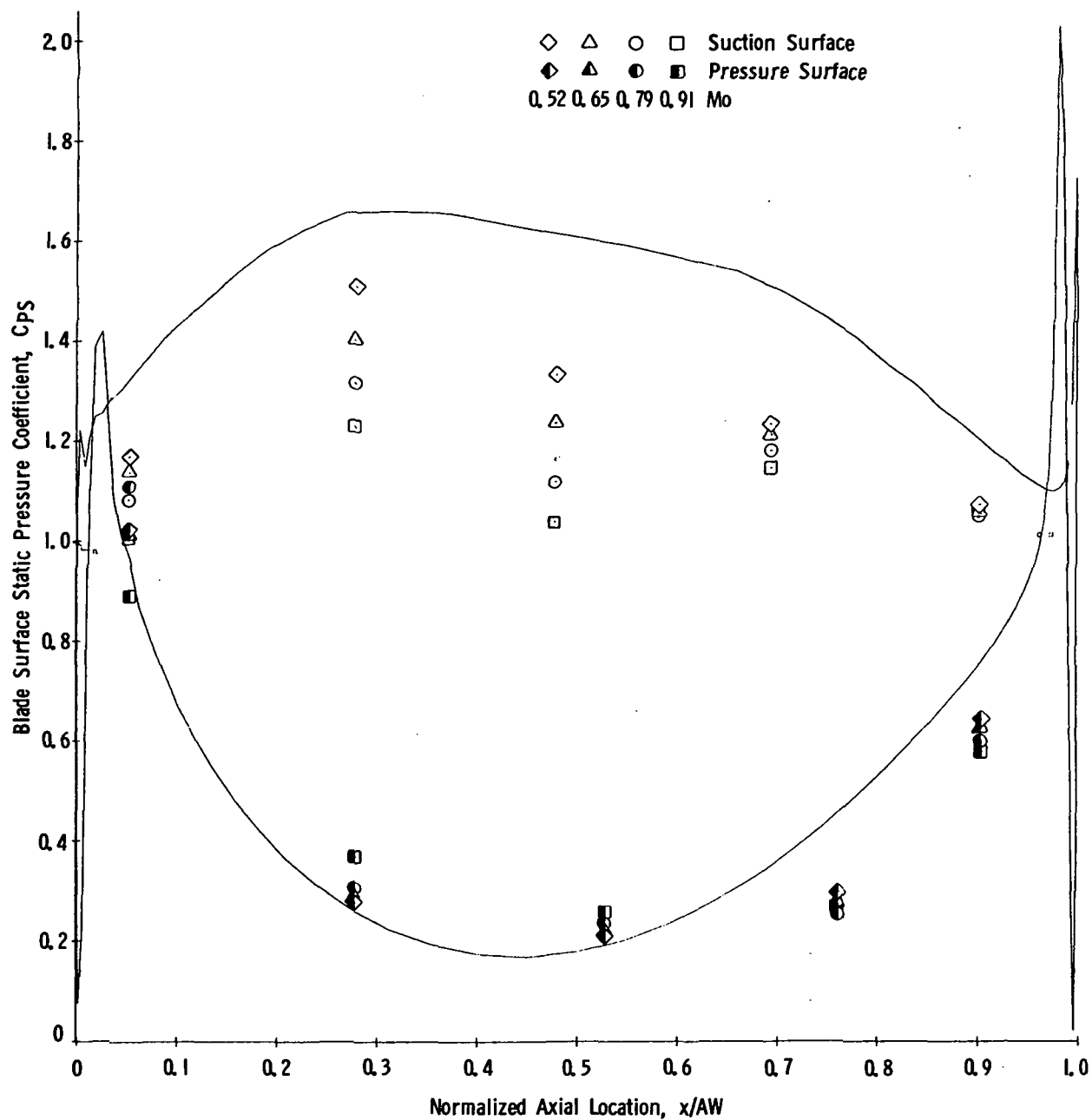


Figure 115. Blade Surface Static Pressure Coefficient Vs. Normalized Axial Location, AB1R, $\sigma/\sigma_d = 1.0$, $i = -5.3^\circ$.

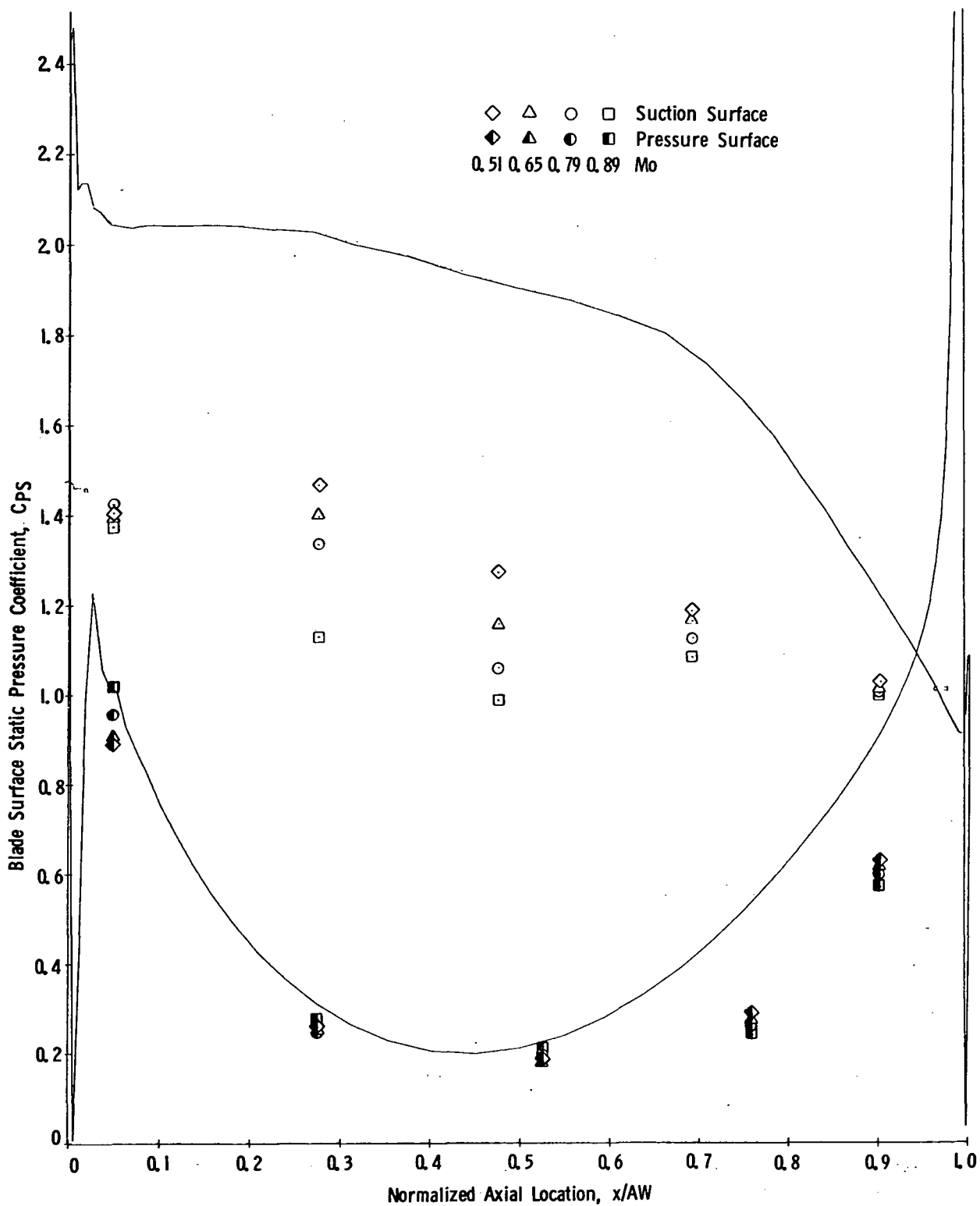


Figure 116. Blade Surface Static Pressure Coefficient Vs. Normalized Axial Location, AB1R, $\sigma/\sigma_d = 1.0$, $i = -0.6^\circ$.

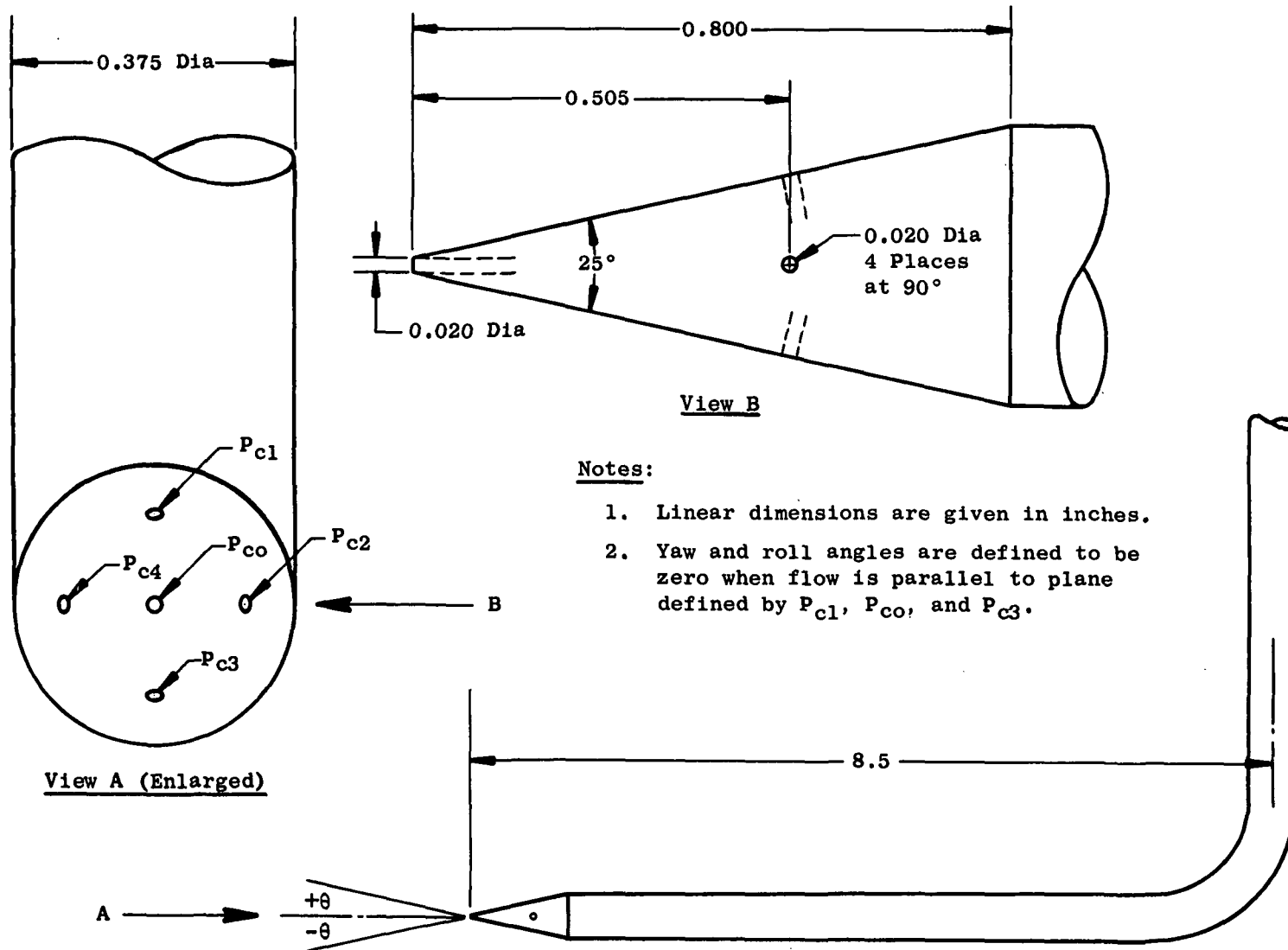


Figure 117. Probe Nomenclature and Dimensional Data.

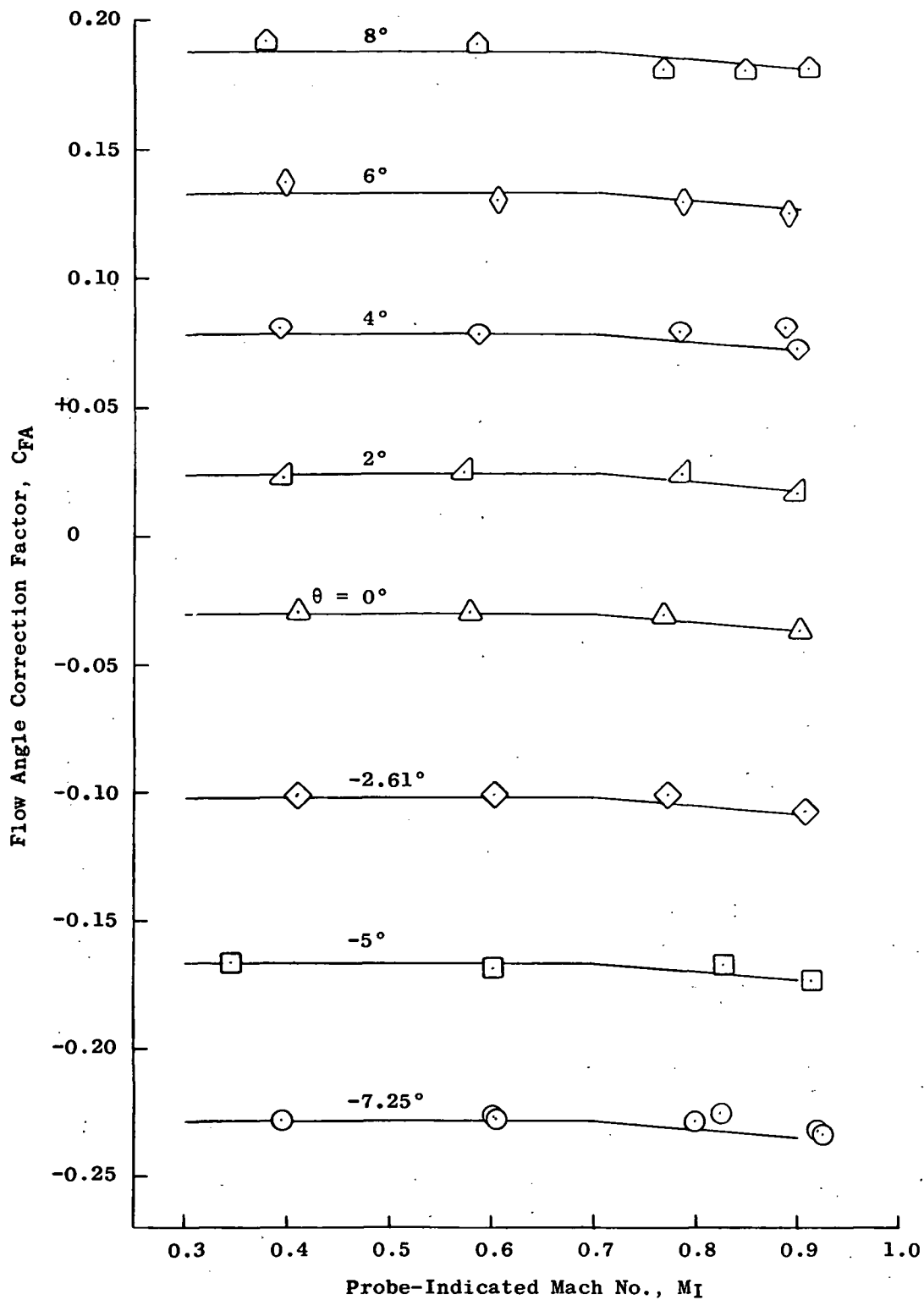


Figure 118. Probe Calibration, Flow Angle Correction Factor.

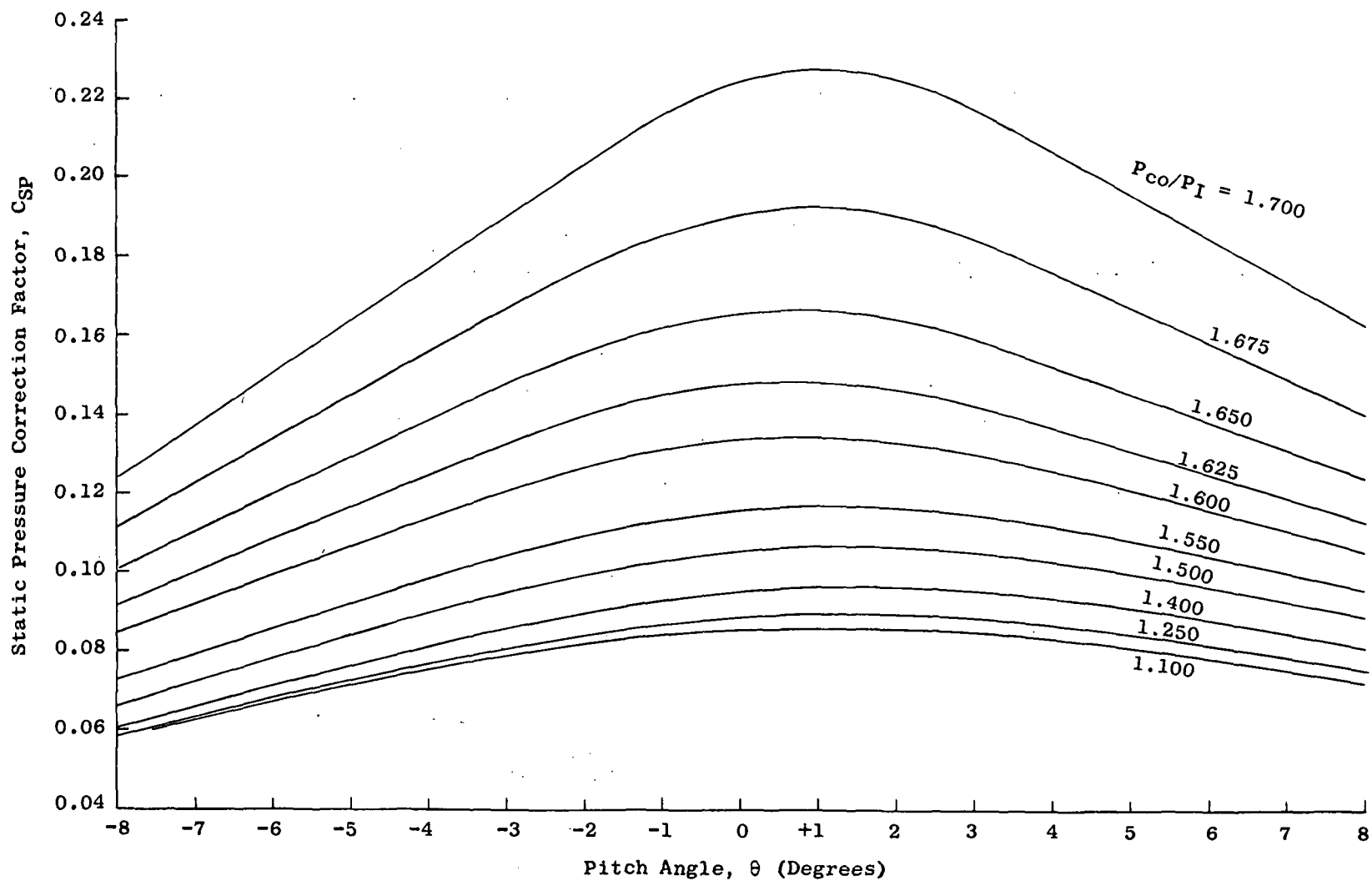


Figure 119. Probe Calibration, Static Pressure Correction Factor, P_{co}/P_I Parametric.

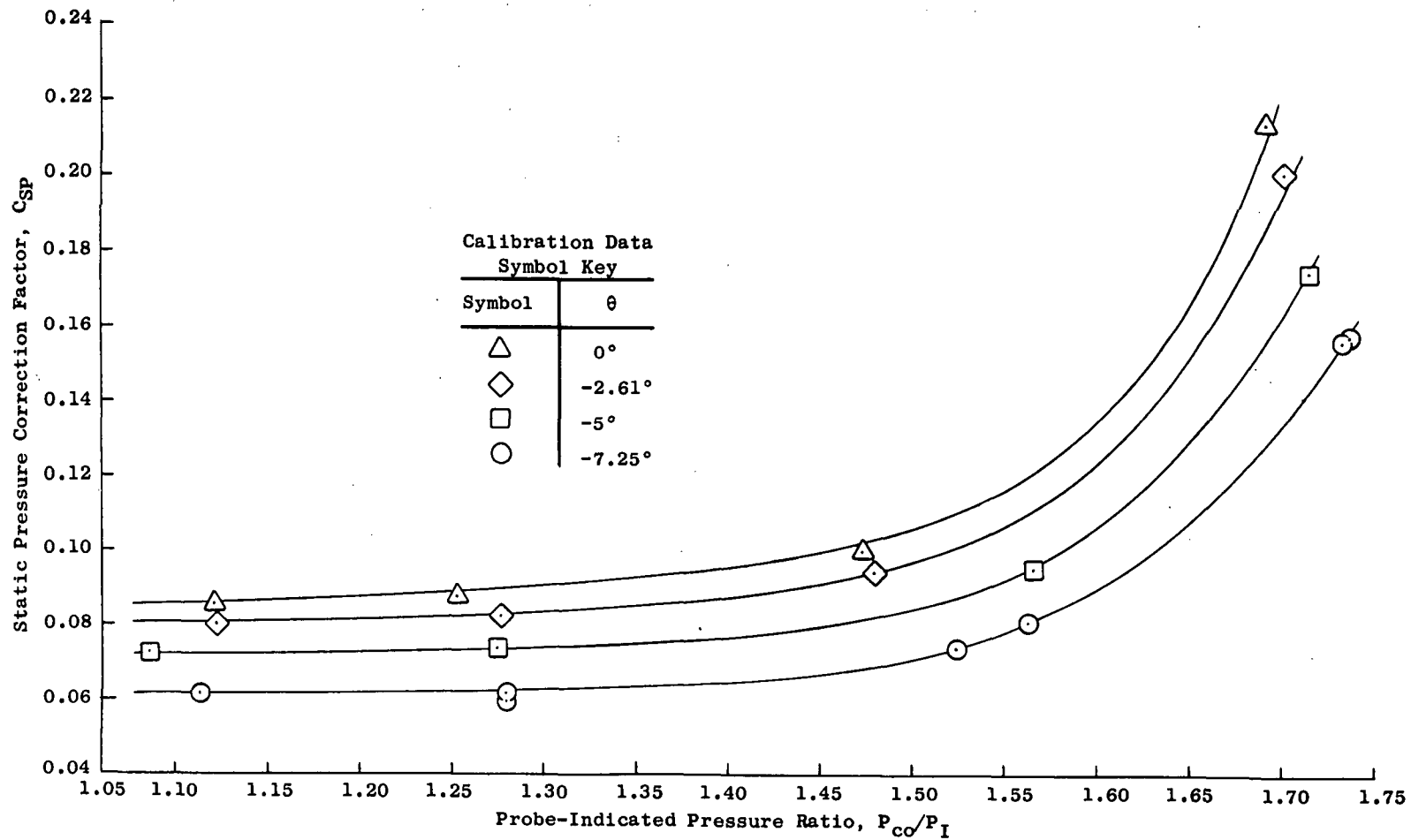


Figure 120. Probe Calibration, Static Pressure Correction Factor, θ Parametric, Negative Incidence.

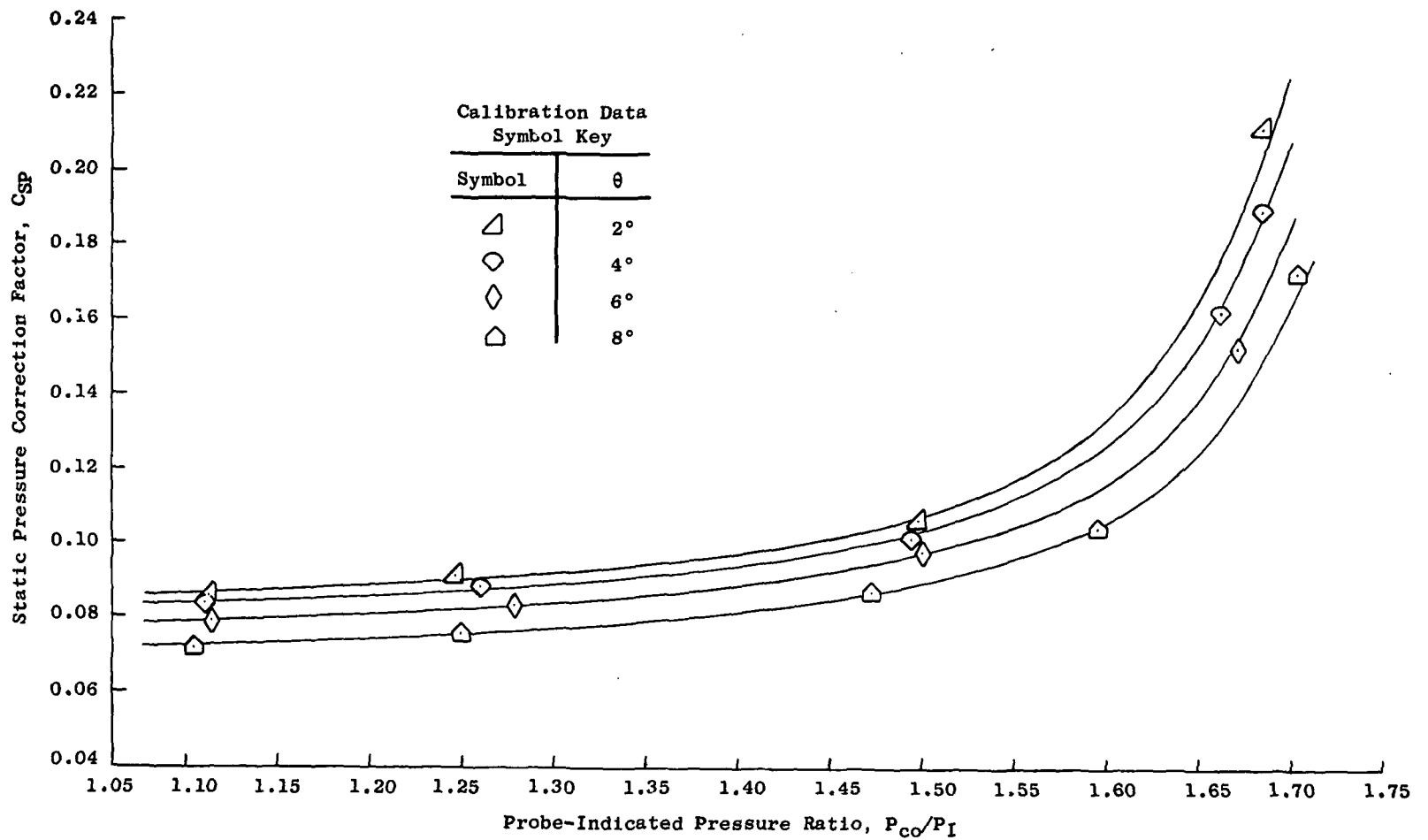


Figure 121. Probe Calibration, Static Pressure Correction Factor, θ Parametric, Positive Incidence.